

# 中国科学技术大学

# 博士学位论文



## Development of Advanced Gaseous Detectors for Muon Tracking and Triggering in Collider Experiments

作者姓名: 管 亮

学科专业: 粒子物理与原子核物理

导师姓名: 汪晓莲 教授 赵政国 教授

朱俊杰 教授

完成时间: 二〇一四年十月





用于大型粒子对撞机实验缪子触发和径迹测量的高级气体探测器研究

四系

管亮

中国科学技术大学



## 中国科学技术大学学位论文原创性声明

本人声明所呈交的学位论文,是本人在导师指导下进行研究工作所取得的成果。除已特别加以标注和致谢的地方外,论文中不包含任何他人已经发表或撰写过的研究成果。与我一同工作的同志对本研究所做的贡献均已在论文中作了明确的说明。

作者签名: \_\_\_\_\_ 签字日期: \_\_\_\_\_

## 中国科学技术大学学位论文授权使用声明

作为申请学位的条件之一,学位论文著作权拥有者授权中国科学技术大学拥有学位论文的部分使用权,即:学校有权按有关规定向国家有关部门或机构送交论文的复印件和电子版,允许论文被查阅和借阅,可以将学位论文编入《中国学位论文全文数据库》等有关数据库进行检索,可以采用影印、缩印或扫描等复制手段保存、汇编学位论文。本人提交的电子文档的内容和纸质论文的内容相一致。

保密的学位论文在解密后也遵守此规定。

☐ 公开 ☐ 保密 \_\_\_\_\_ 年

作者签名: \_\_\_\_\_ 导师签名: \_\_\_\_\_

签字日期: \_\_\_\_\_ 签字日期: \_\_\_\_\_

本论文受到核探测器与核电子学国家重点实验室、国家留学基金委和以下基金支持:  
10775132, 11075156, 11275195.



## 摘 要

现有和未来计划中的高亮度高能量对撞机实验对用于缪子径迹测量和触发判选的传统气体探测器带来巨大挑战。实验对探测器的位置分辨,时间分辨和计数率等同时提出了极其苛刻的要求。本论文介绍在欧洲核子中心ATLAS缪子谱仪升级研究框架下对用于未来对撞机实验缪子触发和径迹测量的新型高级气体探测器的大量研究和发展。论文研究主要围绕微网格气体探测器(Micromegas),窄气隙阻性板室(RPC)和窄隙室(TGC)的相关研究展开。

论文第一部分主要介绍一种新的基于热熔胶热粘接工艺制作微网格气体探测器的方法。相较于传统制作工艺,该制作方法不需要运用光刻蚀技术,使得在普通学校和研究所制作小型模型室用于性能研究和探测器优化成为可能。论文将介绍基于小型热粘接微网格气体探测器模型室所进行的探测器基本性能测试和模拟研究,以及对制作可实际应用的几百平方厘米大小热粘接微网格气体探测器技术工艺的探索。鉴于该制作工艺的灵活性,实验制作了高阻性阳极微网格气体探测器和快信号多层丝网电极平行电离室,对微网格类型气体探测器应用于强子对撞机环境的关键问题-抗打火和快时间分辨进行了探索研究。

论文第二部为基于 $\sim 1\text{ mm}$ 窄气隙阻性板室的高精度在线定位、快速触发系统的研究。该部分介绍为了探索研究窄气隙阻性板室在线和离线定位能力、时间分辨而展开的几次束流实验测试的详细结果。实验结果表明可以利用 $1\text{ mm}$ 左右气隙的阻性板室在探测器前端层面构建亚纳秒--亚毫米-厘米的高精度时空触发逻辑单元用于有效去除大量辐照本底、增强高能缪子的在线判选能力。对基于电木电极的阻性板室进行计数率测试研究表明,阻性板室可以在大于 $15\text{ kHz/cm}^2$ 光子辐照本底下对缪子探测完全灵敏。

论文第三部分介绍对ATLAS缪子谱仪新内端盖(New Small Wheel, NSW)的触发探测器-窄读出条窄隙室的模拟研究。对时间分辨的模拟研究表明单层窄气隙室即可满足对大型强子对撞机束团对撞的区分。其时间分辨不受端盖处所处复杂磁场的影响,从时间性能考虑,可有效胜任端盖处一级缪子触发。对窄隙室电荷产生和信号扩散的详细研究中构建一个数值分析模型。该模型很好的重现了束流测试的读出条信号分布,对深入理解探测器信号的发展、优化探测器结构以实现更高定位精度具有重要指导意义。

**关键词:** 对撞机实验, 缪子触发和径迹测量, 微网格气体探测器, 阻性板室, 窄隙室



# **Development of Advanced Gaseous Detectors for Muon Tracking and Triggering in Collider Experiments**



**Liang Guan**

A dissertation submitted to the faculty of  
University of Science and Technology of China  
in partial fulfillment of the requirements for the degree of

Doctor of Philosophy

Prof. Xiaolian Wang, Prof. Zhengguo Zhao and Prof. Junjie Zhu, Supervisors

Department of Modern Physics

University of Science and Technology of China

October 2014

Copyright © 2014 Liang Guan

All Rights Reserved



## ABSTRACT

# Development of Advanced Gaseous Detectors for Muon Tracking and Triggering in Collider Experiments

**Liang Guan**

Department of Modern Physics  
University of Science and Technology of China  
Doctor of Philosophy

High luminosity and high energy collider experiments impose big challenges to conventional gaseous detectors used for muon tracking and triggering. Stringent requirements, in terms of time and spatial resolutions, rate capabilities etc. are expected. In the context of ATLAS muon upgrade project, we present extensive researches and developments of advanced gas detectors for precision muon tracking and triggering in high rate environments. Particularly, this dissertation focuses on the studies of Micro-mesh Gaseous structure (Micromegas), thin gap Resistive Plate Chamber (RPC) and small strip Thin Gap multi-wire Chambers (sTGC).

In this dissertation, we first present a novel method, based on thermally bonding micro-meshes to anodes, to construct Micromegas detectors. Without employing the traditional photo-lithography process, it is a convenient alternative to build Micromegas. Both experimental and simulation studies of basic performance parameters of thermo-bonded Micromegas will be reported. Development of a new spark-tolerant resistive Micromegas and a fast timing parallel ionization multiplier will be introduced.

Studies on precision tracking and fast triggering based on  $\sim 1$  mm thick thin gap RPCs are reported in the second part. Several beam tests are carried out to explore the timing performance, both on-line and off-line spatial resolutions of thin gap RPCs. Results show that (sub-ns  $\times$  sub-mm  $\times$  cm) logic cells could be realized with thin gap RPCs. High granularity in space and time will be very powerful to remove backgrounds and the precision on-line tracking capability will be precious to improve high momentum muon selectivity. Rate capability measurements of Bakelite RPCs are performed and results show that RPCs with thin gap design could be fully efficient to muons at greater than 15 kHz/cm<sup>2</sup> detected rate.

Simulation studies of the characteristics and performance of ATLAS New Small Wheel (NSW) primary trigger detector-sTGC will be reported in the last part. The timing performance study suggests that sTGC is capable to perform LHC bunch crossing identification in Small Wheel environment. An analytical model is built to describe the charge sharing among sTGC readout strips and understand the required spatial resolution of  $\mathcal{O}(100)$   $\mu\text{m}$  for the ATLAS NSW upgrade.

**Keywords:** Collider Experiments, Muon, Trigger and Tracking, Micromegas, RPC, TGC



## ACKNOWLEDGMENTS

First of all, I am deeply indebted to my supervisors Prof. Xiaolian Wang, Prof. Zhengguo Zhao and Prof. Junjie Zhu, who are unbelievably great and knowledgeable mentors and friends. I am grateful to them for providing me such precious opportunity to work on high energy physics and helping me to achieve this accomplishment. I would like to also express my greatest gratitude to Prof. Bing Zhou who actually acts as my second supervisor during my study at the University of Michigan (UM). She is always encouraging me to find and address questions independently.

I would like to thank Prof. Zizong Xu, Prof. Tianchi Zhao, Prof. Hongfang Chen, Prof. Cheng Li, Prof. Liang Han, Prof. Ming Shao, Prof. Jianbei Liu and Prof. Yanwen Liu for their patient guidance and many useful discussions. I would like to express my appreciations to the UM ATLAS members, especially Prof. John Chapman, Prof. Dante Amidei, Dr. Edward Diehl, Dr. Bob Ball, for their continuous supports and suggestions to my research work. Special thank goes to Dr. Tiesheng Dai, who taught me everything I know about electronics and beam tests. I would like to thank my friends Haolv Feng, Lorenzo Paolozzi, Hongye Song, Haohui Tang, Jinfu Wu, Yusheng Wu, Lailin Xu, Zhiyong Zhang and many others for many joyful and fruitful times.

I would like to thank all my colleagues and friends in the ATLAS muon community for fruitful discussions and uncountable helps during beam tests. Particularly, I would like to mention Dr. Jörg Wotschack, Prof. Giora Mikenberg, Prof. Roberto Cardarelli, Dr. Giulio Aielli, Dr. Jörg Dubbert, Dr. Vladimir Smakhtin, Dr. Meir Shoa and Dr. Yan Benhammou. They have taught me to work both independently and collaboratively. I would like to express my gratitude to Dr. Crispin Williams and Roman Zuyeuski for hosting me in their lab for research on RPC and helping us on the DAQ and trigger system. I would like to thank Dr. Rob Veenhof for inspiring discussions on gaseous detector simulation.

Last but not least, I would like to thank my parents and other family members, especially Dingcui Cai and Ping Wang, for their unconditional love, care and tolerance.



# Contents

<b>Table of Contents</b>	<b>vii</b>
<b>1 Introduction</b>	<b>1</b>
<b>2 A Brief History of Gaseous Detectors</b>	<b>5</b>
2.1 Birth of gaseous detector . . . . .	5
2.2 Geiger counter-detection of single radiation . . . . .	6
2.3 Ionization chamber- discovery from energy measurement . . . . .	9
2.4 Spark chamber- viewing traces from invisibles . . . . .	10
2.5 Wire chambers - boosting discoveries . . . . .	12
2.6 RPC and MPGD - shading lights to future . . . . .	17
2.7 Summary . . . . .	20
<b>3 Principles of Gaseous Detectors</b>	<b>23</b>
3.1 Interaction of charged particles in matter . . . . .	24
3.1.1 Energy loss in matter . . . . .	25
3.1.2 Fluctuation of energy loss in thin absorbers . . . . .	29
3.2 Interaction of photons and neutrons with matter . . . . .	32
3.2.1 Detecting photons . . . . .	32
3.2.2 Detecting neutrons . . . . .	34
3.3 Ionizations in gas . . . . .	35
3.4 Electron and ion transportation . . . . .	39
3.4.1 Drift of electrons in gas . . . . .	40
3.4.2 Drift of ions in gas . . . . .	47
3.5 Avalanche . . . . .	49
3.5.1 Electron multiplication under electric field . . . . .	49
3.5.2 Statistical fluctuations of avalanches . . . . .	52
3.6 Signal induction . . . . .	56
3.6.1 Induced signals from parallel plate structure detectors . . . . .	56
3.6.2 Induced signals from cylinder shape counters . . . . .	58
3.6.3 Signal induced on multiple electrodes . . . . .	60

<b>4</b>	<b>Thermo-bonded Micromegas</b>	<b>63</b>
4.1	Overview	63
4.2	Fabrication of Micromegas with thermo-bonded spacers	66
4.2.1	Micro-meshes and Thermo-bond films	67
4.2.2	Materials qualifications and fabrication procedures	70
4.2.3	Thermal bonding with different tools	79
4.3	Measurement of basic performance parameters	83
4.3.1	Experimental setup	84
4.3.2	Electron transparency	87
4.3.3	Gas Gain and Energy Resolution	90
4.3.4	Uniformity	93
4.4	Simulation studies	100
4.4.1	Penning effect	101
4.4.2	Electron transparency	105
4.4.3	Gain variation	111
4.5	Micromegas with high resistivity anode	114
4.5.1	Introduction and motivations	114
4.5.2	Resistive materials, prototypes and experimental setup	117
4.5.3	Basic performances	120
4.5.4	Rate capabilities	124
4.5.5	Spark probability and tolerance	125
4.6	Parallel ionization multiplier (PIM)	128
4.6.1	Calculation and simulation of fast signal component	129
4.6.2	Electron transmission optimization	132
4.6.3	Prototype fabrication and preliminary tests	135
4.7	Summary	138
<b>5</b>	<b>Thin-gap Resistive Plate Chambers</b>	<b>143</b>
5.1	Introduction	143
5.2	Thin-gap RPC for fast precision muon triggering	148
5.3	Beam test using MDT readout system	151
5.3.1	Beam test setup	151
5.3.2	MDT readout front-end electronics	154
5.3.3	Results	159
5.4	Beam test using NINO based readout system	175
5.4.1	Beam test setup	176
5.4.2	NINO ASIC based readout system	179
5.4.3	Results	187
5.5	Rate capability measurements	200
5.5.1	Introduction	200
5.5.2	Setup and results	202
5.6	Summary	205

---

<b>6</b>	<b>Small-strip Thin Gap Chamber</b>	<b>207</b>
6.1	Introduction . . . . .	207
6.2	Electric field simulation . . . . .	210
6.3	Ionization and electron transportation . . . . .	212
6.3.1	Electron-gas molecular interaction and ionization . . . . .	212
6.3.2	Electron transportation . . . . .	214
6.4	Charge production . . . . .	217
6.4.1	The electron avalanche and its fluctuation . . . . .	217
6.4.2	Induced charge component and charge collection . . . . .	219
6.4.3	Gas gain . . . . .	222
6.5	Timing performance . . . . .	224
6.5.1	Earliest cluster arrival time . . . . .	226
6.5.2	Single layer time spectrum . . . . .	228
6.6	Strip charge sharing . . . . .	230
6.6.1	Raw charge spread on cathode . . . . .	231
6.6.2	Charge dispersion . . . . .	235
6.6.3	PSpice simulation . . . . .	238
6.7	Summary . . . . .	240
<b>7</b>	<b>Summary and outlook</b>	<b>243</b>
	<b>Bibliography</b>	<b>247</b>
<b>A</b>	<b>List of Publications</b>	<b>269</b>



# Chapter 1

## Introduction

The discovery of a standard model compatible scalar boson [1,2] revolutionizes our understanding of nature and matter. It opens a new era for elementary particle physics. However, the journey of the discovery is extremely tough as the tiny signatures of new particles are buried inside remarkably large amount of backgrounds. It is only made possible with modern complex and powerful high energy accelerators as well as sophisticated giant particle spectrometers. As one of the core part is to hunt for possible new particles and phenomena, the particle spectrometer records kinetic and kinematic information of electrons, muons, photons and jets from the decay of heavy particles. In hadron collider experiments, searching for new particles via leptonic channels are very important and of great concern as these channels provide clean signals over enormous QCD backgrounds. Since recording every collision data is impossible, triggering and selecting most interested high energy hard collision events at the hardware level are very crucial . This selection is usually partly done by muon spectrometers, as most muons are penetrating particles. Precision tracking of muons is also highly demanding as it will affect the energy resolution of reconstructed heavy particles.

The muon tracking and triggering in collider experiments are performed by thousand square meters of gaseous detectors due to their scalability, good localization capability. In addition, they are cheap and easy in construction, and they have low material budget which could minimize mul-

multiple scatterings. Taking the ATLAS muon spectrometer as an example, it implements monitored drift tube chambers (MDT) as precision tracking detectors and utilizes resistive plate chambers (RPC) at the barrel and thin gap multi-wire chambers (TGC) plus cathode strip chambers (CSC) at the end-cap for muon triggering. However, muon triggering and tracking with ATLAS spectrometer will be increasingly challenging as the LHC will upgrade in several phases to reach a center of mass energy of 14 TeV and an instant luminosity of  $5\text{--}7 \times 10^{34} \text{ cm}^{-2}\text{s}^{-1}$ . High energy and high luminosity collisions mean that detectors will be exposed to high radiation backgrounds, especially in the forward region. Degradations of MDT spatial resolutions are expected due to the space charge effect and the gain reduction. Additionally, as shown in figure 1.1, the muon level-1 triggering in ATLAS, which is the part of the very first level event selection, only relies on three layers of TGCs at the middle station of the end-cap in the present system. Trigger rates of high momentum ( $p_T > 10 \text{ GeV}$ ) muons are found to be dominantly from the end-cap. Only less than 10% of triggered muons are associated with off-line muons. These “fake” triggers are mostly from cavern backgrounds and it will be very difficult for the present system to maintain the level-1 trigger bandwidth ( $\sim 100 \text{ kHz}$  including calorimeter level-1 trigger) and effectively select high momentum muons.

To profit from the planned LHC upgrade and address the aforementioned challenges in muon tracking and triggering so that the power of searching for new physics could be extended, ATLAS will upgrade the innermost station of its forward muon system after the second long shut down (LS2). The innermost station, named as small wheel, will be replaced by a New Small Wheel (NSW) [3]. Requirements for the NSW are listed in the following:

- Muon momentum resolution:  $< 15\%$  at 1 TeV
- Efficiency:  $> 97\%$  at  $p_T > 10 \text{ GeV}$
- On-line pointing accuracy: 1 mrad

- Timing: capable of LHC bunch crossing identification
- Operate with radiation background: up to  $15 \text{ kHz/cm}^2$  in the inner most region
- Ageing: No degradation up to an accumulated charge of  $1 \text{ C/cm}^2$  (with  $3000 \text{ fb}^{-1}$  integrated luminosity)

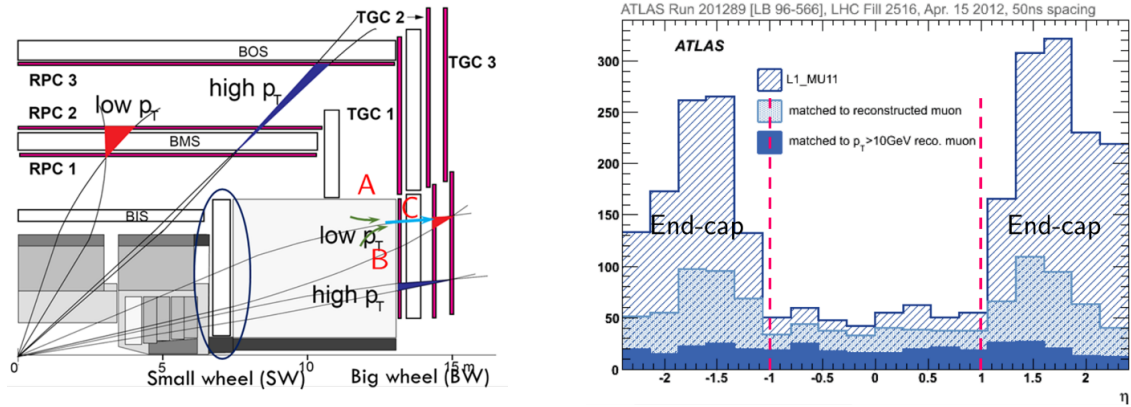


**Figure 1.1** A side view of 1/4 ATLAS muon trigger system (left) and  $\eta$  distribution of Level-1 triggered muon ( $p_T > 10 \text{ GeV}$ ) superimposed with  $\eta$  distribution of off-line reconstructed muons (right).

In the context of the ATLAS muon system upgrade, extensive studies are carried out on three types of advanced gaseous detectors: Micro-mesh gaseous structure detector (Micromegas), Resistive Plate Chamber (RPC) and Thin Gap multi-wire Chamber (TGC). All these detectors will be used in the upgraded ATLAS muon spectrometer. However, developments on these muon tracking and triggering devices could be extended to other applications in future collider experiments.

The content of this dissertation is organized as follows. A brief review of the development of gaseous detectors and their roles in historic discoveries will be given in chapter 2. Fundamental principles of particle interactions with the matter and the detection of particles using gaseous detectors will be introduced in chapter 3. Chapter 4 presents the development of a novel method

to fabricate Micromegas detectors, simulation of Micromegas characteristics, studies on spark-tolerant high resistivity anode Micromegas and fast timing parallel mesh ionization multipliers (PIM). Chapter 5 presents the second topic on studies of precision tracking and fast triggering based on thin gap RPCs. The third topic on the simulation studies of the ATLAS NSW primary trigger detector-sTGC will be presented in chapter 6. A summary and an outlook of these advanced gaseous detector developments will be given in chapter 7.

# Chapter 2

## A Brief History of Gaseous Detectors

In this chapter, a brief review of the history of the gaseous detector development is presented, with personal perspective and emphasis on how the gaseous detectors contributed to most significant discoveries of sub-atom physics from 19<sup>th</sup> century.

### 2.1 Birth of gaseous detector

The emergence of gaseous ionization detectors dates back to more than a hundred years ago, when the phenomena of spontaneous radiation was first discovered and a new era for elementary particle physics and modern physics was opened. In 1896, shortly after Rontgen discovered X-ray and Becquerel revealed the presence of radiation from uranium salt, Marie Curie used an electroscope with an ionization chamber to study the radioactive matters. She found the fact, first noticed by Becquerel, that the discharge of electroscope due to the bombardment of the invisible radiation, could be used to measure the radiation intensity. Although at that time, the charge carriers, electrons and ions, were unknown until research works were done by J.J. Thomson between 1897 and 1899 [4–7], she had already used this simplest form of gaseous detector to discover new radioactive elements, polonium and radium.

In 1912, Hess found the first evidence of radiation originating from extraterrestrial source [8]. He boarded a balloon with three Wulf electroscopes [9] to measure the radiation intensity as a function of altitude, as he was traveling up to 5 km above the ground. He observed that ionization charges produced by the radiation at high altitude were three times larger than that at the ground level, which contradicted with the assumption of the ground origination of radiations. This is another example showing that such embryonic state gaseous device has played a crucial role in historical discoveries, which take advantage of ionization effects in gas.

## 2.2 Geiger counter-detection of single radiation

In the early days, the means of detecting ionization charge with electroscopes could only use air as gas media and no amplification of the charge was involved. Ionizations caused by individual radiations were too weak to create noticeable effects. Therefore, only intense penetrating radiation can be studied. The detection of individual radiation using gas-filled detectors was not so long after the electron was discovered by Thomson. In 1908, Rutherford and Geiger developed an alpha particle counter [10], as a part of their alpha spectrometer, to deal with the problem of counting the number of emitted alpha particles. They learned the fundamental ionization mechanism discovered by Townsend [11, 12] that ions could be produced by colliding ionized particles with neutral gas molecules in strong electric fields. An automatic electrical method of alpha particle counting was developed. As depicted in figure 2.1, they constructed a detecting vessel which was a brass cylinder tube with a central wire that has a diameter of 0.45 mm. The tube was exhausted to a pressure of a few tens of mbar. The outer wall of the tube was connected to the negative pole of the battery while the central wire was connected to an electroscope. The alpha particles could be fired from a source located inside the exhausted firing tube as shown on the left side of the plot. Ionizations induced by an alpha particle entering the detecting vessel were immediately magnified

and the large current lead to a sudden movement of electroscope needles, which became easily detectable. The tube was believed to be the first cylinder-shaped gaseous detector that had ever been made. The electroscope served as a convenient readout device before modern electronics was invented. Numerous experiments using such instrument for in-depth studies of alpha radiations from various radioactive sources eventually emerged the successful explanation of the nature of alpha radiations [13, 14].

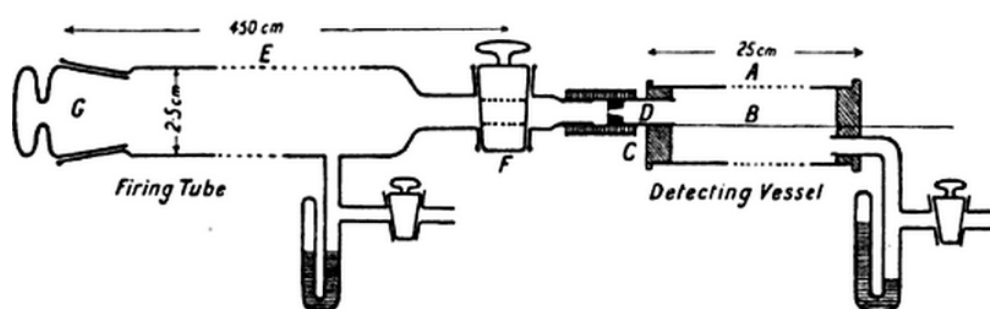


**Figure 2.1** The schematic of the gas-filled cylinder tube developed by Rutherford and Geiger to count alpha particles [10].

The counter invented by Rutherford and Geiger in 1908 was only sensitive to alpha particles and the counting rate was limited to a few counts per minute due to the long time needed for electroscope needles to discharge and settle down between successive detections of alpha particles. In 1928, together with Muller, Geiger improved the early Geiger counter and latter it became known as the Geiger-Muller counter [15]. The schematic view of the counter is shown in figure 2.2. This improved version was implemented with the vacuum tube technology, which made the tube to be compact and portable. It was sealed with low pressure inert gas such as helium or argon and was sensitive to not only alpha radiations, but also beta and gamma radiations. However the detection principle for the latter two forms of radiations is quite different from the former. It is in fact an indirect detection of secondary electrons knocked out of the inner metal tube wall by external electrons or gamma radiations. It is worth noting the method used to read out the signal from the

counter: Currents produced from electron avalanches in the proximity of the central wire create voltage drops across  $\sim G\Omega$  resistors which are usually connected to the detector in series. The output voltage signal could be suitably registered by an electroscope or a louder speaker [16]. This is believed to be the opening of an era for electrically reading out signals from gaseous detectors.

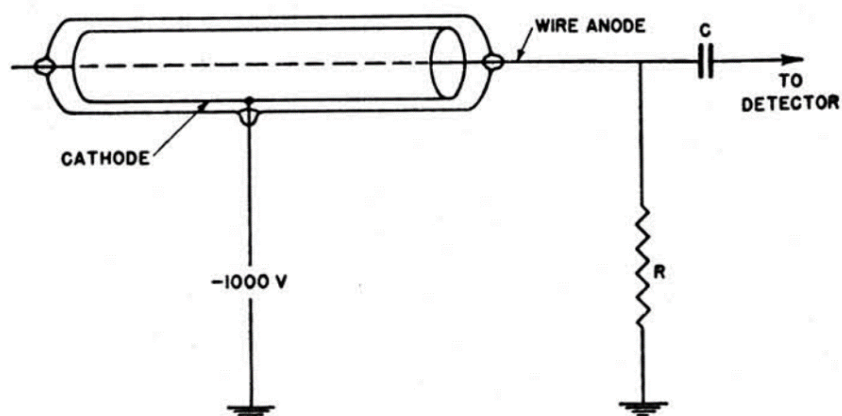


**Figure 2.2** The schematic view of a Geiger-Muller counter [17].

The Geiger-Muller counter was further improved by Liebson [18] and others in late 1940's. A small fraction of halogen or polyatomic admixture was added to the mono-atomic gas. This led to stable operations of such counting tubes over significantly longer time and at a much lower voltage. The counter became widely used afterwards in various research fields, for instance, X-ray spectroscopy [19], astroparticle physics [20]. At the same time, extensive studies on the avalanche and quenching mechanisms of the gaseous counters were carried out.

Geiger-Muller counter's popular application relies on its high output voltage signals which simplify the design of the readout system. It provides an economic solution for radiation counting systems. However counter output signals are almost identical due to the excessive growth of electron avalanches along the wire. Therefore, measurements of radiation energy losses using counter output charge signals are impossible. Moreover, a long recovery time after the discharge is needed

and counting rates are usually limited to no more than a few kHz per tube.

## 2.3 Ionization chamber- discovery from energy measurement

Another example in which the gaseous detector provided an essential tool for the sub-atom physics research is the discovery of neutrons in 1932 [21]. Around 1930, fundamental building blocks of the nature were presumed to be only protons and electrons. Shortly after that, researchers found that an unknown form of radiation was emitted when some light elements were bombarded by alpha particles. This type of non-ionizing radiation with high penetrating power was first assumed to be gamma ray. Chadwick set up an experiment, as illustrated in figure 2.3 to do further investigations on it. His experimental setup consisted of a source chamber, in which alpha particles from polonium were fired towards beryllium or boron, and an ionization chamber, where ionizations of recoiled protons, from the scattering of the unknown radiation with light elements, such as helium, nitrogen, were detected. He also put paraffin between two chambers and observed an increase of current in the ionization chamber. It indicated a large amount of protons had been knocked out by the unknown radiation.

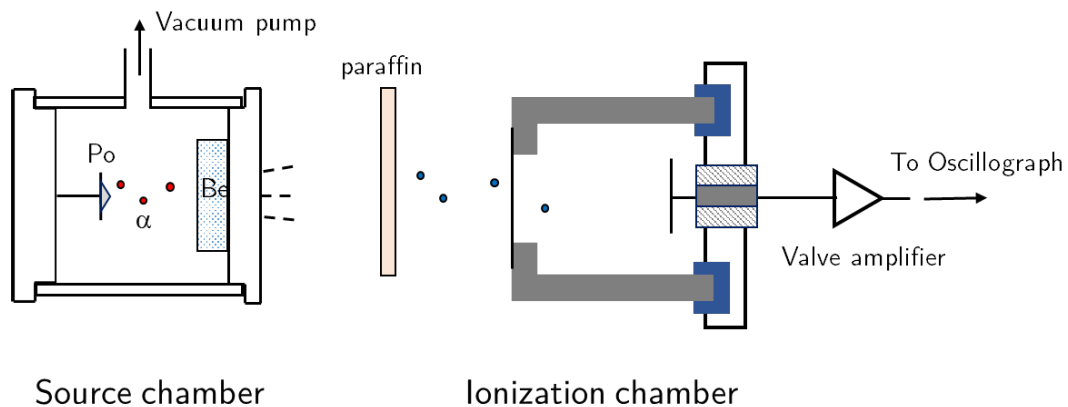


**Figure 2.3** Chadwick's experimental setup to prove the existence of neutron.

He found that there were two serious problems in explaining the radiation with the aforementioned assumption. Firstly, the scattering cross-section of protons by the unknown radiation were orders of magnitude larger than the predicted value of protons scattered by photons, which is believed to be similar to the Compton scattering of electrons by photons. Secondly, the energy of the neutral radiation predicted by the energy conservation law was greater than what could be released from the interaction of a few MeV alpha particles with beryllium atoms which resulted in  $C^{13}$  and massless photons. Therefore, he concluded that the new radiation could not be gamma rays but should be neutrons, massive particles with no net charge. Using the conservation law of energy and momentum, he derived that the mass of neutrons is roughly the same as the mass of protons.

The critical roles that the ionization chamber had played in this striking discovery were the measurement of particle energy and the identification of the radiation. It is particularly interesting to note that the energies of the recoiled protons recorded in the ionization chamber were derived in two approaches. One is to detect the number of ion pairs created in the ionization process which is directly proportional to the proton energy deposition. The other one is to measure the range of the protons and to infer the velocity and thus the energy of the proton from velocity-range curves. Both methods rely on the proportionality of the ionization with the energy deposition, as interpreted by Townsend in his theory of gas ionization [22]. It should be noted that, at that time, the energy measurement was made possible only for heavily ionizing particles, such as alphas and slow protons which could produce a few tens of thousands of ion pairs. However, the energy of low energy X-rays and electrons were still difficult to measure due to their low ionization yields.

## 2.4 Spark chamber- viewing traces from invisibles

Gaseous detectors in the early 20<sup>th</sup> century were primarily cylinder-shaped counters used for radiation counting while cloud chambers were used for capturing traces of invisible particles. It was

until around 1940s, spark chambers were developed and became the first type of gaseous detector for position sensing. The development of spark chambers was first motivated by improving the response time of radiation counters to study the gamma decay. The time it takes for a cylinder-shaped counter to respond to an external radiation was found to be notably long, due to relatively long time needed for ionized electrons to drift over long distances to the central wire. Researchers started to develop parallel plate counters with a few millimeters thick gas gaps. Sparks with very short charge pulses were noticed across the sensitive area as cosmic rays passed through the plates [23]. In 1953, the first photograph of luminous sparks associated with the cosmic-ray was imaged and published [24]. Later on, several improvements, including stacking multiple plate layers, employing external trigger detectors, optimizing filling gas and plate charging circuit, were made [25, 26] to make the device more reliable and useful for tracking. The simple structure along with aforementioned progresses made spark chambers mature to be constructed in large scales for recording multiple trajectories of ionizing particles in the 1960s.

In 1962, the existence of the second type neutrino, later known as muon neutrino, was announced from the experiment hosted at Alternating Gradient Synchrotron (AGS) facility at Brookhaven national laboratory [27]. The experiment was designed to record interactions of high energy neutrinos with matter to verify the uniqueness of the neutrino specie. Neutrinos were first produced in association with muons from pion decays as described by:

$$\pi^{\pm} \rightarrow \mu^{\pm} + \nu \quad (2.1)$$

Muons were absorbed by thick steel walls made from old battleship plates [28], leaving only neutrinos to interact within the detector volume through following processes:

$$\begin{aligned} \nu + p &\rightarrow \mu^{+} + n \\ \nu + n &\rightarrow \mu^{-} + p \end{aligned} \quad (2.2)$$

If the assumption that neutrinos only have one specie holds true, electrons should be produced with the same probability as muons from interactions in analogy to reactions illustrated in fig-

ure 2.2. The key task of the experiment was to observe and distinguish possible productions of electrons or muons from the neutrino interactions. It was made possible through the central element of the experimental apparatus, a 10-ton spark chamber filled with high pressure neon gas. Muons would leave luminous sparks along their trajectory, whereas electrons would initiate distinct showers. Feature of charged tracks visualization together with position measurements that spark chambers had provided for pattern recognition eventually led to the impressive finding that only muons were produced in the neutrino interaction, which confirmed the existence of a second type of neutrinos, different from those produced in beta decays.

## 2.5 Wire chambers - boosting discoveries

Wire counters with broad usage in earlier researches for radiation counting were unable to meet high demands, in terms of rate and energy measurements, for modern particle physics experiments. Extensive researches were carried out in an attempt to confine avalanche sizes inside the counter, and development of proportional counters with parallel plate structures or wires were reported [29] in 1930s and afterwards. Similarly, spark chambers were soon found to be unsuitable for experiments in the ever growing field of high energy physics where searching for rare processes and recording large amount of particle data became essential.

As researchers were working on the improvement of spark chambers and introducing multiple wires in spark counters for neutron and gamma detection [30, 31], a breakthrough was made by Chapark and his colleagues in late 1960s, when they introduced their newly invented multi-wire proportional chamber (MWPC) [32, 33]. This magnificent development was based on their previous experiences of dealing with spark chambers. They constructed new chambers with groups of closely spaced thin wires stretched in between two parallel plate electrodes. Gas gaps were chosen to be a few millimeters. Signals could be read out by amplifiers connected to individual wires. It

was originally thought by others that the mutual induction between closely coupled neighboring wires would destroy the chamber's ability to measure positions. However, their work demonstrated that such induction was in fact negligible and charged particles could be localized with an accuracy on the order of wire spacing. Moreover, there are a number of advantages over other detectors used at that time. These chambers with small gas gaps and appropriate gas mixtures plus operational high voltage could prevent the avalanche from overgrowth and could evacuate ions in a relatively short time, and it still keeps a high efficiency even for minimum ionizing particles. As a result, time resolution, on the order of a few tens of nanoseconds, and a dramatically increased rate capability compared with those obtained from Geiger-Muller counters are obtained. Moreover, two dimensional readout with a sub-mm spatial resolution were also achieved using segmented cathode electrodes. Bubble chambers and spark chambers were then replaced by MWPCs in high energy and nuclear physics experiments for charged particle tracking. The easiness of reading out fast signals from MWPC with a large number of affordable advanced electronics plus the possibility to process digital data via computers make them very suitable for the acquisition of massive charged particle track information.

A few years after the first publication of MWPC, a variant of multi-wire chamber called the drift chamber (DC) [34] was developed for position measurements. This new type of wire chamber reconstructs track hit positions with respect to the sensing wire based on the principle first introduced by Chapark and his co-workers at CERN in 1969 [35]. This principle of deriving locations of incident charge particles is based on measuring the drift time of the liberated primary ionizations. DCs are usually constructed with wider anode wire separations compared with MWPC. Potential wires, with potentials identical to cathodes plates, are inserted between sensing anode wires in order to create a more uniform drift electric field. The achieved position resolutions of DCs at the time of the first publication were about 0.5 mm. However, compared with MWPC, it considerably reduced the number of readout channels in order to get a comparable spatial resolution.

In 1976, a new instrument, the time projection chamber (TPC) was proposed by Nygren [36] to reconstruct multiple charged particle trajectories simultaneously in three dimensions. It was considered to be an essential part for the magnetic spectrometers in electron-positron collider experiments. The conceptual detector was imagined to be composed of a large gas-filled drift volume and a readout plane similar to the multi-wire proportional chamber structure. The track projection on readout plane was obtained from wires and segmented cathode pads as the case in MWPC whereas the third coordinate along the chamber depth direction could be calculated using drift times of individual ionization clusters. A number of progresses were made shortly after the proposal even TPC was still in its infancy. Among them, some important works were optimizing the gas mixture for better linear dependence of the drift velocity on the electric field, reducing electron diffusions as well as introducing gating wires to eliminate slowly drifting ions produced in the avalanche process, which otherwise would distort the drift field. The first TPC was successfully constructed and started its operation in 1983 at SLAC [37, 38]. Spatial resolutions on the order of 0.2 mm in the projection plane and 0.35 mm in the chamber depth direction were achieved [39].

After their inventions, all these wire chambers were immediately implemented in major particle physics experiments such as experiments on SPS, LEP at CERN and on PETRA at DESY. MWPC and Drift chambers were constructed in large scales for muon tracking and TPCs were employed as inner tracker detectors to perform particle tracking, identification and transverse momentum measurements. With these detector components, the number of tracks, events and data recorded were increased enormously in 1980s and onwards.

Several notable discoveries of standard model particles were made possible at the end of the 20<sup>th</sup> century thanks to the rapidly developing gaseous detectors. Most notably, the existence of strong force mediator, gluon, was confirmed by TASSO, PLUTO [40], JADE and MARK-J experiments at DESY in 1979. Gluon is discovered by appearances of triple-jet events from electron positron annihilations as illustrated in figure 2.4. The annihilation creates a quark-antiquark pair

which eventually results in two jets opposite in the azimuthal angle. The third jet is expected to come from gluon bremsstrahlung. The central task of these experiments was to identify jets with high transverse momenta which are composed of groups of high energy charged particles. Therefore, the spectrometers were built very similarly with multiple layers of proportional wire chambers for central charged particle tracking, calorimeters for energy deposition measurement and drift chambers outside the magnetic yoke for muon tracking. Take the PLUTO experiment as an example, the structure of the spectrometer [41] is shown on the left side plot of figure 2.5. A spatial resolution of about 0.15 mm was obtained and resulted in a momentum resolution  $\sigma/p$  of 3%  $p_T$  ( $p_T > 3$  GeV) in a 1.69 Tesla magnetic field [42]. Due to the momentum conservation, momenta of three jets could be projected to two dimensional “event planes” for jets separation and display. One of the three-jet events from the PLUTO experiment is shown on the right side plot of figure 2.5. Three jets were evidently isolated, proving the presence of a gluon, and their compositing charged tracks were recorded clearly by the wire chamber tracking system.

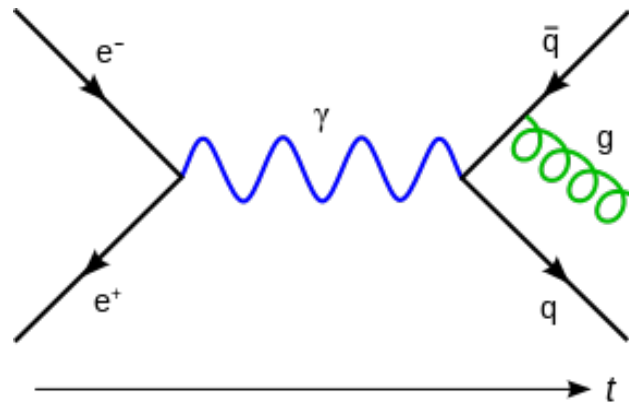


**Figure 2.4** Gluon bremsstrahlung process in electron positron annihilation.

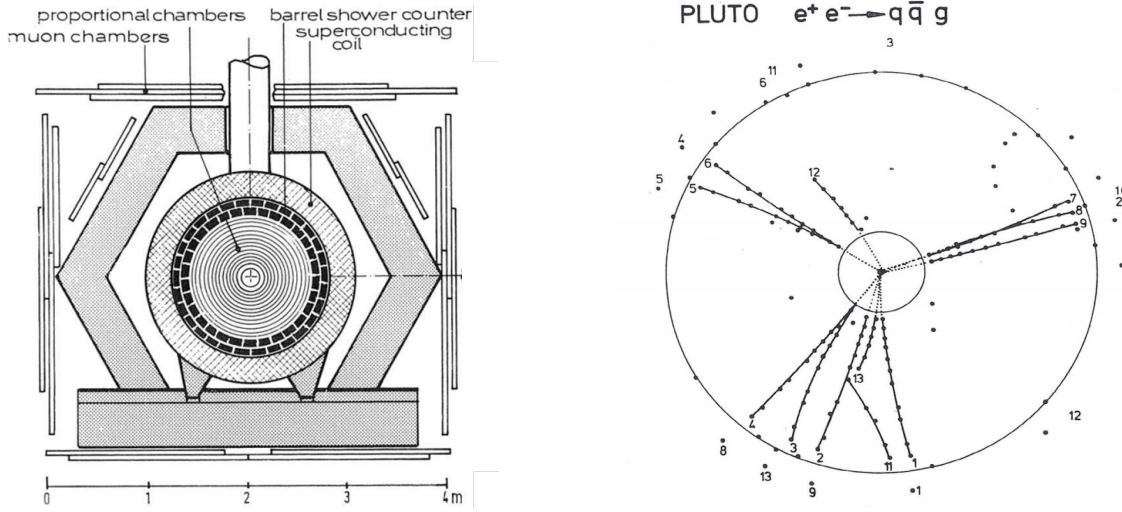


**Figure 2.5** Side view of the layout of spectrometer for PLUTO experiment (left) and a display of a three-jet event captured by PLUTO experiment (right) [42]. Proportional chambers for central tracking and drift chambers for muon detection are indicated on the left side plot.

Another milestone achievement from large spectrometers utilizing these wire chamber technologies was the discovery of weak force carriers, W and Z bosons, by the UA1 and UA2 experiments [43–46] at CERN in 1983, a decade after the neutral current interaction was observed. A cut view of the UA1 detector [47] was shown on the left side plot of figure 2.6. The cylinder central tracking detector, based on six separate layers of drift chambers, with 5.8 meter length and 2.3 meter diameter, was reported to be the largest drift chamber of its time [48]. The outermost muon detectors were also constructed from a large amount of drift chamber cells. The W and Z bosons can decay leptonically or hadronically. Since the hadron collisions produce vast QCD backgrounds, the leptonic decay channels are the golden searching channels. More specifically, the hunt for W boson implies searching for events consist of a charged lepton with large transverse momenta and an associated large missing energy. Similarly, Z boson will be reconstructed from events with two high energy leptons of opposite electric charges. Discoveries were soon announced thanks to the high energy accelerator and the spectrometers dedicated for tracking and calorimetry.

The first Z event recorded from UA1 detector [49] is shown on the right hand side of figure 2.6. The white dashed lines are the reconstructed tracks of the high energy electron and position from the Z decay.

Wire chambers and their derivatives are still actively used for trigger and tracking in recent large particle experiments including experiments on LHC as well as heavy ion collision experiments on RHIC. Thousands of tracks per collision are recorded in TPCs and multi-wire and drift chambers with a coverage of tens of thousands of square meters are usually employed. An example application of the wire chambers, for the future ATLAS detector upgrade, will be discussed in more details in chapter 6.

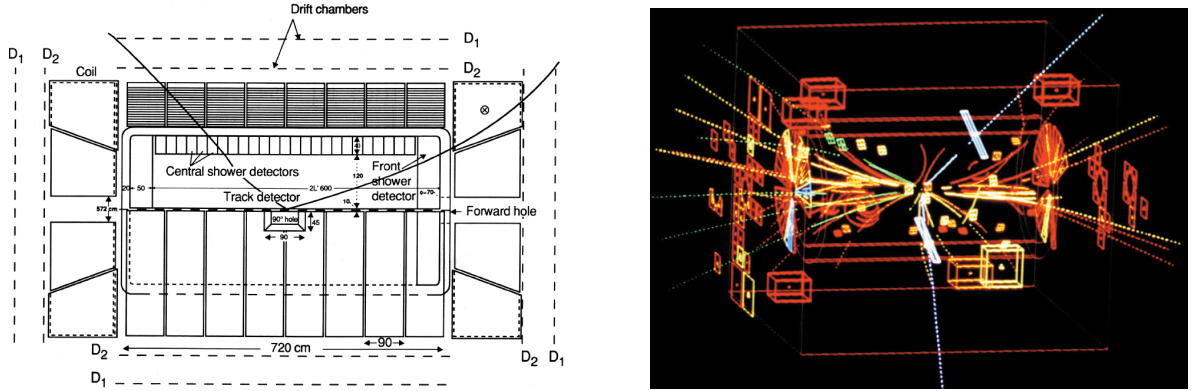


**Figure 2.6** A cut view of UA1 detector (left) and a candidate event display for  $Z \rightarrow e^+e^-$  (right).

## 2.6 RPC and MPGD - shading lights to future

The resistive plate chamber (RPC), invented in 1981 [50], is a gaseous detector consisting two highly resistive parallel plate electrodes and a few mm thick gas gaps. The resistive electrodes used for RPC are either specially treated Bakelite plates or glasses. Usually, highly quenched gas mixtures are used and high voltages are applied on outer surfaces of the electrodes. Induced

signals could be read out by signal pick up boards capacitively coupled to the resistive electrode. Unlike wire chambers which only have strong electric fields near wires to create avalanches, RPCs have strong electric fields over 50 kV/cm across the whole gas gap. Therefore the electrons drift velocities are high and avalanches develop immediately at where primary ionizations are created. As a consequence, electron induced signals are very sharp and the time resolution is on the order of a few nanoseconds. The RPC detectors are also different from spark chambers which also have parallel plate structure but use metal electrodes. The resistive electrodes, first introduced by Pestov and his colleagues [51] in a spark counter, could limit the amount of energy released by the electron multiplication process. The streamer mode has current of a few orders of magnitude larger than that from proportional avalanche mode. However, the detector could stably work under the streamer mode and is immune to sparks due to the absorption of UV photons emitted in the electron recombination process by the quencher gas and the prevention of a large amount of free electrons from the electrode involving in the break-down process. The use of Bakelite material allows the chambers to be economically produced in large scales and be tailored to any shape. The conventional Bakelite RPCs operated under the streamer mode were immediately made into practical use for muon triggering in large spectrometers or cosmic ray counting in ground-based astroparticle physics observatories.

Since its advent, this technology has been grown rapidly. One of the notable innovations is the development of multi-gap resistive plate chamber (MRPC) [52]. It implements multiple resistive plate electrodes, usually made of regular glass, inside the gas gap. The plates split the sensitive volume into a few hundred-micron-thick gaps. The primary ionizations and the avalanche development are confined within the narrow gap. The induced signals are transparent to outermost readout strips or pads. This configuration reduces the arrival time fluctuation of the ionization cluster thus the timing jitter, but it still keeps the detection efficiency to be high thanks to the pronounced signals summed up from individual gaps. The excellent time resolution, feasibly achievable at around

50 ps, makes it very attractive to be used as the time-of-flight (TOF) detector for particle identification. Example applications are the MRPC TOF trays used by ALICE and STAR experiments for the separation of pions, kions etc.

Confronted by the unprecedented requirements of modern particle physics experiments, the RPC detector is developing towards the combination of high rate capability, high precision in timing and localization. Since RPC's rate capability is limited by the voltage drop due to current flowing through the high resistive electrode, the improvement goes into two directions. One is to develop low resistivity electrode such as low resistivity Bakelite materials or semi-conductor glass. The other way is to explore the possibility to reduce the amount of charge released per detected count and thus the overall current. The later approach consequently drives the development of fast sensitive low-noise front-end electronics for detecting smaller signal amplitudes. Simultaneous determination of charged tracks in space and time with high precision is of particular interests in muon triggering at high radiation backgrounds. The development in this aspect will be elaborated in chapter 5.

Micro pattern gaseous detector (MPGD) emerges in late 1980s as the rate capability and granularity of multi-wire chambers approach their limitations. The first attempt was made around 1988 when the micro-strip gas chamber (MSGC) [53] was made. Alternating anode and cathode strips, spaced a few hundred microns, were etched on an insulating substrate by photo-lithographic process. A significantly larger number of hits could be resolved per unit area per unit time due to reduced readout element spacing as well as fast evacuation of charges, or more specifically, the positive ions. However, a few weaknesses and imperfections were lately found. Particularly, the gain is limited to  $10^4$  before it breaks the insulator and the aging of the detector under continuous radiation environment causes instabilities over long term.

Various new types of micro pattern gaseous detectors are developed to address these issues. Among them, most notably, are Micromegas [54] developed by Y. Giomataris and gas electron

multiplier (GEM) [55] invented by F. Sauli. The philosophy of operating these devices at high counting rate is similar to that of MSGCs'. Special configurations of their structures, confining strong electric fields in specific narrow regions, lead to counting rates exceeding  $10^5$  Hz/mm<sup>2</sup> [56, 57] at a reasonable avalanche size. Both types of detectors and many of their variants are used in present particle physics experiments with high rate demands. Meanwhile, extensive developments on trackers based on micro pattern gaseous detectors are carried out [58, 59]. MPGDs based trackers have the potential to achieve spatial resolutions competitive to silicon-based trackers [60] but at lower cost, faster response. Its low material budget feature could reduce multiple scatterings when used as inner trackers.

Due to the micro-structure nature, MPGDs are relatively fragile and would easily break up if any imperfection of raw material or dust is present in the production. Therefore, the greatest challenge for their applications in large spectrometer systems is the production in large scale. Moreover, they are much more sensitive to sparks which could be caused by dense ionizations. This is of particular concern in the circumstance where heavily charged hadrons are present. For this reason, many researches have been targeted on the spark-protection mechanism and detailed discussions will be presented by chapter 4.

## 2.7 Summary

Gaseous detectors trace the invisible radiations and particles through the ionization process. They have been used to explore the fundamental particles and their interactions since a hundred years ago. As the scale and complexity of the particle physics experiments increase dramatically over the last century, the gaseous detectors evolve from solo devices, for qualitatively examining the radiation intensity, to be part of giant experimental spectrometers consisting million channels of readout electronics to quantitatively study the energy, trajectories and flight time of enormous

---

amount of particles. Revolutionary innovations of the gaseous detectors are not emerged from epiphany but are rather from the inspiration of decades of accumulated work.



## Chapter 3

# Principles of Gaseous Detectors

Gaseous detectors explore the ionizing radiation through detecting the electric “signature” left by interactions between incident particles and the gas media. The interactions through electromagnetic processes transfer part or all of the incident particle energy to gas atoms or molecules. The energized gas atoms will then ionize and produce free moving electrons and ions. Usually, an electric field is applied across the electrodes separated by a specially filled gas. Signals are ultimately induced on the readout electrodes as electrons and ions move across the gas volume. Counting, traces, passage time, and energy loss in the gas could therefore be used to study the radiation in great details.

Since the knowledge on interactions of particles with matter is prerequisite for understanding how gaseous detectors identify particles and radiations, it will be introduced at the beginning of this chapter. The transportation of ionized electrons and ions in the gas medium, basic mechanisms on the development of avalanche and the induction of signals are briefly discussed in the following subsections.

### 3.1 Interaction of charged particles in matter

When a charged particle passes through the matter, it mainly interacts with a sea of electrons and nucleus in the medium via electromagnetic forces. It will lose its kinetic energy basically through two categories of processes. Firstly, it could impart its energy to the medium through electric processes, i.e. ionization and excitation. Bonded electrons from the atoms could be knocked out or the atoms could be excited and release low-energy photons. Secondly, it could lose the energy through several radiative processes, i.e. bremsstrahlung, pair production and photo-nuclear interaction. Bremsstrahlung is a process in which electromagnetic radiations are emitted when a fast charged particle is deflected and decelerated by nucleus or electrons. Pair production creates electron and positron pairs via virtual photons when high energy charged particle traveling through the Coulomb field of nucleus. Photo-nuclear interaction is the inelastic scattering process of the charged particles with nucleon or nucleus. All these interactions are illustrated in figure 3.1.

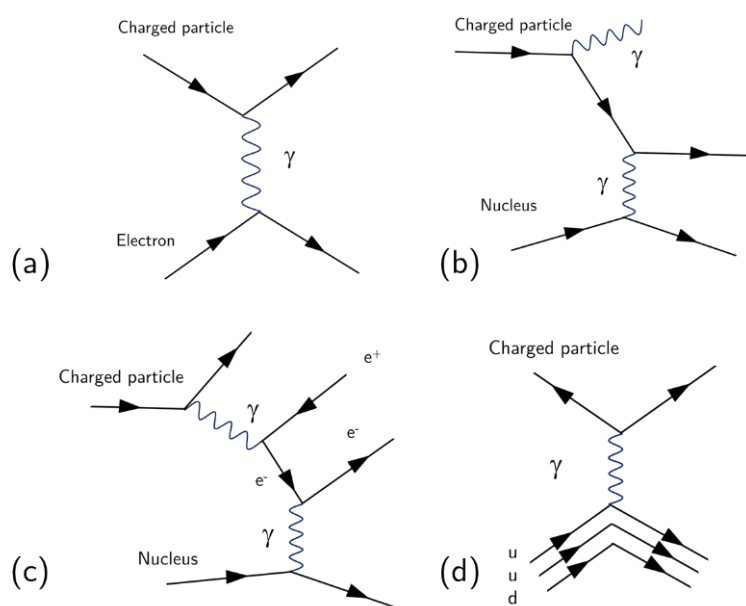


**Figure 3.1** Interaction of charged particle with matter: (a) Ionization process; (b) bremsstrahlung (c) pair production; (d) photo-nuclear interaction.

### 3.1.1 Energy loss in matter

Considering a charged particle of mass  $M$  and velocity  $\beta c$ , its momentum  $p$  is given by

$$p = \gamma M \beta c \quad (3.1)$$

The maximum kinetic energy,  $T_{max}$ , that could be transferred to a free electron of mass  $m_e$  in the collision process is given by

$$T_{max} = \frac{2m_e c^2 \beta^2 \gamma^2}{1 + \frac{2\gamma m_e}{M} + \left(\frac{m_e}{M}\right)^2} \quad (3.2)$$

For instance, a muon with energy of 1 GeV could transfer a maximum energy of about 100 MeV to an electron through a single collision process. The situation is different for a light charged particle, the electron, which is approximately 200 times lighter than the muon. The incident electron could impart all of its kinetic energy to the free electron. Most frequently, charged particles only transfer very small amount of energy, typically below 100 eV, in a single interaction. Multiple collisions happen in a thin absorber with a large variance of the energy loss. The mean energy loss, also called stopping power, of heavy charged particles in the matter due to ionizations and excitations was first derived by Bethe based on the first-order Born approximation [61]. However, this theory only extends to a certain energy range. Several corrections [62–67] were made to take atomic shell effect, polarization and other radiative effects into account. The electric part of the energy loss, specifically for muons, is given by the modified Bethe formula:

$$-\left\langle \frac{dE}{dx} \right\rangle_{electric} = K \frac{Z}{A} \frac{1}{\beta^2} \left[ \frac{1}{2} \ln \frac{2m_e c^2 \beta^2 \gamma^2 T_{max}}{I^2} - \beta^2 - \frac{\delta(\beta\gamma)}{2} - \frac{C}{Z} + \frac{1}{8} \frac{T_{max}^2}{(\gamma M c^2)^2} \right] + \Delta \left| \frac{dE}{dx} \right| \quad (3.3)$$

where the negative sign denotes the loss of energy. All the variables and parameters are described in table 3.1.

The shell effect correction term  $-C/Z$  is needed especially at low energy, since the probability of interactions with electrons in the inner shells of atoms is negligible when the incident particle speed is close to the orbital velocity of electrons. The polarization correction term  $-\delta$  is added

Symbol	Description	Unit
$c$	Speed of light	$\text{m}\cdot\text{s}^{-1}$
$m_e$	Electron mass	$\text{MeV}\cdot\text{s}^{-1}$
$r_e$	Classical electron radius	fm
$N_A$	Avogadro constant	$\text{mol}^{-1}$
$K$	$4\pi r_e^2 N_A m_e c^2$	$\text{MeV}\cdot\text{cm}^2\cdot\text{mol}^{-1}$
$Z$	Atomic number of the medium	
$A$	Atomic mass of the medium	$\text{g}\cdot\text{mol}^{-1}$
$\beta$	Muon velocity	$c^{-1}$
$\gamma$	Lorentz factor of the muon	
$T_{\max}$	Maximum transferable kinetic energy	MeV
$I$	Average excitation energy	eV
$M$	Muon mass	MeV
$\delta$	Polarization effect correction factor	
$C$	Shell effect correction factor	
$\Delta dE/dx $	Bremsstrahlung energy loss correction	

**Table 3.1** Definitions of variables in electric energy loss formula for the muon.

as the dielectric polarization of the medium shields the electric field far from the particle hence reduces the long-range interaction cross section as well as the energy loss. Other minor correction terms including spin and bremsstrahlung corrections are also added with the last two terms of equation 3.3. As the particle energy continues to increase, the radiative energy loss becomes significant and finally dominant.

The total energy loss,  $-\langle \frac{dE}{dx} \rangle$  is usually parameterized as

$$-\langle \frac{dE}{dx} \rangle = -\langle \frac{dE}{dx} \rangle_{electric} - \langle \frac{dE}{dx} \rangle_{radiative} \cdot E \quad (3.4)$$

The energy  $E_c$  at which radiative and electric energy losses are identical is called critical energy. The total energy loss for a positive muon in copper as a function of its momentum [68], as an example, is shown in figure 3.2. Most notably, it is approximately inversely proportional to  $\beta^{-5/3}$  when  $\beta\gamma$  is between 0.1 and 1. Then it reaches a minimum at which the corresponding muons are called minimum ionizing particles (MIP). The total energy loss starts to increase with  $\ln(\beta\gamma)$  when  $\beta\gamma$  is greater than 4. It should be noted that after the polarization and other radiative corrections are included, the electric energy loss gradually reaches a plateau which is called the Fermi plateau. The plateau occurs at a muon momentum of around a few hundred GeV/c. As the muon energy reaches ultra-relativistic region, the energy loss increases at a dramatically fast pace due to radiative processes.

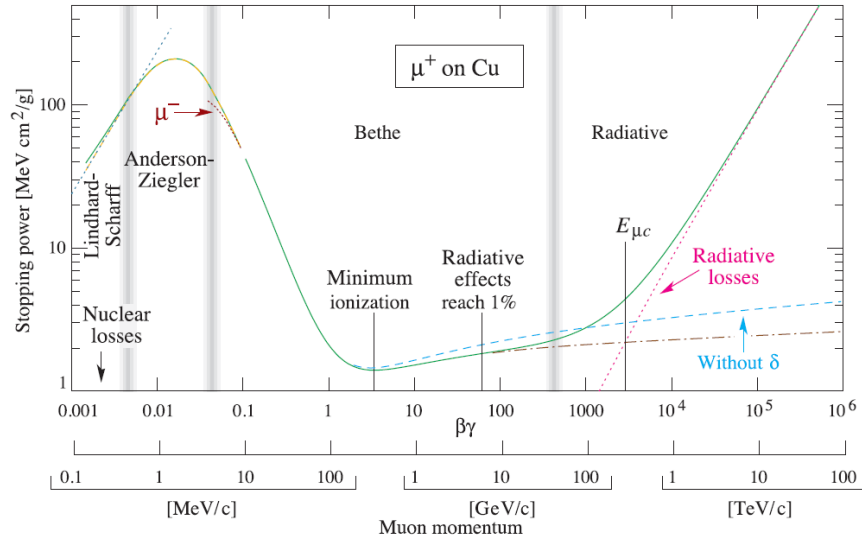


**Figure 3.2** Stopping power of positive muon in copper.

For gaseous detectors used for muon triggering in collider experiments, typically muons with energy more than a few GeV are of great interests. Their ionization energy loss in the thin gas medium is comparable to those of MIPs, which is roughly estimated to be [69]

$$-\left\langle \frac{dE}{dx} \right\rangle \approx 2 \frac{\text{MeV}}{\text{g/cm}^2} \quad (3.5)$$

On average, MIPs leave about a few keV/cm energy in the gaseous detector filled with gas at 1 atm pressure. A simulated example of energy loss from several charged particles in a 2.8 mm thick gas medium filled with CO<sub>2</sub> and n-pentane (50:50) at atmospheric pressure and 17 Celsius temperature is shown in figure 3.3. MIPs have an average energy loss of about 1 keV in the gas gap. The Fermi plateau appears at the energy of around 100 GeV with an energy loss approximately 30% larger than the minimum ionization energy loss.

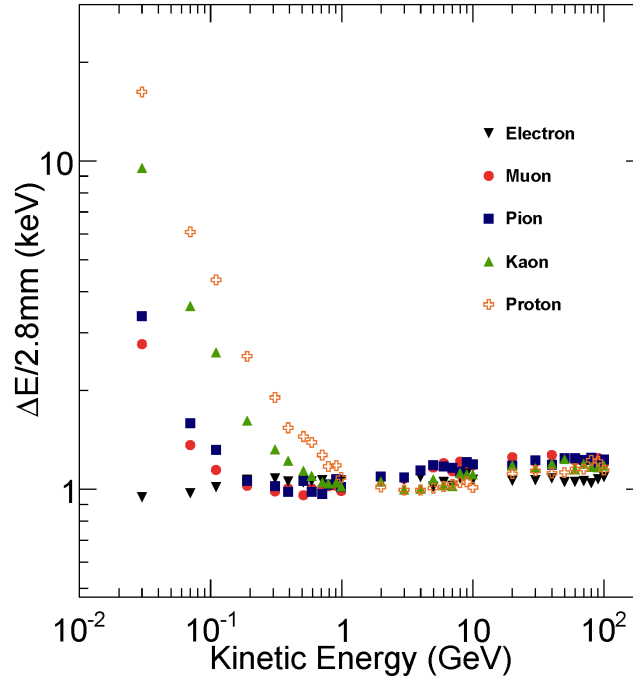


**Figure 3.3** Simulated energy loss of charged particles in CO<sub>2</sub>:n-pentane (50:50) gas mixture.

### 3.1.2 Fluctuation of energy loss in thin absorbers

Electric interactions of charged particles with electrons and nucleus in matter are discrete even in thin materials. Therefore, they have statistical natures. These interactions are mainly categorized into two types [70]. One type of interaction is long distance collisions with relatively low energy transfers which result in the liberation of free electrons or excitations of the atoms. Another type of interaction is short distance collisions with large energy transfers. Occasionally energetic electrons, also called delta electrons or delta rays, could be knocked out with energy greater than a few keV. They have ranges that are more than a few tens of microns in the gas media at normal atmospheric pressure and room temperature. Delta rays could give rise to secondary ionizations. Probabilities for these various types of interactions with atoms as a function of the transferred

energy are qualitative represented in figure 3.4.

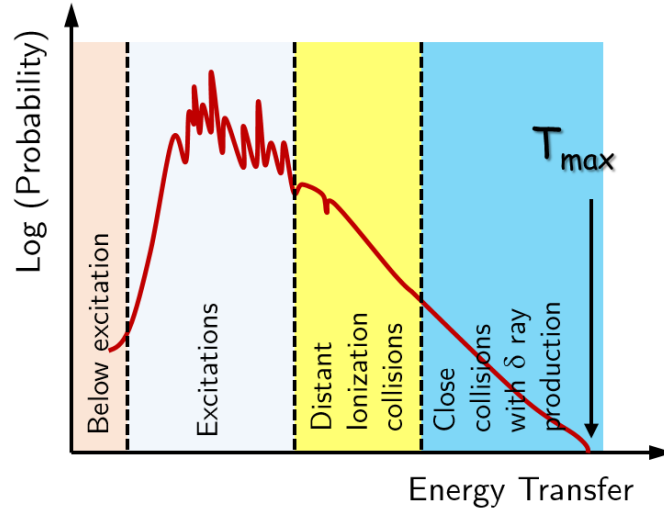


**Figure 3.4** Probability of electric interactions as a function of energy transfer.

The fluctuations of the total deposited energy by fast charged particles in a thin or light absorber, such as gas medium or thin silicon layer, are described by the Landau distribution [71] [10] or more precisely by the Landau-Vavilov-Bichsel distribution [72]. The Landau probability density function  $L(E)$ , describing the energy loss, is given by [73]

$$L(E) = \frac{1}{2\pi i \infty} \int_{c-i\infty}^{c+i\infty} \exp[s \ln(s) + uE] ds, \quad ds \geq 0 \quad (3.6)$$

where  $c$  is any positive real number. It is a complex function and is usually handled numerically. Another convenient approximation of the distribution is given by the Moyal [74] and reads

$$L(\lambda) = \frac{1}{\sqrt{2\pi}} \exp \left[ -\frac{\lambda + \exp(-\lambda)}{2} \right] \quad (3.7)$$

where  $\lambda$  is the parameter characterizing the deviation of the energy loss from the most probable energy loss. A simulated example of energy loss of 180 GeV/c muon passing through a 2.8 mm thick CO<sub>2</sub>:n-pentane (55:45) gas mixture is depicted in figure 3.5. The distribution is skewed

towards the low energy end and has a long tail at the high energy end representing the occasional large energy transfers.

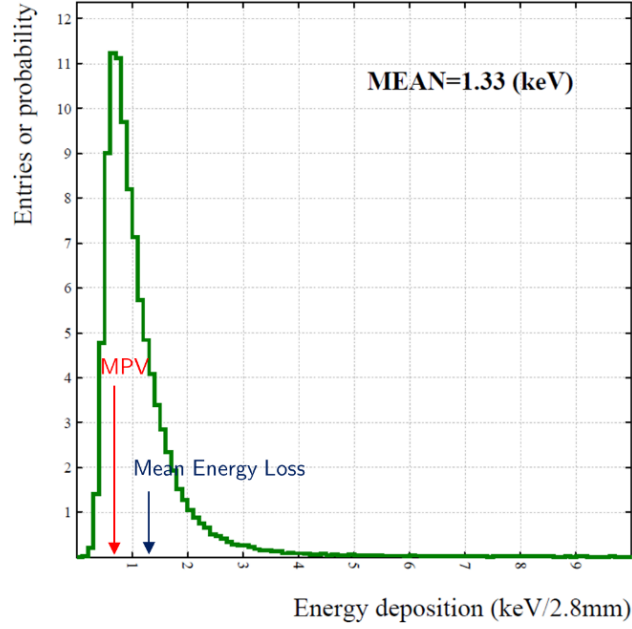


**Figure 3.5** Simulated energy loss distribution of 180 GeV/c muons in a 2.8 mm thick gas volume filled with a mixture of CO<sub>2</sub> and n-pentane (55:45).

The general formula determining the most probable value (MPV) of the energy loss is given by

$$\Delta E_{MPV} = \xi \left[ \ln \frac{2m_e c^2 \beta^2 \gamma^2}{I} + \ln \frac{\xi}{I} + 0.2 - \beta^2 - \delta(\beta\gamma) \right] \quad (3.8)$$

where  $\xi$  equals to  $(K/2)(Z/A)(x/\beta^2)$  MeV and  $x$  is the equivalent thickness in unit of  $g \cdot cm^{-2}$ . The mean energy loss is larger than the MPV, as can be seen from figure 3.5. The large fluctuation limits the energy resolution of the gaseous detector for MIPs. Although, the energy resolution is of little concern for muon trigger and tracking applications, wide dynamic range has to be considered for the design of readout electronics due to the wide spread of energy depositions thus signal amplitudes.

## 3.2 Interaction of photons and neutrons with matter

### 3.2.1 Detecting photons

Photons do not have charge and thus do not directly generate ionizations in matter. While the photon cannot transfer its energy to free electrons due to the violation of momentum conservation, its energy could be absorbed by electrons if they are bonded by an atomic nucleus. Basically, there are three types of interactions for photons, namely photoelectric process, Compton scattering and pair production. Therefore, photons can be indirectly detected when they are “converted” into charged particles. Distinct from interactions of charged particles with matter, a photon will transfer all of its energy to electrons or only scatter with electrons through a single collision and leave with a lower frequency. The probability of such energy transfer is governed by basic principles of quantum mechanics. As a consequence, the range of photon in the absorber cannot be defined. Instead, the intensity  $f$  of emerging photons after passing through a medium with thickness  $x$  and density  $\rho$  is given by

$$f = f_0 e^{-\mu \rho x} \quad (3.9)$$

where  $f_0$  is the original photon flux and  $\mu$  is the mass attenuation coefficient usually expressed in  $\text{g}^{-1} \cdot \text{cm}^2$ . This attenuation coefficient is determined by cross sections of the above mentioned interactions as well as the material atomic number. A mean-free path, after which the photon intensity is reduced to  $1/e$  of its original value, could be defined as the inverse product of  $\rho$  and  $\mu$ .

The photoelectric effect is essentially the absorption of a photon by an electron from a particular atomic shell when the photon energy  $E_\gamma$  exceeds the quantum energy level of that electron. The probability for a photon to be absorbed is the sum of all possibilities to transfer its energy to electrons on all shells with binding energy less than  $E_\gamma$ . There is a maximum in the interaction probability when  $E_\gamma$  is very close to the binding energy of a certain shell. After that, it falls rapidly as the photon energy continues to increase. Calculations of the total interaction cross section are

sophisticated due to the involvement of electrons from multiple shells. Generally, it is proportional to  $Z^5/E_\gamma$  when  $E_\gamma$  is much greater than 0.511 MeV and has a dependence of  $Z^5(I_0/E_\gamma)^{7/2}$  to  $Z$  when  $E_\gamma$  is less than 0.511 MeV but higher than the ionization energy of those electrons. Released photon-electrons are approximately perpendicular to the photon incidence direction when  $E_\gamma$  is less than a few tens of keV and more forward directions are favored at the energy beyond that. This process plays an important role in the absorption of low energy photons. Moreover, it is shown in the later chapter that it provides an approach to calibrate the radiation energy measured by the gaseous detectors due to its complete absorption of photon energy.

When the photon energy is in the range from few tens of keV to few tens of MeV, another process, Compton scattering, becomes more significant. In this process, photons could undergo incoherent inelastic scattering with quasi-free electrons and transfer part of its energy to electrons. The remaining energy  $E'_\gamma$  is given by

$$E'_\gamma = \frac{E_\gamma}{1 + \frac{E_\gamma}{m_e c^2} (1 - \cos \theta_\gamma)} \quad (3.10)$$

where  $\theta_\gamma$  is the angle between the incident photon and its outgoing direction. The maximum energy transfer occurs at backscattering when the photon is bounced back. The total cross section was first calculated by Klein and Nishina and could be found elsewhere [69]. It is generally proportional to the atomic number  $Z$  of the medium. An important feature of Compton scattering is that the photon energy is partially transferred. Since scatterings are somewhat in random directions and scattered photons have very rare chances to initiate a second interaction in thin gaseous detectors, their incidences result in a continuum in the measured energy spectrum with a backscattering photo-peak at the low energy end.

The third type of photon interaction is the pair production process. When a photon passes through Coulomb fields of electrons or atomic nucleus, if its energy is greater than twice the rest energy of electrons, it could be converted into a pair of electron and positron. This process is very rare for thin gaseous detectors and usually electrons or positrons converted from the heavy element

material in front of them are detected.

Contributions of various processes to the total photon interaction cross section as a function of the photon energy are reproduced from [75] and are shown in figure 3.6 for an argon medium. Note that the total cross section also includes the contribution from elastic scattering processes which are not discussed here.

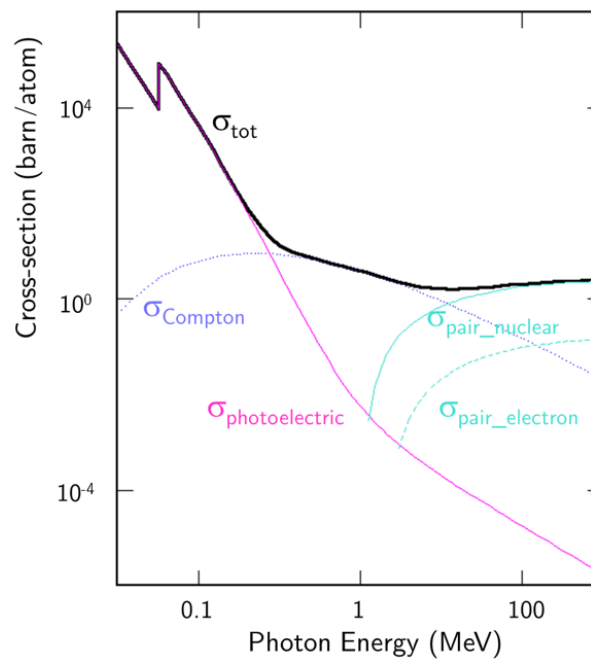


**Figure 3.6** Photon total cross sections as a function of energy in argon.

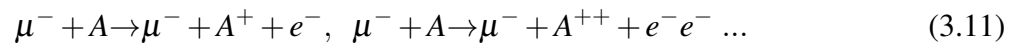
### 3.2.2 Detecting neutrons

Similar to photons, neutrons cannot be detected unless they are converted into charged particles through collisions. Interactions of neutrons with matter are of various types, from elastic or inelastic scatterings with nucleons to nuclear reactions producing heavy charged particles such as protons and helium nucleus. The neutron interaction cross section depends on the atomic properties of the traversing media as well as the neutron energy. Generally, the cross section has a

logarithmic falling with the neutron energy in substances with  $\text{He}^3$ ,  $\text{Li}^6$  or  $\text{B}^{10}$  [76]. Thermal neutrons with a typical energy of 0.025 eV could be easily detected by gaseous counters filled with  $\text{BF}_3$ . The philosophy for detecting fast neutrons is to moderate them to lower energy in order to increase the probability of neutron-induced reactions. Proton-rich substances are often used since neutrons could have maximum energy transfers with protons of the same mass. The recoiled alpha particles from neutron reactions usually have very short ranges in the gas medium and produce dramatically denser ionizations than MIPs. Therefore, they are to some extent harmful to gaseous detectors used for muon detections in hadron collider experiments.

### 3.3 Ionizations in gas

The ionization and excitation phenomena when charged particles passing through the matter have been discussed in Section 3.1.1. For the passage of a charged particle in the gas media, liberated charge carriers can freely move within the volume. The total number of ionized electron-ion pairs  $N_T$  carries the information about the energy loss of the charged particle. Ionizations can be categorized into three groups. One of the groups contains ionization clusters from the primary ionization encounters. Each cluster has one, or occasionally more than one, ionized electrons. This process is illustrated for a muon incidence by



A simulated statistical distribution of primary ionizations from passages of 180 GeV/c muons in a 2.8 mm gas gap filled with  $\text{CO}_2$ :n-pentane (55:45) at atmospheric pressure and 17 Celsius temperature is shown in figure 3.7. On average, there are 23 primary ionization collisions in the gas gap. It should be stressed that the total number of primary ionization  $N_p$ , the product of the mean number of primary ionization clusters and the average cluster size, only accounts for a portion of total ionizations.

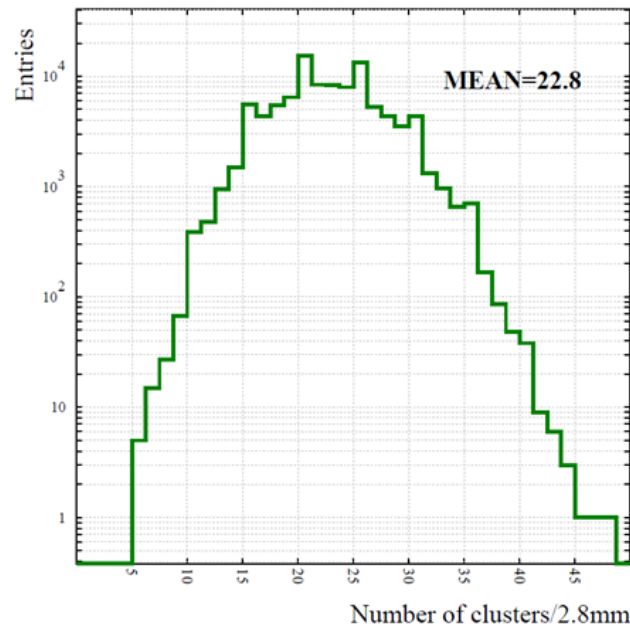
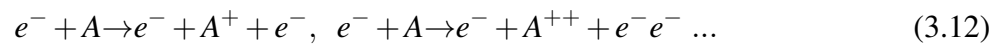


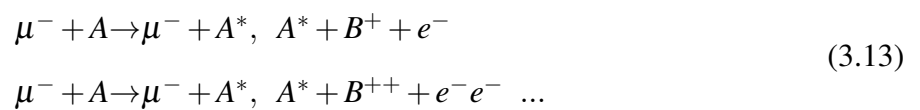
**Figure 3.7** Number of primary ionization clusters produced in a 2.8 mm thick gas volume filled with CO<sub>2</sub> n-pentane (55:45) mixture.

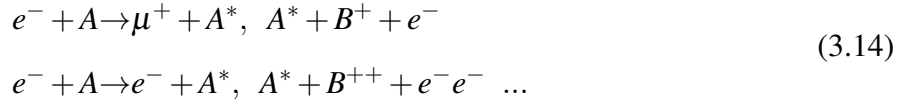
The second group contains ionized electrons which are not directly ejected from the atoms encountered by the charged particle itself but resulted from collisions of primarily ionized electrons with atoms. This process is called secondary ionization and is illustrated as



It produces much more electron-ion pairs in the gas media.

Third type of electron-ion pair production is related to the transfer of energy from those atoms excited by the passage of charged particles or the primary energetic ionized electrons. This process could happen when the energy transfer from the excited atom is high than the ionization energy of electrons orbiting another nearby atom. These reactions could be illustrated by





The phenomenon of producing additional ionization by collisions between excited gas atoms and another type of gas atoms with lower ionization potentials is called Penning effect [77]. It makes important contributions to the growth of avalanches and could significantly increase the total amount of electrons produced after the amplification process. This will be discussed with more details in the study of Micromegas detector in chapter 4.

The primary ionization encounters in a gas medium are stochastic processes. It is convenient to define a parameter  $\lambda$  called the mean free path.  $\lambda$  is the average distance that a charged particle have traveled between two successive ionization encounters. Assuming the electron density of the absorbing material is  $\rho$  and the ionization cross section is  $\sigma_i$ ,  $\lambda$  is then given by

$$\lambda = 1/(\rho\sigma_i) \tag{3.15}$$

If the detector has a thickness of  $h$ , the mean number of primary ionization interaction  $n_p$  produced from perpendicular incidences of charge particles is given by

$$n_p = h/\lambda \tag{3.16}$$

Since ionization encounters are independent of each other, the fluctuation of primary ionization collisions inside the gas gap follows the Poisson distribution. The appearance of having  $k$  primary encounters,  $P(n_p, k)$  is given by

$$P(n_p, k) = \frac{n_p^k}{k!} e^{-n_p} \tag{3.17}$$

Therefore, the efficiency of the detector is determined by

$$1 - P(n_p, 0) = 1 - e^{-n_p} \tag{3.18}$$

For a CO<sub>2</sub> dominant mixture at standard pressure and temperature, there are roughly 34 primary ionization interactions per centimeter for MIPs. The efficiency for a 1 mm thin gas gap chamber

filled with such gas mixture is 96.7%, which is sufficient for trigger and tracking applications. Reducing the gas gap further by half will result in an usually unacceptable efficiency of less than 85%. This is the reason why single gap gaseous detectors used in muon spectrometers are always thicker than 1 mm.

To determine the total ionization  $N_T$ , a few quantitative parameters should be noticed. The first parameter is the ionization energy  $I_0$  which is the minimum energy required to remove an electron from atoms in ground states. It is usually of tens of eV due to the fact that participating electrons come from outer shells of atoms which are less bonded. The second parameter is usually called the  $W$ -value which is the mean work required to produce an electron-ion pair.  $W$ -value is larger than  $I_0$  simply due to the fact that part of the energy from the incident particle could be dissipated to electrons in inner shells in excitation process or to nucleus by absorbing part of its momentum. The typical value of  $W$  in gas is about 30 eV. If a charged particle deposits an energy of  $\Delta E$  in the gas gap, the total ionization  $N_T$  is determined by

$$N_T = \Delta E / W \quad (3.19)$$

It should be mentioned that  $W$  has a dependence with the energy of the incoming particle but is almost constant for relativistic particles. In addition, it is slightly different for heavily charged particles, such as alpha particles, when compared with that for unit charge particles such as electrons or muons. A summary of the ionization related parameters in several regularly used gases in large detector systems is shown in table 3.2.

Besides the average number of ionizations in the gas media  $N_T$ , its statistical variation should also be considered in circumstances where energy measurements are important. Usually charged particles leave few tens or hundreds of electron-ion pairs in gas gaps of gaseous detectors. They can be considered to follow the Gaussian distribution with a standard deviation of  $\sqrt{N_T}$ . However, the actual fluctuation is smaller than that derived from a Gaussian distribution by a factor of  $\sqrt{F}$ .  $F$  is called the Fano factor [78] which depends on the gas mixture. The typical value of the Fano

Gas	Density ( $\text{g}\cdot\text{cm}^{-3}$ )	$I_0$ (eV)	$W_\alpha$ (eV)	$W_\beta$ (eV)	$dE/dx$ * ( $\text{keV}\cdot\text{cm}^{-1}$ )	$N_p$ *	$N_T$ *
Ne	$8.39 \times 10^{-4}$	21.6	36.6	36.4	1.45	13	40
Ar	$1.66 \times 10^{-3}$	15.7	26.4	26.3	2.53	25	97
CH <sub>4</sub>	$6.66 \times 10^{-4}$	12.6	21.9	27.1	1.61	28	54
CF <sub>4</sub>	$3.78 \times 10^{-3}$	16.0		54.0 *	6.38	63	120
CO <sub>2</sub>	$1.84 \times 10^{-3}$	13.8	34.3	32.8	3.35	35	100
iC <sub>4</sub> H <sub>10</sub>	$2.49 \times 10^{-3}$	10.6		26.0 *	5.67	90	220

\* Measured results are for unit charge MIPs

**Table 3.2** Ionization parameters for several gases at NTP (20 °C and 1 atm).  $I_0$ : ionization energy;  $W_\alpha$  and  $W_\beta$ : mean works to produce one electron-ion pair for alpha and beta incidences, respectively;  $dE/dx$ : mean energy loss;  $N_p$  and  $N_T$ : primary and total ionizations, respectively.

factor for ionizations in rare gases or their mixtures is around 0.2. Measured or calculated values for some mixtures are reported in [79,80]. The reduction in the ionization fluctuation is essentially due to the fact that the energy losses of incident particles and secondary ionizations in gas are not purely random. The energy conservation requirement and the discrete nature of electron energy levels limit the number of ways in which ionization yields could fluctuate.

### 3.4 Electron and ion transportation

As discussed in Chapter 2, gaseous detector is suitable for quantitatively studying the properties of the radiation due to the easiness to collect ionized electrons and ions with an electric field. The movement of these charge carriers has distinct characteristics, such as drift velocity, diffusion and capture processes, compared with that in solid state detectors such as silicon detector. Moreover, the negative charge carriers, the electrons, have very different drifting behaviors compared

with the positive charge carries, the ions produced simultaneously with the electrons. Therefore, understanding their drifting behaviors is mandatory for working with gaseous detectors.

### 3.4.1 Drift of electrons in gas

Without an electric field, when electrons at outer shells of gas atoms are released, they have isotropic multiple collisions with neighboring atoms and gradually lose their energies through inelastic scatterings. After they have been “cooled” down by the atoms, electrons eventually recombine with atoms or molecules. The only energies left are due to their thermal motions after they reached thermal equilibrium. At room temperature, the average electron thermic energy  $T_e$  is determined by the well-known theorem of equipartition of energy states

$$\langle T_e \rangle = \frac{m \langle v \rangle^2}{2} = \frac{3}{2} k_B T \quad (3.20)$$

where  $\langle v \rangle$  is the average velocity of the thermal motion,  $k_B$  is the Boltzmann constant and  $T$  is the temperature of the gas in unit of Kelvin. This results in an average electron energy of 0.0035 eV at room temperature. The thermic energy follows the Maxwell-Boltzmann distribution. Due to thermal movements, a point-like electron cloud will diffuse in space. The probabilities to find electrons at more distant places increase with time. Assuming the mean free path for an electron between collisions is  $\lambda_0$  and the mean time  $\tau$  between two collisions is given by

$$\tau = \frac{\lambda_0}{\langle v \rangle} \quad (3.21)$$

The probability that no collision takes place after time  $t$  is

$$P(t, 0) = \frac{1}{\tau} e^{-\frac{t}{\tau}} \quad (3.22)$$

The electron cloud extension  $r^2$  at the time when the first collision takes place is determined by [81]

$$r^2 = \int_0^\infty \frac{1}{\tau} e^{-\frac{t}{\tau}} \left( \frac{\lambda_0}{\tau} t \right)^2 = 2\lambda_0^2 \quad (3.23)$$

After time  $t$ , the number of collision  $n$  is equal to  $t/\tau$ . The charge cloud is now expanding to

$$\sigma^2(t) = n \cdot 2\lambda_0^2 = 2Dt \quad (3.24)$$

where  $D$  is defined as the diffusion coefficient and is given by

$$D = \frac{\sigma^2(t)}{2t} = \frac{\lambda_0^2}{\tau} = \frac{2}{m} \langle T_e \rangle \tau \quad (3.25)$$

The electron probability density function is described by a Gaussian distribution of the form

$$\rho(\vec{r}) = \varepsilon \exp\left(-\frac{\vec{r}^2}{4Dt}\right) \quad (3.26)$$

where  $\varepsilon$  is the normalization factor. Since the diffusion is isotropic as mentioned before, it is convenient to decompose it into three dimensions, which yields

$$\sigma_x(t) = \sigma_y(t) = \sigma_z(t) = \sqrt{\frac{2}{3}Dt} \quad (3.27)$$

When an electric field is present, if ionized electrons are neither absorbed by atoms nor attached by ions, they tend to have organized movements superimposed on the random thermal movements. The steady-state movement of an electron in an electric field results in a macroscopic velocity of  $V_D$  roughly along the field lines.  $V_D$  is called the drift velocity and depends very much on the electric field as well as the gas medium pressure. It could be qualitatively expressed as

$$V_D = \mu E / P \quad (3.28)$$

where  $E$  is the electric field and  $P$  is the pressure normalized by standard atmospheric pressure.  $\mu$  is a characteristic parameter called mobility, which is related to the mean time between collisions  $\tau$  by

$$\mu = \frac{e}{m} \tau \quad (3.29)$$

where  $m$  is the mass of the charge carrier and  $e$  is the unit charge on an electron.

It is also normal that gaseous detectors are placed inside a magnetic field and the movement of electrons is subject to the government of Lorentz forces. The equation of motion is given by

$$m \frac{d}{dt} \vec{V}_D = e(\vec{E} + \vec{V}_D \times \vec{B}) - m \frac{\vec{V}_D}{\tau} \quad (3.30)$$

where  $B$  is the external magnetic field strength. The first term on the right hand side represents the Lorentz force and the last term models the friction force between the electron and its surrounding gas atoms and molecules. The solution for the equation gives the drift velocity

$$\vec{V}_D = \frac{\mu}{1 + \mu^2 B^2} [\vec{E} + \mu(\vec{E} \times \vec{B}) + \mu^2(\vec{E} \cdot \vec{B})\vec{B}] \quad (3.31)$$

One should remember that the cyclotron frequency  $\omega$  of the electron in the magnetic field  $B$  is determined by

$$ev_c B = m\omega^2 r_c \quad (3.32)$$

where  $r_c$  and  $v_c$  are cyclotron radius and velocity, respectively. The mobility  $\mu$  is then related to  $\omega$  by

$$\mu B = \omega \tau \quad (3.33)$$

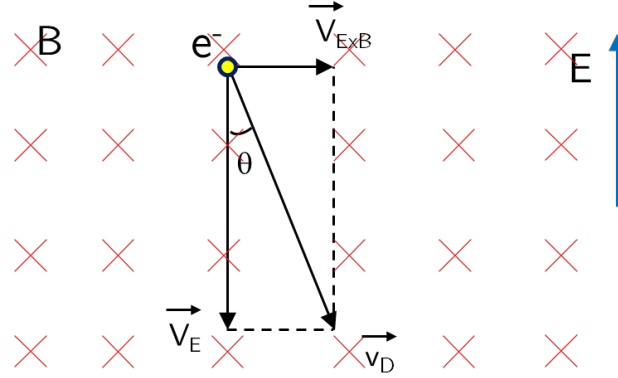
The expression for drift velocity could be rewritten as

$$\vec{V}_D = \frac{\mu}{1 + \omega^2 \tau^2} [\vec{E} + \omega \tau \frac{\vec{E} \times \vec{B}}{B} + \omega^2 \tau^2 \frac{(\vec{E} \cdot \vec{B})\vec{B}}{B^2}] \quad (3.34)$$

The second term of the equation describes the motion in the direction perpendicular to both  $E$  and  $B$ . The last term reflects the component in the  $B$  direction. With this general expression, one could derive the drift velocity for various field configurations. If the  $B$ -field is zero, then  $V_D$  in equation 3.34 is simplified and gives the same result as interpreted in equation 3.28 with the  $E$  modified to  $E/P$ . If there is a non-zero  $B$ -field, for the case  $B$  is parallel to  $E$ , there is no force caused by the magnetic field.  $V_D$  is the same as that only  $E$ -field is present. For the other case when  $B$  is perpendicular to  $E$ , the electron drifts at an angle  $\theta$  with respect to the electric field direction.

Its movement direction is pictorially shown in figure 3.8. The magnitude of the drift velocity could be derived from equation 3.34 to be

$$|\vec{V}_D| = \frac{\mu|\vec{E}|}{\sqrt{1 + \omega^2\tau^2}} \quad (3.35)$$



$$|\vec{V}_E| = \frac{\mu|\vec{E}|}{1 + \omega^2\tau^2} \quad |\vec{V}_{EXB}| = \frac{\mu\omega\tau|\vec{E}|}{1 + \omega^2\tau^2}$$

**Figure 3.8** Drift of an electron under and electromagnetic field with a  $B$  field perpendicular to  $E$ .

The angular deviation  $\theta$ , between the electron drift velocity and the electric field, is called the Lorentz angle, which can be written as

$$\theta = \tan^{-1}(\omega\tau) \quad (3.36)$$

The Lorentz angle for drift electrons in a given gas mixture is of particular concern when gaseous detectors used for measuring track hit positions are placed inside a  $B$  field perpendicular to  $E$  field. Especially for TPC or any gaseous detector reconstructing charged particle hit positions based on electron drifting time, dedicated corrections might be needed because the electron trajectories are now bent. As can be seen from equation 3.36, the Lorentz angle is closely related to the  $B$ -field strength and the mean electron collision time  $\tau$ .  $\tau$  is somewhat gas and  $E$  field dependent.

Therefore, proper selection of operational gases with low Lorentz angle parameters is favorable to minimize such unwanted magnetic field effect for tracking.

Now one could look back at the diffusion of electrons in an electric field. Since the electrons now have macroscopic movements long electric field lines, it is convenient to define two types of diffusions. One is the transverse diffusion, which characterizes the lateral displacements of electrons due to the diffusion in the plane orthogonal to the electric field. The other one is the longitudinal diffusion, which describes the variation of electron drift velocity along the  $E$  field direction and thus their arrival time on readout electrodes. Recalling the diffusion width given by equation 3.27 for three independent dimensions, when there is no electric field, the transverse diffusion width after time  $t$  is given by

$$\sigma_T(t) = \sqrt{\frac{4}{3}Dt} \quad (3.37)$$

and the longitudinal diffusion width after time  $t$  is the same as that shown in equation 3.27

$$\sigma_L(t) = \sqrt{\frac{2}{3}Dt} \quad (3.38)$$

If one recalls the relationship between drift velocity and electric field from equation 3.28, the diffusion coefficient given by equation 3.25, and the dependence of mean free time between collisions  $\tau$  with mobility  $\mu$  from equation 3.33, the diffusion width of the electron cloud at time  $t$  after starting with a point-like cloud in the presence of an electric field  $E$  could be rewritten as

$$\sigma_x(t) = \sqrt{\frac{2}{3}Dt} = \sqrt{\frac{2}{3} \frac{2 \langle T_e' \rangle}{m} \tau \frac{L}{\mu E}} = \sqrt{\frac{4 \langle T_e' \rangle L}{3 e E}} \quad (3.39)$$

It must be noted that the mean electron energy  $\langle T_e' \rangle$  is no longer only the thermal equilibrium energy of  $3k_B T/2$  but also includes the energy gained from the external electric field. Usually the gas with a mean electron energy comparable to the thermal equilibrium energy is called “cold gas”, and those with mean electron energies larger than the thermal energy scale is called “hot gases”. An example showing the electron energy dependences with the electric field for hot and cold gases

are depicted in figure 3.9 [82]. The characteristic electron energy in the plot is  $2/3$  of the mean electron energy discussed here. As can be seen from the plot, argon gas is a hot gas, which has electron energy greater than the thermal energy scale even in an electric field with a field strength of a few V/cm. In contrary,  $\text{CO}_2$  is a cold gas with electrons at thermal energy level up to a few kV/cm. It is explained in [83] that the cold gas could have various degrees of freedom to absorb the electron energy.

From equation 3.39, one could find that in general the electron diffusion is reduced as the  $E$  field strength increases. Simulated longitudinal diffusion coefficients as a function of the electric field for several argon and isobutane mixtures are shown in figure 3.10 to demonstrate this point. In addition, the diffusion is more significant if the electron energy is high. Therefore, cold gases with low electron energy are favored for drift chambers, in which diffusions are expected to be as low as possible.

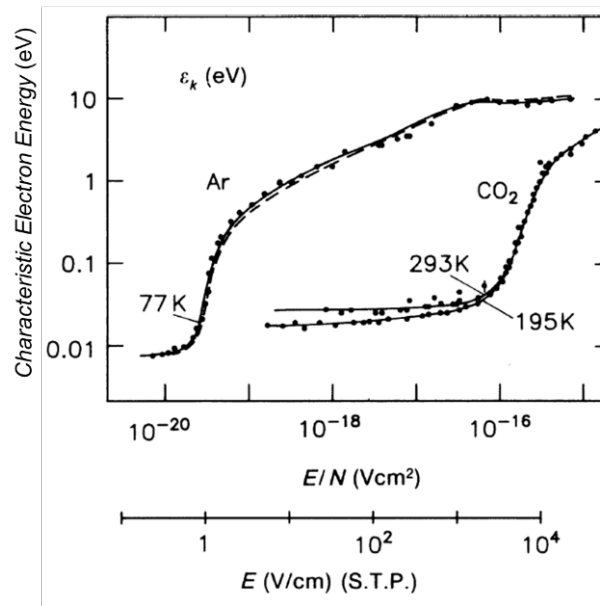


**Figure 3.9** Characteristic electron energy for Ar and  $\text{CO}_2$  as a function of the electric field [82].

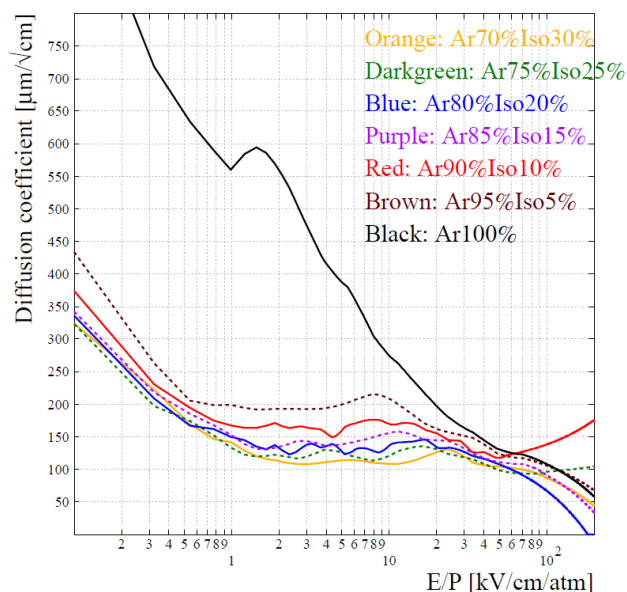


**Figure 3.10** Longitudinal diffusion coefficient as a function of the reduced electric field ( $E/P$ ) in argon and isobutane mixtures. “Iso” in the plot legend refers to isobutane.

Besides drift and diffusions inside the gas medium, ionized electrons could also get lost by attachment and recombination processes. The attachment process is that electrons are absorbed by the gas atoms and molecules to form negative ions. Since negative ions are heavy and slow moving, attachments result in the loss of ionization hence the induced signal amplitude, which are mostly unwanted for gaseous detector operations. Though negative ions could be formed in any gas, they are only notably stable in a few gases and their mixtures. Among them are water vapor, halogen and oxygen gases of which atoms or molecules have large electron affinity. They are usually called electronegative gases. The mechanisms of the attachment process are basically discriminated in two types. One is the absorption of low energy electrons in two-body process. In this process, electrons are directly attached to an atom or to a molecule which later breaks up into two constituents and one of them becomes negative ion. This is typical for halogen gases such as Freon. Another process is the absorption of electrons through three-body processes. Electrons could join molecules to form excited metastable negative ions, and they become stable negative ions if a third party

molecule collides with them and absorbs their excitation energies. Also the unstable molecules, formed by two different types of molecules, could disintegrate into stable negative ions and neutral particles when hit by electrons. This type of process plays an important role for electron attachment in oxygen. Since these electronegative gases could dramatically change the electron drift behavior and cause notable ionization losses even at smallest admixture, the cleanness of operational gases and the tightness of gaseous detectors are of mandatory requirements. When the electric field is low, electrons or negative ions could recombine with positive ions and this also results in the reduction of ionization charges that could have been collected by electrodes.

### 3.4.2 Drift of ions in gas

Ions drift in an electric field in opposite direction to electron drifts. Unlike electrons which are light and diffuse in all directions by frequent elastic collisions with gas atoms, ions are much heavier than electrons and thus have much less diffusions when they drift towards the detector cathodes. Their movements are much less disordered than electrons. They drift almost exactly following the electric field lines.

The drift velocity for ions could also be expressed as equation 3.28. However, now  $\mu$  refers to the ion mobility and  $m$  is the mass of ions. Since ions are three orders of magnitude heavier than electrons, their mobility is three orders of magnitude smaller than that of electrons. The typical drift velocity for electrons is around  $5 \text{ cm}/\mu\text{s}$ , whereas ions usually only drift at a speed of around  $50 \text{ }\mu\text{m}/\mu\text{s}$  in an electric field of few hundreds of  $\text{V}/\text{cm}$ . This can be seen from figure 3.11 [84] for several types of ions in their own noble gas medium. The ion mobility in low electric fields tends to be constant. This has been explained in [83] that, in low electric fields, ions with energy at thermal level regain an energy equal to the thermal energy after each collision. In high electric field, the ion mobility decreases with  $1/\sqrt{E}$ . The detailed derivations and discussions can also be found in [83]. There are a number of ion mobility measurements reported in literatures [85, 86]

for noble gases as well as several polyatomic gases. In general, the ion mobility in a moderate electric field of less than a few kV/cm and at normal temperature and pressure varies from  $0.2 \text{ cm}^2 \cdot \text{V}^{-1} \cdot \text{s}^{-1}$  up to  $10 \text{ cm}^2 \cdot \text{V}^{-1} \cdot \text{s}^{-1}$ . From the general review of the experimental results, heavier gases tend to have lower ion mobility. The ion mobility for mixed gas  $\mu_{mix}$  could be calculated by using Blanc's law [87]

$$\frac{1}{\mu_{mix}} = \sum \frac{f_i}{\mu_i} \quad (3.40)$$

where  $f_i$  and  $\mu_i$  are the fraction of  $i^{\text{th}}$  gas and the ion mobility of  $i^{\text{th}}$  gas, respectively.

Due to the slow movement of ions in the electric field, ion-induced current is much smaller than that induced by rapidly drifting electrons. As a consequence, it is difficult to collect induced charges promptly in some detector configurations. For instance, in wire chambers of a few millimeters thick, it takes a few hundreds of microseconds for ions to drift from the vicinity of anode wires to cathode plates. Moreover, it causes space charge effect and is a limiting factor for the detector to operate at high rate.

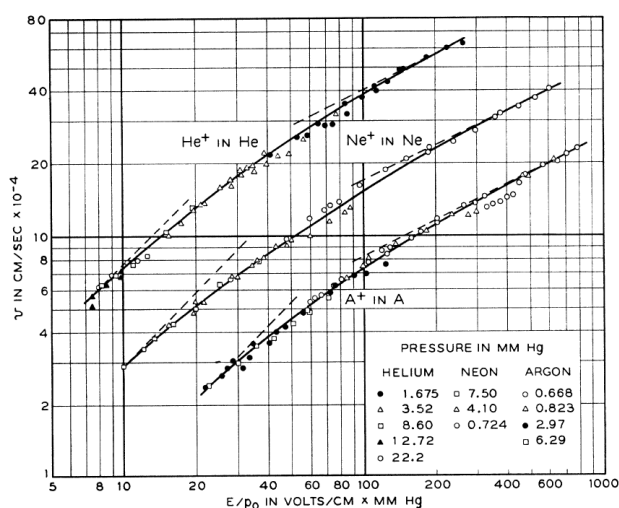


**Figure 3.11** The drift velocity of  $\text{He}^+$ ,  $\text{Ne}^+$  and  $\text{Ar}^+$  in their own gases as a function of the reduced electric field. The broken lines have slopes of 1 and 1/2 for those on the left and on the right, respectively [84].

## 3.5 Avalanche

### 3.5.1 Electron multiplication under electric field

A minimum ionizing particle usually leaves only a few tens of ionized electron-ion pairs in a few millimeters thick gas gap. Unlike solid state silicon detectors in which electrons liberated by the ionization process do not have any multiplication during the period of charge collection, ionized free electrons in a gas medium could be accelerated by the external electric field and initiate avalanches. This significantly increases the total amount of charge that could be collected on the electrode. The avalanche is developed when the electric field is sufficient to accelerate electrons to surpass the ionization potentials of the gas atoms before they encounter atoms or molecules. Assuming that a free electron is immersed in a constant electric field and it could gain enough energy to ionize gas atoms after travels a short distance  $\lambda$ , the number of ionization encounters per unit length is given by

$$\alpha = \frac{1}{\lambda} \quad (3.41)$$

where  $\alpha$  is called the first Townsend coefficient and  $\lambda$  is the mean free path between ionization collisions as mentioned in equation 3.15. If the number of electrons at a point  $x$  is  $N(x)$ , then the number of fresh electrons produced at a small interval  $dx$  is

$$dN(x) = N(x)\alpha dx \quad (3.42)$$

Moving  $N(x)$  in equation 3.42 to the left hand side and integrating the equation from the avalanche starting point to  $x$  on both sides yield the multiplication factor  $M$  which is given by

$$M = \frac{N(x)}{N_0} = e^{\alpha x} \quad (3.43)$$

where  $N_0$  is the number of electrons before the avalanche process, and  $M$  is called the gas gain.

Now one could look at a more realistic case considering that not every collision after a mean free path  $\lambda_0$  will give rise to an ionization. Since an electron has to gain an energy equal to the

ionization energy in a drift length of  $\lambda$  in order to knock out a secondary electron,  $\lambda$  is related to the electric field strength  $E$  by

$$\lambda = \frac{I_0}{eE} \quad (3.44)$$

It should be noted that the ionization only occurs when there is no previous collision took place before the electron has traveled a distance of  $\lambda$ . Otherwise the electron will lose its energy via scattering with atoms. Recalling equation 3.17, the probability of no collision encounter in a drift length of  $\lambda$  is given by

$$P = e^{-\frac{\lambda}{\lambda_0}} \quad (3.45)$$

Given the fact that  $\lambda_0$  reduces proportionally with the inverse of the electron density  $\rho$  and thus the pressure  $p$  of the gas medium, as has been interpreted in equation 3.15, a more realistic description of the first Townsend coefficient, taking into account the total number of collisions per unit length  $1/\lambda_0$ , is given by

$$\alpha(E) = \frac{1}{\lambda_0} e^{-\frac{\lambda}{\lambda_0}} = A p e^{-\frac{B}{E/p}} \quad (3.46)$$

where  $A$  and  $B$  are two positive constants depending on gas. For a parallel plate chamber with a gap thickness of  $d$ , if the voltage applied across two electrodes is denoted as  $U$ , the gas gain is given by

$$M = \exp \left[ A p d e^{-\frac{B p d}{U}} \right] \quad (3.47)$$

This relationship was first derived by Rose and Korrf [88] and found to be in good agreement with experimental measurements. In order to take a closer look at the dependence of the gas gain on the electric field, one could differentiate equation 3.47

$$\frac{\partial}{\partial U} \ln(M) = A p d \exp \left[ -\frac{B p d}{U} \right] \frac{B p d}{U^2} = \alpha \frac{B p d}{U^2} \quad (3.48)$$

If  $\alpha$  is proportional to  $U^2$  hence  $E^2$ , one could derive from equation 3.48 that the  $\ln(M)$  has a linear dependence on the applied voltage  $U$  or the gas gain  $M$  can be interpreted to be growing exponentially with  $U$ . This indeed holds true for parallel electrode detectors such as Micromegas

that the measured gas gains in various gas mixtures behave in this way. The linear dependence of  $\alpha$  with  $E^2$  is valid as long as the electric field is kept at a proper range. Examples for two argon and isobutane mixtures are shown in figure 3.12 to demonstrate the presence of such proportionality. The region highlighted in light blue corresponds to an electric field strength of 30-50 kV/cm, which is the typical field strength in a Micromegas detector with around 0.1 mm amplification gas gap.

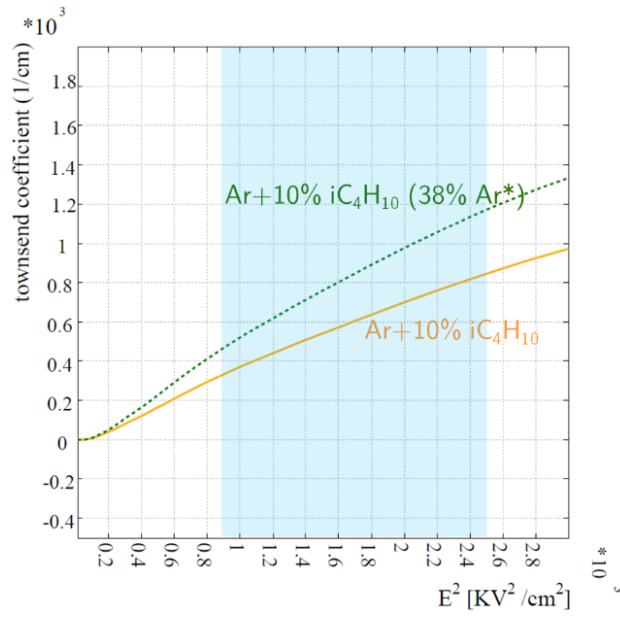


**Figure 3.12** The first Townsend coefficient as function of squared electric field strength in two argon and isobutane mixtures.

The mechanism of gas amplification for cylinder-shape proportional counters is the same as for parallel electrode detectors. However, the electric field in a cylinder-shape counter has a  $1/r$  dependence with the radial distance to a wire. Avalanches only take place a few tens of microns near the wire where a strong electric field is present. It is found that the gas gain as a function of the applied voltage for proportional tubes cannot be well fitted by the Rose-Korff formula. The Diethorn formula [89] shown in equation 3.49 is introduced to describe their correlations

$$\ln(M) = \frac{\ln 2}{\ln(b/a)\Delta V} \ln \left[ \frac{V}{\ln(b/a)aE_{min}(\rho/\rho_0)} \right] \quad (3.49)$$

where  $\Delta V$  and  $E_{min}$  are two gas-dependent constants.

For detectors with more sophisticated electric field configurations, gas gains need to be calculated by integrating the  $E$ -field dependent first Townsend coefficient  $\alpha$  over an electron drift path. This usually needs to be handled numerically using computer programs. When the electric field in the detector is sufficiently high, an avalanche could further grow to an extent that created ions distort the original electric field and reduce the proportionality of total produced electrons to the original ionization. The avalanche process becomes more complicated in excessively high electric fields and produces metastable states which eventually give rise to glowing discharges.

### 3.5.2 Statistical fluctuations of avalanches

Due to the stochastic nature of the avalanche process, the number of electrons obtained from the amplification fluctuates around the mean value of the gas gain calculated in the previous section. The naive assumption to consider is that each electron ionized by the charged particle initiates an avalanche which is independent to the rest. When the number of avalanche-initiating electrons  $N_e$  is large, a Gaussian distribution for the total number of finally produced electron is followed according to the central-limit theorem. The mean value of the total number of electrons is the product of  $N_e$  and the mean number of electrons generated in a single electron avalanche. Its variance is determined by  $N_e$  and the variance of individual avalanches.

In order to investigate avalanche fluctuations initiated by single electrons, it is convenient to introduce a characteristic length parameter  $x_0$

$$x_0 = \frac{U_i}{E} \quad (3.50)$$

where  $U_i$  is the ionization potential of the gas atom and  $E$  is the electric field strength that electrons have experienced.  $x_0$  gives the distance required for an electron to be accelerated to be capable to ionize an atom.

Firstly, one could consider the case that in weak electric fields,  $x_0$  is usually small compared with  $1/\alpha$ , the mean free path between two consecutive ionizations. This means that in a small interval  $dl$ , an electron always has a probability  $p = \alpha dl$  to cause an ionization, irrespective of its collision history. The probability for obtaining  $k$  fresh electrons in  $n$  collisions is given by the binomial distribution

$$P'(k, n, p) = \frac{n!}{k!(n-k)!} p^k (1-p)^{n-k} \quad (3.51)$$

Therefore, the probability to find  $n$  electrons after a small interval  $dl$  following a distance  $l$  is determined by

$$P(n, l + dl) = P(n, l)P'(1, n-1, p) + P(n-1, l)P'(0, n, p) + \mathcal{O}(dl^2) \quad (3.52)$$

The first term in equation 3.52 is the probability to have exactly  $n$  electrons after a path length  $l$  and no fresh electron produced in the interval  $dl$ . The second term is the probability to have  $n-1$  electrons after  $l$  and one ionization happening among  $n-1$  collisions in  $dl$ . The third term represents the sum of contributions from higher order corrections which are negligible. By inserting equation 3.51 and neglecting higher order terms, equation 3.52 could be rewritten as

$$P(n, l + dl) = P(n, l)(1-p)^n + P(n-1, l)(n-1)p(1-p)^{n-2} \quad (3.53)$$

Differentiating equation 3.53 and taking into account  $p = \alpha dl$ , one could obtain

$$\frac{d}{dl}P(n, l) = -P(n, l)n\alpha + P(n-1, l)(n-1)\alpha \quad (3.54)$$

If one defines a parameter  $u = \int_0^l \alpha(l') dl'$ , equation 3.54 could be simplified as

$$\frac{d}{du}P(n, u) = \frac{d}{dl}P(n, l) / \frac{du}{dl} = P(n-1, u)(n-1) - P(n, u)n \quad (3.55)$$

When  $n = 1$ , the solution for equation 3.55 is given by

$$P(1, u) = e^{-u} \quad (3.56)$$

The solution for equation 3.55 could be derived by inserting equation 3.56 into the differential equation and repeating the solving procedure for  $n > 1$ . Finally, the probability of finding  $n$  electrons in an avalanche is given by

$$P(n, u) = e^{-u} (1 - e^{-u})^{n-1} \quad (3.57)$$

Substituting  $u$  with length  $l$ , equation 3.57 is expressed as

$$P(n, l) = \frac{1}{e^{\int_0^l \alpha(l') dl'}} \left( 1 - \frac{1}{e^{\int_0^l \alpha(l') dl'}} \right)^{n-1} \quad (3.58)$$

Note that the term  $\exp[\int_0^l \alpha(l') dl']$  is the mean gas gain for an electron traveled a path length of  $l$ , which could be denoted as  $\bar{n}$ . If the avalanche size is large enough, equation 3.58 could be rewritten as

$$P(n, l) = \lim_{\bar{n} \rightarrow \infty} \frac{1}{\bar{n}} \left( 1 - \frac{1}{\bar{n}} \right)^{n-1} = \frac{1}{\bar{n}} e^{-\frac{n}{\bar{n}}} \quad (3.59)$$

As can be seen from equation 3.59, for single electron avalanches in weak electric fields, the fluctuation follows an exponential distribution. This means productions of a smaller number of electrons are more favorable in avalanches. The standard deviation of the gain fluctuation  $\sigma(l)$  is given by

$$\sigma(l) = (\bar{n}) \quad (3.60)$$

The assumption that the electron multiplication process is independent of the electron collision history faces difficulties in explaining the avalanche fluctuations in strong electric fields, which is no longer exponentially distributed but rounded at the lower end of the avalanche size distribution [90]. In an attempt to explain this phenomenon, Legler [91] introduced a parameter which is defined as

$$\chi = \frac{\alpha(E)U_i}{E} = \alpha(E)x_0 \quad (3.61)$$

As discussed before, in weak electric fields, the distance that an electron traveled between ionization collisions  $1/\alpha$  is sufficiently longer than  $x_0$ , hence  $\chi \ll 1$ . As the electric field increases,

the ionization mean free path for electrons is shortened and gradually becomes comparable to  $x_0$ , hence  $\chi$  approaches 1. It is especially worth noting that as  $\chi \rightarrow 1$ , electrons which have ionization encounters lose their energy by  $eU_i$ . They do not participate in the ionization process unless they have gained enough energy. The energy distribution of avalanche electrons thus have sudden changes especially at the early stage of an avalanche development. The assumption that all electrons in the avalanche process hold equal probability of ionizations should be withdrawn. A theory was proposed by Legler that in strong electric fields, the first Townsend coefficient  $\alpha$  depends on the avalanche size as well as the distance the electron has traveled [92]. The “round” effect of the avalanche distribution in homogeneous strong electric fields has been reproduced based on this theory. As the electric field becomes stronger and thus the mean avalanche size and  $\chi$  increase, the variance of the distribution reduces and the peak in the probability distribution approaches the mean. In non-uniform strong electric fields, as is the case for wire chambers in which electric fields have  $1/r$  dependences with the distance to wires, the single electron avalanche fluctuation for sufficiently large avalanche size was found by Alkhazov [93] to resemble the Polya distribution given by

$$P(n|\bar{n}, \theta) = \frac{1}{\bar{n}} \frac{\theta^\theta}{\Gamma(\theta)} \left(\frac{n}{\bar{n}}\right)^{\theta-1} e^{-\frac{n\theta}{\bar{n}}} \quad (3.62)$$

where  $\theta$  is the scale parameter related to  $\chi$  and  $\bar{n}$  is the mean number of electrons produced in the avalanche. The variance of the distribution is given by

$$\sigma^2 = \frac{\bar{n}}{\theta} = \bar{n}^2 f \quad (3.63)$$

where  $f$  is the width parameter describing the magnitude of fluctuations. Though the physics meaning of scale and width parameters are dubious, they are usually used to characterize the energy resolution of the detectors.

To summarize, the reduction of avalanche fluctuation in strong electric fields is closely related to the avalanche electron energy distribution. The equal probability of ionization for avalanche electrons should be abandoned and the electron collision history plays an important role in the

determination of avalanche growth. In general, smaller number of ionized electrons at the early stage means electrons have less ionization encounters thus reserve their energy and probability for later ionization collisions. The overall effect is the reduction of the probability for developing very small size avalanches given a large mean avalanche size. Therefore, fluctuations of produced electrons for avalanches developed in strong electric fields deviate from exponential distributions at lower ends and exhibit peaks in their distributions. Further understanding of the avalanche fluctuation requires models incorporating sophisticated energy-dependent ionization and excitation cross sections. Microscopic Monte Carlo simulation is a more suitable way and recent progresses could be found in [94].

## 3.6 Signal induction

Signals from gaseous detectors are essentially charge currents induced by movements of ionized electrons and ions in the gas medium. Recalling from section 3.4 that electrons have typical drift velocities of  $5\text{--}10\text{ }\mu\text{s/cm}$  in the gas whereas ions drift towards cathodes at the velocity of about three orders of magnitude slower than that for electrons, typical current signals from gaseous detectors have fast electron induced component of a few ns or less and slow ion induced component of a few hundred nanoseconds or longer. In general, determination of induced charge currents on an electrode is based on the calculation of induced charge density as a function of time. The time structure of signals from two typical detector geometries will be briefly introduced in the following.

### 3.6.1 Induced signals from parallel plate structure detectors

For parallel plate structure detector, electrons and ions are moving towards two opposite sides in an uniform electric field. Assuming an electron-ion pair is produced at a distance  $x$  to the cathode of a parallel plate chamber with a thickness of  $d$ . The energy required to move such electron to the

anode is given by

$$eU \frac{d-x}{d} = \frac{1}{2}CU^2 - \frac{1}{2}CU'^2 \quad (3.64)$$

where  $C$  is the capacitance of the detector.  $U$  and  $U'$  are the voltages across the detector before and after the movement of the electron, respectively. Two terms on the right hand side of equation 3.64 are the original and reduced energies stored on the parallel plate chamber, respectively. Taking into account that the voltage difference,  $U - U'$ , on the electrode for moving the charge is negligible compared with  $U$ , the induced signal amplitude on the electrode is given by

$$\Delta U_e = U - U' = \frac{e}{C} \frac{d-x}{d} \quad (3.65)$$

Similarly, one could obtain the signal amplitude induced by the movement of the ion to be

$$\Delta U_i = \frac{e}{C} \frac{x}{d} \quad (3.66)$$

The total amplitude of  $e/C$ , given by summing the electron and the ion induced parts, is reasonable as no net charge is produced inside the gas gap. The induced charge current from the electron and ion movements as a function of time  $t$  are given by

$$I_e(t) = e \frac{v_e t}{d}, \quad t \in [0, \frac{d-x}{v_e}) \quad (3.67)$$

$$I_i(t) = e \frac{v_i t}{d}, \quad t \in [0, \frac{x}{v_i}) \quad (3.68)$$

where  $v_i$  and  $v_e$  are ion and electron drift velocities, respectively. Since electrons and ions are drifting at constant velocities in an uniform electric field, there is a steady current flowing through the detector at the beginning. When electrons reach the anode, no further current is produced. Ions continue to induce current which is three orders of magnitude smaller than the original electrons induced current. More complicated situations in which ionizations are produced along the charged particle track inside the gas gap could be handled by superimposing individually induced currents at different places and taking account currents induced by fresh ionizations created in avalanche

processes. It is worth noting here that the avalanche is growing towards the anode. Therefore, majorities of the electrons are produced near the anode and thus contribute very little to the total induced charge amplitude. Usually a long charge collection time is needed in order to produce a pronounced signal to be registered by the front-end electronics. Thinner gas gaps, higher electric fields and gas with higher ion mobility are favored to improve the timing performance of the detector. This will be further discussed in chapter 4.

### 3.6.2 Induced signals from cylinder shape counters

The second type of most frequently used gaseous detector is proportional tubes consisting of a thin anode wire and a cylinder tube wall that is a few millimeters from the wire. Assuming that the tube has a radius  $r_a$  and the tube wall has a radius  $r_c$ , if a positive high voltage  $U$  is applied to the anode wire and the tube wall is grounded, the electric field strength and the potential at a distance  $r$  to the anode wire center could be derived from Gauss's law to be

$$E(r) = \frac{CU}{2\pi\epsilon_0 r} \quad (3.69)$$

$$\varphi(r) = \int_a^r E(r) dr = \frac{CU}{2\pi\epsilon_0} \ln \frac{r}{a} \quad (3.70)$$

where  $\epsilon_0$  is the dielectric constant in the vacuum and  $C$  is the capacitance per unit length along the wire, which is determined only by the detector geometry and is given by

$$C = \frac{2\pi\epsilon_0}{\ln(b/a)} \quad (3.71)$$

Assuming no energy is compensated, the electric energy change due to the movement of charge  $q$  by a small step of  $dr$  is given by

$$\frac{1}{2}lCU^2 - \frac{1}{2}lCU'^2 = qE(r) dr = q \frac{d}{dr} \varphi(r) \quad \text{or} \quad lCU dV = q \frac{d\varphi(r)}{dr} dr \quad (3.72)$$

Inserting equation 3.69 into equation 3.72, the induced signal amplitude  $dV (= U - U')$  is given by

$$dV = \frac{q}{2\pi\epsilon_0 l} \frac{1}{r} dr \quad (3.73)$$

Assuming electrons and ions are produced at the same distance  $s$  from the wire center, their induced signal amplitudes on the anode could be derived by integrating equation 3.73 over their radial traveling distances

$$V_{elec} = \int_a^{a+s} dV = \frac{-q}{2\pi\epsilon_0 l} \ln \frac{a+s}{a} \quad (3.74)$$

$$V_{ion} = \int_{a+s}^b dV = \frac{-q}{2\pi\epsilon_0 l} \ln \frac{b}{a+s} \quad (3.75)$$

Both electron and ion induced signals on the anode wire are of negative polarity and the ratio of these two components is

$$\frac{V_{elec}}{V_{ion}} = \frac{\ln(a+s) - \ln a}{\ln b - \ln(a+s)} \quad (3.76)$$

For a wire counter with a wire radius of  $25 \mu\text{m}$  and a counter radius of  $1.4 \text{ mm}$ , if avalanches are mostly developed within  $10 \mu\text{m}$  from the wire surface, it could be calculated using equation 3.76 that electron induced signals are around 10% of those induced by ions. It should be pointed out that this calculation represents a similar situation for multi-wire chambers with same wire diameter and an anode-cathode separation equals to the counter radius mentioned here. Such configuration, a single wire counter with a small tube diameter or a multi-wire counter with thin gas gap, gives rises to a small yet non-negligible fraction of electron induced fast signals. In contrary, electrons induced signals in typical single wire proportional counters with tube diameters of a few tens of millimeters and avalanches development within a few  $\mu\text{m}$  from the wire surface, have less than 1% contribution to the total induced charge amplitudes.

A very important aspect in view of applying wire counters in a high counting rate experiment is to understand the time structure of its output signals. One should have noted that there is a long ion tail from the counter. This usually limits the counting rate before the space charge effect becomes prominent. In order to improve the rate capability, front-end electronics with a short shaping time are employed to integrate part of the signal and filter out the rest of the slow ion induced part. To aid the design of front-end amplifier sensitivity, it is essential to estimate the amount of charges collected by the electronics compared with the total charges produced inside the gas gap.

Assuming the signal is dominantly induced by ions drifting from the surface of the anode wire, the ion position  $r$  as a function of time could be determined by recalling the relationship between the ion drift velocity and the ion mobility given by equation 3.28

$$\frac{dr'}{dt} = \mu_{ion} \frac{E(r')}{P} = \frac{\mu_{ion}}{P} \frac{CU}{2\pi\epsilon_0 r'} \quad (3.77)$$

$$\int_a^r r' dr' = \frac{\mu_{ion}}{P} \frac{CU}{2\pi\epsilon_0} \int_0^t dt \quad \text{or} \quad r(t) = \sqrt{a^2 + \frac{\mu_{ion}CU}{\pi\epsilon_0 P} t} \quad (3.78)$$

Considering the  $r-t$  function for the ion given by equation 3.78, the signal amplitude as a function of time could be derived from equation 3.73

$$V(t) = - \int_0^t dV = - \frac{q}{2\pi\epsilon_0 l} \ln \frac{r(t)}{a} = - \frac{q}{4\pi\epsilon_0 l} \ln \left( 1 + \frac{\mu_{ion}CU}{\pi\epsilon_0 a^2 P} t \right) \quad (3.79)$$

It can be seen from equation 3.79 that the induced charge amplitude has a logarithmic dependence with time. Given the fact that in a typical wire counter has a tube radius of a few cm, ions produced in the vicinity of wires need a few hundreds of microseconds to be fully collected by the cathode plane. More than half of the induced charges are produced after a few hundreds of nanoseconds, which is comparable to or exceeds the maximum shaping time constant of pre-amplifiers in modern front-end chips [95, 96]. Therefore, operating wire chambers with a higher gas gain is required to compensate the signal amplitude lost due to incomplete collection of the charge produced inside the chamber.

### 3.6.3 Signal induced on multiple electrodes

It is quite common that planar electrodes of the gaseous detectors are segmented for precision tracking. Charge signals are spread out to multiple readout electrodes and hit positions better than the readout electrode pitch could be obtained using charge centroids. The general theorem for calculating induced charges current on different electrodes, due to the movement of a charge carrier inside the gas gap, is derived by Ramo using Green reciprocity [97]. The induced current

on an electrode is given by

$$I(t) = -\frac{d}{dt}Q(t) = -qv[x(t)]E_w \quad (3.80)$$

where  $q$  is the original charge inside the gas gap, and  $Q(t)$  is the time-dependent induced charge on a particular electrode.  $v$  and  $E_w$  are the drift velocities of the original charge carriers and the weighting field of that particular electrode, respectively. The weighting field of an electrode is equivalent to the electric field vector obtained by setting the interested electrode to unit potential and all other electrodes to the ground. An example weighting field for the central readout strip of a wire chamber is calculated using finite element method (FEM) and is depicted in figure 3.13. It is worth noting that the unit for  $E_w$  is 1/cm rather than V/cm, which could be verified from equation 3.80.

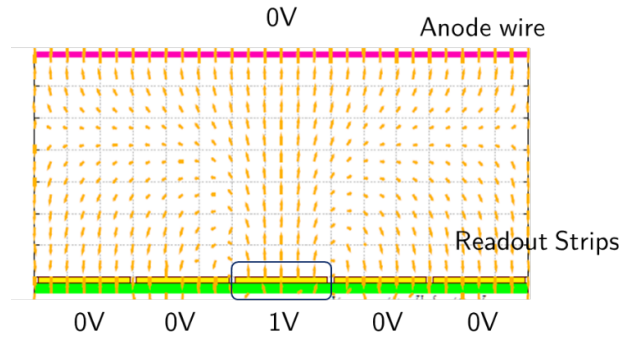


**Figure 3.13** The calculated weighting field of the central readout strip in a wire chamber.

The induced charge  $Q$  on an electrode at time  $t$ , when original charge moved from their initial position  $x_0$  to a new position  $x_1$ , could be calculated by integrating equation 3.80

$$Q(t) = \int_0^t I(t')dt' = -q \int_0^t E_w \frac{dx}{dt'} dt' = q[\phi(x_1) - \phi(x_0)] \quad (3.81)$$

where  $\phi(x)$  is called weighting potential and its relationship with weighting field  $E_w$  is given by

$$E_w(x) = -\nabla\phi(x) \quad (3.82)$$

$\varphi(x)$  is the absolute potential value at position  $x$  when the interested electrode is given a unit potential and the rest electrodes are grounded. It could be seen from equation 3.81 that the induced charge depends on the starting and ending points of moving charge carriers but not their exact trajectories. When electrodes are connected with impedances, corrections to equation 3.80 are required in order to calculate induced charge currents, since the current change only takes place when it flows among electrodes. It is also quite often for newly developed gaseous detectors to implement resistive electrodes with external readout strips or pads capacitively coupled to them. Complete theory of determining the signal shapes on these readout elements is not presented. Alternative analytical models are usually developed, which treat the charge sharing among readout elements into two steps: the induced charge extends on the resistive electrodes, and induced charge on the resistive electrode disperses in the distributed resistive-capacitive network formed by the resistive plane and the readout plane. A detailed example model which describes the charge sharing among the readout strips of a thin gap multi wire chamber will be presented in chapter 6.

# Chapter 4

## Thermo-bonded Micromegas

### 4.1 Overview

A typical structure for Micromegas detector is shown in figure [4.1](#). It has two asymmetric gas gaps separated by a micro-mesh. The upper gas gap is called the drift or conversion gap, usually a few mm thick. The lower gas gap is named as the avalanche or amplification gap, only about a hundred microns thick. Negative potentials are usually applied on the micro-mesh and the drift electrode while the readout strips are connected to the ground. The electric field is about a few hundreds of V/cm in the drift gap and is a few tens of kV/cm in the amplification gap due to the extremely thin gas gap formed between the micro-mesh and the anode readout plane. When a charged particle passes through the detector, it produces ionizations in the drift gap along its track. These ionized electrons are guided by the drift electric field towards the amplification gap where avalanches are developed in the strong electric field. For the detection of photons, they could be converted into photo-electrons or impart part of their energy to electrons through Compton scattering inside the conversion gap.

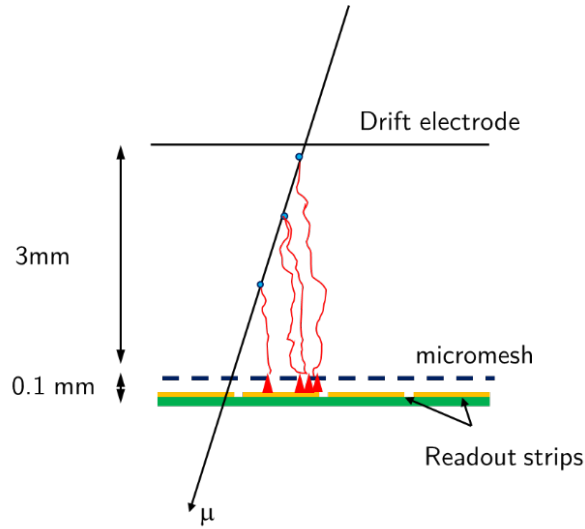


**Figure 4.1** Typical structure of a Micromegas detector.

Thanks to the thin amplification gap structure, most of the ions created in the avalanche could be collected by the micro-mesh in a few hundreds of nanoseconds, or even a few tens of nanoseconds if the amplification gap is further reduced [98]. The high rate capability, easily exceeds a few MHz/cm<sup>2</sup> due to the fast evacuation of ions, plus excellent spatial resolution, achievable of a few tens of microns using finely segmented readout electrodes, make the Micromegas detector well suited for precision muon tracking. However, there are several issues in view of applying such detector technology for muon trigger and tracking in hadron collider experiments. Firstly, similar to other micro pattern gaseous detector technologies, it is undoubtedly challenging to construct the detector to m<sup>2</sup> scale. The maximum sizes of presently constructed and experimentally implemented Micromegas detectors are  $35 \times 36 \text{ cm}^2$  and  $40 \times 40 \text{ cm}^2$  in T2K [99] and COMPASS [100] experiments, respectively. The Micromegas detector contains micro-structures which in turn sets very strict requirement on the mechanical precision of constructions. In addition, the micro-structures tend to be relatively fragile under high electric field if any dust or debris is present. As a result, there is also very tight restriction on the cleanness of constructional materials and handling during

fabrication processes. Secondly, it is quite well known that standard Micromegas with micro-mesh facing the metallic anode plane could develop discharges in hadron environment where dense ionizations are produced inside the drift gap after the passage of heavily charged particles. Due to the large capacitance from the thin amplification gap between two parallel planes, the discharges or sparks, releasing large amount of energy, are destructive to sensitive front-end electronics connected to readout elements. Moreover, the long dead time associated with sparks [101], could dramatically reduce the detection efficiency. Thirdly, owing to the long ion induced charge collection time, typically a few hundreds of nanoseconds, signals from typical Micromegas detectors have long rise time and relatively large jitter. Their timing performances are inferior to those from RPCs. Optimizations of the detector structure, gas mixture might be needed for precision trigger applications, in which good timing capability is essential for bunch crossing identifications.

In this chapter, a novel method to construct Micromegas detectors is first presented in section 4.2. It is based on the thermal bonding of micro meshes to anode planes using thermo-bond films. Details on attempts to fabricate small prototypes will be introduced. Basic performance parameters of these thermo-bonded Micromegas prototypes are measured and reported in section 4.3. Various simulation studies on improving the gain uniformity, optimizing electron transmission through micro-meshes are discussed in section 4.4. Finally, motivated by applying the Micromegas detector technology for muon tracking and triggering in hadron collider experiments, attempts to develop spark-resistant Micromegas in an unconventional approach will be presented in section 4.5. In addition, based on the thermo-bonding fabrication method, the development of a Micromegas variant called Parallel Ionization Multiplier (PIM) with fast signals will be introduced in section 4.6.

## 4.2 Fabrication of Micromegas with thermo-bonded spacers

A couple of methods have been developed to construct the amplification gap of a Micromegas detector. The original method is to suspend a micro-mesh on an anode plane using nylon fishing lines [102] with diameters around one hundred microns. Two more advanced fabrication approaches which have been successfully developed and used for presently operational experiments are bulk [103] and micro-bulk [104] techniques. The bulk Micromegas fabrication technique is based on photo-lithography processing. A layer of micro-mesh is laminated with a thin layer of photo-resistive film on a printed circuit board (PCB). Most part of the photo film is etched by the lithography process and only small covered spots are left to form mesh-supporting pillars which are usually 2-3 mm apart. The micro-bulk technique to fabricate Micromegas is based on the etching of thin Kapton foils. There are copper layers on both sides of a Kapton foils. Copper layers are etched on one side of the Kapton to form the micro-mesh and on the other side to form the readout patterns, such as strips or pixels. The Kapton foil itself is partially removed to produce supporting pillars. There are mainly two types of micro-meshes used in the Micromegas structure. One is the woven wire mesh using metallic wires of a few tens of microns in diameter. It has very good mechanical strength and is usually produced in industry at large scales. Therefore, such kind of mesh has been employed in the bulk Micromegas production. The other type of meshes is chemically etched or electro-formed. These meshes, such as those formed in a micro-bulk Micromegas structure, are only a few microns thick. They have very good uniformity and well defined geometric structures. Electron transmissions through these meshes are relatively easy because they are less likely to be trapped by the wire edges around the mesh openings. However, these ultra-thin meshes are very fragile and thus are very difficult to be used for meter-scale applications.

Though photo-lithography processes used for producing bulk Micromegas are quite common in industry which produces PCBs, it is still of great interest to find other convenient approaches which allow researchers to easily construct Micromegas prototypes in their labs for various purposes of

research and developments. A fabrication method which could simply and quickly change the detector structure, size and shape, is desired to optimize detector operational parameters or verify new ideas. Motivated by these considerations, a novel approach to fabricate Micromegas or its variants with micro-meshes is developed. The core part of the innovation is to use commercial thermo-bond films as spacers and separators for the Micromegas amplification gaps. The film could attach a stretched woven wire mesh to an anode readout plane and keep an equal distance between these two planes. Details on the material properties and the detector fabrication procedures will be reported in the following subsections.

#### 4.2.1 Micro-meshes and Thermo-bond films

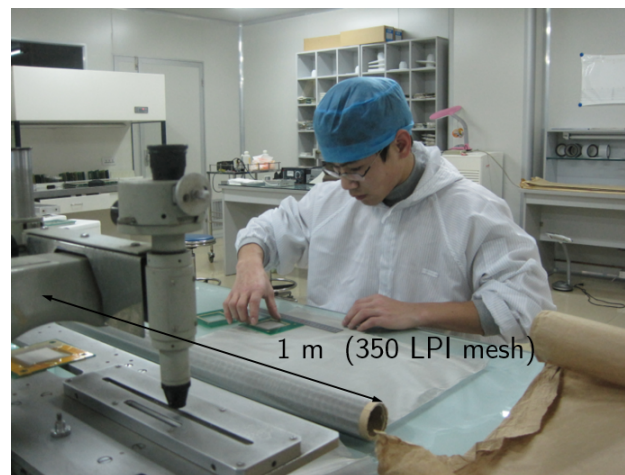
The micro-meshes used in the Micromegas prototype fabrication are standard stainless steel woven wire meshes. Woven meshes are basically characterized by two factors: lines per inch (LPI) and the weaving method. LPI is the number of wires per inch in the direction perpendicular to wires. Given a fixed wire diameter, mesh openings are smaller thus the mesh is less transparency to light. Assume the mesh openings are squares, it is usually convenient to define a parameter called optical transparency  $T$ , which is given by

$$T = \left( \frac{L}{D+L} \right)^2 \quad (4.1)$$

where  $L$  is the mesh opening size and  $D$  is the wire diameter. The woven micro-meshes also have two different weaving methods: plain or twill weaving. The plain weaving has orthogonal wire crossings at each intersection and forms a crisscross pattern. The twill weaving usually has fewer crossings and thus the mesh constructed is less sturdy.

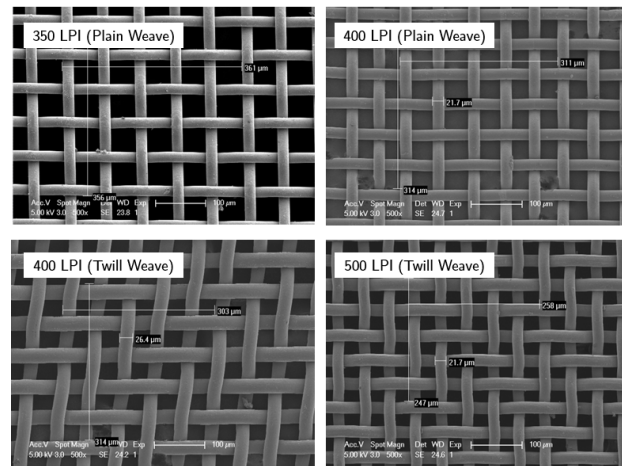
In our experiments, we have attempted to use 350 LPI, 400 LPI and 500 LPI stainless steel wire meshes. The 400 LPI wire meshes are available both in plain and twill weaving format. The rest of the meshes are plain weaved. All these meshes come from industrial mass productions and are delivered in rolls with a width of 1 meter. A roll of 350 LPI plain weaved mesh is shown

in figure 4.2. All four types of meshes are scanned using scanning electron microscope (SEM) and their magnified images are shown in figure 4.3. Irregular shapes of the mesh openings and non-parallelism of wires are quite significant for 400 LPI twill weaved mesh. Variations in mesh openings are also clearly visible for 400 LPI plain weaved mesh and are less apparent for 350 LPI plain weaved mesh. Wire diameters as well as mesh opening sizes are measured during the SEM scans and these geometric parameters along with the calculated optical transparency for four meshes are listed in table 4.1. The largest optical transparency is about 50% for 350 LPI mesh and the least one is only around 30%.



**Figure 4.2** A roll of 350 LPI woven wire mesh with 1 m width.

Mesh type (LPI)	Wire diameter ( $\mu\text{m}$ )	Hole size ( $\mu\text{m}$ )	Optical transparency (%)
350 (Plain Weave)	21.7	50.5	49
400 (Plain Weave)	21.7	40.5	42
400 (Twill Weave)	26.4	34.2	32
500 (Plain Weave)	21.7	29.9	34

**Table 4.1** Geometric parameters of woven wire meshes**Figure 4.3** Four stainless steel woven meshes imaged by scan electron microscope (SEM).

The thermo-bond film is a kind of specially formulated flexible adhesive film, which is solid at room temperature and could be activated by heat and pressure for bonding a variety of substrates such as metal, paper or many plastics. Bonding films we used are produced by 3M [105] and Transilwrap [106] companies and are 80  $\mu\text{m}$  or 152  $\mu\text{m}$  thick. Photos of thermo-bond films in 200-500 mm wide rolls or Letter sized sheets are shown in figure 4.4. Other thicknesses in the range of few tens of microns to a few hundreds of microns are also available but have not been tried. Bonding films are generally composed of a thin layer of polyester core sandwiched between

two dry polymer adhesive layers. The ratio of three layer thicknesses is either 1:4:1 or 2:2:2. Since the core polyester layer does not melt at nominal film cure temperature, the main differences of the former configuration compared with the latter are the former configuration has slightly weaker bonding strength and less reduction in thickness when melted and pressed for bonding. Thin films, less than  $100\ \mu\text{m}$  thick, may only contain adhesive polymers.

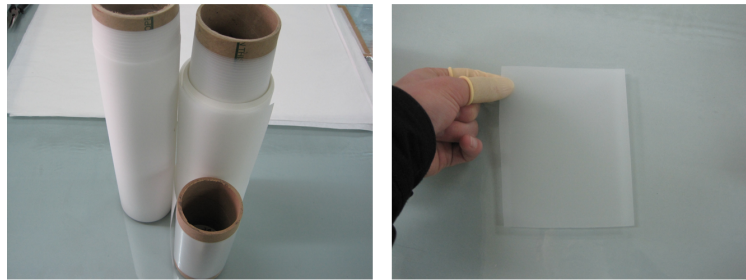


**Figure 4.4** Thermo-bond films in rolls (left) and sheet (right) formats.

Thermo-bond films typically have similar electrical and mechanical properties. Take 3M bonding film type 406 as one example, measured properties are listed in table 4.2. These bonding films are excellent insulators and have exceptionally good bonding strength, especially to metal substrates including the stainless steel woven mesh that we used. The thicknesses of these films are also found to be very uniform, variations are usually within  $2\ \mu\text{m}$ . These features make them suitable to be used as separators or spaces in Micromegas structures. Though physical parameters vary from film to film, the typical temperature for the film to melt and become adhesive is about 100 to 160 Celsius. Usually pressures around  $1\ \text{kgf/cm}^2$  are applied during thermal attaching processes in order to make firm contact between substrates and bonding films.

### 4.2.2 Materials qualifications and fabrication procedures

In total, several tens of thermo-bonded Micromegas prototypes have been fabricated with sizes from  $2\ \text{cm} \times 4\ \text{cm}$  up to about  $20\ \text{cm} \times 20\ \text{cm}$ . The maximum size, however, appears to be limited

<b>Physical</b>	Thickness	0.08 mm
	Color	Translucent
	Softening range	149-160 °C
<b>Electrical</b>	Dielectric constant	2.4 @1 MHz
	Dielectric breakdown strength	2300V/mil
	Volume resistivity	$5.9 \times 10^{17} \Omega \cdot \text{cm}$
<b>Mechanical</b>	Tensile strength @ break	2600 psi
	Overlap shear strength (bond to FR-4)	1120 psi
	90 peel strength (bond to FR-4)	10 pounds per inch of width
	Overlap shear strength (bond to steel)	1120 psi
	90 peel strength (bond to steel)	10 pounds per inch of width

**Table 4.2** Physical, electrical and mechanical properties of 3M™ bonding film 406.

by our unrefined thermal treatment tools. General procedures of fabrication, improved after many unsatisfactory attempts, are illustrated in figure 4.5. All processes are performed inside a class 100,000 clean room. They could be divided into the following steps:

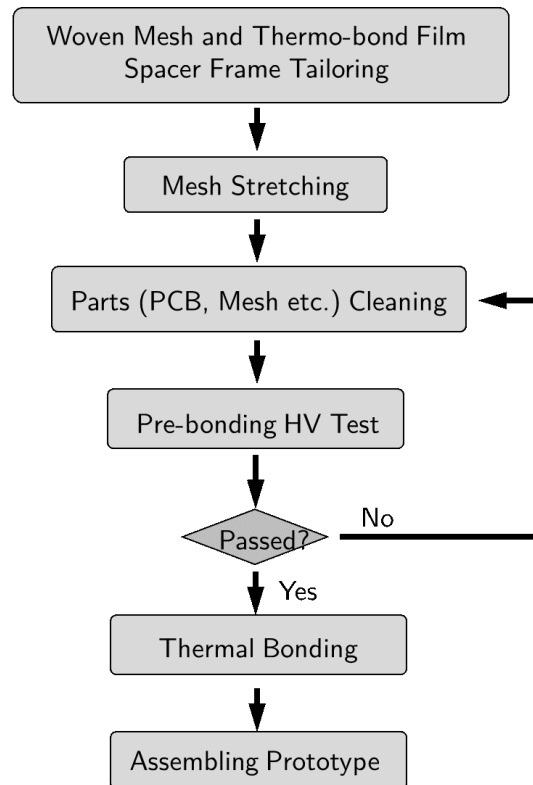


**Figure 4.5** Procedures to fabricate thermo-bonded Micromegas.

- **Material preparation:** In this stage, woven meshes are tailored to make both avalanche and drift electrodes. Due to the common presence of defects on the woven mesh, it is important to check the mesh before stretched and bonded. A high precision, a few- $\mu\text{m}$  resolution, optical gaging system as shown in figure 4.6 has been used to survey any suspicious region. Several types of mesh defects are identified and depicted in figure 4.7. The presence of broken wires on the mesh will definitely trigger sparks at shape wire tips hence caused detector failures. Thin amplification structures are also vulnerable to debris and dusts even though

they might be insulators. When these dusts are left in the tiny gas gap, they could be charged up and initiate discharges. As they eventually become carbonized and conductive, persistent shortage or break down will take place. Once dusts or floating wire segments are found, meshes need to be brushed to remove them. If the mesh is found to be broken or any sign of sharp folding at some points, it will be withdrawn.

For the preparation of mesh-supporting materials, thermo-bonded films are cut into rectangular-shaped frames with a typical width of 5-7 mm and round-shaped spacers with diameters of 5 mm. These thermal bond film frames are intentionally made wide as they will be used as to support the stretched meshes. Openings inside the rectangular frame define active areas of the fabricated Micromegas prototypes. Round spacers are placed inside active areas when the unsupported mesh span exceeds several centimeters.

- **Mesh stretching:** Woven meshes are stretched using several self-developed stretching tools. These tools are shown in figure 4.8. The mid-sized mesh stretching tool is equipped with force sensors which could measure total forces in two orthogonal directions. For small and large prototypes, meshes are stretched using much simpler and lighter aluminum frames. These frames are assembled from four separate side-bars and the meshes are hold by inch-wide strips on top. When the screws at the corners of the frame are tightened, side-bars on two opposite sides move away from each other and thus flatten meshes. The tensions on the mesh in this case are monitored by a tensiometer. After the mesh is stretched, it is attached to a transfer stainless steel frame using cyanoacrylate adhesive. This kind of adhesive have excellent bonding strength but will completely lose adhesion within few seconds in hot water. Therefore, it is ideal for quick transfer of stretched meshes and allows instant reworking using the same frame. Typical tensions applied to the mesh are 10-20 N/cm.
- **Material cleaning and pre-bonding HV test:** Dedicated cleaning are performed for all

parts used for building the Micromegas detector. Nylon screws, stiffening aluminum plates and PCBs etc. are immersed in the acetone and cleaned with ultrasonic cleaner to remove oils left on their surfaces. The stretched mesh, which has been bonded to the transfer frame, is usually too large to be placed inside the container filled with acetone liquid. Moreover, the acetone solution is aggressive to cyanoacrylate adhesive used to fix the mesh on the frame. As a result, stretched meshes are not cleaned by the ultrasonic cleaner. They are first gently soaked by alcohol and then cleaned with high pressure distilled water. Finally, meshes are purged by compressed dry nitrogen from the center to all edges. It is found that blowing the mesh with high pressure dry gas is an effective way to remove many attached dusts which are otherwise hard to remove by water and alcohol. Several photos taken during the cleaning process are shown in figure 4.9.

Before placing all parts to bond the micro-meshes on the anode PCB, it is important to check if there are any defects which have not been visually identified. This is indeed true that when the mesh size is large, visual check of every tiny spot is impossible. Moreover, tensions on meshes may not be uniform after they are attached to the transfer frame. Worse still, meshes may loosen if the adhesive loses its bonding strength after mesh cleaning. Continuing the fabrication process without careful inspections of each individual part could result in failure and thus waste of time and materials. To cope with these issues, we have developed a practical way to verify the perfectness of the parts used to form narrow amplification gaps. Pre-bonding HV test for the materials is carried out and the setup is illustrated in figure 4.10. The test is performed at room temperature under dry air with relative humidity less than 40%. An anode PCB, separated by a 160  $\mu\text{m}$  thick thermo-bond film frame, is placed on top of the stretched mesh. High voltage is applied to the mesh while the anode PCB is kept at ground potential. If discharges do not occur when more than 900 V is applied to the mesh, subsequent thermal bonding processes usually result in successful amplification

gaps. In fact, experiments have been performed to find sparking voltages for different mesh tensions. Results for unsupported mesh spans of 3-4 cm are listed in table 4.3. Basically, mesh tensions around 7 N/cm could satisfy the need of suspending the mesh on the anode. However, with such tension on the mesh, notable mesh sagging in the center of active area is observed if more than 800 V is applied. Given that typical Micromegas operational voltages in argon based mixtures are 400-650 V, we have practically kept tensions of the mesh on the transfer frame to be more than 10 N/cm.

- **Thermal bonding of amplification gaps:** The bonding of micro-meshes to the anode PCBs using thermo-bond films involves application of heat and pressure. Heat could be applied from either side or both sides of the bonding film. The simplest way is to apply the heat using a hot plate. The hot plate we used has a heating area of about 30 cm × 30 cm with a temperature uniformity within 10 degrees. For small prototypes, stretched mesh, thermo-bond film frame and anode PCB are placed in order on the top of the flat hot plate. Heat is applied from the bottom of the PCB and the thermo-bond film is activated when its internal temperature reaches about one hundred Celsius. When the surface of the film melts, it could be easily identified by its change in transparency. At this stage, pressures are applied from the top side of the mesh using a hand-held rubber roller. It should be pointed out that silicone based papers are placed on the mesh so that the rubber roller is isolated from the mesh and no melted glue from the bonding film will be attached to the roller. When heat is not even at some corners of the bonding film frames, hot air gun is used as an extra heating source to supply hot air from the top of the mesh.

Although, this kind of thermal bonding technique is not refined and depends on the executor's experience, it has been found that the successful rate is relatively high and results could be reproduced by many other students even without prior knowledge on the bonding process. For larger size meshes, it is unpractical to handle the bonding by hands. There-

fore, other methods using hot roller and hot press machine have been tried and preliminary experiences will be discussed in the following subsection.

- **Prototype Assembling:** After bond film frames are cooled down and become solid, woven meshes are cut from the transfer frame and glued to the HV contact points using conductive epoxy glue. The “bulk” amplification structure, together with drift electrode and stiffening plates are assembled. The finished prototypes are placed inside an aluminum gas box with an opening on the top lid for testing.

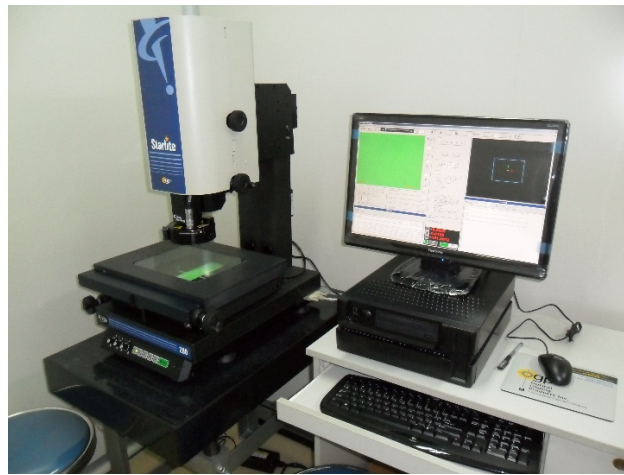


**Figure 4.6** Optical gaging system used to investigate micro-meshes.

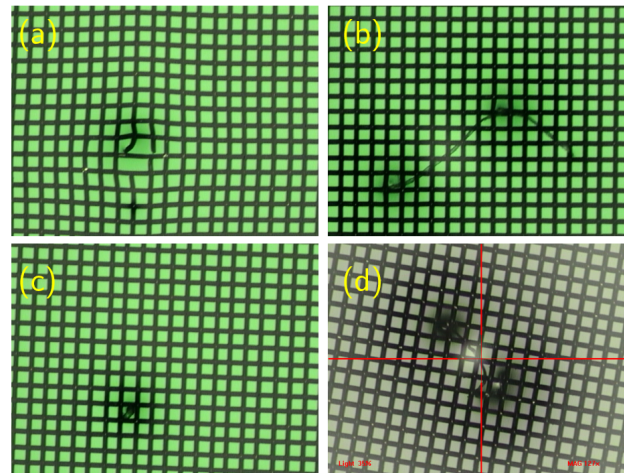


**Figure 4.7** Several types of mesh defects and effect of damage to the mesh due to defects: (a) broken mesh; (b) additional wire attached to the mesh; (c) debris; (d) burned points after frequent sparks developed at where defects located.

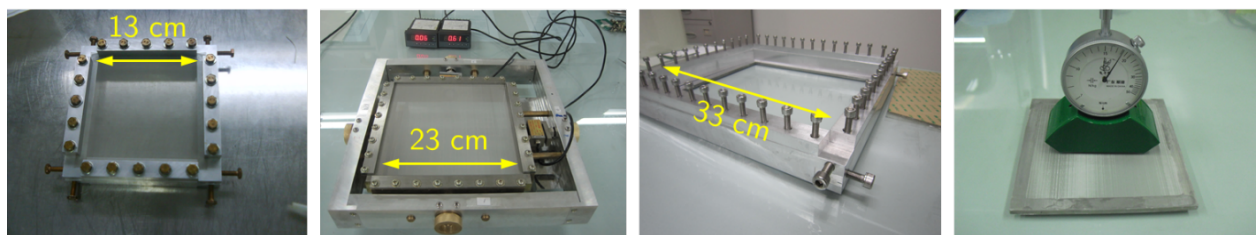


**Figure 4.8** Three mesh stretching tools developed with different sizes. The one in the middle is implemented with tension measurement sensors. The rightmost photo shows that a tensiometer is used to measure the mesh tension.

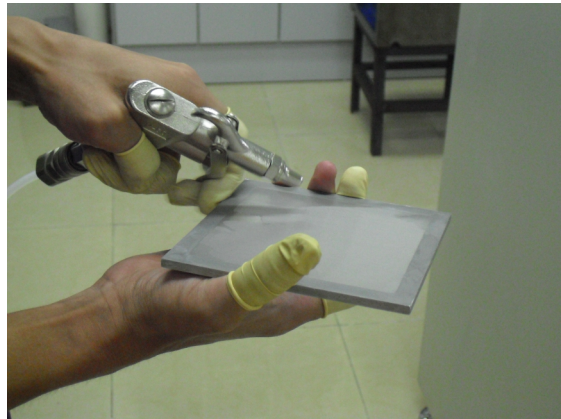


**Figure 4.9** Photos taken during the cleaning process.

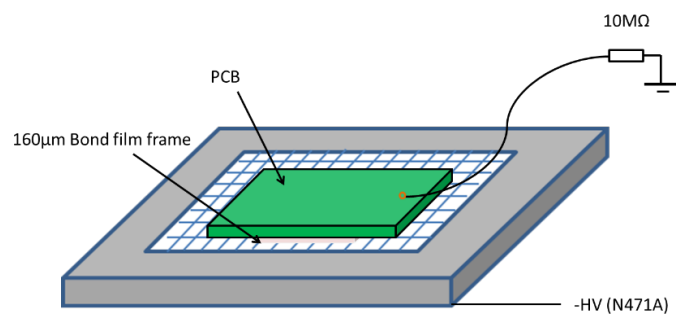


**Figure 4.10** Pre-bonding mesh high voltage withstanding test setup

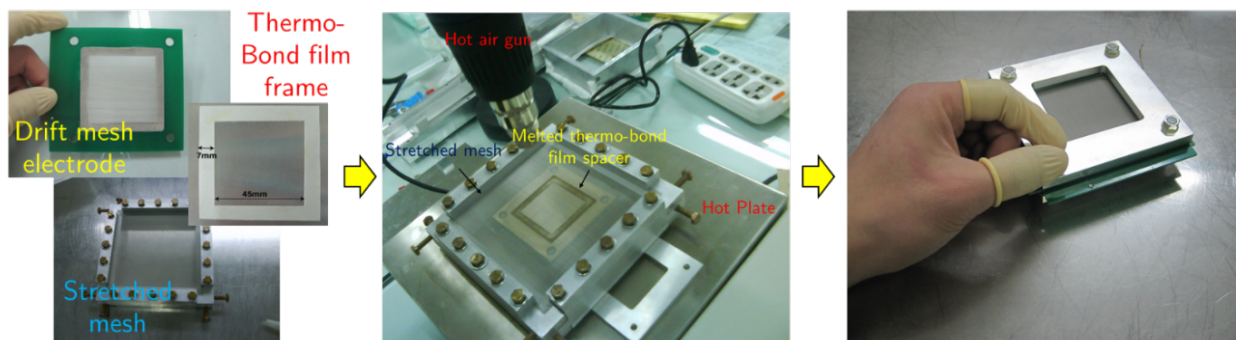


**Figure 4.11** Photos taken for some important fabrication steps (From left to right: material preparation, thermal bonding and prototype assembling)

Mesh tension in $x$ direction (N/cm)	Mesh tension in $y$ direction (N/cm)	sparking voltage (V)
3.6	3.5	850
5.8	5.5	930
7.7	7.4	940
12.5	11.8	1020

**Table 4.3** Mesh tension vs. sparking voltage.

In summary, key steps of the thermo-bond Micromegas fabrication are the mesh stretching and cleaning and thermal bonding. Photos taken during these fabrication steps are shown in figure 4.11. Overall, it is quite convenient to build a small prototype in a few hours. Since the materials used are all commercially available and widely used in industries, it has the potential to be an alternative and economic approach to construct Micromegas detectors for charged particle tracking and imaging applications.

### 4.2.3 Thermal bonding with different tools

Besides hand thermal-bonding, several semi-automatic approaches are also explored and some of them may have the potential to produce large size chambers. The most challenging aspect of bonding meshes to PCBs is to deliver proper and uniform pressure and heat to the bonding film and substrates. Pressures applied when the film is still solid are of no help. However, once the film is melted, sufficient pressure needs to be applied to the film immediately in order to ensure good contacts of two materials. Another point of concern is the activation of the thermo-bond film. Heating during the bonding process is not directly applied to the film but thermally transmitted through PCBs. Temperature settings for the heating sources are few tens of degrees higher than the

film activation standard and the temperature rise on the film could take few tens of minutes. The slow transmission of heat from thick PCB substrates and quick dissipation at some edges of the film exposed to the air result in non-simultaneous activation of the film. Therefore, special care in controlling the temperature and heat curing time should be taken into account to avoid overheating hence collapse of the film.

In order to improve the repeatability of good mesh bonding instances, the first method tried is to use fixing plates to give constant pressure during the thermal bonding. This method is illustrated on the left hand side plot of figure 4.12. The whole set with stretched mesh, thermo-bond film frame and anode PCB etc. is clamped by two 10 mm thick fixing aluminum plates. Pressure is applied when the screws at four edges of the fixing plates are tightened. The overall thicknesses measured from the outer faces of the fixing plates are kept at the same value with variations less than 100  $\mu\text{m}$ . With this setting, the pressure is expected to be roughly uniform across the thermo-bond frame. The fixed amplification structure is then placed on the hot plate with either the mesh side or the PCB side facing the heating panel. Some photos showing the preparations, thermal processing and the produced amplification structure are shown on the right hand side of figure 4.12. Prototypes with gas gains exceeding  $10^4$  have been successfully constructed. The advantage is that no intervention is needed during the thermal attaching procedure. However, it is found that controlling the pressure uniformity with setting screws is very difficult. For larger area with pressure applied via screws around fixing plate edges, the bending of aluminum fixing plates will be severe. Therefore, it is concluded that such method could only be helpful for producing small prototypes.

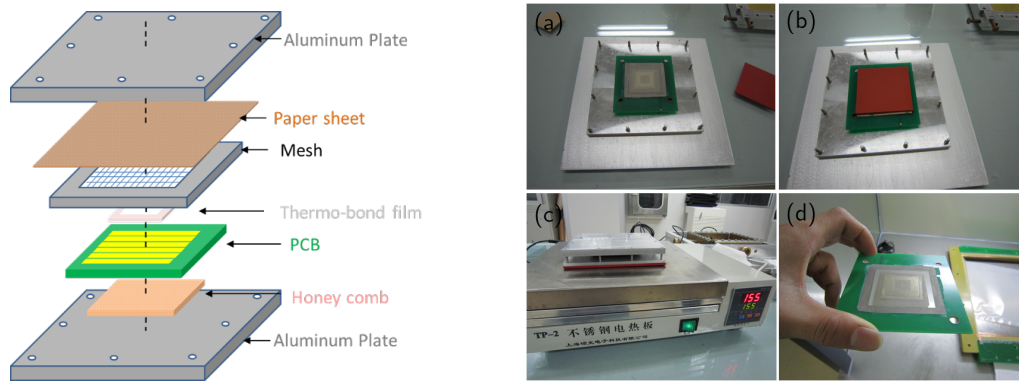


**Figure 4.12** Scheme of using clamping plates to apply pressure for bonding (left) and photos showing the thermal bonding processes and the produced amplification structure (right).

The second approach for the amplification gap bonding is to use the hot rubber roller. A photo of the hot roller we used is shown on the left hand side of figure 4.13. It is a typical equipment used to laminate plastic covers on paper products and is similar to that used to laminate photolithographic films for bulk Micromegas fabrication. There are two vertically placed heated rolling rods, of which temperature, rolling speed and rotating direction could be adjusted individually. Surfaces of the rods are covered with silicone rubber. The heating parts are buried inside the central stainless steel cylinder bars. The pictorial view of the thermal bonding process is represented on the right hand side of figure 4.13. Similar to the method using hot plates, the rolling rods are pre-heated to a temperature that is few tens of degrees higher than the film activation standard. Stretched mesh together with bonding film, PCB or back supporting plates will go through two rollers. Pressures are applied to the mesh via two rollers. Due to the maximum adjustable temperature for the roller is only about 165 degree, single rolling is not sufficient to pass the required heat to the bonding media. As a result, the entire bonding set has to roll back and forth several times before the bonding is firm and solid.

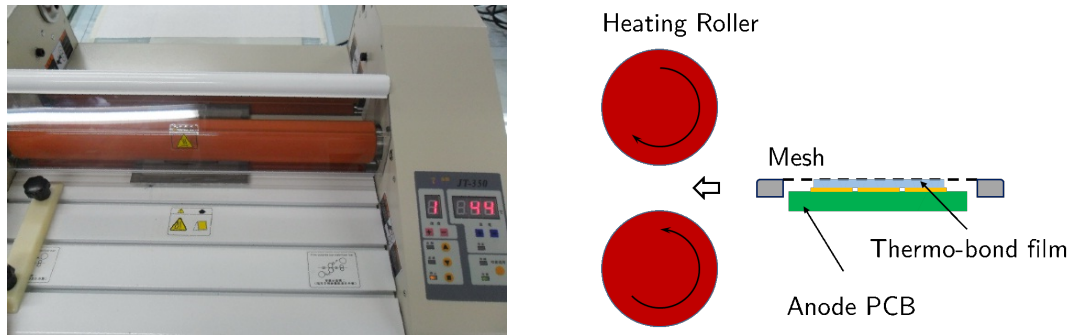


**Figure 4.13** A heated roller used for mesh bonding (left) and a pictorial representation of the mesh bonding process (right).

The obtained amplification structures have been tested in the lab. The test results of these prototypes, in terms of energy resolution and gain uniformity, are found to be inferior to those obtained from prototypes bonded on a hot plate and pressed using a hand-held rubber roller. Several reasons which caused defects are identified. Among them are undesirable repetitive rolling processes which lead to shifts of bonding films and uneven heating condition, and non-adjustable roller pressure, which passed the excessive forces to the stretched mesh-mesh lost tension after removed from the roller. Other issues include lack of protecting bonding film on the top of the micro-mesh so that unsupported mesh span is not pressed downwards by the soft rubber. Unfortunately, no suitable heat-rolling machine is available to address these problems at the time of testing, therefore its feasibility for thermal bonding is not proved. Nevertheless, as the hot rolling technique is quite mature in industry, this is still believed to be a promising way to produce thermo-bonded Micromegas in large size if the pressure and heating temperature could be adjusted in a wide range and harder rubber coating of the rods could be selected.

The third method for mesh bonding is to use a hot press machine. The press machine we used is shown in figure 4.14 with a working area of 25 cm  $\times$  25 cm. It has upper and lower two stainless steel hot plates. The pressure is applied from the top plate by a gas cylinder filled with compressed air. The pressure can be adjusted and the pressing time can be set to arbitrarily long. Thanks to the

two-side heating configuration, the machine could provide even heating. Two amplification gaps, one on the top of the PCB and another one at the bottom, could be fabricated on a single PCB. Micromegas chambers with active areas of  $20\text{ cm} \times 20\text{ cm}$  are produced using this machine and test results are quite promising [107].

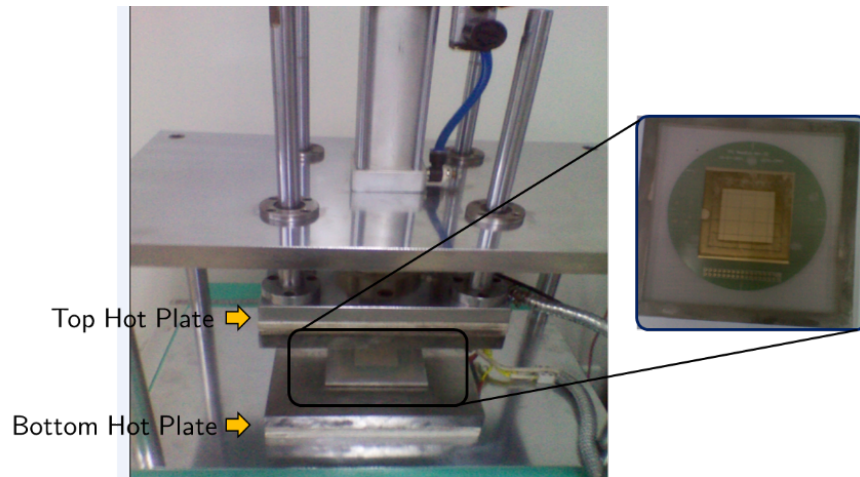


**Figure 4.14** Thermal bonding using hot press machine.

To produce even larger size thermo-bonded Micromegas chambers, the press machine could be placed precisely up-right and the top hot plate keeps flexibly contacting on the mesh. A uniform pressure across the whole working area may be given by a gas-filled vessel at the back side of the plate which is connected to a flexible head. Attempts using this modified machine are presently under consideration and investigation.

### 4.3 Measurement of basic performance parameters

To evaluate the basic performance of the thermo-bonded Micromegas, small prototypes with active areas of around  $40\text{ mm} \times 40\text{ mm}$  are first used. No mesh-supporting spacers inside the active area are used for these small prototypes. Anode readout planes of the prototypes consist of squared

readout pad arrays of  $3 \times 3$ . Each pad has an area of  $15 \text{ mm} \times 15 \text{ mm}$  and pads are spaced  $0.3 \text{ mm}$  apart. All these readout pads are connected together to the same ground through  $10 \text{ M}\Omega$  resistors. The drift mesh electrodes and the avalanche micro-meshes are supplied with negative high voltage using CAEN N471A dual-channel HV module. The module has a current resolution of  $1 \text{ nA}$ . The normal leakage current for the prototypes are less than  $1 \text{ nA}$  thus any abnormal leakage current or discharges could be easily detected. The gas mixture used in the tests is either argon with a small fraction of isobutane ( $i\text{C}_4\text{H}_{10}$ ) or  $\text{CO}_2$  mixed with argon. Concentrations of gas components are individually controlled by mass flow controllers. Gas mixtures flow at normal temperature and pressure (NTP) with flow rates of 1-2 liters per hour.

### 4.3.1 Experimental setup

The general view of the experimental setup and the readout chain are shown in figure 4.15. Micromegas prototypes inside a gas box is irradiated by a  $^{55}\text{Fe}$  source with a radioactivity of  $5 \text{ mCi}$ . The  $^{55}\text{Fe}$  source emits  $5.90 \text{ keV K}_\alpha$  and  $6.49 \text{ keV K}_\beta$  X-rays [108] when it decays to  $^{55}\text{Mn}$  via electron capture process. X-rays from the source penetrate a  $15 \mu\text{m}$  thick window made of polyvinyl chloride foil and enter the drift gap under the drift mesh electrode. They primarily interact with gas media via photo-electric process. When they are converted into photo-electrons, auger electrons are also produced from same atoms. Therefore, measurements of full X-ray energy are realized.

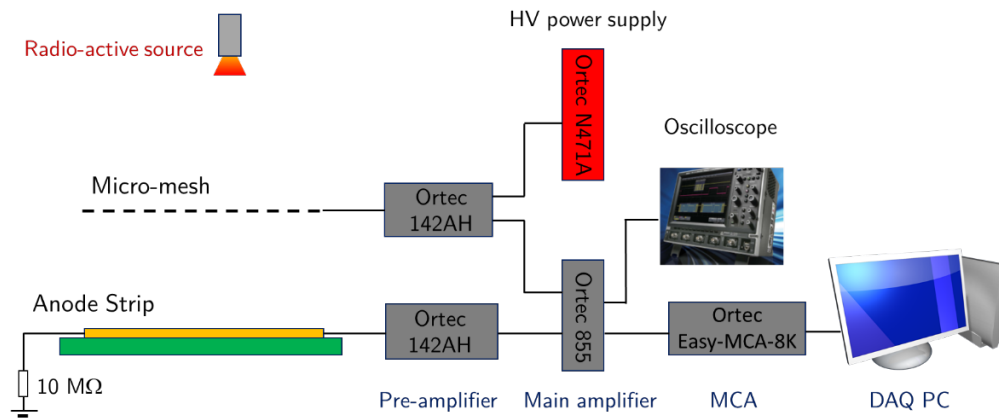


**Figure 4.15** Setup for Micromegas performance evaluation and the electronics readout chain.

Both micro-mesh and grouped anode strips are connected to Ortec 142 AH pre-amplifiers followed by an Ortec 855 shaping amplifier. Amplitudes of the output signals from the main amplifier are registered by an Ortec Easy-MCA-8K multi-channel analyzer, which has been connected to a PC for data acquisition. The whole readout chain is calibrated so that the relationship between the pre-amplifier input charge and the output MCA counts are determined. Signals from amplifiers are also inspected or recorded by an oscilloscope.

As shown in the simplified block diagram [109] in figure 4.16, there are HV ports on the pre-amplifiers which can withstand voltages up to 3 kV. It is found that the noise level from the Micromegas readout electrodes could be reduced dramatically if high voltages are fed through these pre-amplifiers, in which dedicated noise filter networks are implemented. Therefore, HV supplies for micro-meshes are always provided with this connection scheme. The pre-amplifier has a sensitivity of 1 V/pC and an internal calibration capacitor is included so that step voltage pulses could be converted to charges and used for calibration.

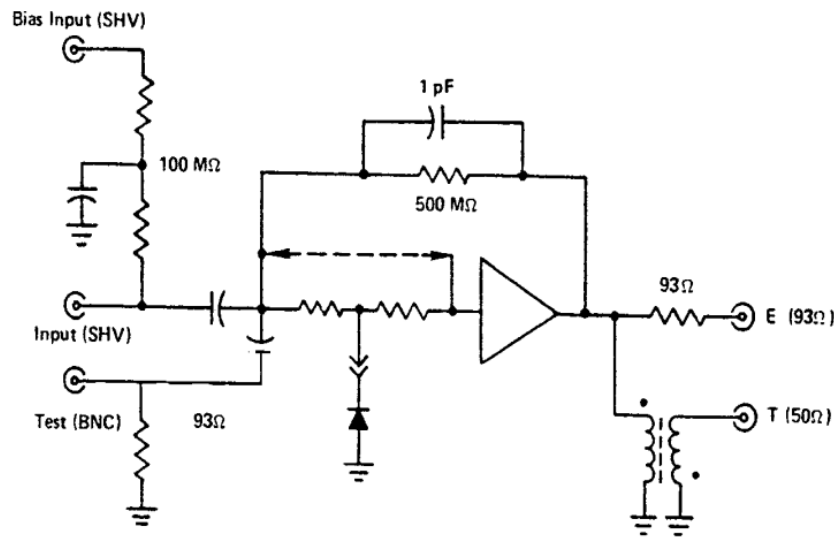


**Figure 4.16** Simplified block diagram of Ortec 142 AH pre-amplifier.

A picture of the Micromegas test bench established in the lab is shown in figure 4.17. It is basically composed of a gas system which is capable of mixing up to four gas components, a mechanical structure and an electronics readout crate. A movable motor platform which could hold an X-ray gun or radioactive sources, and a large shielding box are equipped later in the test bench and are not shown here. The study of the Micromegas basic performance parameters include measurements of electron transparency for the mesh, gas gain and energy resolution, as well as uniformity under different operational voltages.

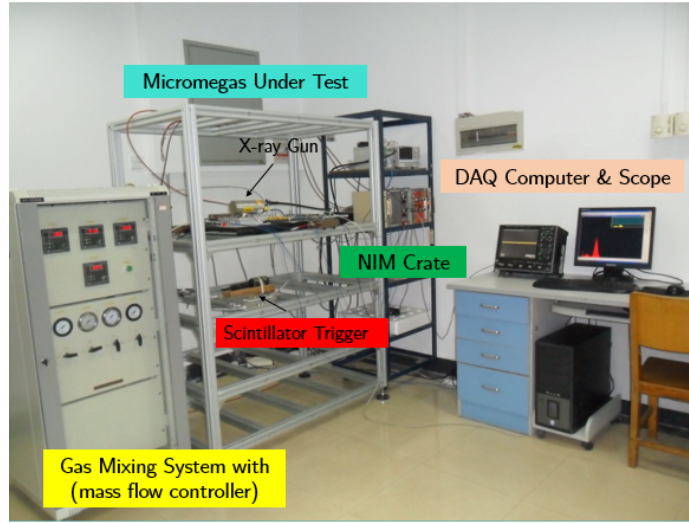


**Figure 4.17** Micromegas detector test bench.

### 4.3.2 Electron transparency

As reported in [98], electric fields in Micromegas detectors are uniform in drift and amplification gaps except small regions close to the avalanche mesh electrode where funnel-shaped fields are present. The electric field lines from the drift gap are compressed to the mesh openings towards the amplification gap. The compression strength is related to the electric field ratio  $\eta_e$  between the two gas gaps, which is defined as

$$\eta_e = \frac{E_a}{E_d} = \frac{V_a}{V_d - V_a} \frac{h_d}{h_a} \quad (4.2)$$

where  $E_a$  and  $E_d$  are electric fields of avalanche and drift gas gaps.  $V_a$ ,  $V_d$ ,  $h_a$ ,  $h_d$  are high voltages on the avalanche and drift electrodes, thicknesses of avalanche and drift gaps, respectively. The higher electric field ratio is, the tighter field lines are compressed thus diffusing electrons from the drift gap are less likely to be trapped by the mesh. In order to evaluate the electron transmission probability through the mesh, it is therefore natural to introduce a parameter called electron transparency for Micromegas detector with a certain mesh geometry and operation gas. When the

voltage on avalanche mesh electrode thus the amplification electric field is fixed, variations of the 5.9 keV photo-peaks in the measured  $^{55}\text{Fe}$  spectra with drift electrode voltage represent the change of electron transparency.

For Micromegas prototypes constructed with four different woven meshes, measured photo-peak positions as functions of electric field ratios in Ar: $\text{iC}_4\text{H}_{10}$  (95:5) are shown in figure 4.18. The photo-peak position rises to MCA high channel as the field ratio increases and reaches a plateau after a certain field ratio. As will be discussed in the following section, the plateau indicates a maximum electron transparency, but not necessarily a full electron transparency, is achieved. Peak positions decrease as electric field ratios continue to increase. This is due to the ionization recombination in the drift gap and hence the loss of signal amplitude when the drift electric field is low. Widths of these plateaus have large variations and the narrow plateau for Micromegas with 350 LPI mesh is likely due to the gas mixture contamination by electronegative gases. The maximum electron transparency are obtained when the electric field ratio is around 100 for Micromegas with 350 LPI mesh and great than 500 for the prototype with 500 LPI mesh. It is obvious that electrons are harder to cross the mesh if the mesh optical transparency is low or the mesh is very thick. Since the typical electric field in the amplification gap is about 30-50 kV/cm, an optimum field ratio of 400-500 for 400 LPI ( $\phi_{\text{wire}}=30\text{ }\mu\text{m}$ ) and 500 LPI ( $\phi_{\text{wire}}=22\text{ }\mu\text{m}$ ) mesh means the drift electric field need to be kept below 100 V/cm. This will result in very slow drift of electrons in the drift gap. Therefore, these meshes are not suitable for practical use and thus only Micromegas with 350 LPI mesh are used in the following studies.

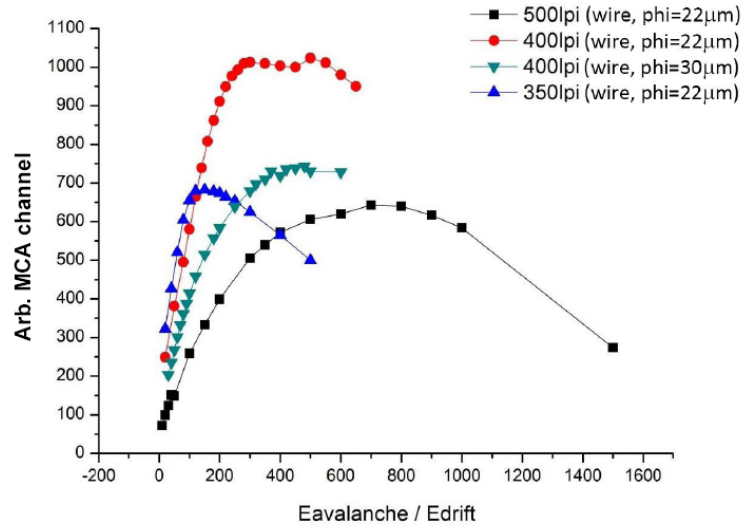


**Figure 4.18** The 5.9 keV photo-peak position as a function of electric field ratio.

For a Micromegas prototype with 350 LPI mesh, dependences of electron transparencies with electric field ratios are measured at two different avalanche electrode voltages in Ar: $iC_4H_{10}$  (95:5). Results are shown in the left side plot of figure 4.19. As expected, the electron transparency curves have similar shapes and are independent of the strength of the amplification electric field. Measurements are also performed in several argon and isobutane mixtures with isobutane concentrations from 4% to 20%. Measured photo-peak variations are shown on the right hand side of figure 4.19. Compared with most isobutane-rich mixture Ar: $iC_4H_{10}$  (96:4), minimum electric field ratios required for maximum electron transparencies are about 40% smaller for Ar: $iC_4H_{10}$  (80:20) mixture. This is apparently due to smaller magnitude of transverse diffusion for electrons in isobutane-rich mixture. Setting the field ratio to around 100 in these mixtures allows high electron transparency plus high electron drift velocity at an optimum drift field of few hundreds of V/cm. Dependence of electron transparency with mesh geometric parameters and gas mixtures are also studied with simulation tools and results will be reported in section 4.4.2.

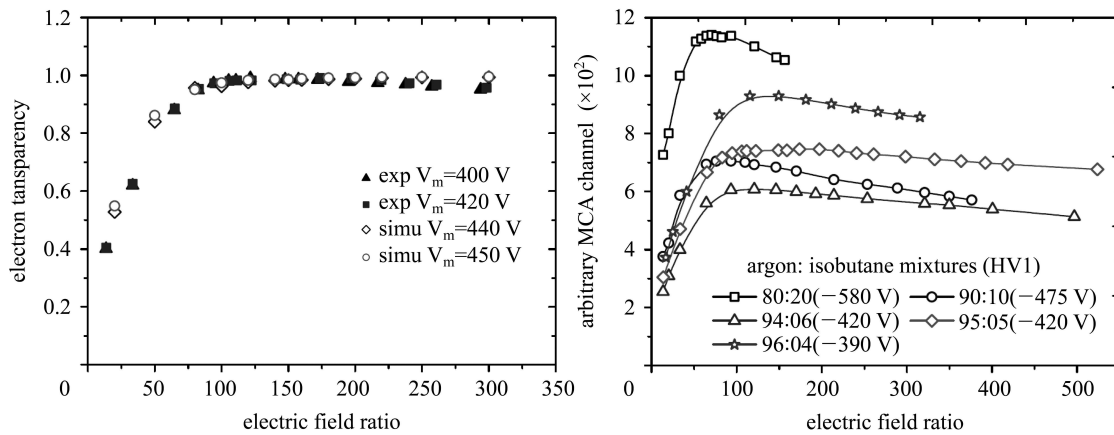


**Figure 4.19** Electron transparencies measured for a Micromegas with 350 LPI mesh: at two different voltages (left) and in several argon and isobutane mixtures (right).

### 4.3.3 Gas Gain and Energy Resolution

A typical  $^{55}\text{Fe}$  source spectrum measured by the thermo-bonded Micromegas is shown in figure 4.20. It is obtained at a gas gain of 3000 in  $\text{Ar}:\text{iC}_4\text{H}_{10}$  (94:6) mixture. The main peak of the spectrum is the superimposition of 5.90 keV and 6.49 keV photo-peaks. The smaller peak exhibits at the lower end is mainly the escape peak of 5.90 keV X-rays in argon. Since K-shell electrons in argon atoms have a binding energy of 3.2 keV [110], they leave with an energy of 2.7 keV when they are knocked off argon atoms by 5.90 keV photons. If argon characteristic X-rays are emitted after outer shell electrons transit to the inner vacancies, it is likely that they will escape the gas gap and leave only 2.7 keV energy to be detected as an escape peak. Therefore, the ratio between the 5.9 keV photo-peak and its escape peak is approximately 2. This fact could be used to check the linearity of the readout electronics.

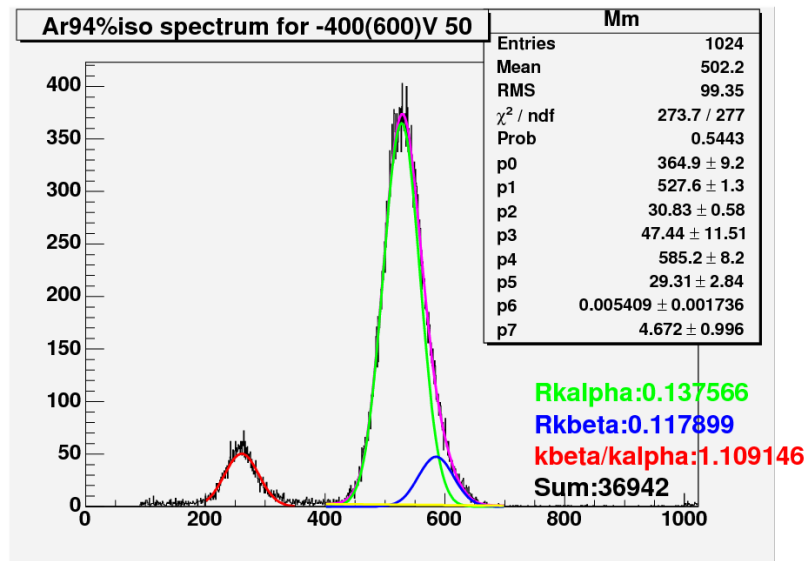


**Figure 4.20**  $^{55}\text{Fe}$  spectrum measured in Ar:iC<sub>4</sub>H<sub>10</sub> (94:6) mixture at a gas gain of 3000.

For gas gain measurements, the drift electrode voltage changes as the avalanche electrode voltage increases so that electric field ratios for maximum electron transparencies are ensured. Gas gains are calculated using

$$M = \frac{Q}{N_0 e} = \frac{N}{N_0} \quad (4.3)$$

where  $Q$  is the total charge collected per detected photon. It is converted from the obtained 5.9 keV photo-peak channel using the calibrated charge-MCA-channel correlation.  $e$  is the unit charge on an electron, and  $N$  is the total number of electrons produced per detected photon, which is given by  $Q/e$ .  $N_0$  is the mean number of ionizations created inside the drift gap by absorptions of 5.9 keV photons.  $N_0$  is given by  $E/W$ , where  $E$  is the photon energy and  $W$  is the mean work required to produce an ionization in the Micromegas operational gas. For mixed gas,  $W$  is given by

$$\frac{1}{W} = \sum_{i=1}^n \frac{1}{W_i} \frac{Z_i P_i}{\sum_{i=1}^n (Z_i P_i)} \quad (4.4)$$

where  $W_i$ ,  $Z_i$ ,  $P_i$  are mean ionization work, effective atomic number and partial pressure for  $i^{\text{th}}$  gas

component, respectively. Recalling table 3.2,  $N_0$  for argon-rich Ar:iC<sub>4</sub>H<sub>10</sub> mixtures is calculated to be around 230.

In order to determine the photo-peak positions as well as the energy resolution for 5.9 keV X-rays, the main peaks of the measured spectra are fitted with two Gaussian functions and a linear function. These two Gaussian functions represent 5.90 keV and 6.49 keV photo-peaks and the linear function is an approximation of the noise floor. Finally, the obtained gas gain as a function of the mesh voltage is shown on the left hand side plot of figure 4.21. Maximum gas gains exceed  $10^4$  are obtained in all argon-isobutane mixtures before the onset of frequency sparks.

Dependences of energy resolutions (FWHM) for 5.9 keV X-rays with gas gains are also extracted from the spectra and results are shown on the right hand side of figure 4.21. Energy resolutions are worse than 20% when gains are smaller than  $10^3$ . In all tested gas mixtures, they are found to be better than 18% with over an order of magnitude in gain. Resolutions deteriorate as gas gains continue to increase. Nevertheless, they are still below 20% at the highest gas gains of  $2\text{--}3 \times 10^4$ . For a qualitative understanding of the energy resolution variation, its dependency on ionization yield, and gas gain should be stated [111]

$$\left(\frac{\sigma_N}{N}\right)^2 = \left(\frac{\sigma_{N_0}}{N_0}\right)^2 + \frac{1}{N_0} \left(\frac{\sigma_M}{M}\right)^2 \quad (4.5)$$

where  $\frac{\sigma_N}{N}$ ,  $\frac{\sigma_{N_0}}{N_0}$ ,  $\frac{\sigma_M}{M}$  are relative variances of total produced electron, initial ionizations in the drift gap and gas gain for single electron initiated avalanches, respectively. This is based on simple assumptions that ionization probabilities are identical for all electrons and avalanches are independent of each other. The  $1/N_0$  contribution of the multiplication process to the fluctuation of the total electron population was evaluated by Snyder [112]. Since the fluctuation of initial ionizations is the same, the worse energy resolution measured at low gas gain is linked to a relatively large contribution from the multiplication process. The deterioration of resolution at high gain is due to the additional avalanche fluctuations caused by photon emission processes. Such effect is more pronounced in mixtures short of polyatomic molecule [113] which have vibrational and rotational

energy levels to absorb energies from excited atoms and prevent excessive gain growth. This could be noted from the bottom right plot of the energy resolution in figure 4.21 that energy resolution in Ar:iC<sub>4</sub>H<sub>10</sub> (96:4) mixture is worse than that in Ar:iC<sub>4</sub>H<sub>10</sub> (94:6) at a gain of  $2 \times 10^4$ . The best energy resolution for 5.90 keV X-rays presently achieved by a thermo-bonded Micromegas is actually obtained from the spectrum shown in figure 4.20. The best energy resolution obtained is 13.7%( FWHM), and is slightly better than that obtained from a bulk Micromegas [103].

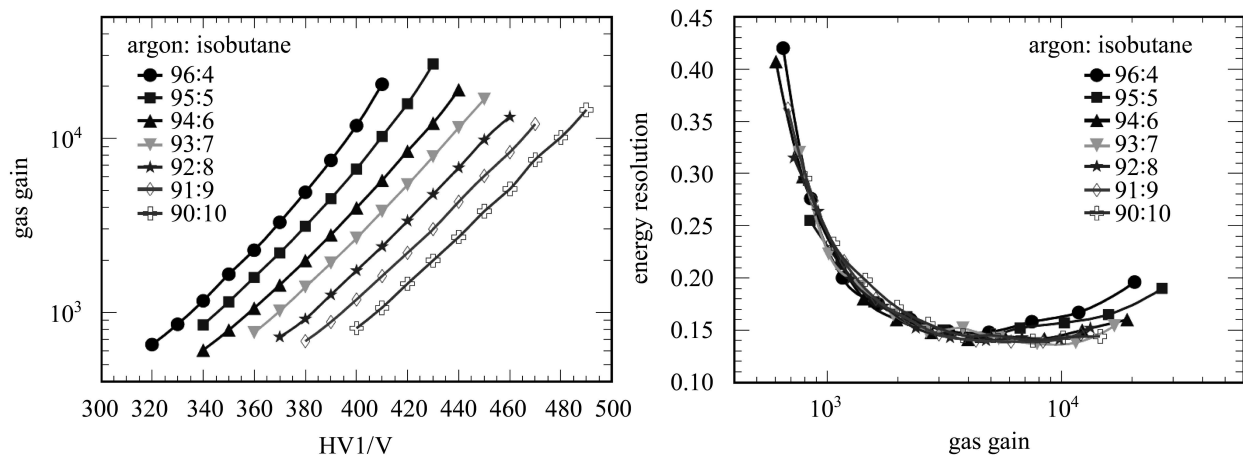


**Figure 4.21** Gas gain as a function of high voltage on the mesh (left) and dependence of energy resolution (FWHM) with the gas gain in several argon and isobutane mixtures

#### 4.3.4 Uniformity

Homogeneous pulse amplitude responses across entire detector active area, within a few percent [114], is required for energy measurements in applications such as TPC readout. Though the requirement on gain variations is not that stringent for tracking and triggering applications, it is practically desirable to keep the gain variations within 20%-50% around the mean value [115,116]. In order to evaluate the gas gain uniformity of thermo-bonded Micromegas prototypes, <sup>55</sup>Fe spectra are taken from different places inside active areas when detectors are operated under the same condition. An experimental setup for gain uniformity measurement is shown in figure 4.22. Two

orthogonal slits with widths of 1 mm are etched at the top lid of the gas box. Active areas of Micromegas prototypes are scanned in two directions with steps of around 5 mm. Gas gain and energy resolution as a function of the scanned position for a typical prototype with 45 mm  $\times$  45 mm active area are shown in figure 4.23. Measurements are taken at gas gains of  $10^4$  in Ar:iC<sub>4</sub>H<sub>10</sub> (95:5) mixture. Results show that gain variations are roughly within 10% over the entire unsupported area except points near the edges. The energy resolution for 5.9 keV X-rays are quite uniformly distributed around 20% (FWHM). Though results are quite promising, performance differences in the two scanned direction could be noted. This is closely related to the thermal attaching process. Since pressures during the bonding processes are given by hand, it is difficult to control and deliver them uniformly on thermo-bond film frames. Small variations, on the order of a few microns in avalanche gap thicknesses, result in changes of amplification electric fields hence gas gains. It must be stressed that the good result shown here is not a singular. Gain variations tested from few tens of prototypes are usually within 20% of their average values. Measurement results for two additional prototypes are shown in figure 4.24 as examples to prove the repeatability of uniformity performances.

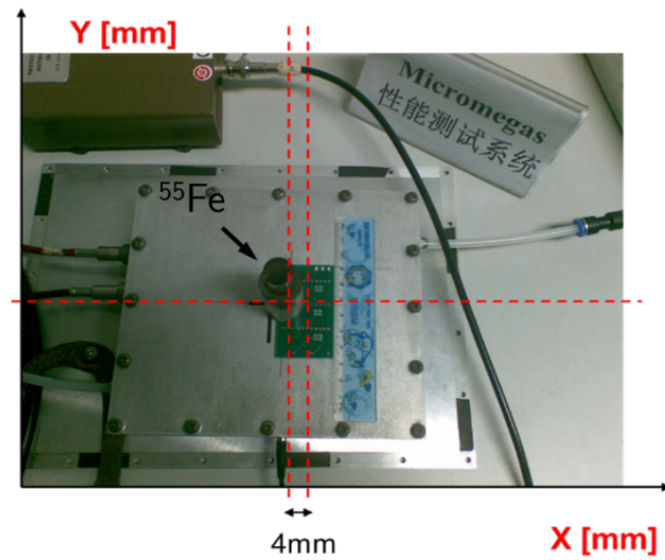


**Figure 4.22** Experimental setup for gain uniformity measurements.

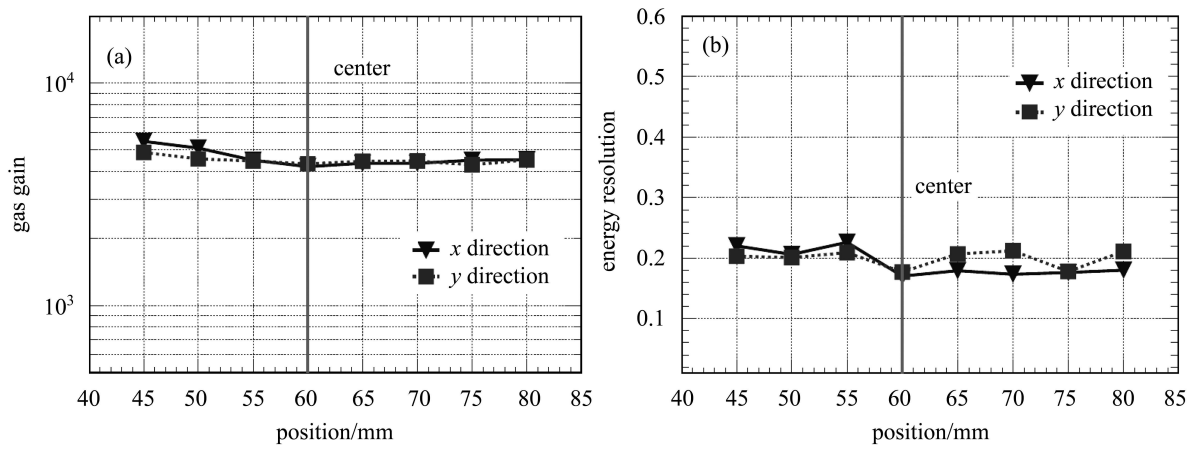


**Figure 4.23** Gas gain (left) and energy resolution for 5.9 keV x-rays as a function of scanned position in a thermo-bonded Micromegas with an unsupported mesh span of 45 mm wide.

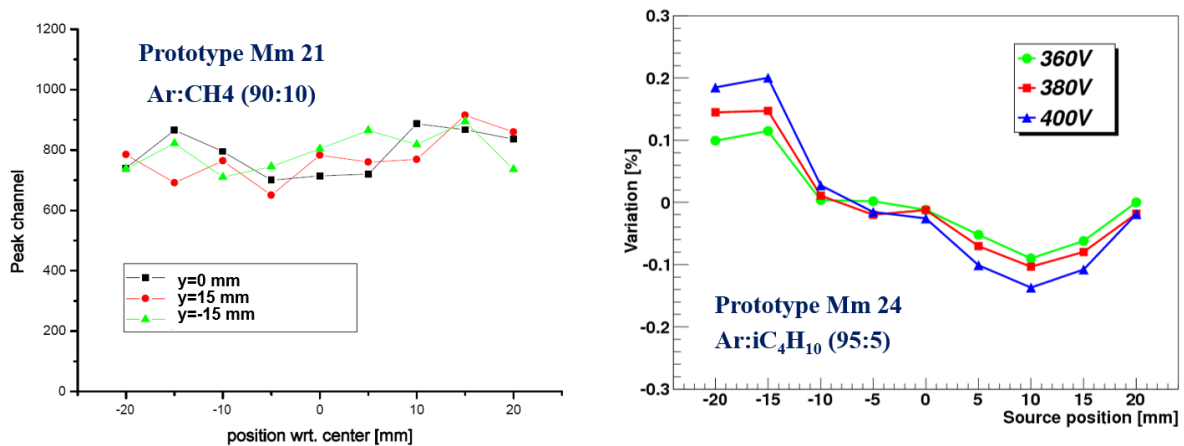


**Figure 4.24** Additional examples to show the gas gain uniformities of thermo-bonded Micromegas. Both prototypes have active areas of 45 mm  $\times$  45 mm.

Though variations of gas gain for small Micromegas prototypes are reasonably small, even with uncontrolled thermal bonding processes, it is imperative to understand the origins of gas gain changes so that the fabrication process could be refined and optimizations could be performed to achieve a better and well controlled uniformity for larger chambers. Basically, variations of gas gains are caused by differences in amplification gap thickness. In order to estimate the impact of gap thickness to the gain variation, one could use the simple expression given by equation 3.43 and assume the first Townsend coefficient  $\alpha$  is constant for a certain gap thickness. Recalling equation 3.46 which describes  $\alpha$  for parallel plate structures,  $\ln \alpha$  is proportional to  $-1/E$  if gas parameters A and B are assumed to be constant for a given gas pressure. The simulated  $\alpha$  for neon and several argon-isobutane mixtures is plotted in figure 4.25 as a function of  $-1/E$ . Note that the region corresponds to normal Micromegas amplification electric fields, 30-50 kV/cm, is highlighted in light red. Now considering that for our thermo-bonded Micromegas, the finished avalanche gaps are somewhat around 120  $\mu\text{m}$  using 160  $\mu\text{m}$  thick thermo-bond film frames. One could calculate that for a reduction of 5  $\mu\text{m}$  in gas gap, reductions of gas gains for avalanche electrode voltages set to 400 V and 500 V are 13% and 20%, respectively. This suggests that gas

gains are extremely sensitive to the gas gap uniformity.

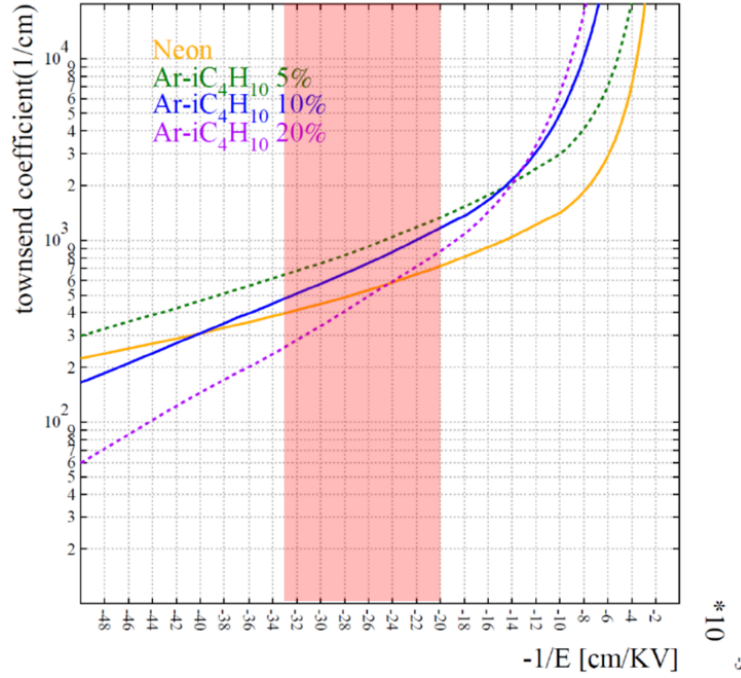


**Figure 4.25** The simulated first Townsend coefficient as a function of  $-1/E$ .

Recalling equation 3.47, the Rose-Korff formula describing the gas gain, its differentiation gives

$$\frac{\partial M}{M} = \alpha d \left( 1 - \frac{Bpd}{U} \right) \frac{\partial d}{d} \quad (4.6)$$

This indicates that there is a minimum in gain variation when the gas gap is equal to  $U/Bp$ . The optimum gap thickness is typically around few tens of microns to one hundred microns. Considering that micro-meshes used are thick woven meshes, reducing the amplification gap of thermo-bonded Micromegas to less than one hundred microns is undesirable and will likely introduce field non-uniformity near the mesh and many technical difficulties in fabrication. Therefore, the direction for thermo-bonded Micromegas to maintain a reasonable gain uniformity is to explore means to improve bonding process and to keep parallelism between meshes and anode PCBs. In addition, careful selection of operational gas, with the first Townsend coefficient less sensitive to the change

of electric field, could help to improve the gain uniformity to some extent. This will be discussed in section 4.4.3.

Besides gap thickness variations caused by the change of thermo-bond film frame thickness after thermal processing, two other influential facts are also identified. The first fact is the PCB deformation due to the uneven strength on two sides. This is pictorially demonstrated in figure 4.26. The PCB side with stretched mesh has strengths around PCB edges. It bends towards the mesh and results in a larger gap in the center. Therefore it is quite usual that the gain measured in the center are smaller than that obtained at all edges. For small prototypes, this could be corrected by adding correctional forces from the backside of the PCB. Practically, to provide such correctional forces, thin copper foils of one hundred microns thick have been attached to the PCB backplane near the edges. Then the bulk amplification structure is screwed from the outermost edges on a rigid honey comb plate. Effectiveness of the correction is shown figure 4.27. In Ar: $iC_4H_{10}$  mixture, gain variation of about 20% is remarkably corrected to less than 5%. While this method of correction is not suitable for larger area chambers, attaching another layer of mesh to form amplification gaps on both sides of PCBs could help to balance forces. This idea is verified during the fabrications of 200 mm  $\times$  200 mm chambers using hot press machine.

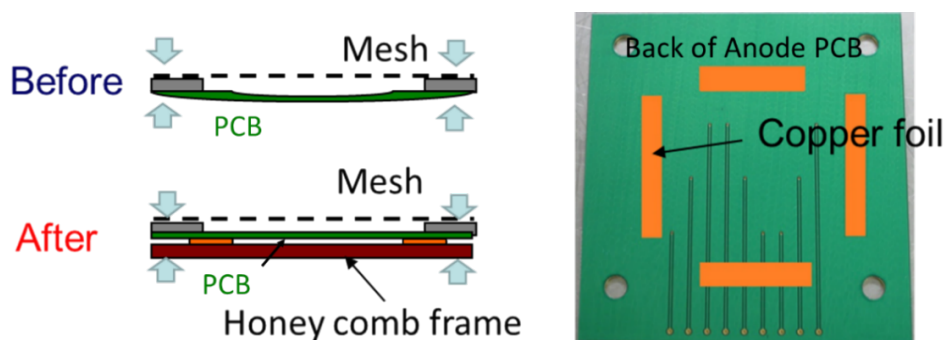


**Figure 4.26** Demonstration of amplification gap change due to PCB warping and the correction by adding additional force on its backside using copper foils.

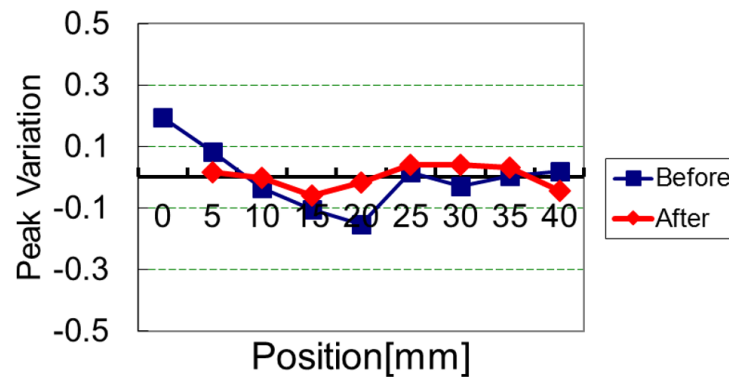


**Figure 4.27** 5.9 keV photo-peak variations before and after the correction shown in figure 4.26

The second fact is the mesh sagging under high electric field. The maximum width of the unsupported mesh span we have constructed is around 50 mm. Chambers with unsupported span larger than that is found to be very difficult to obtain the same performance as those from small prototypes. Large deflection of the mesh in the center due to attractive electrostatic force could be visually observed from the diffraction pattern under light. To qualitatively study the mesh deflection, a precision measuring microscope is used to measure the change of vertical positions of the unsupported mesh center when high voltage is applied on the mesh. The microscope has an estimated vertical position measurement precision of  $\pm 1 \mu\text{m}$ . The measured mesh sagging at different high voltages are shown in table 4.4 for two thermo-bonded Micromegas prototypes. The micro-mesh for Prototype I is completely unsupported inside the active area of  $40 \text{ mm} \times 40 \text{ mm}$ . The active area of Prototype II is  $100 \text{ mm} \times 100 \text{ mm}$  and is divided into three 2.5-3 mm wide regions by two 3 mm wide thermo-bond film strips. For typical operational voltages ranging from 400 V to 600 V in argon based mixtures, the mesh sagging is 1-4  $\mu\text{m}$  for Prototype I. Gain variation up to 10% is expected due to this deflection. The mesh deflection for Prototype II is quite obvious due to the insufficient tension on the mesh. It could be concluded that spacers with separations no more than 30 mm and sufficient mesh tension as mentioned in section 4.2.2 are

Applied voltage (V)	Sagging in Prototype I ( $\mu\text{m}$ )	Sagging in Prototype II ( $\mu\text{m}$ )
0	0	0
400	1	4
500	3	5
600	4	6
700	5	8

**Table 4.4** Mesh sagging in the center of the active area when applied with different voltages.

essential to minimize gain variations caused by mesh sagging. Keeping the operational voltage at around 500 voltages will help to control the gain variation due to mesh deflection to less than a few percent according to the discussion right above equation 4.6.

## 4.4 Simulation studies

Motivated by gaining better understandings of detector operational mechanisms and providing some theoretical grounds to support the optimization of thermo-bonded Micromegas fabrication processes and detector operations, dedicated simulation studies using gaseous detector simulation tools have been performed. Simulation topics are particularly chosen to focus on the studies of penning effect, electron transparency and gas gain variations. Considerations on selecting topics are the comparability of simulated results with experimental measurements accessible with our lab setup, as well as the urgency in guiding the detector design.

The main simulation tool used is the Garfield [117, 118] software package. It has interfaces with the Magboltz package [119, 120] which calculates various electron transport parameters and the HEED program [121] which computes ionizations of gas molecules by passages of charged

particles. Garfield program can perform three-dimensional Monte-Carlo (MC) simulation of the electron drift, diffuse and multiplication inside a specific detector geometry.

#### 4.4.1 Penning effect

As discussed in chapter 3, energies transferred to gas atoms and molecules will give rise to both ionizations and excitations. When more than two gas components are mixed together, if excitation levels for gas atoms or molecules from one type of gas are higher than the first ionization level of those from another type of gas, penning effect will take place. Additional ionizations could happen when excited atoms at higher excitation levels transfer their energies to the low-ionization-state gas atoms or molecules. Example gas mixtures with relatively strong penning effect are argon-isobutane mixtures. Excitation and ionization levels for two gas components, without distinguishing fine structures, are shown in figure 4.28. Ionization states are represented in thick dark-blue lines. Excited argon atoms at  $s$ ,  $p$ ,  $d$  levels, with energies of 11.6 eV, 13.0 eV and 14.0 eV, could transfer energies to isobutane molecules and result in an ionization. Conversely, super-excited isobutane molecules with energies of 17 eV may also impart their energies to argon atoms with ionization levels of 15.7 eV. Exact yields of additional ionizations are determined by excitation frequencies of these excitation states and the probability for an excited atom or molecule to transfer its energy to another gas atom with a low-lying ionization level.

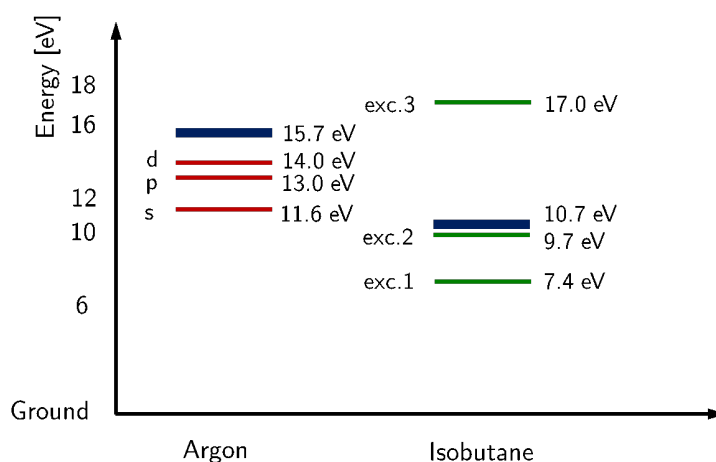


**Figure 4.28** Excitation and ionization levels for argon and isobutane.

Due to the fact that penning effect is not considered in Magboltz for calculations of the first Townsend coefficients, simulated gas gains in argon and isobutane mixtures are always smaller than those obtained from experimental measurements. In order to estimate the fraction of argon excimers which participated in ionizations, it is simply presumed that all excited states of argon atoms, denoted as  $\text{Ar}^*$ , have the same probability of ionization encounters. Therefore, it is easy to recalculate gas gains based on the modified first Townsend coefficient and find out the fraction of ionization-participating argon excimers which gives the best match between the simulation and the experimental data. Such comparisons for several argon-isobutane mixtures at atmospheric pressure are shown in figure 4.29 and the extracted fractions of  $\text{Ar}^*$  participated in penning transfers are listed in table 4.5. For  $\text{Ar}:\text{iC}_4\text{H}_{10}$  (90:10), it is estimated that about 39% of excited argon atoms have transferred their energy to isobutane molecules and caused extra ionizations. This number is comparable to the 40% number reported in [122] with more dedicated calculations and measurements. Overall, results suggest a higher probability of ionizing energy transfers for isobutane-rich mixtures. In reality, the above assumption of equal contribution from all excited states is considered to be inaccurate and the sophistication of penning transfers could be glimpsed

from figure 4.30 where the excitation frequency of various excitation states as a function of electric field in three argon and isobutane mixtures are shown. In the Micromegas operational electric field strength range, 30-50 kV/cm, excitation frequencies for argon  $s$ ,  $p$ ,  $d$  levels increase as the isobutane concentration decrease. This is contrary to the first impression that higher frequencies of excitation result in higher probabilities of ionizing energy transfers. Moreover, as viewed from the calculated first Townsend coefficient shown in figure 4.31, electric fields required to level up the excitation rates and initiate penning transfers are different for admixtures with different gas compositions. Most recent in-depth studies of penning transfers can be found in [122].

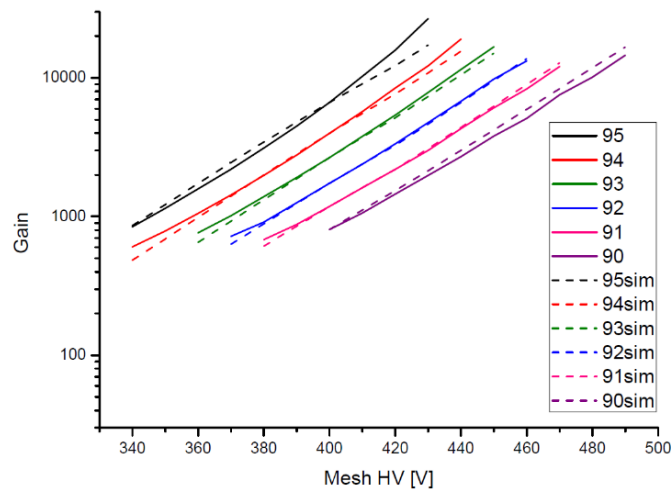


**Figure 4.29** Comparison of measured (solid lines) and simulated (dashed lines) gas gain in argon-isobutane mixtures. Argon concentrations are shown in the plot legend.

$iC_4H_{10}$ (%)	Argon excimers participated in ionizations (%)
5	35.0
6	35.2
7	35.9
8	37.8
9	38.0
10	38.7

**Table 4.5** Fractions of excited argon atoms participated penning transfer in several argon isobutane mixtures

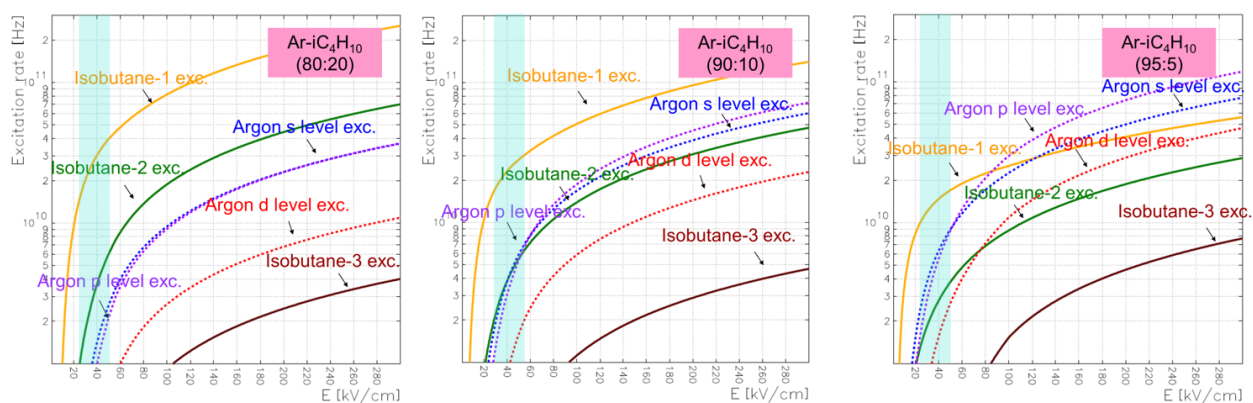


**Figure 4.30** Excitation rates of different states in three argon-isobutane mixtures.

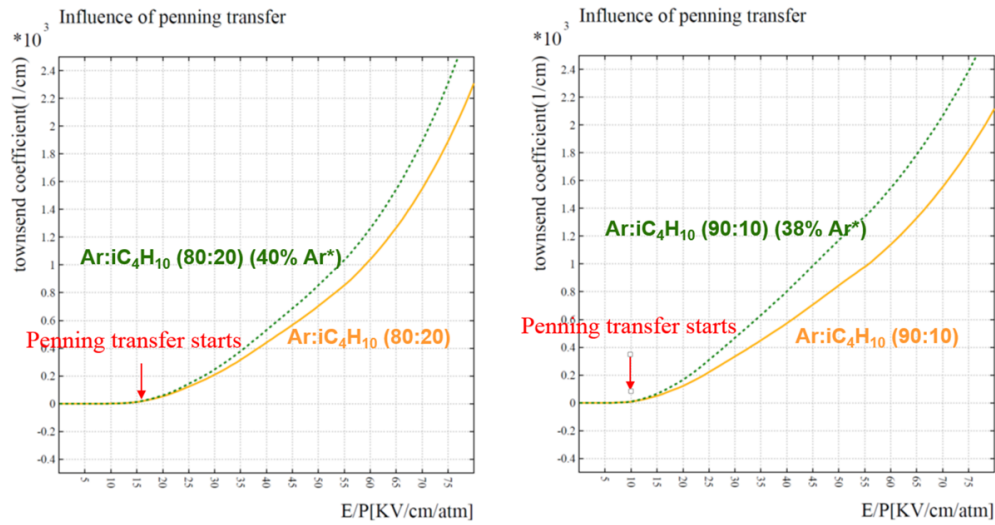


**Figure 4.31** The first Townsend coefficient as a function of electric field calculated with and without penning transfer using Magboltz.

#### 4.4.2 Electron transparency

The electron transparency is studied experimentally by measuring the change of 5.9 keV X-ray photo-peak as a function of the electric field ratio between two gas gaps. However, the exact fraction of electrons that have passed the micro-mesh without being absorbed is unknown, especially for low optically transparent meshes and highly diffusing gaseous. It is quite convenient to examine this quantity from simulation since the electron transportation parameters computed by the Magboltz package have been proven to be quite precise and MC simulation using Garfield software are widely used. The simulation in Garfield requires the import of three-dimensional electric field data which will be used for electron transportation calculations. Ansoft Maxwell 3D [123] based on finite element method (FEM) has been used to compute and generate the need field data.

The main difficulties for such simulation are the modeling of the micro-mesh and the computation of the electric field for electron transportation calculations in Garfield since woven wire meshes do not have regular and simple shapes. Two mesh models, as shown in figure 4.32, have

been built for the electron transparency study. The model on the left side assumes that the woven wires lie in the same plane. This has been found later in the Garfield simulation that it results in a too optimistic estimation of the electron transparency and hence this model is abandoned. Instead of constructing a complicated wire crossing model, a simple model, with wires in one direction vertically spaced one wire diameter away from the centers of wires in the perpendicular direction, is found to be very effective to mimic the real geometry of the mesh. The validity of this model is checked by comparing the simulated electron transparency curve in a given gas admixture with the measured photo-peak variation curve normalized by the maximum peak position. Exact matches of the shape as well as the field ratio when the electron transparency reaches the plateau suggest the suitability of the simulation. All simulated results presented here are obtained using the second model in figure 4.32.

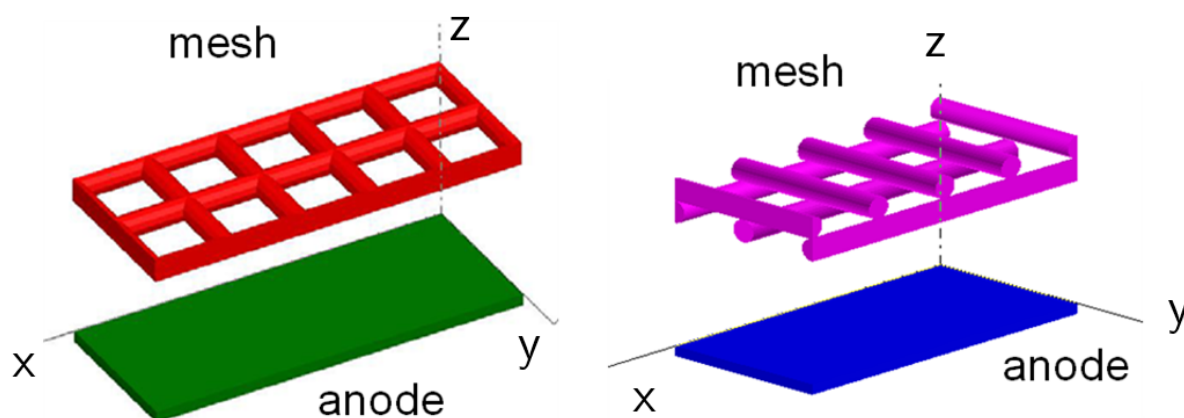


**Figure 4.32** Two 3D micro-mesh models constructed for electron transparency study.

In the Garfield simulation of electron transparency, free electrons are liberated in the drift gap of the constructed Micromegas model and are then traced using microscopic methods in which interactions are simulated at the molecular level. Ending-points and their status, such as attachment, drifting out of defined gas volume, are recorded so that the exact electron transmission rate across

woven-meshes can be obtained. For those electrons trapped by the mesh, figure 4.33 provides views of their typical termination locations. Mesh grids are reconstructed by these electron trajectory ending points and are clearly visible from the left side plot of figure 4.33. As shown on the right hand side plot of figure 4.33, it is also quite interesting to find out that most of the electrons are ended on upper surfaces of top wire-plane. Diffusing electrons from the drift gap tend to be confined by the funnel-shaped electric field across mesh openings and can mostly be transmitted to the lower avalanche gap if they have successfully survived from being captured by the top surface of the woven mesh.

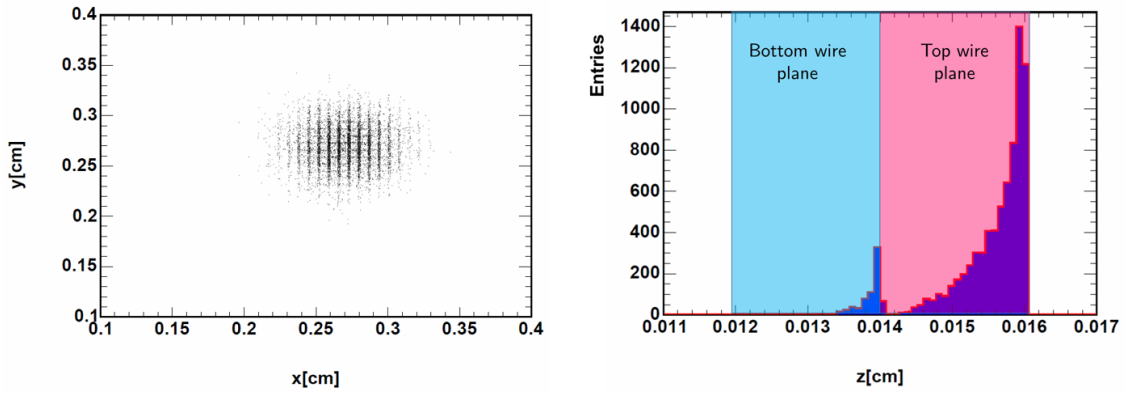


**Figure 4.33** Ending-points of electrons trapped by the mesh.

As losses of electrons penetrating the woven mesh are caused by the transversal diffusion process, electron transparency are determined by the mesh geometric parameters, specifically by its thickness, the optical transparency, and the transverse diffusion coefficient of the gas medium. Impacts of these parameters to the electron transmission are individually simulated and results are listed below:

- **Influences of mesh thickness:** In Ar: $iC_4H_{10}$  (95:5) mixture at normal pressure and temperature, the simulated electron transparency as a function of the electric field ratio for two types of meshes with the same optical transparency and wire diameter but different mesh thick-

nesses is shown figure 4.34. Thinner mesh tends to have higher electron transmission rates at low field ratios. Since the mesh optical transparencies are relatively large, both meshes could guarantee full electron transmission through the mesh if sufficiently high field ratio is chosen. The relatively small impact of the mesh thickness to the electron transparency could be partly understood from the discussion above that electrons are mostly captured at the top surfaces of the mesh.

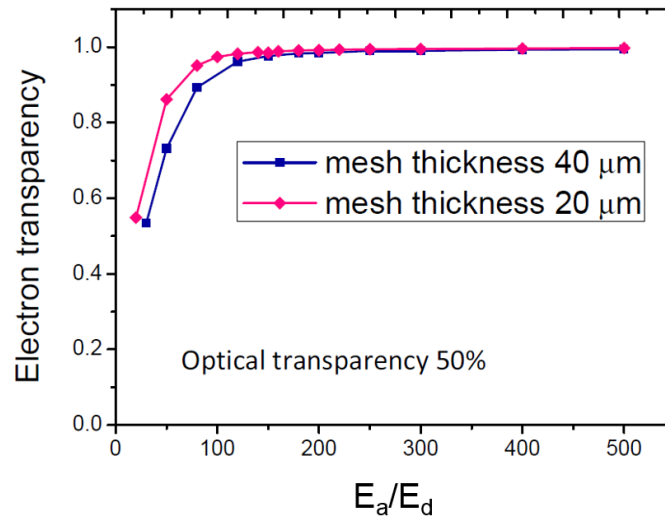


**Figure 4.34** Electron transparency as a function of electric field ratio for two kinds of woven meshes (same optical transparency and different mesh thicknesses).

- **Influence of mesh optical transparency:** In this simulation study, wire diameters of the woven meshes are fixed at 20  $\mu\text{m}$ , which are very close to the value chosen for massively produced 300 LPI or denser woven meshes. Four mesh models with different mesh optical transparencies are constructed. Corresponding mesh opening sizes are listed in table 4.6. Dependences of the electron transparencies with field ratios for four meshes are simulated and results in three typical gas mixtures for Micromegas operations are shown in figure 4.35. While the mesh with 50% optical transparency has full electron transparency in all gas mixtures, in the extreme case that mesh only has an optical transparency of 10%, it is impossible

Optical transparency (%)	Open square size ( $\mu\text{m} \times \mu\text{m}$ )
10	$9 \times 9$
20	$16 \times 16$
30	$24 \times 24$
40	$34 \times 34$
50	$48 \times 48$

**Table 4.6** Mesh opening size meshes with different optical transparencies (wire diameters are  $20 \mu\text{m}$ ).

for electrons to pass the mesh no matter which electric field ratio is used. For a moderate mesh optical transparency, 20%-40%, the electron transmission rate gradually reaches the plateau as the field ratio increase. However, significant fractions of electrons are still captured by the mesh even if the detector is operated at the plateau condition. Electron transparencies for meshes with less than 30% optical transparencies can never reach 80%.

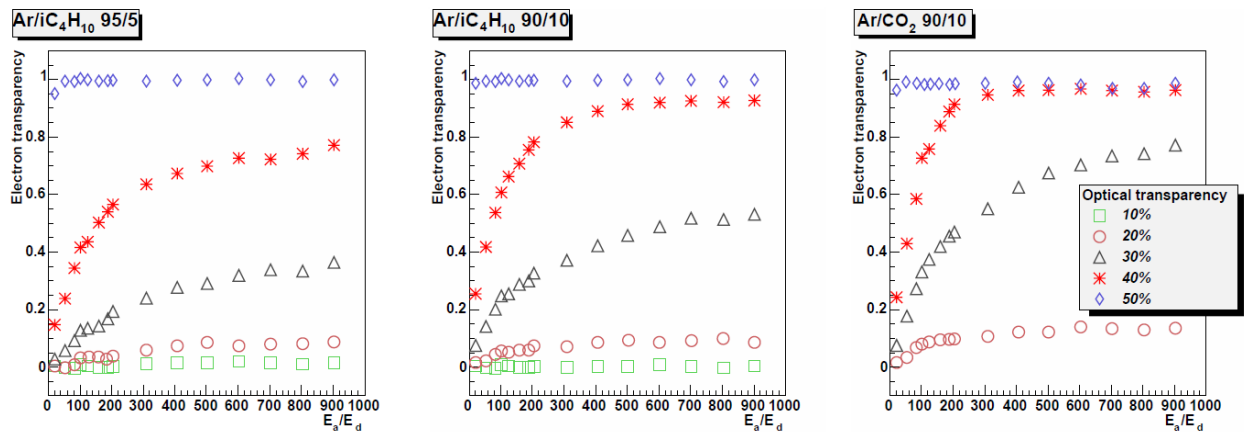


**Figure 4.35** Electron transparency as a function of electric field ratio for four different optical transparencies in Ar: $\text{C}_4\text{H}_{10}$  (95:5) (left), Ar: $\text{C}_4\text{H}_{10}$  (90:10) (middle) and Ar: $\text{CO}_2$  (90:10) (right).

- **Influence of operational gas:** In this study, meshes with optical transparencies of 40% and 50% are selected. Dependences of electron transparencies on electric field ratio are simulated in few more gas mixtures based on argon and neon. Results are shown in figure 4.36. For 40% optically transparent mesh, the left hand side plot shows clear differences of electron transmission rate for different gas mixtures. While electron transparency can be as high as 95% in Ne:CO<sub>2</sub> (90:10), it is less than 90% in all rest gas admixtures. This is what one would expect. As seen from figure 4.37, the transversal diffusion coefficients for the “cold” CO<sub>2</sub>-mixed gases are a factor of two larger than those for “hot” gases with argon and a small fraction of isobutane. The difference in electron transparencies becomes much less apparent if the mesh optical transparency reaches 50%. Almost full electron transparencies are obtained at relatively low electric field ratios in all gases.

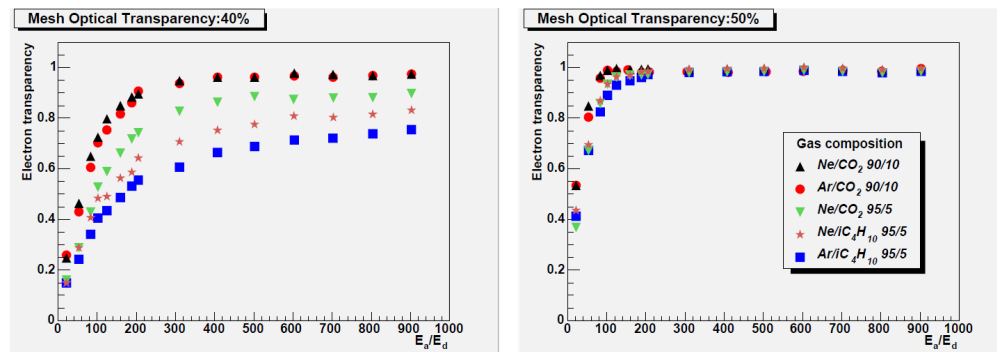


**Figure 4.36** Dependences of electron transparencies with field ratios in five gas mixtures for 40% (left) and 50% (right) optically transparent woven meshes (wire diameters are 22  $\mu\text{m}$ ), respectively.

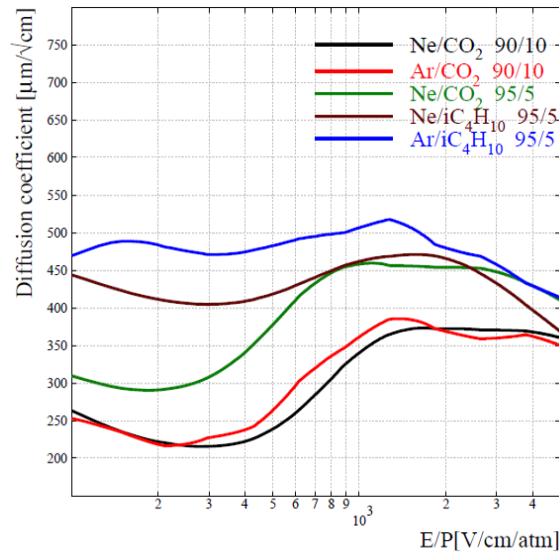


**Figure 4.37** Transversal diffusing coefficient for highly and moderately diffusing gas admixtures.

To conclude this study, transversal diffusion plays the key role in the determination of electron transmission through the mesh. If the mesh is less optically transparent, operating detectors in highly diffusing gas would result in electron losses when they cross the mesh. In addition, very high field ratios are required to compress field lines from drift gap towards the mesh opening centers so that maximum electron transmission rates could be reached. In this case, Micromegas detectors are forced to be operated with very low drift electric field, less than one hundred V/cm, which is undesirable. Simulation results suggest that typical woven meshes with 50% or higher optical transparency will be sufficient to guarantee full electron transmissions through meshes.

#### 4.4.3 Gain variation

Gas gain variations due to gap non-uniformity have been discussed in section 4.3.4. It is known that avalanche gap thicknesses of thermo-bonded Micromegas detectors are difficult to be reduced to few tens of microns, which is the optimum gap thickness with least sensitivity to gap deformations

and variations. The detector gain uniformity is in any case subject to high demanding of gap parallelism. One of the options for improving the uniformity in this situation is to properly select the gas with the first Townsend coefficient changing less rapidly with respect to the electric field. Pure neon as shown in figure 4.25 is a good example gas. In order to estimate changes of the gain with respect to the gap thickness in different gas mixtures, Simulations of single electron avalanches are performed using the Garfield program. Gas gaps with thicknesses from 10  $\mu\text{m}$  to 200  $\mu\text{m}$  are tried. The simulated results in three argon-isobutane mixtures and pure neon at room temperature and atmospheric pressure are presented in figure 4.38. High voltages on the avalanche mesh electrode are set between 300 V to 500 V, which are the proper settings for Micromegas operating in argon with a fraction of isobutane. Since the thermo-bonded Micromegas has a gas gap of around 120  $\mu\text{m}$ , for a fixed voltage on the mesh, the simulated gas gain variation curves show steeper slopes for isobutane-rich mixtures. Therefore, argon-isobutane mixtures with very low isobutane concentrations are favored for Micromegas operations from the uniformity point of view. In an attempt to verify this idea, special experiments are carried out to test the uniformity of the same Micromegas prototype in Ar:iC<sub>4</sub>H<sub>10</sub> (90:10) and Ar:iC<sub>4</sub>H<sub>10</sub> (95:5) gas mixtures. Considering that the mesh sagging at high electric field will contribute to the overall gap thickness change, it is based on the study presented in table 4.39 that voltages on the mesh for all tests have to be kept at around 400 V. The contribution to the gain variation due to mesh sagging is believed to be negligible. The measured uniformity for the 45 mm  $\times$  45 mm sized Micromegas in two gas mixtures are shown in figure 4.39. The reduction of the gain variation from 10% to around 5% in argon-rich gas is clearly visible.

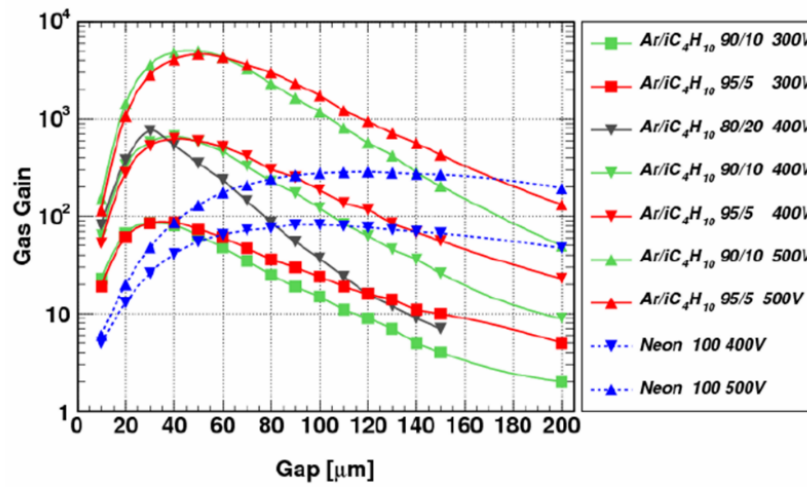


**Figure 4.38** Simulated gas gain as a function of gap thickness.

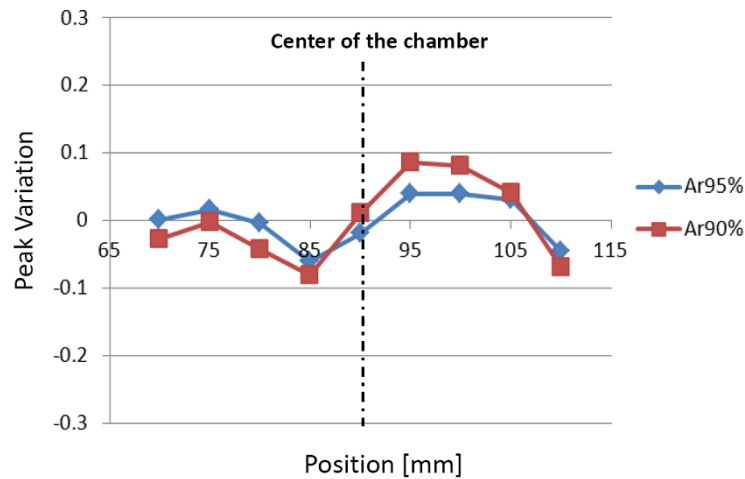


**Figure 4.39** Gas gain variation measured for a Micromegas prototype with two different argon-isobutane gas mixture.

It is also suggested from the simulation results in figure 4.38 that gas gain is insensitive to the gap thickness change in neon if the gap thickness is greater than one hundred microns. Considering that the gain in pure neon is relatively small for a typical mesh voltage of 500 V in argon-isobutane mixtures, addition of a small quantity of polyatomic gas, such as CF<sub>4</sub> or isobutane, should help the

detector to achieve reasonably large gains while still maintains the insensitivity to gap thickness variations. Very preliminary tests of a 30 mm  $\times$  30 mm thermo-bonded Micromegas prototype in the Ne:CF<sub>4</sub> (95:5) mixture are carried out. A typical <sup>55</sup>Fe spectrum and the measured uniformity at a gain of few thousands are shown in figure 4.40. Results are quite encouraging as gas gains greater than 10<sup>4</sup> and very good energy resolution for 5.9 keV X-rays are obtained. Gas gain variations are found to be less than 3%. Further experimental studies with neon-based mixtures are likely to give rise to good performances for larger area thermo-bonded Micromegas devices, in terms of response uniformity, tracking precision and energy resolution.

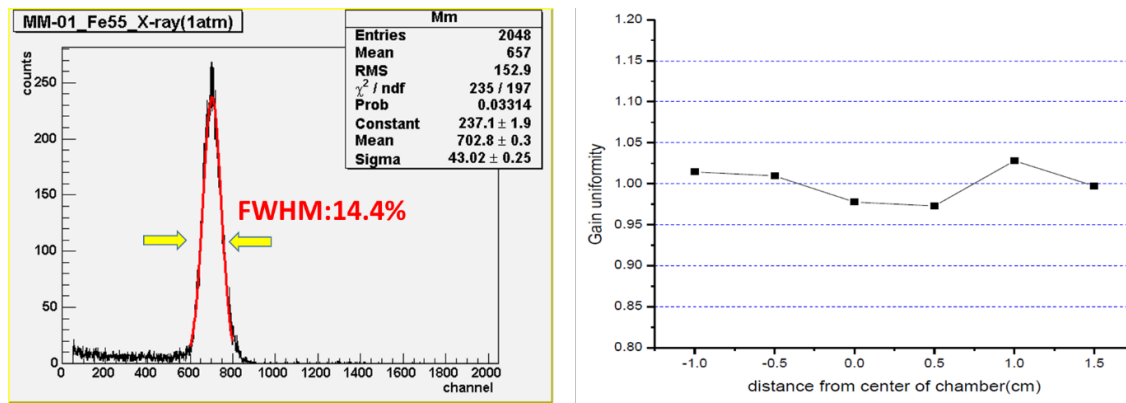


**Figure 4.40** Measured <sup>55</sup>Fe spectrum in Ne:CF<sub>4</sub>(95:5) mixture (left) and gain uniformity (right).

## 4.5 Micromegas with high resistivity anode

### 4.5.1 Introduction and motivations

It is well known that for gaseous detectors, there is a limit on the total amount of charge that can be produced inside the gas gap without initiating a breakdown discharge. This phenomenon is first studied by Raether for parallel-plate chambers [124] and is named as “Raether limit” afterwards by other researchers. The maximum charge before a breakdown happens is called critical charge

$Q_{crit.}$ , which is defined as

$$Q_{crit.} = N_0 M_{max} \quad (4.7)$$

where  $N_0$  and  $M_{max}$  are the total initial ionizations produced inside the gas gap and the maximum achievable gain, respectively.  $Q_{crit.}$  for well-made micro-pattern gaseous detectors is found to be only about  $10^6$ - $10^7$  [125, 126]. Typically, MIPs produce few tens to one hundred ionizations in the Micromegas drift gap of a few millimeter thick. The maximum gas gains are on the orders of  $10^4$  whereas the stable and safe operational gains for standard bulk Micromegas detectors are a few thousands [127]. However, even at moderately low gains, Micromegas detectors are subject to high voltage breakdowns and discharges in hadron environments, where highly ionizing particles are present.

For applications of Micromegas in muon tracking and triggering for hadron collider experiments, the biggest challenge is to make detectors spark tolerant. The general approach is to introduce resistive electrodes. One of the methods of implementing resistive electrode is to adhere a thin resistive film to the metallic readout anode plane using insulating glues [128, 129]. Another method, developed at CERN, is to place on anode strip plane a thin layer of Kapton or epoxy, on top of which resistive strips are formed by depositing thin resistive pastes [130]. Resistive film and strips are electrically isolated from readout strips and signals are induced on the readout strips, which are capacitively coupled to the resistive electrodes. Resistive film is grounded at its periphery and resistive strips terminated at the strip ends. For applications involving large size chambers, the surface resistivity of the resistive layer has to be kept at a low value, a few  $k\Omega/\square$ - $1M\Omega/\square$ , so that charges deposited on the electrode could be quickly dissipated.

Motivated by reducing the spark rate and the amount of charges in the discharge, increasing the operational gain and creating lateral signal spread on the readout electrodes so that wide readout elements can be used for hit positions reconstruction, an alternative approach is attempted to implement resistive electrodes in the Micromegas structure. In this approach, high resistivity ma-

terial, with bulk resistivity greater than  $10^9 \Omega\cdot\text{cm}$ , are glued directly without insulating layer to the readout pads using a semi-conductive glue with similar or slightly lower resistivity. The schematic view of the designed high resistivity anode Micromegas is shown in figure 4.41. Unlike the aforementioned resistive Micromegas with insulated thin resistive layers, the resistive materials used as anodes in such detector structure can be several millimeters thick. In this case, the lateral spreads of signals on few-millimeter-wide readout strips are expected and the number of readout channels for precise position measurements can be reduced by using the centroid method. In addition, the dissipation scheme for charges deposited on the resistive electrode is different in such device: induced charge currents flow directly to the ground through metallic readout pads underneath.

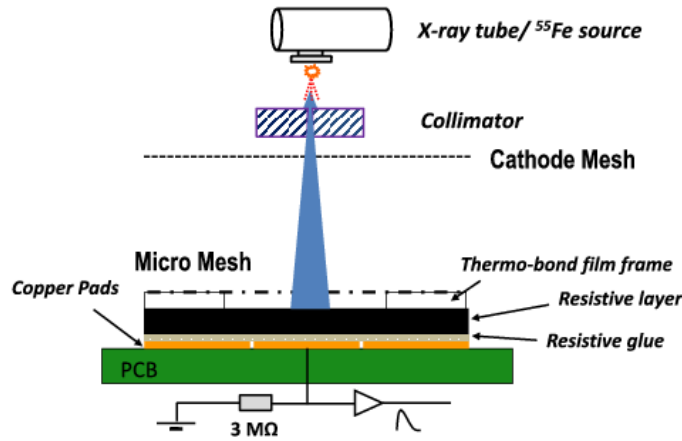


**Figure 4.41** Schematic view of Micromegas with high resistivity anode.

Such RPC-like structure, with a few millimeters thick resistive anode has already been tried in parallel mesh chambers [131, 132] for spark protection and charge dispersion. However, finding suitable high resistive material suitable for high rate applications has been a long-sought question. The material resistivity uniformity, mechanical properties as well as machinability and scalability are all of great concern. In view of applying the high resistive material to Micromegas detectors, the material also needs to have a smooth surface. After many searches, we have settled down to two potentially useful high resistive materials, namely carbon-filled polycarbonate plastic sheets

and semi-conductive (resistive) glasses. Along with thin regular glass sheets, these materials have been used to construct small Micromegas prototypes with high resistivity anode. Discussions on the material properties and studies of the detector performance, such as gas gain, energy resolution, rate capacity and spark protectiveness, for these high resistivity anode Micromegas devices will be presented in the following subsections.

### 4.5.2 Resistive materials, prototypes and experimental setup

A summary of the basic properties of experimented resistive materials are shown in table 4.7. The semi-conductive glass sheet [133] has a bulk resistivity of around  $10^{10} \Omega \cdot \text{cm}$  and a thickness of 0.7 mm. The surface smoothness is excellent as it is finely polished. The size of the glass sample we used is small, about  $6 \text{ cm} \times 3 \text{ cm}$ . However, glasses with sizes of  $30 \text{ cm} \times 30 \text{ cm}$  and thicknesses from 0.5 mm to 2 mm are readily available.

The carbon-filled polycarbonate is essentially the plastic polymer resin loaded with micron-sized graphite particles. Its conductivity is determined by the fraction of carbon powders mixed into the base plastic resin. The conductive mechanism of such composite semi-conductive plastic with a low carbon-loading fraction is believed to be due to the electron hovering and inter-particle transfers. A quantitative theory of fluctuation-induced tunneling has been used to describe its conductivity [134]. As shown in figure 4.42, the resistivity changes as a function of temperature for carbon-loaded composites, and the resistivity of composite plastics are extremely sensitive to the carbon-loading fraction. For resistivity of around  $10^9 \Omega \cdot \text{cm}$ , to achieve a bulk resistivity uniformity of few times, rather than few orders of magnitudes, around the average value, the variation of the carbon loading fraction for the entire material needs to be controlled well below 1%. The Zelux SD-P carbon-loaded polycarbonate sheets [135] that we used are mainly used for electrostatic discharge (ESD) protection. Therefore, the bulk resistivity is not ideally uniform over a large area. Nevertheless, the bulk resistivity of several small-size samples cut from the large sheet are

Resistive Material	Bulk resistivity ( $\Omega\cdot\text{cm}$ )	Thickness (mm)	Available size
Semi-conductive glass	$\sim 10^{10}$	0.7	30 cm $\times$ 30 cm
Carbon-filled Polycarbonate	$\sim 10^{11}$	1.5	Large
Regular glass	$\sim 10^{13}$	0.4	Large

**Table 4.7** Resistive materials studied to make high resistivity anode Micromegas.

measured to be quite uniformly distributed around  $10^{11} \Omega\cdot\text{cm}$ . These small sheets with thicknesses of 1.5 mm are then used for prototype chamber fabrications.

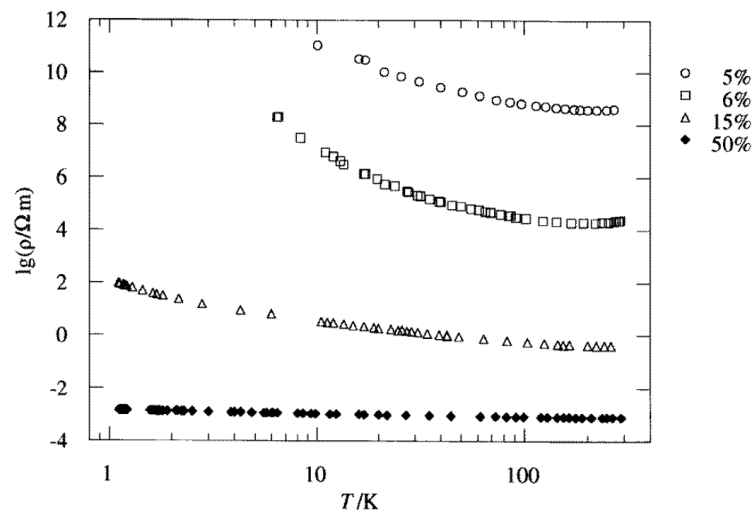


**Figure 4.42** Resistivity as a function of temperature for carbon-loaded composites [134].

The regular glass sheets used for prototype chamber construction have bulk resistivity close to  $10^{13} \Omega\cdot\text{cm}$  and thicknesses of only 0.4 mm. These glasses are originally used for making MRPCs for other projects. Photos of these resistive materials are shown in figure 4.43.



**Figure 4.43** Photos of resistive materials. From left to right: semi-conductive glass, carbon-filled polycarbonate and regular floating glass.

Construction of high resistivity anode Micromegas prototypes is similar to those standard thermo-bonded Micromegas chambers except resistive sheets are glued to anode PCBs prior to thermal bonding process. For testing gas gains and energy resolutions,  $^{55}\text{Fe}$  source is used. The detected photon rates are estimated around  $400 \text{ Hz/cm}^2$  for most cases. Cosmic rays are triggered using two scintillators as shown in figure 4.44. For rate capacity study, an intense X-ray gun with a copper target is employed. Detectors are illuminated by 8 keV Cu characteristic X-rays as well as low energy bremsstrahlung photons. Rate adjustments are performed by changing the filament current of the X-ray gun, the spacing between the X-ray exit-window and the detector as well as collimator slit width. The setup with the X-ray gun operating is shown in figure 4.45.

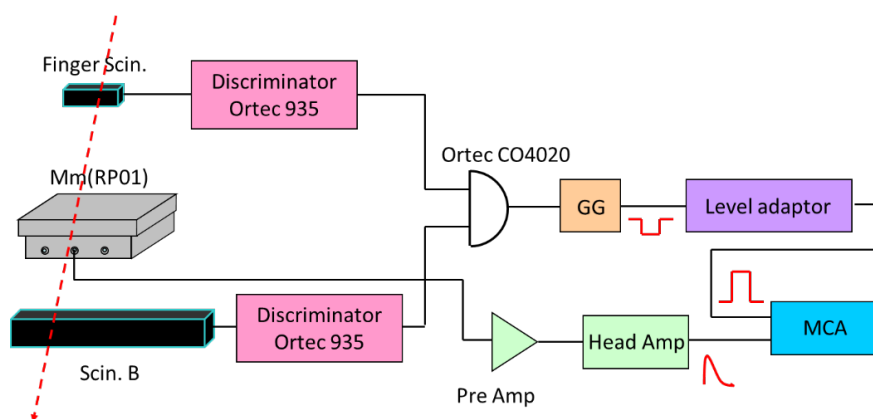


**Figure 4.44** Trigger logic for cosmic ray spectrum measurements.

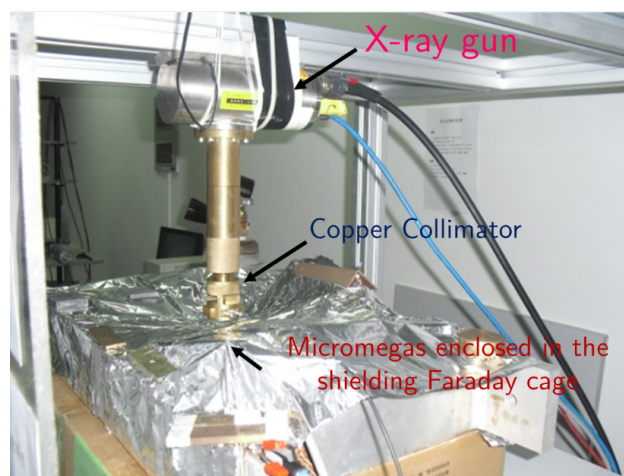


**Figure 4.45** Experimental setup for detector rate capability measurements.

### 4.5.3 Basic performances

The typical energy spectra of  $^{55}\text{Fe}$  of the three prototypes in  $\text{Ar}:\text{iC}_4\text{H}_{10}$  (95:5) gas mixture are shown in figure 4.46. The best energy resolution of 14.7% (FWHM) is obtained with the resistive glass anode, when the mesh voltage is set to 320V and the gas gain is 1100. For prototypes with carbon-filled polycarbonate and regular glass anodes, their best energy resolutions are 25.6% and 15.7% at gas gains of 1300 and 1700, respectively. The non-uniformity of the surface resistivity, in particular for the polycarbonate filled with irregular carbon particles, might have contributed to the deterioration of energy resolutions. Cosmic ray spectra were also taken and checked for these resistive prototypes. An example cosmic ray spectrum, superimposed with a  $^{55}\text{Fe}$  spectrum taken under the same condition, is shown in figure 4.47. The ratio of two spectra peaks, representing the difference of initial ionizations in the drift gap, is consistent with the theoretical calculation.

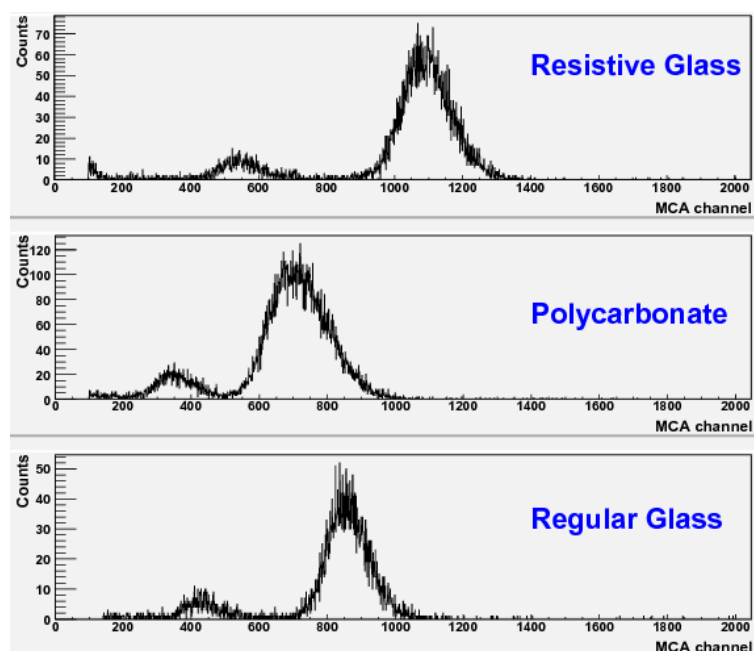


**Figure 4.46** Energy spectra of  $^{55}\text{Fe}$  X-rays. From top to bottom are spectra measured from Micromegas prototypes with resistive glass, carbon-filled polycarbonate and regular glass anodes, respectively.

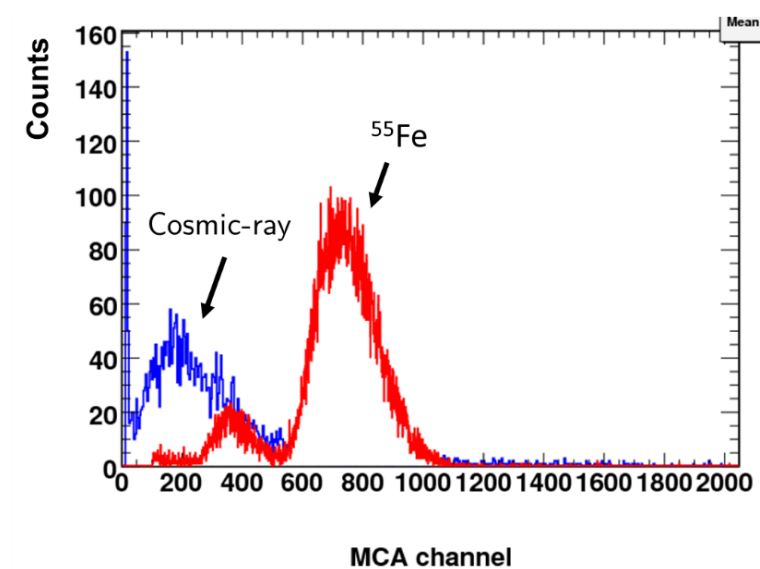


**Figure 4.47** Comparison of a cosmic spectrum with a  $^{55}\text{Fe}$  spectrum taken with the same voltage setting in  $\text{Ar}:\text{iC}_4\text{H}_{10}$  (95:5).

Energy resolutions of 5.9 keV X-ray as a function of the gas gain in Ar:iC<sub>4</sub>H<sub>10</sub> (95:5) gas mixture are given in figure 4.48. The energy resolution of the prototype with the resistive glass anode does not degrade significantly as the gas gain increases, while the resolutions of the other two types of prototypes deteriorate as the gas gain increases. We believe that degradation of energy resolutions as the gas gains increase for the two prototypes with higher resistivity anodes is mainly caused by the gain fluctuations due to the charging up of the resistive surface under the X-ray exposure. Degradations of energy resolutions become less prominent when the rate of the X-ray is much reduced. Energy resolutions measured in the Ar:CO<sub>2</sub> (80:20) gas mixture are typically 10% worse than that obtained in Ar:iC<sub>4</sub>H<sub>10</sub> (95:5) at the same gas gain.

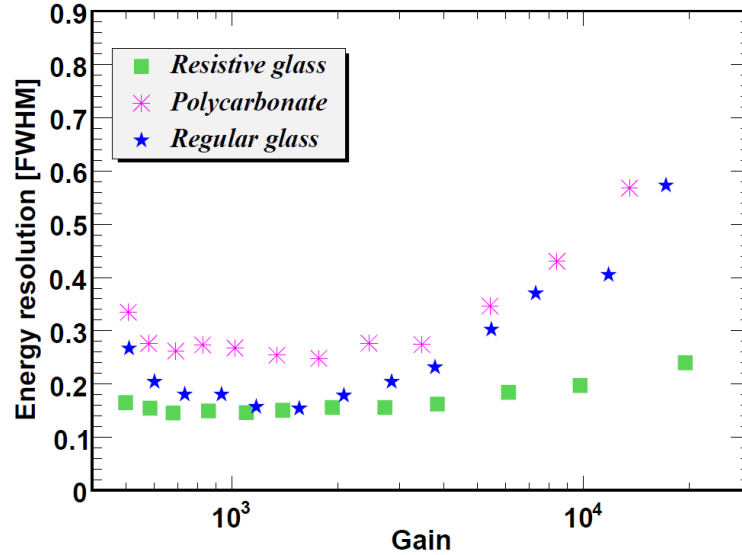


**Figure 4.48** Energy resolution (FWHM) of 5.9 keV X-rays as a function of gas gains measured by three types of high resistivity anode prototypes in Ar:iC<sub>4</sub>H<sub>10</sub> (95:5).

The measured gas gains as a function of the high voltage on micro-meshes are shown in figure 4.49. Gas gains from a standard Micromegas without resistive layer protection are also shown in the plot for reference. Micromegas prototypes with high resistivity anodes can reach maximum gas gains of greater than 10<sup>5</sup> without abnormal leakage current and high voltage breakdowns,

whereas the standard Micromegas suffers from frequent sparks at a gas gain of about  $2 \times 10^4$ .

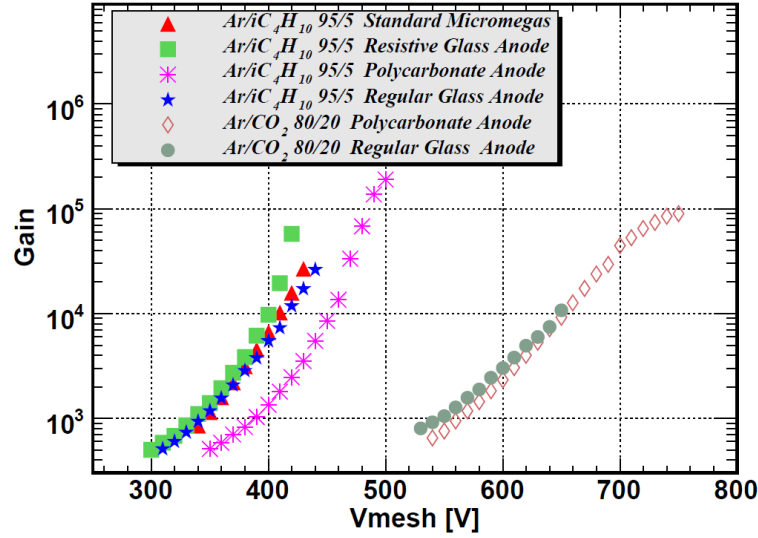


**Figure 4.49** Dependences of gas gains with micro-mesh voltages for resistive Micromegas prototypes and a standard Micromegas without resistive protection.

Under high rate illuminations, charges may gradually accumulate on the high resistivity anode surfaces, causing the electrical potential difference between the anode and micro-mesh to decrease with time. This charging up effect results in the reduction of gas gain with time until an equilibrium is reached. An example of the anode surface charging up and gas gain reduction in the carbon-filled polycarbonate anode prototype is shown on the left side of figure 4.50. Data for each spectrum were taken in 150 seconds. Severity of the charging up effect for the polycarbonate and resistive glass anode prototypes at different gains is summarized and shown on the right hand side of figure 4.50. Counting rates are estimated to be 200 Hz/cm<sup>2</sup> and 400 Hz/cm<sup>2</sup> for the resistive glass and polycarbonate prototypes measurement, respectively. The rate difference is due to the difference in X-ray conversion efficiencies in drift gaps with different thicknesses, when these two prototypes are tested. The gas gain of the polycarbonate anode prototype in Ar:CO<sub>2</sub> (80:20), at  $1.2 \times 10^4$ , drops immediately after the X-ray exposure starts and reaches a stable value that is about 15% lower than the initial gas gain within about 30 minutes. The charging up effect for the

prototype operated at lower gain is less prominent. It is not observed at  $200 \text{ Hz/cm}^2$  counting rate in the resistive glass anode prototype, whereas the gas gain reduction for the regular glass anode prototype (not shown in figure 4.50) is much more severe under a similar condition, that makes the detector unable to be operated at a rate of few hundreds of  $\text{Hz/cm}^2$ .

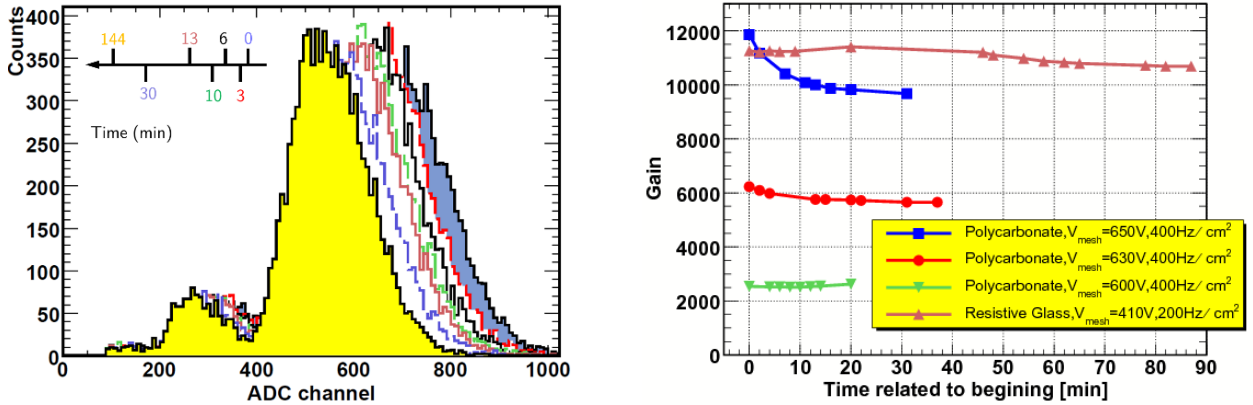


**Figure 4.50** Gas gain reduction with time in a Micromegas with carbon-filled polycarbonate anode (left) and a summary of charging up effect in polycarbonate and resistive glass anode prototypes at different gas gains (right).

#### 4.5.4 Rate capabilities

In order to understand rate limitations of Micromegas with high resistivity anodes, prototypes are exposed to X-rays from the micro-focus X-ray gun. Data taking starts immediately after the X-ray gun is turned on. A 5 mm thick copper collimator is used to reduce the X-ray intensity. The slit opening of the collimator is  $2 \text{ mm} \times 0.3 \text{ mm}$  and that defines the detector illumination area. Relative gain changes as a function of counting rates for three types of prototypes in  $\text{Ar}:\text{iC}_4\text{H}_{10}$  (95:5) are shown in figure 4.51. Three sets of data are taken at different high voltages and gas gains are shown for each prototype. The initial values of gas gains are shown in the box located in the lower left corner of the figure. As expected, the gain reduction with rate is much steeper in prototypes with higher resistivity anodes or when the prototypes are operated at higher gains. Note

that an 8 keV copper  $K_{\alpha}$  X-ray photon generates about 300 free electrons in drift gaps while a MIP liberates only about 30 electrons in a 3 mm drift gap required for minimum ionization detection in argon based gas mixtures. The rate capabilities of these detectors would be about one hundred times higher if they are tested using MIPs under the same conditions.

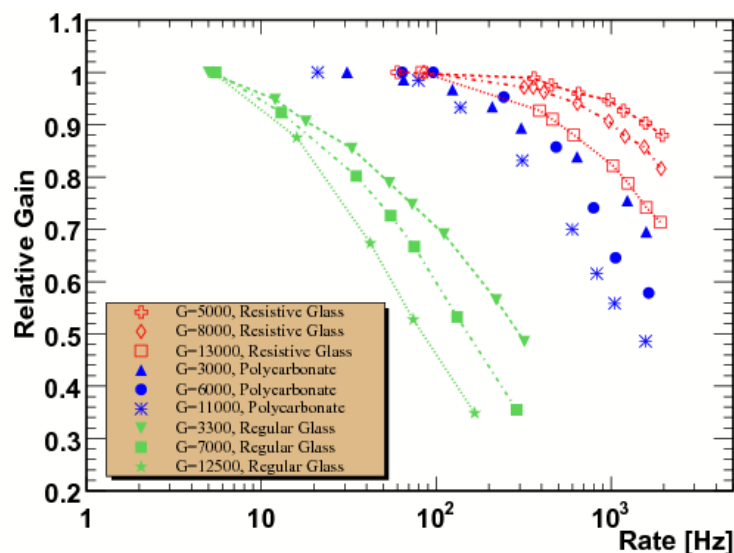


**Figure 4.51** The gas gain reductions as functions of counting rates in the resistive glass, carbon-filled polycarbonate and regular glass anodes at different gains.

#### 4.5.5 Spark probability and tolerance

Large spark-like pulses in our Micromegas prototypes with high resistivity anode are extremely rare. Here, sparks-like pulses that we observed are abnormally large pulses. They are not as large as sparks occur in a standard Micromegas. Two approaches are used to study such large pulses under different conditions in our prototypes. The first approach is “spark counting” by sending amplified signals from the micro-mesh to a discriminator and counting pulses with amplitudes exceeding certain thresholds. Rates of spark-like pulses recorded at gas gains ranging from several to ten thousands are counted when the prototypes are illuminated by the  $^{55}\text{Fe}$  X-ray source. Since

the normal avalanche size with a gain of about  $10^4$  is roughly 0.3 pC for 5.9 keV X-ray signals, the discrimination threshold for large pulse counting is set to 0.75 pC, which is 2.5 times larger than the largest charge that could be deposited from a normal avalanche. Ratios of large amplitude signal rates to the X-ray counting rates at different gains are plotted in figure 4.52 for prototypes with resistive polycarbonate and resistive glass anodes. The regular glass prototype is not included since its “spark” rate is extremely low and is not measurable.

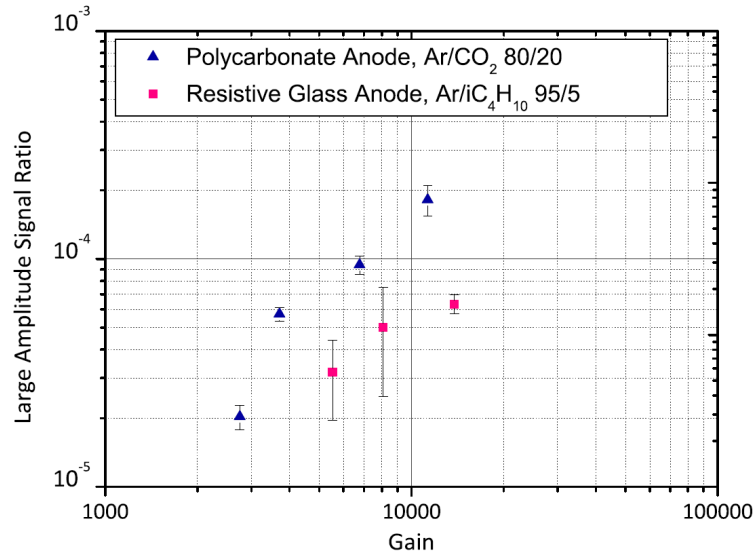


**Figure 4.52** Probability of abnormally large amplitude signals as a function of gas gain in two resistive prototypes.

The second approach that we used to study this phenomenon is to directly couple signals from the readout pad to the 50  $\Omega$  impedance input of a digital oscilloscope without any amplifier. Plots in figure 4.53 show typical accumulated “spark” waveforms. Figure 4.53 (a) shows “spark” waveforms in the resistive glass anode prototype at a gas gain of  $2 \times 10^4$  in Ar:iC<sub>4</sub>H<sub>10</sub> (95:5) mixture. Figure 4.53 (b) and figure 4.53(c) are for the polycarbonate anode prototype with gas gains of about  $3 \times 10^4$  and  $4 \times 10^4$  in Ar:CO<sub>2</sub> (80:20) gas mixture at different discrimination thresholds. It is found that “sparks” associated with X-rays in the cases shown figure 4.53 (a) and figure 4.53

(b) have similar durations of less than 100 ns. Their amplitudes are typically less than 0.1 V and the total amount of charges released are on the order of a few hundred pC. The spark rate increases when the gain is raised. For the polycarbonate anode prototype operated at mesh voltage of 700 V, we have observed rare large pulses with amplitudes larger than 0.5 V, which are shown in figure 4.53 (c). The probability for such large pulses to happen is less than  $2 \times 10^{-4}$  per detected X-ray photon and the amount of charges in each pulse can reach a few nC. Nevertheless, the charge sizes of such pulses are still small compared to those from sparks in a comparably sized standard Micromegas made of metallic mesh facing the metallic anode.

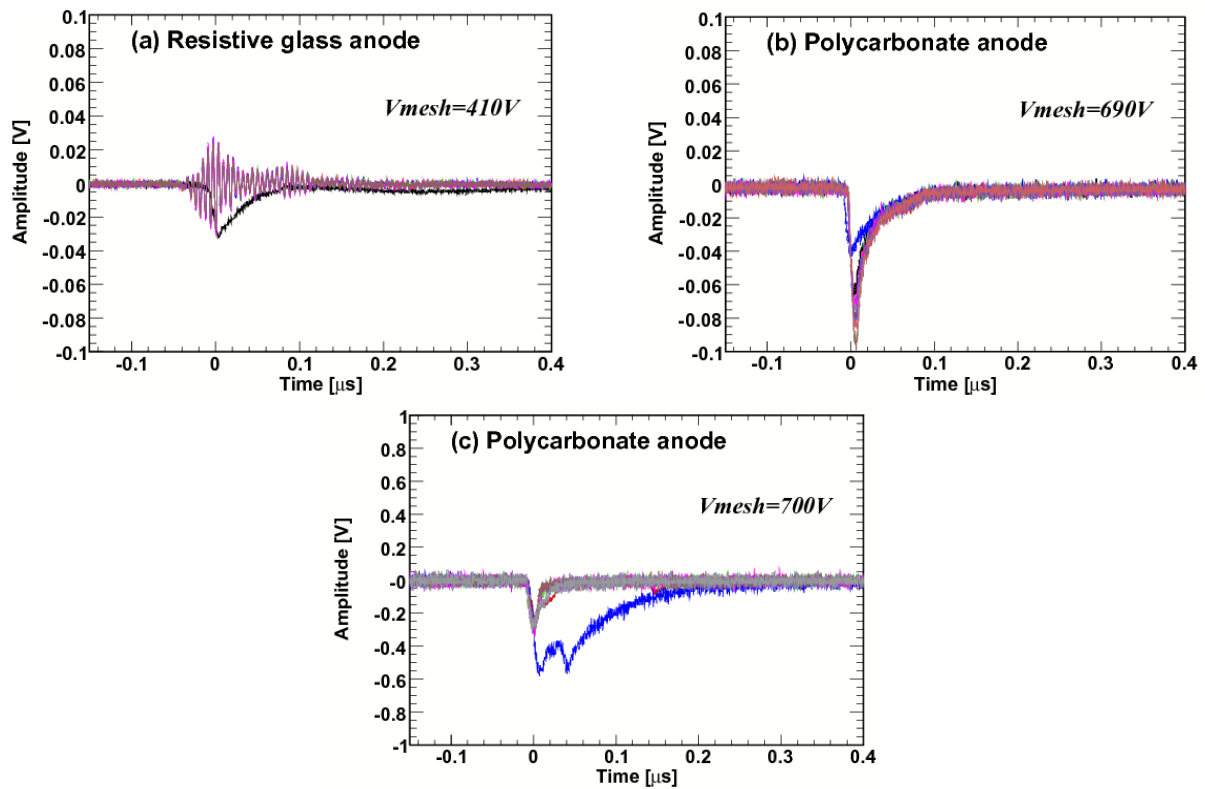


**Figure 4.53** Typical waveforms of sparks-like pulses in prototypes with resistive glass and polycarbonate anodes.

## 4.6 Parallel ionization multiplier (PIM)

Parallel Ionization Multiplier (PIM) [136–138], primarily designed for tracking low energy beta rays or minimum ionizing particles, has a similar structure as Micromegas with micro-mesh electrodes. The difference is that PIM employs more than one layers of micro-meshes and usually there are multiple gas gaps on top of the anode readout plane for electron drifting, charge transfer or multiplication purposes. One typical PIM configuration for minimum ionizing particle detection is to implement a few millimeters thick drift gap followed by several few-hundred-micron thick avalanche gaps in cascade, or occasionally a few millimeters thick charge transfer gaps with relatively low electric fields inserted between these amplification gaps. Avalanches could develop in multiple gaps and the charge cloud could be spread out to reduce the spark probability. With this particular setting, the ion induced signals are still the dominant part of the total collected signals on anode readout elements. Therefore, the signal has a relatively long rise time and the detector has a moderate timing performance as those for traditional Micromegas detectors. For certain tracking applications where timing are also crucial, a large fraction of electron induced fast signals from the detector is desired.

Motivated by improving the timing performance for parallel-mesh structure detectors, we have designed a PIM structure with the configuration illustrated in figure 4.54. It incorporates a drift gap of few-millimeter thick, an amplification gap of around  $300\ \mu\text{m}$  in the middle and an induction gap of around  $120\ \mu\text{m}$  at the bottom. The device could be conveniently constructed with the stainless steel woven wire meshes and thermo-bond films. It will work in a GEM-like mode, in which electrons generated from the avalanches between meshes M1 and M2 will be partly extracted and transferred to the bottom induction gap. Fast electron induced signals are expected from the anode readout plane.

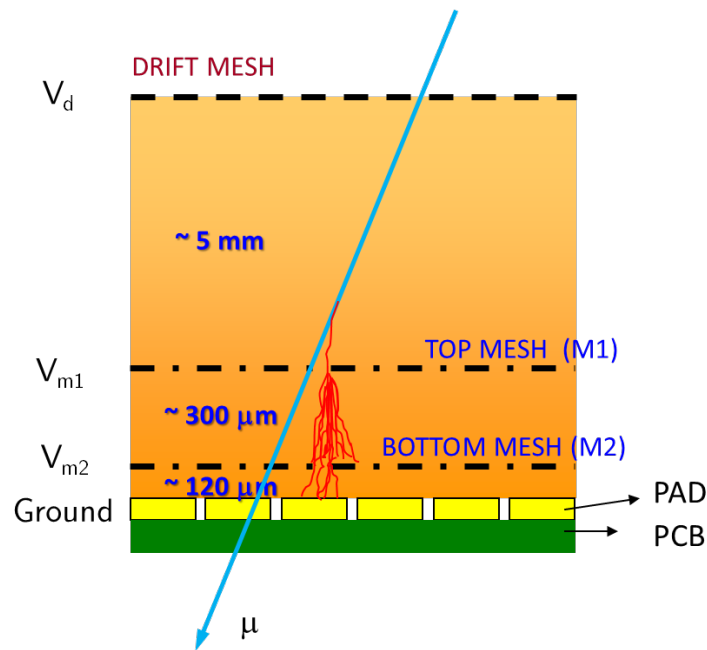


**Figure 4.54** The schematic view of the PIM structure

In order to understand the composition of induced signal on the anode, theoretical calculations and simulations are performed and results will be discussed in the following. Optimizations of the detector electric field configuration for an optimal electron transmission across multiple meshes are also studied with simulation tools. Preliminary verification of the designed PIM structure and test results from small PIM prototype will also be presented.

#### 4.6.1 Calculation and simulation of fast signal component

In order to calculate constitutions of induced signals on the anode of Micromegas or PIM devices, it is simply assumed that the electric field in the Micromegas avalanche gap or PIM induction gap is uniform. Therefore, the first Townsend coefficient  $\alpha$  is constant over the electron drift path. The total induced signal can be divided into three categories:

- Signals induced by initial electrons passing through the micro-mesh

- Signals induced by avalanche-generated electrons drifting towards the anode
- Signals induced by avalanche-generated ions drifting towards the mesh

As illustrated in figure 4.55, assuming that there are  $N_0$  electrons successfully passed through the micro-mesh (mesh M2 in the PIM case), at a distance  $x$  from the micro-mesh, the number of fresh electrons or ions  $dN$ , produced in the avalanche process in a small interval  $dx$ , is given by

$$dN = N_0 e^{\alpha x} \alpha dx \quad (4.8)$$

Recalling equation 3.65 and equation 3.66 for calculating the induced signal amplitude by the presence of a charge in a parallel plate structure, the induced signals due to the movement of ions and electrons are given by

$$U_+ = \int_0^d \frac{e}{C} \frac{x}{d} dN = \frac{N_0 \alpha e}{Cd} \left( \frac{d}{\alpha} e^{\alpha d} - \frac{1}{\alpha^2} e^{\alpha d} + \frac{1}{\alpha^2} \right) \quad (4.9)$$

$$U_- = \frac{N_0 e}{C} + \int_0^d \frac{e}{C} \frac{d-x}{d} dN = \frac{N_0 e}{C \alpha d} (e^{\alpha d} - 1) \quad (4.10)$$

where  $d$  is the thickness of gap and  $C$  is the capacitance of the parallel structure formed between the micro-mesh and the anode plane.  $U_+$  and  $U_-$  are the signal amplitudes induced by ions and electrons, respectively. The first term in equation 4.10 is the signal amplitude induced by initial electrons entering the gas gap.

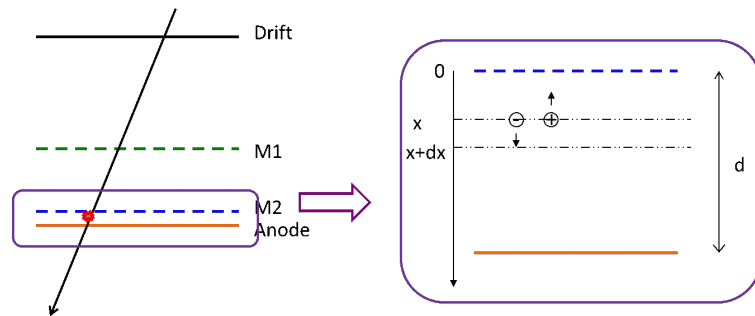


**Figure 4.55** Illustration of electron-ion pair movement in the PIM induction gap.

If one defines a parameter  $\eta$ , which is the fraction of electron induced signal amplitude, it is given by

$$\eta = \frac{U_-}{U_+ + U_-} = \frac{M - 1}{\alpha d M} = \frac{M - 1}{M \ln(M)} \quad (4.11)$$

where  $M$  is the gas gain for the gas gap given by  $\exp(\alpha d)$ . According to equation 4.11, the computed electron induced charge component  $\eta$  as a function of gas gain in the Micromegas avalanche gap or PIM induction gap is shown in figure 4.56. If the gas gain equals to one, which means no amplification is taken place, only electrons passed the mesh induce signals on the anode. Therefore, the prompt signal is 100%. For the typical Micromegas configuration, when gas gains of few thousands are expected, the prompt signal is only 10%. This is further verified with simulate charge signals at two different gas gains using the Garfield program. The induced current signals at gas gains of around 5 and 700 are shown in figure 4.57. Prominent ion tails are clearly visible at a gain of 700. The integrated electron induced signal of 50% at a gain of 5 and 17% at a gain of 700 are in very good agreement with the calculation.

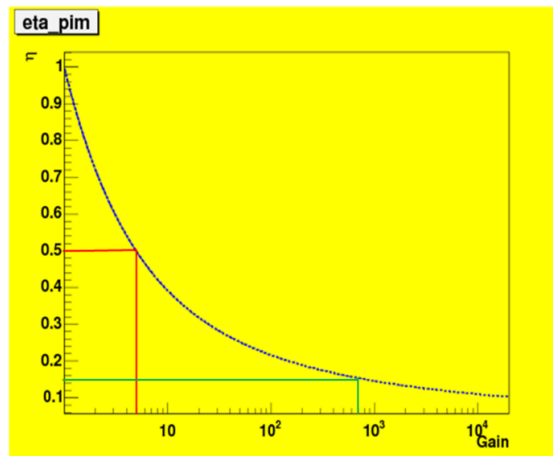


**Figure 4.56** Dependence of electron induce fast signal component with the gas gain.

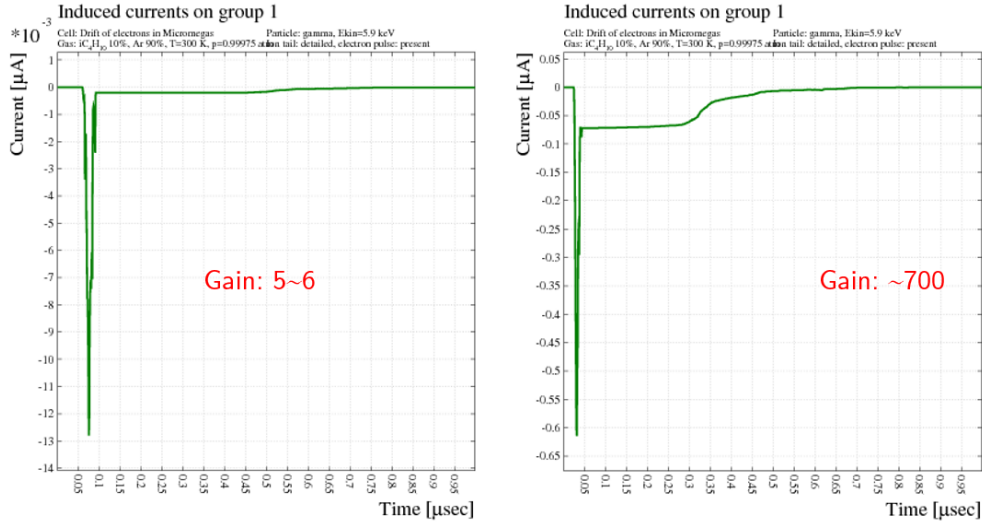


**Figure 4.57** Induced current signals in the Micromegas avalanche gap or PIM induction gap for two gas gains.

Assuming for the given PIM structure, the total effective multiplication factor comparable to that from the Micromegas could be obtained, if the gas gain in the induction gap can be controlled to 2-3, almost 60-70% of the total charge signal on the anode is prompt electron induced signal. This gives a very sharp rise of the signal hence a good timing performance. In addition, the total charge collection can be finished in few tens of nanoseconds instead of few hundred nanoseconds, which is needed for Micromegas.

#### 4.6.2 Electron transmission optimization

As discussed in the above subsection, the main challenge for our proposed PIM structure is to obtain an effective gas gain of a few thousands or even higher. This is indeed of great concern due to the special arrangement of electric fields in the avalanche and induction gap. In contrary to the case for Micromegas where field lines from the upper gap are compressed towards the mesh opening and most of the electrons are allowed to pass the mesh, the electric field lines from the

avalanche gap of PIM structure are mostly terminated on the bottom mesh (M2). Therefore, only a fraction of electrons from the avalanche will be able to enter the induction gap. This is illustrated in figure 4.58.

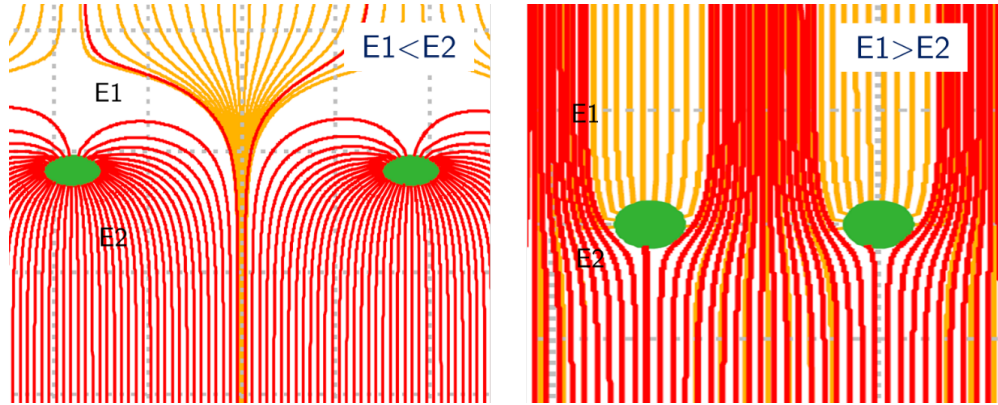


**Figure 4.58** Electric field lines across meshes for a smaller (left) and larger (right) electric field setting in lower gas gap.

For PIM with electro-formed micro-mesh of  $5\ \mu\text{m}$  thick and a large optical transparency, about 25% of the electrons from the high electric field gap could be extracted [137]. If mechanically more robust thick woven meshes are used, the electron extraction probability might be too low for the detector to be useful. In order to assess the viability to construct a PIM prototype with the 50% optically transparent woven mesh used for thermo-bonded Micromegas fabrication, MC simulation of the electron extraction coefficient is performed using the Garfield program. The obtained electron extraction coefficient as a function of electric field ratio between the avalanche and induction gap in several gas mixtures are shown in figure 4.59. At a gas gain of 2-3 in the induction gap, the fraction of electrons that could be extracted from the avalanche gap is close to 10%. Though this fraction is not very high, it is considered still to be useful. Given the fact the real mesh is laminated to reduce its thickness, our simulation is on the pessimistic side and underestimates on the fraction. The simulation also suggest that for a mesh separation of 0.3 mm, the displacement of the two mesh layers does not affect the electric field uniformity and the electron

transmission behavior.

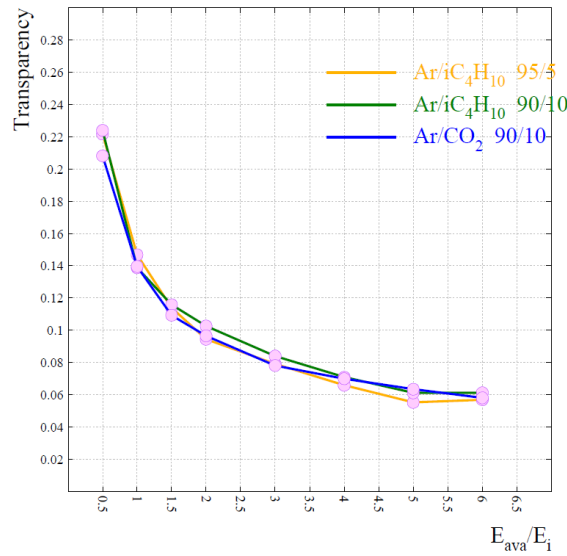


**Figure 4.59** Electron extraction coefficient as a function of electric field ratio between the avalanche and induction gas gaps in PIM.

Assuming the electric field ratio between the avalanche and induction gaps,  $E_{ava}/E_i$ , is kept at 2 so that more than 10% electron extraction coefficient for the bottom mesh of the avalanche gap could be achieved, it is expected that the gas gain from the induction gap will be low. For a typical amplification field of 30 kV/cm, the simulated gas gain as a function of the field ratio  $E_{ava}/E_i$  is shown in figure 4.60. Considering the calculation given in equation 4.11, with gas gains between 1.5 and 3 in the induction gap for the case of  $E_{ava}/E_i$  equals to 2, 70% of the total charge signals are expected to originate from fast-moving electrons.

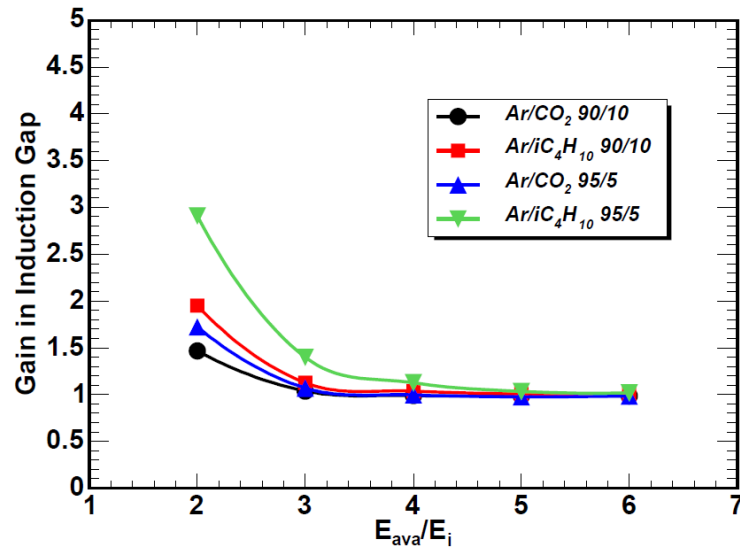


**Figure 4.60** Simulated gas gain in the induction gap as a function of electric field ration between avalanche and induction gas gaps (Electric field in avalanche gap is fixed at 30kV/cm).

### 4.6.3 Prototype fabrication and preliminary tests

Given the above systematic studies, a small PIM prototype with parameters listed in table 4.8 is constructed to verify the design and measure its basic performance. A photo of the constructed 30 mm  $\times$  30 mm prototype is shown in figure 4.61. The prototype is tested in the Ar:iC<sub>4</sub>H<sub>10</sub> (95:5) mixture. Typical simultaneous signals from micro-meshes and anode readout pads, after amplified by charge-sensitive amplifiers, are shown on the left hand side of figure 4.62. The signal for either micro-mesh has a rise time of more than 500 ns. This reflects the long time needed to collect the dominant ion induced charges in a 0.3 mm wide avalanche gap. The ratio between the anode and micro-mesh signal amplitudes, representing the electron extraction coefficient of the bottom mesh (M2), is found to be around 15%. In fact, these signals are taken with an avalanche-induction gap field ratio of 4. The measured electron extraction coefficient is encouragingly larger by a factor of two than the simulated result.

Active area	30 mm $\times$ 30 mm
Drift (Conversion) gap thickness	6 mm
Avalanche gap thickness	$\sim 0.3$ mm
Induction gap thickness	$\sim 0.13$ mm
Micro-meshes	350 LPI stainless steel woven ( $\phi_{wire}=22 \mu\text{m}$ )

**Table 4.8** Basic parameters of the constructed PIM prototype.

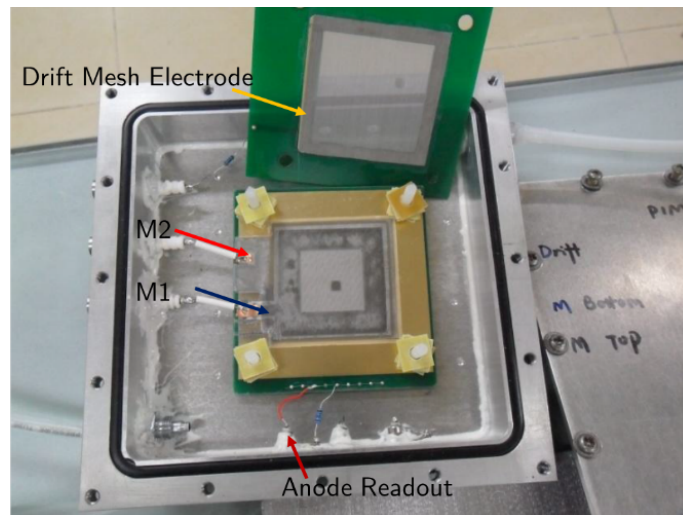


**Figure 4.61** A photo of the constructed PIM prototype with an active area of about 30 mm  $\times$  30 mm.

The  $^{55}\text{Fe}$  spectra are recorded from the anode readout in order to study the gain, electron transparency and extraction coefficient etc. A typical  $^{55}\text{Fe}$  spectrum with an effective multiplication of  $10^4$  at the anode is shown on the right hand side of figure 4.62. An energy resolution (FWHM) of 28% is obtained. Though this is not superb, it is completely acceptable for tracking purposes.

The electron transparency of the top mesh (M1) is measured with voltages ( $V_{M1}$ ,  $V_{M2}$ ) on two inner micro-meshes fixed. The 5.9 keV photo-peak variation as a function of the voltage difference

between the top mesh and the drift electrode is shown on the left hand side of figure 4.63. A maximum electron transparency is obtained when the voltage on the drift electrode is about 80 V higher than that on the top mesh.

If one defines the effective gas gain  $M_{eff}$  as the total number of electrons reached the anode divided by the total number of initial ionizations  $N_0$  in the drift gap, it is given by

$$M_{eff} = \frac{N}{N_0} = \varepsilon_1 \varepsilon_2 M_1 M_2 \quad (4.12)$$

where  $\varepsilon_1$ ,  $\varepsilon_2$ ,  $M_1$ ,  $M_2$  are electron transparency of top mesh (M1), electron extraction coefficient for bottom mesh (M2), gas gains in avalanche and induction gaps, respectively. For the effective gas gain measurements, the voltage on the drift electrode is set to be 80 V higher than that on the top mesh, so that close to 100% electron transparency of the top mesh is guaranteed. The electric field ratio between the avalanche and induction gaps on both sides of the bottom mesh is kept at constant so that the electron extraction efficiencies are the same during the measurements. The electric field in the induction gap is kept below 6 kV/cm to ensure that there is very little multiplication development in this region. The measured effective gas gain as function of the absolute voltage difference between mesh M1 and mesh M2 are shown on the right hand side plot of figure 4.63. A maximum effective gas gain of  $10^4$  is obtained before the prototype becomes unstable to operate. Considering that in our configuration,  $\varepsilon_1$  is close to 1 and  $\varepsilon_2$  is around 15%. The actual gas gain in the avalanche gap should have exceeded  $4 \times 10^4$ . Running such device at an effective gas gain of a few thousands is quite stable.

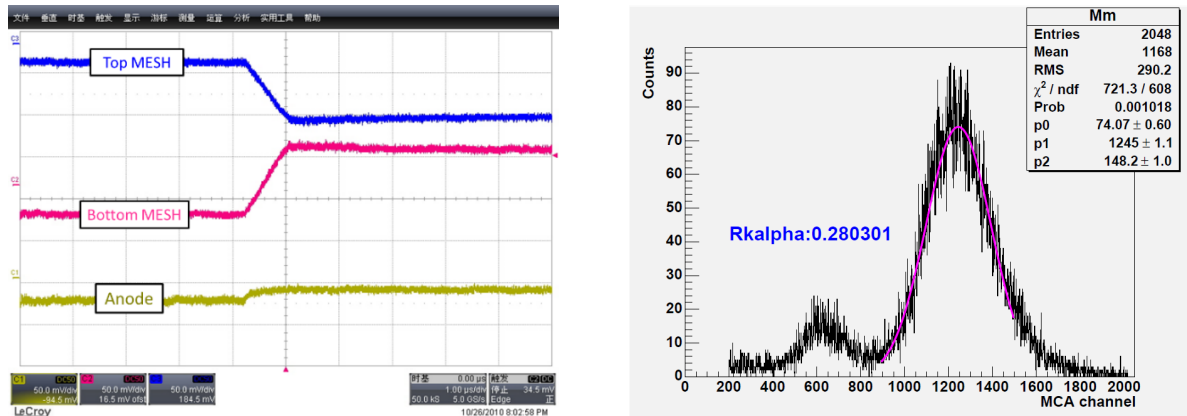


**Figure 4.62** The induced signals on PIM readout electrodes (left) and the obtained  $^{55}\text{Fe}$  spectrum from the anode readout at an effective gain of  $10^4$  in Ar:iC<sub>4</sub>H<sub>10</sub> (95:5) (right).

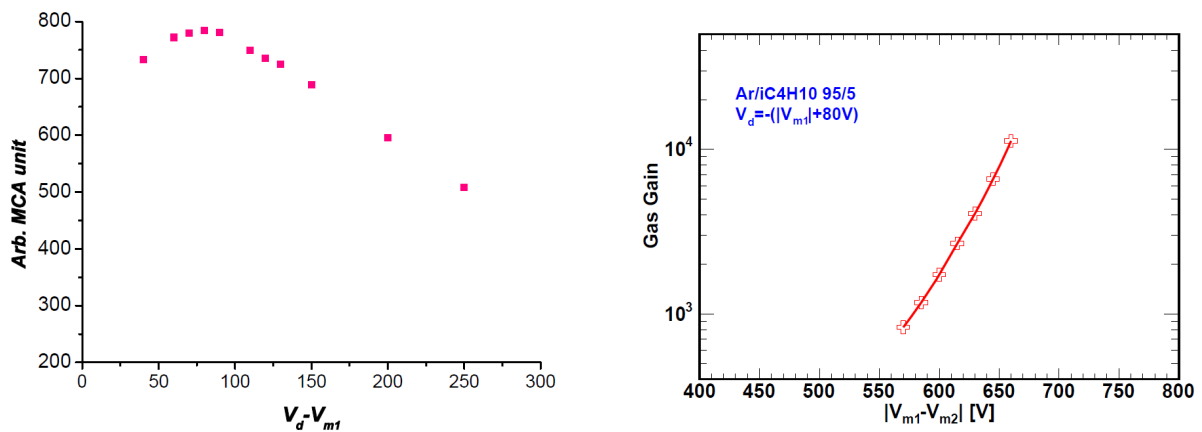


**Figure 4.63** Electron transparency for the top mesh (M1) (left) and the effective gas gain as a function of absolute voltage difference between mesh M1 and mesh M2.

## 4.7 Summary

In the chapter, a novel method to fabricate Micromegas detector is presented. The amplification gap is produced by thermally bonding a layer of stretched stainless steel woven wire mesh on the anode plane using thermo-bond film frames and spacers. The thermo-bond film is a kind of

adhesive film with very good thickness uniformity, excellent dielectric and mechanical properties. It is ideal for bonding various substrates, such as FR-4 and stainless steel mesh that have been used for Micromegas fabrication. It is usually activated by heat and pressure and has good bonding strength when properly handled. The construction of thermo-bonded Micromegas detectors do not involve the photo-lithography process which is required for bulk Micromegas fabrication. Together with the wide commercial availability of thermo-bond films, it allows one to produce moderate-sized Micromegas detectors in almost every labs with hot plate or any other hot press machines.

Tests of small prototypes with 350 LPI stainless steel woven meshes show that gas gain up to  $2 \times 10^4$  could be reached. Very good energy resolution (FWHM), 13.7% for 5.9 keV X-rays is obtained in argon-isobutane mixture. In fact, it is slightly better than that from the bulk Micromegas of around 20%. The gas gain uniformity across 45 mm mesh span can be within 10%. In most cases, 20% gas gain variation around its mean inside active areas are achievable and results are reproduced conveniently. While it is not ideal for energy measurements, the uniformity is completely acceptable for tracking and trigger applications. It should be pointed out that thermo-bonded Micromegas with sizes of 20 cm  $\times$  20 cm, limited by the working area of the hot press machine, have been constructed using a non-refined hot press machine. Results are comparable with those obtained from small prototypes. It is believed that productions of thermo-bonded Micromegas at least with sizes of that used in COMPASS experiment are possible using refined hot pressing tools.

Simulation studies of the characteristics of thermo-bonded Micromegas are performed. They have been particularly focused on the penning effect, electron transparency of woven meshes and the optimization of gas mixtures for better gas gain uniformity. From the comparison of simulated results with experimental data, it is found that the fraction of excited gas atoms participated in the ionization process in penning mixtures of argon and isobutane is higher for isobutane-rich mixtures. The estimated penning transfer probability for Ar:iC<sub>4</sub>H<sub>10</sub> (90:10) mixture generally agrees

with the dedicated calculations and measurements reported by other researchers. The simulation study of electron transparency for thick woven wire mesh suggests that full electron transparency cannot be assumed in some highly diffusing gas, such as argon with a small fraction of isobutane, if the optical transparency of the mesh is smaller than 40%. For typical woven mesh constructed from wires with diameters of around  $20\ \mu\text{m}$ , optical transparency higher than 50% is recommended. The influence of gas transverse diffusion to the electron transparency is very minor in this case. The simulation study of the dependence of gas gain with gas gap show that improvement of gain uniformity in thermo-bonded Micromegas, with thicker than a hundred microns amplification gaps, is possible by careful selection of gas mixture in which the first Townsend coefficient has less sensitive with electric field. An example gas mixture suitable for relatively large amplification gap is neon with a small fraction of quencher gas such as  $\text{CF}_4$ .

Motivated by developing spark-tolerant Micromegas to be used in harsh hadron collider environment and creating a lateral spread of charge signal on the Micromegas anode so that wider readout element could be used, an alternative way of constructing resistive Micromegas is studied. In this approach, high resistivity material, with bulk resistivity higher than  $10^9\ \Omega\cdot\text{cm}$ , is directly attached to the metallic readout plane using high resistivity glues. Three high resistivity materials, semi-conductive glass, carbon-filled polycarbonate and regular glass, have been used to construct small prototypes. Systematic studies of their gas gains, charge up effects, rate capabilities as well as spark protectiveness are carried out. Test results show that gas gains of around  $10^5$  could be obtained with these resistive Micromegas detectors. The charge up effect, basically the gas gain drop with the accumulation of charge on the thick resistive electrode, is observed for polycarbonate anode Micromegas at a gain of  $10^4$  with few hundreds  $\text{Hz}/\text{cm}^2$  rate, whereas the effect is negligible for resistive glass Micromegas with an order of magnitude smaller bulk resistivity at  $10^{10}\ \Omega\cdot\text{cm}$ . Protectiveness of the high resistivity anodes are quite obvious, the total amount of charge released is limited to less than a few nC. The total dead time due to sparks are less than few hundreds of

nanoseconds. The rate capabilities of these prototypes are measured with an intense X-ray gun with a copper target. While it is apparent that Micromegas with regular glass anode cannot be operated at a rate higher than a few hundreds  $\text{Hz/cm}^2$  due to extremely high resistivity of the glass, the semi-conductive glass anode Micromegas is estimated to be able to work at more than few tens of  $\text{kHz/cm}^2$ . The carbon-filled polycarbonate will be useful if the resistivity can be controlled at around  $10^9\text{-}10^{10} \Omega\cdot\text{cm}$ .

Motivated by improving the timing performance of parallel-mesh structure detectors, a parallel ionization multiplier (PIM) structure with a few-mm thick drift gap followed by a few-hundred-micron thick avalanche gap and a hundred-micron thick induction gap is proposed. These gaps are separated by woven wire mesh and could be realized using thermo-bond films as frames and spacers. In this structure, ionized electrons in the drift gap will be guided by the electric field towards the avalanche gap where multiplications occur. A small fraction of electrons generated in the avalanche gap will be transferred to the induction gap where signals are induced on the anode plane. In this specific configuration, the detector operates at a “GEM-mode” with only fast electron signals induced on the anode. However, gas gain of few tens of thousands could be reached with one amplification gap. The dependence of the prompt electron induced signal component with the gas gain in the avalanche gap of the Micromegas detector or the bottom induction gap of PIM structure are calculated and simulated. Both studies, in good agreement with each other, suggest that more than 60% of the total induced signal will be fast electron signal if the gas gain in the PIM induction gap is kept as low as 2-3. Compare with Micromegas operates at the same gas gain, a faster rise time of the induced signal thus an improved timing performance as well as a shorter charge collection time, around few tens of nanoseconds, are expected from PIM. A small PIM prototype is constructed in order to assess the viability of operating such PIM structure at GEM-mode. An effective ionization multiplication factor up to  $10^4$  is obtained on the anode with proper electric field configuration. In addition, it is experimentally verified that about 15% of the

electrons from the 350 LPI woven micro-mesh separating the avalanche and induction gap can successfully pass the mesh. All these studies partly demonstrated the potential of using PIM for minimum ionizing particle tracking and triggering.

# Chapter 5

## Thin-gap Resistive Plate Chambers

### 5.1 Introduction

The resistive plate chamber (RPC) is a type of parallel plate structure gaseous detector. It usually consists of two several-mm-thick high resistivity plates separated by a few mm, or multiple resistive plates stacked on top of each other with several-hundred-micron spacers. High voltages are distributed over the outer surfaces of the outer resistive plates, which are coated by thin graphite layers with around few  $\text{M}\Omega/\square$  surface resistivity. Signals readout elements are capacitively coupled to RPC chambers. For RPCs with single few-millimeter-thick gaps, they are usually called trigger RPCs and mainly used for muon triggering in large collider experiments or ground based cosmic ray experiments. Most widely used trigger RPCs are constructed from Bakelite materials. Bakelite plates, formed by laminating thin melamine layers on the phenolic resins, are very good resistive electrodes with resistivity from  $10^9 \Omega\cdot\text{cm}$  to  $10^{12} \Omega\cdot\text{cm}$ . They are light-weighted plates which can be produced at the scale of few meters and be tailored to various shapes. Those RPCs with several hundred-micron-thick gas gaps are usually called timing RPC. They are mostly constructed with thin glass plates. Thanks to the small gas gap, ionizations are locally confined which

yields good time resolution of less than 100 ps [139].

For trigger RPCs used in collider experiments, gap thicknesses are usually chosen to be 2 mm. Their time resolutions are around 1-3 ns [140, 141] and space resolutions are around few mm using centimeter-sized readout strips or pads [142, 143]. However, muon triggering in present or potential future high energy and high intensity collider experiments tends to be increasingly challenging. Utilizing detectors both high in spatial resolution and timing resolution becomes crucial. Again taking muon triggering in the forward region of ATLAS detector as an example, interested muons with high transverse momentum have to be selected out of about 15 kHz/cm<sup>2</sup> [3] radiation backgrounds at the hottest innermost region, among which are mostly photons and neutrons [144]. Charged particle backgrounds, such as electrons, protons etc. are also present. Though in small portions compared with photons and neutrons, due to their power to penetrate multiple detector layers, charged backgrounds are more likely to confuse the trigger detectors and urge them to generate fake triggers at first place. The simulated time distributions of arrival muon and background hits, after time of flight subtracted, at the muon small wheel within one LHC bunch crossing time of 25 ns are shown in figure 5.1 [145]. Around 90% of muons comes within 2 ns. In contrary, 90% of those neutrons and photon arrives later than 2 ns. If trigger detectors are designed to work with a tight acceptance time window of 2 ns, synchronized with bunch crossing clocks, the 15 kHz/cm<sup>2</sup> rates per detector plane would be reduced to 1.5 kHz/cm<sup>2</sup>, among which only 30% is from uncorrelated photon and neutron hits. The coincidence rate of two detector layers in one LHC bunch cross time is as low as 0.005 cm<sup>-2</sup>, which is substantially lower than muon and charged track coincidence rates. The charged particle backgrounds, also named as correlated backgrounds because they come in time with proton collisions, can be further removed if precision tracks could be reconstructed at the online level to check their origins. Based on this discussion, effective and powerful means of removing vast majority of backgrounds can only be reached using trigger detectors with sub-nanosecond time resolution as well as a very good spatial resolution at the trigger level.

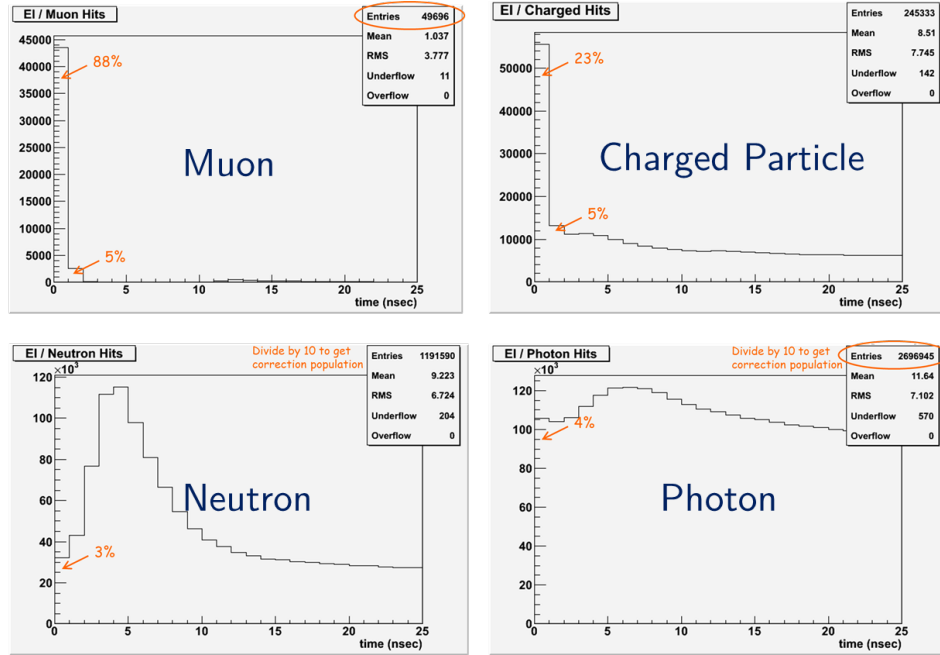


**Figure 5.1** Time distribution of arrival muon and background hits at the ATLAS muon small wheel within one LHC bunch crossing time (25ns) with time of flight subtracted. Note that the top-right plot for charged particles also includes muon counts [145]

Since RPCs are unique gaseous detectors with excellent timing capability, they are very suitable to be used in a trigger system that meets the stringent trigger requirements as discussed above. The scheme for an example fast and precision trigger system based on RPC detectors is shown in figure 5.2. In this trigger system, there are two large-scale RPC triplets which are separated by a few tens of centimeters. For each RPC detector layer in a triplet, it is equipped with fine pitch strips perpendicular to the precision tracking coordinate. Strips are read out from both ends using mean-timer circuits [146]. The mean-timer circuit contains a bunch of delay cells with delay time steps of a few hundred picoseconds. The hit position along the strip direction is encoded in the first coincidence gate. Since the sum of signal arrival times from both strip ends is expected to be independent of hit positions along the strip, the first coincidence output given by the mean-timer is solely determined by the detector timing jitter. Assuming the detector has a time resolution of

around 500 ps, a 2 ns acceptance window, synchronized with the bunch crossing clock, could be set to make two out of three coincidences among three contiguous RPC layers in a triplet. Further fast coincidences between two triplet stations within around 10 ns could be used to select candidate charged tracks. Limited charge and timing information from readout strips of relevance could be subsequently read out followed by the triplet coincidences and could be sent to off-detector processing units. It should be emphasized that for trigger applications where timing budget is low, sophisticated calculations of charge centroids to determine the hit position might not be allowed. However, with the implementation of narrow readout strips, simple digital readout, only using hit information of yes or no from strips, is capable to provide a reasonably good pointing accuracy. For instance, if the hit position is defined as the center of the strip when only one strip is fired, and the middle between two strips when two are fired, and so forth, the position resolution of single RPC layer with 1 mm strip pitch should be better than 0.3 mm. For two triplet stations separated by 300 mm, as the case for two trigger wedges in ATLAS muon New Small Wheel, an on-line angular resolution of less than 1 mrad from the trigger system could be obtained. Such a trigger system with good angular resolution, high granularity and fast coincidence capability will be very powerful and robust to remove backgrounds as soon and as much as possible yet keep a very high muon trigger efficiency. For applications where good pointing accuracies are not tightly required, the strip pitch could be increased to reduce the number of readout channels. The excellent timing capability is still beneficial to improve muon selectivity.

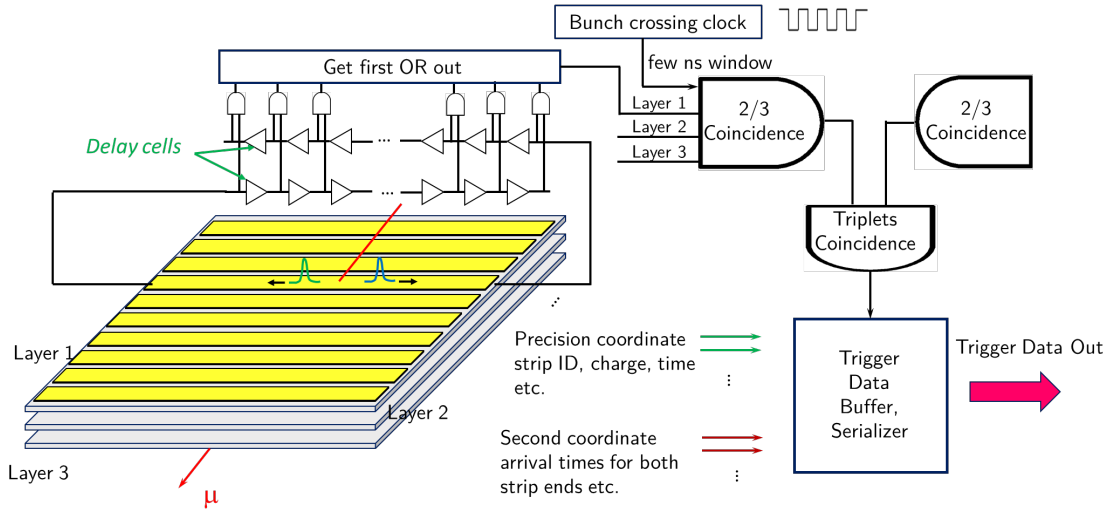


**Figure 5.2** The scheme of an example fast and precision trigger system based on thin gap RPC.

The success of constructing a fast precision trigger system as described above relies on realization of a sub-ns timing performance and a sub-mm spatial resolution at the on-line level in a single RPC. Though excellent timing capability is well-known for MRPC and lab tests of RPC position resolutions using charge interpolation method [147, 148] or based on calculations of signal propagation time in graphite layer [149] suggest a few-hundred-micron localization capability is achievable, there is no systematic study exists to prove the possibility to combine these performances together in a simple RPC structure. Motivated by developing RPCs suitable for fast tracking trigger, special RPC detectors with dedicated readout structures are designed and several test beam campaigns have been carried out to study their performances and assess their viabilities of performing trigger tasks in challenging circumstances. The detector design considerations and detailed descriptions of the constructed RPC detector structure are presented in section 5.2. Beam tests are carried out on the CERN SPS-H8 beam line with 180 GeV/c muons. Setup and test results of these RPCs based on two types of front-end readout electronics are presented separately in section 5.3 and section 5.4. In addition, test results of rate capabilities for high-rate Bakelite RPC

will be briefly introduced in section 5.5.

## 5.2 Thin-gap RPC for fast precision muon triggering

Starting the improvement by reducing the gas gap from 2 mm for conventional RPC detectors to around 1 mm, the time jitter from RPCs should be reduced to less than a nanosecond due to better confinement of primary ionizations. Further reducing the gap gas will result in notable efficiency losses as discussed in chapter 2. Such RPC structure is named as thin-gap RPC simply to distinguish it with those used in the present muon spectrometers of collider experiments. To determine the hit position with precision of less than 1 mm at the on-line level, the simplest solution is to use readout strips of around few mm. In this case, the total thickness of the RPC chamber including resistive electrodes is also needed to be optimized so that the induced charge could be dispersed right to 2-3 strips.

An existing RPC design very close to our needs is that used for constructing 1 m<sup>3</sup> sized digital hadron calorimeter (DHCAL) in Argonne National Laboratory (ANL) [150]. Using readout pads of 1 cm × 1 cm in size, the hit multiplicity in those 1.2 mm gas gap RPCs with thin glass electrodes is close to unity under regular operational condition, suggesting a small charge profile in the readout plane. Therefore, we have used similarly structured thin-gap glass RPCs, with fine pitch readout strips instead of pads, for our beam test studies. A cross-sectional view of the RPC is shown in figure 5.3. Two float glass plates with thickness of 0.85 mm on the ground side and 1.15 mm on the high voltage side are used as resistive electrodes for the RPC. The volume resistivity is around 10<sup>12</sup> Ω·cm thus chambers are used for exploring the intrinsic time and spatial resolutions rather than for high rate operation. Two glass plates are separated by 1.15 mm diameter plastic tubes, which are fixed using nylon mono-filament fishing lines along the longest direction of the chamber. The outer surfaces of two glass plates are painted with resistive paint maintaining a sur-

face resistivity of  $1\text{--}5\text{ M}\Omega/\square$ . Signal pick-up boards, separated by a thin layer of Mylar film, are capacitively coupled to the ground side of the chamber. The strip width and pitch of the signal pick-up board are 1 mm and 1.27 mm, respectively. Negative high voltages are applied to the high voltage side resistive paint of these glass chambers during tests.

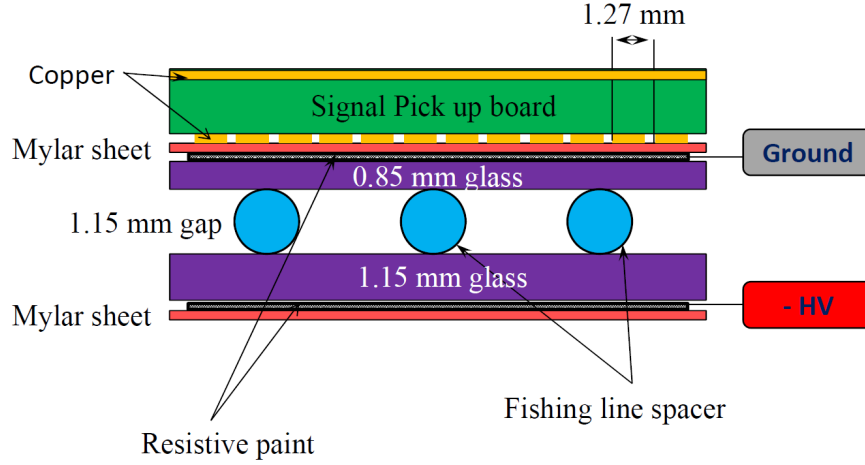


**Figure 5.3** Cross-sectional view of the thin-gap glass RPC structure.

The glass chambers used for beam tests have sizes of  $96\text{ cm} \times 32\text{ cm}$  and a photo of one glass chamber under cosmic test is shown in figure 5.4. The spacer tubes of glass chambers, shown on the left hand side of figure 5.5, are cut shorter than the chamber length. As shown on the right of figure 5.5, gas flowing inside the chamber follows a zig-zag path and is more evenly distributed to the thin gas gap. The operational gas used is a three-component mixture of Freon (94.7%), Isobutane (5%) and  $\text{SF}_6$  (0.3%). With the normal working high voltage set at around 6.5 kV, the dark current of the meter-long chamber is less than  $0.1\text{ nA/cm}^2$ .

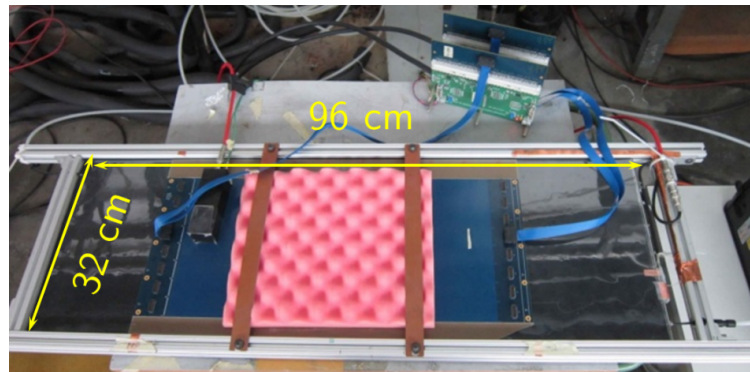


**Figure 5.4** A photo of the thin-gap glass RPC chamber with signal pick-up board under the foam.

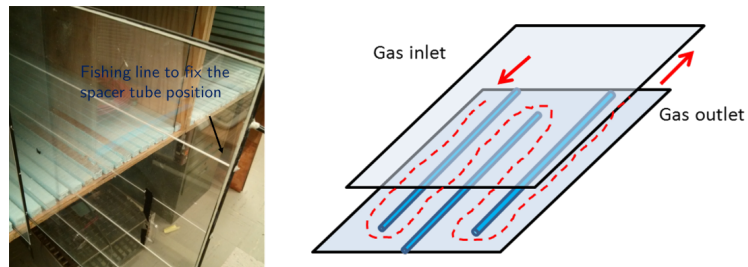


**Figure 5.5** Unpainted glass chamber showing the spacers (left) and gas flow inside the chamber (right).

### 5.3 Beam test using MDT readout system

#### 5.3.1 Beam test setup

Primarily aimed at studying spatial resolutions of the thin-gap RPC chamber with fine readout strip pitch, beam test of the glass RPC with a readout system used for ATLAS monitored drift tube (MDT) chambers [151] is employed. The beam line setup is shown in figure 5.6. The glass RPC is placed about 30 cm away from one side surface of a small-tube MDT chamber (sMDT). The sMDT chamber [152], an improved version of ATLAS MDT detector for high rate operation, has eight layers of drift tubes with 15 mm diameters. The chamber is filled with 3 bar absolute pressure Ar(93%):CO<sub>2</sub>(7%) mixture. The single tube spatial resolution, depending on the track hit position with respect to the central wire, is on average measured to be around 120  $\mu\text{m}$ . The whole sMDT chamber is able to measure muon tracks with an angular accuracy of 0.4 mrad thus provides an external reference for the RPC spatial resolution measurements. Two closely coupled round-shaped small scintillators, with diameters of 1 cm, are placed close to the glass RPC in order to measure local efficiencies. Two large scintillator paddles with one vertically installed at the upstream of the beam line and the other one horizontally placed at the downstream, are used to make coincidences and provide common triggers to the entire readout system. There are also two Bakelite RPCs sit on the beam line for some advance front-end electronics studies, which are not discussed. A photo of the entire setup is shown in figure 5.7.

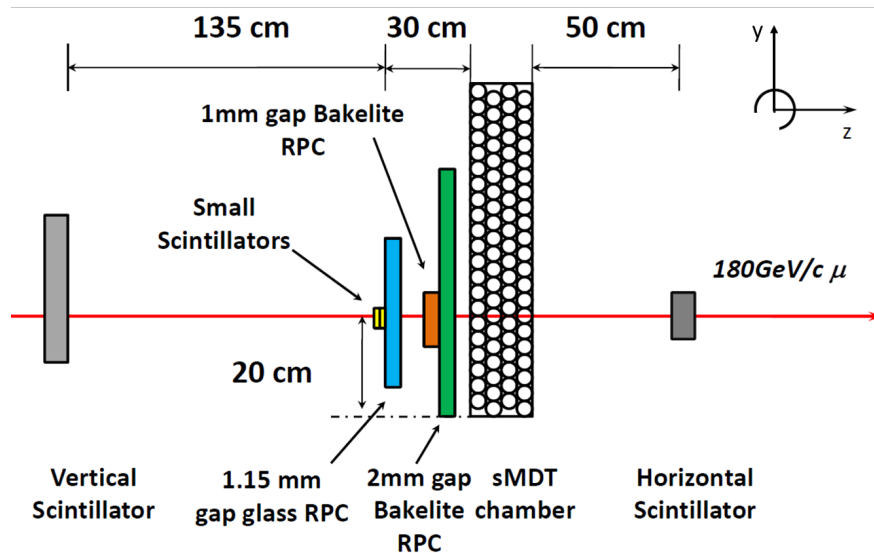


**Figure 5.6** Schematic view of the beam test setup with glass RPC read out by MDT electronics.

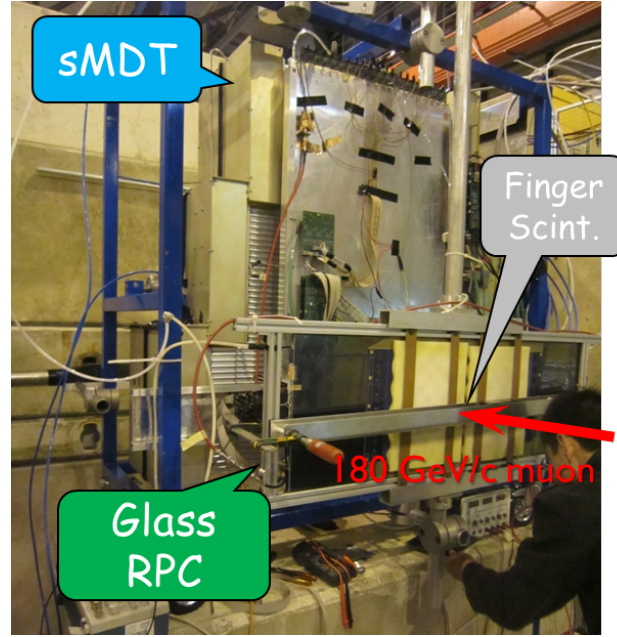


**Figure 5.7** A photo of the beam test setup.

A schematic view of the readout connections is shown in figure 5.8. In total, there are 72 strips read out in three bands. A group of 24 strips is connected from both ends to two adapter boards named as “Hedgehog cards” through blue ribbon cables of about 50 cm in length. MDT front-end boards, named as MDT mezzanine cards, are plugged on the hedgehog cards and 24 channels of signals from one RPC strip band are connected to inputs of three Amplifier-Shaper-Discriminator (ASD) chips. Discriminated signals are digitized inside the ATLAS Muon TDC (AMT) chip on the same front-end board and sent to an off-detector processing module called chamber service module (CSM). The CSM has communications with the DAQ system installed on a PC through optical fibers. It provides controls and settings to ASD and AMT chips as well as collecting data from many front-end boards. It should be emphasized that the glass RPC strips are read out using exactly the same DAQ system which also controls and reads data from sMDT chamber. Therefore, data from the glass RPC is automatically synchronized with sMDT data, allowing easy tasks to find muon reference tracks from the sMDT chamber.

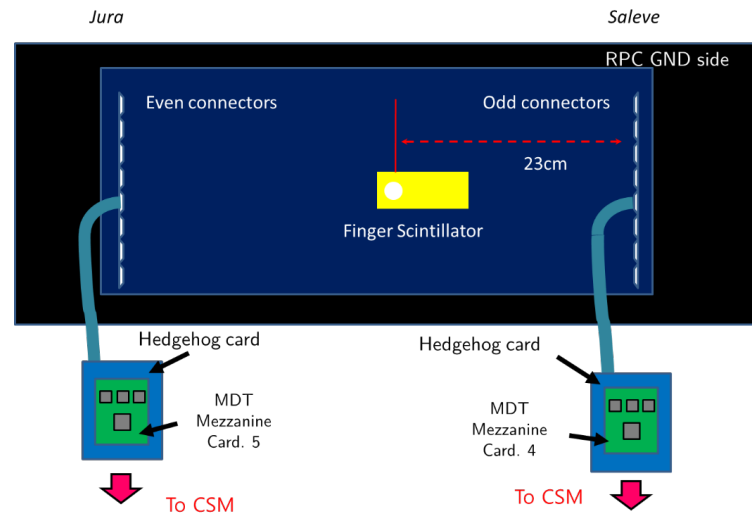


**Figure 5.8** Schematic view of the glass RPC readout connection.

In order to provide timing references to the glass RPC chamber, discriminated signals from two small scintillators as well as their coincidence signals are sent to a separated mezzanine card connected to the same CSM for digitization. The connection scheme is shown in figure 5.9. Signals are attenuated to amplitudes of a few mV to be accommodated within the ASD chip input range.

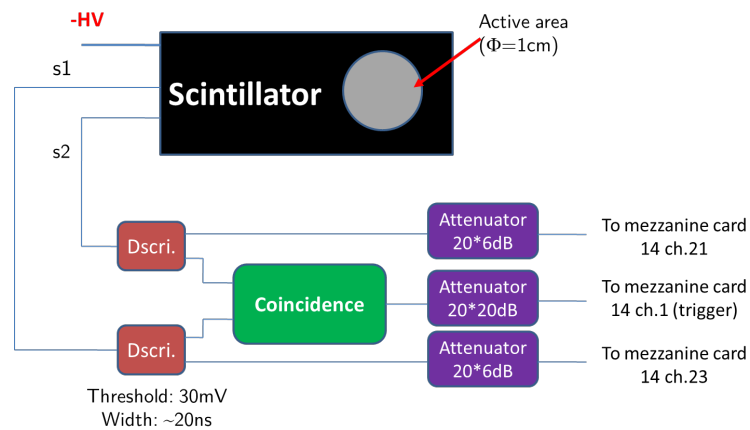


**Figure 5.9** Scheme for digitizing output signals from two small scintillators.

### 5.3.2 MDT readout front-end electronics

A photo of the MDT front-end mezzanine card is shown in figure 5.10. One of the core part of the MDT front-end mezzanine card is the ASD [153] ASIC (Application Specific Integrated Circuit). Its simplified block diagram is depicted in figure 5.11. Input signals from the chamber will first be amplified by a pre-amplifier associated with a pseudo-preamplifier. Several stages of differential amplifiers are followed to further amplify the original signal and perform bipolar shaping. The shaped output signals are fed into a discriminator and a Wilkinson ADC where charges are integrated on a holding capacitor within an adjustable gate width and the capacitor later discharges a constant preselected rate. The output signals are sent out through a pair of differential line with LVDS level standard. Pulses are handled differentially throughout the entire processing chain for good stability and noise immunity. There are two operation modes for the ASD chip: ADC mode and Time-over-Threshold (ToT) mode. For ADC mode operation, signal arrival times are defined by the recorded leading edges and charges are encoded as the output pulse width of the Wilkinson ADC. For ToT mode operation, signals from discriminators are sent out to the output driver. Whenever signal crosses the threshold, it is detected and recorded. The time when the leading edge of a pulse crosses the threshold defines the signal arrival time and the time between the leading and trailing threshold crossings represents the charge.

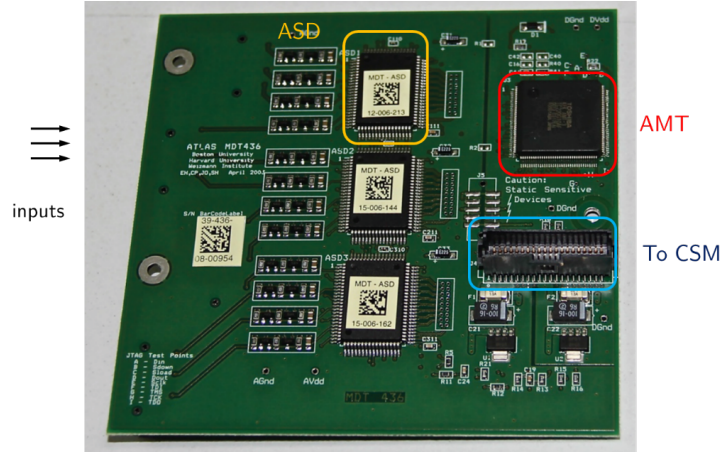


**Figure 5.10** A photo of MDT Mezzanine card.

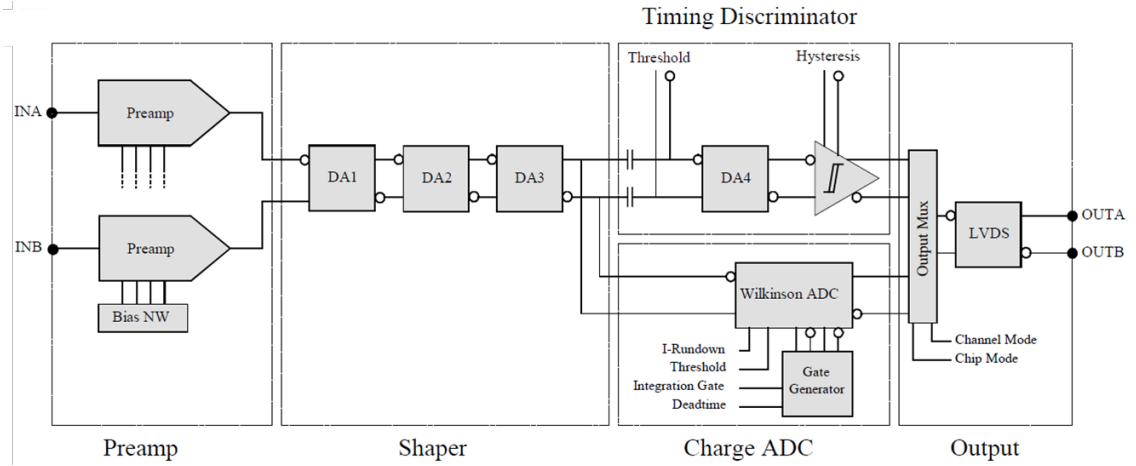


**Figure 5.11** Simplified block diagram of MDT ASD chip.

The Wilkinson ADC output pulse width as a function of the input charge for several gate width settings is shown in figure 5.12. Non-linear dependency of output width with input charge is clearly visible. This in fact introduces a non-negligible systematics in determining hit positions when charge weighting method is used. The output width is saturated at around 200 ns. Due to the better representation of charge using ADC mode compared with ToT mode. Only ADC mode is used during the tests. A list of key parameters for entire ASD chip is summarized in table 5.1.

Channel per chip	8
Input impedance	120 $\Omega$
Noise level	ENC = 6000 e <sup>-</sup> rms
Shaping	Bipolar, 15 ns shaper peaking time
Sensitivity	8.9 mV/fC
Nominal threshold	40 mV

**Table 5.1** MDT ASD specifications [153].

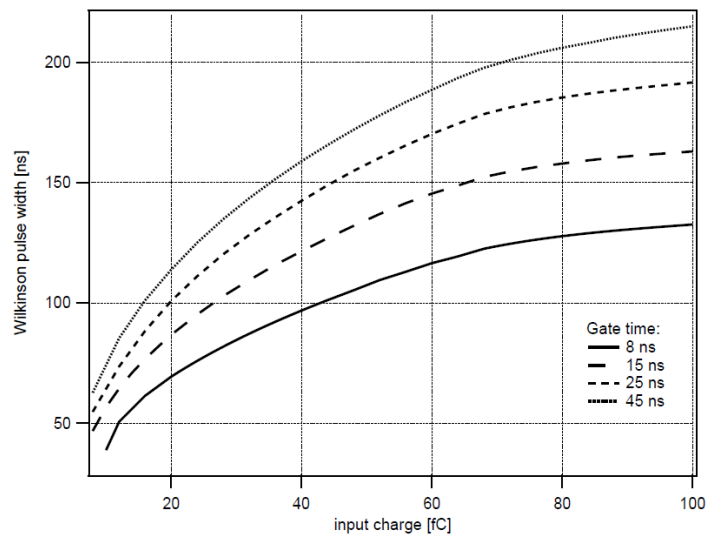


**Figure 5.12** Pulse width as a function of input charge.

Another key ASIC chip on the front-end mezzanine board is the AMT chip. The simplified block diagram [154] is shown in figure 5.13. The chip is running with a 40 MHz frequency system clock. The system clock, multiplied to 80 MHz using internal phase locked loop (PLL), is provided to the internal ring oscillator with 16 taps. It is then used as a reference to digitize the input signals and yields a digitization resolution of 0.78 ns. There are in total 24 channel inputs of the AMT

chip accepting signals from three octal-channel ASD chips. For each channel, 4 events could be buffered before they are written to a common level-1 buffer with a depth of 256 words. The chip also accepts triggers signals in the meantime. The event count and the trigger time tag are stored in an 8 words deep first in first out (FIFO) unit. Trigger-event matches are performed to select hits related to the trigger using the pre-configured matching parameter. Matched event data are passed to a 64-word deep readout FIFO and eventually sent to the off-detector CSM which handles data from 18 mezzanine cards.

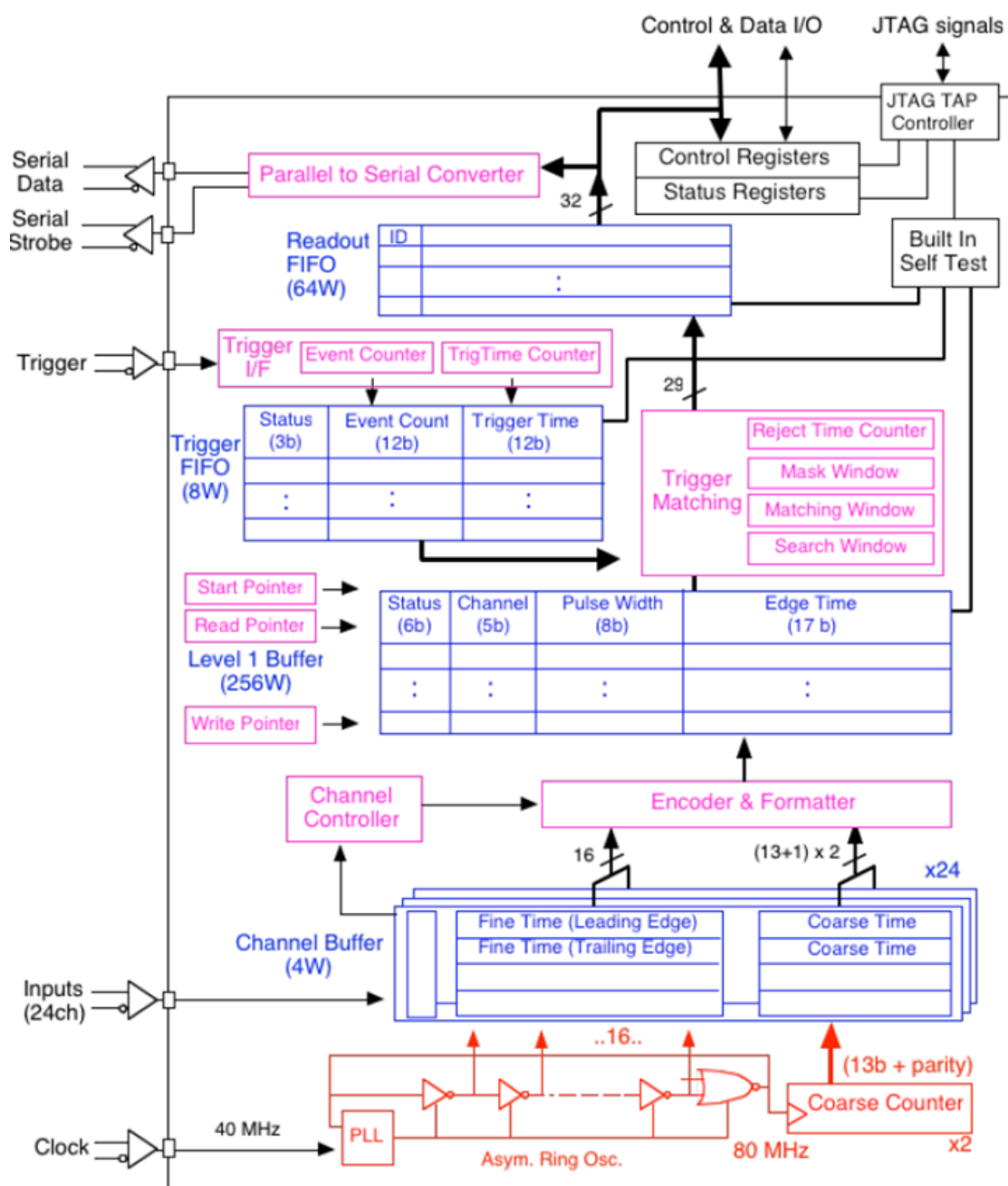


**Figure 5.13** Simplified block diagram of AMT chip [155].

The match of a trigger signal and its related hits information from readout channels is illustrated in figure 5.14. When a trigger signal is accepted, a trigger time is defined as its coarse time tag

minus an offset (`bunch_count_offset`). Searches of validate hits start from the trigger time and end at the trigger time plus a match window. An extended search within the search window is used to find out all hits which might have not been written to level-1 buffer in strict time order. To speed up the trigger match process and to prevent buffer overflow, older hits before a specified reject time are rejected. This is done using a separated reject time counter with an adjustable “`reject_count_offset`” to determine which hit should be rejected.

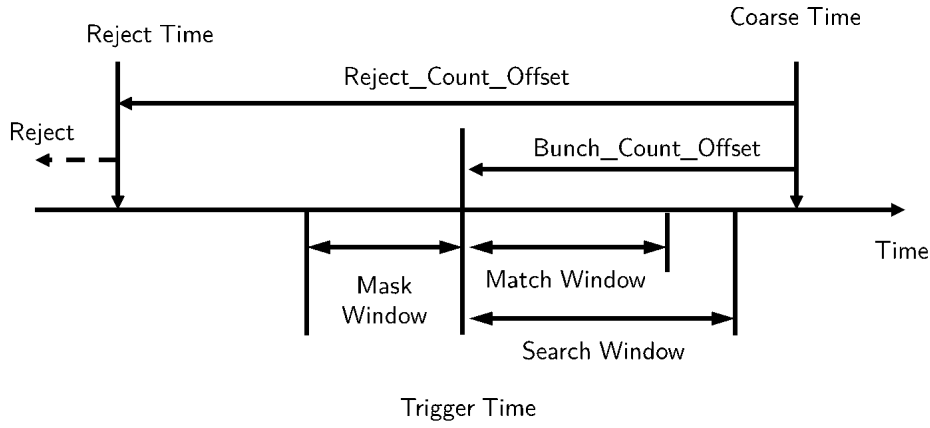


**Figure 5.14** Illustration of trigger matching in AMT chip.

### 5.3.3 Results

#### 5.3.3.1 Charge and raw time spectra

Typical recorded charge spectra from both ends (denoted as End A and End B, respectively) of a strip is shown on the left two plots of figure 5.15. Each ADC count in fact represents output charge pulse width of 0.78 ns from Wilkinson ADC. Pedestal counts well below 50 ADC counts have been cut and are not displayed in the spectra. Deviations of spectra shapes from landau distributions are mainly due to the non-linear representation of charge. The long tails at the lower ends of the spectra are partly due to smaller induced charges on that strip when muons have fired on

its neighboring strips. Even reading from both ends, the average ADC of 177 counts when the RPC is operated at around 6.5 kV, is exceedingly large compared with the average ADC counts of 70 for MDTs [156]. Recalling the pulse width and input charge correlation given in figure 5.12, charged centroid measurements from the glass RPC strips are very much limited by the insensitivity of the front-end electronics to the induced charge variations. Nevertheless, a reasonable digitization precision of the output pulse width, 0.78 ns, still leaves rooms for improving the hit localization precision when charge information is used. Very good correlation of the measured charged from two opposite ends of a strip is clearly visible and result is shown on the rightmost plot of figure 5.15. This good correlation has also been observed for other strips. Therefore, analysis of the muon hit positions can be performed using data from either strip end.

Typical leading edge time spectra recorded from both ends of a strip are shown in figure 5.16 for effective thresholds of -58.75 mV (top two plots) and -108.75 mV (bottom two plots), respectively. The negative threshold setting is simply due to the fact that induced signals from strips on the RPC ground side are of negative polarity. All raw timing distributions are roughly flat and the clear absence of any random count at side bands indicates the data recorded is almost free from any background, noise hits. Changing the threshold does not alternate the results. It is believed to be due to the low noise rate of the glass RPC chamber.

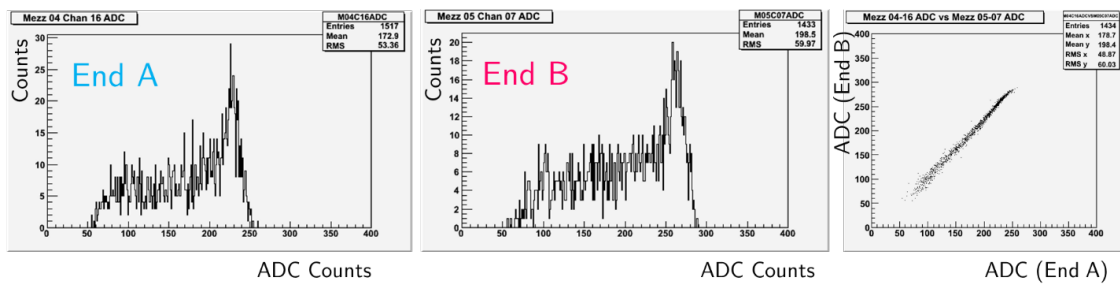


**Figure 5.15** Typical charge spectra at two ends of a strip (left two plots) and their correlations (rightmost plot).

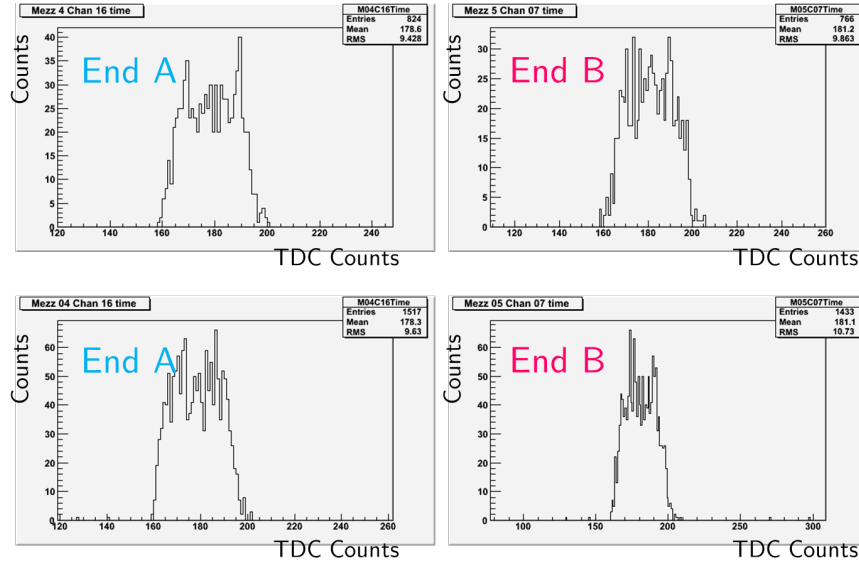


**Figure 5.16** Leading edge raw time distributions from two ends of a strip for effective thresholds of -58.75 mV (top two plots) and -108.75 mV (bottom two plots), respectively.

### 5.3.3.2 Hit distribution, efficiency and cluster size

Distributions of muon hits on two ends of strips are shown in figure 5.17, when hits are also found on two small scintillators. Missing hits at End A of strip 9 and strip 11 are due to two dead channels from the connected mezzanine card. Counts are less at side strips because the scintillators are of round shapes and thus trigger narrower areas near the edges.

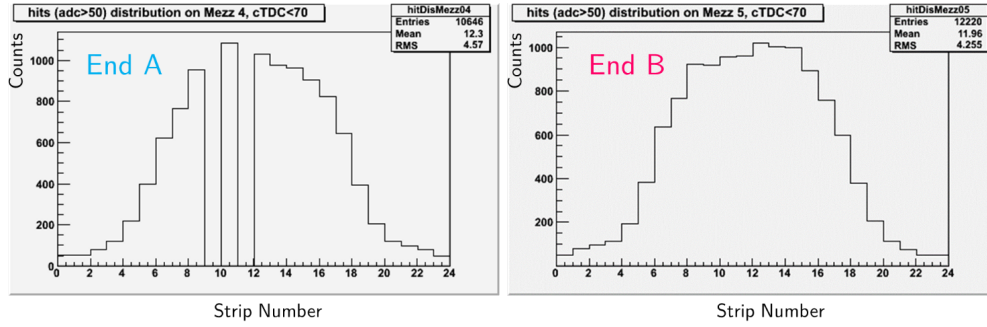


**Figure 5.17** Distributions of hits on two opposite ends of strips triggered by a small round-shaped scintillator.

For the study of glass RPC local efficiency, hits from both small scintillators, digitized by the same MDT readout system are required. Since these scintillators give independent signals and they are triggered by those large scintillator paddles, requiring hits from two small scintillators is in fact making logical coincidences of all four scintillators and thus confirms the passage of muons. Areas of two overlapping small scintillators are smaller than that covered by 72 strips thus they could be used for monitoring RPC efficiency change. Searches of the glass RPC responses to muons are started by looking for the strip with earliest signal arrival time. If at least one strip is fired, a 20 ns time window is opened, starting from that earliest arrival time, to look for any hit from neighboring strips associated with that muon track. A cluster is defined as a group of contiguous strips found with hit in the given searching time window or a group of fired strips with no more than one missing strip. The number of events with hits associated with muon tracks divided by all small scintillators triggered events gives the efficiency of the chamber. The measured efficiency and average cluster size as a function of absolute high voltage is shown in figure 5.18. The glass chamber efficiency reaches the plateau at 6.3 kV and a plateau of more than 700 V is obtained. The measured maximum efficiency is found to be more than 97%. In addition, as shown in table 5.2, the measured efficiency at 6.5 kV is almost unchanged when the absolute value of the effective threshold is raised to twice as high as the recommended threshold for MDT readout. Given the

Effective threshold (mV)	Efficiency (clusize size $\geq 1$ )
-48.75 mV	97.4 % $\pm$ 0.3 %
-78.75 mV	97.2 % $\pm$ 0.2 %
-98.75 mV	97.8 % $\pm$ 0.2 %

**Table 5.2** Dependence of efficiency with threshold. High voltage is set to 6.5 kV.

fact that MDT ASD is designed for detecting a few tens of fC charged whereas the average RPC prompt charge at the working point is on the order of a few hundred pC, insensitivity of efficiency to the threshold change at 6.5 kV is expected.

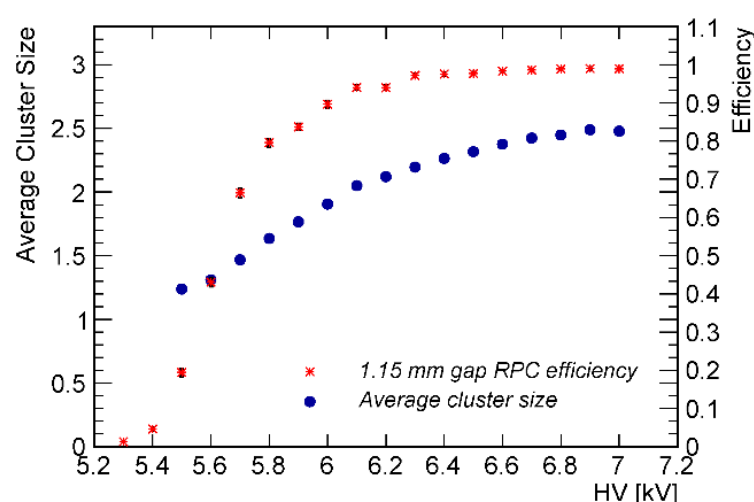


**Figure 5.18** Efficiency and average cluster size as a function of absolute high voltage.

For the RPC hit cluster study, it is found that the average cluster size increases from 1.2 at 5.5 kV to 2.5 at 7.0 kV. In addition, as shown on the left hand side of figure 5.19, the number of clusters for most cases is found to be only one. This is another evidence that the chamber is quite quiet during the operation. A working point of 6.5 kV for the chamber is eventually selected for further time and spatial resolution studies. The distribution of the cluster size for those event

with only one cluster at the working point is shown on the right of figure 5.19. On average, there are 2.3 strips fired. This is less than ideal since clusters with more than three strips are desirable for centroid calculations. Optimizations of RPC detector geometries are considered in the future development to better match the charge spread on the readout plane and the readout strip pitch.

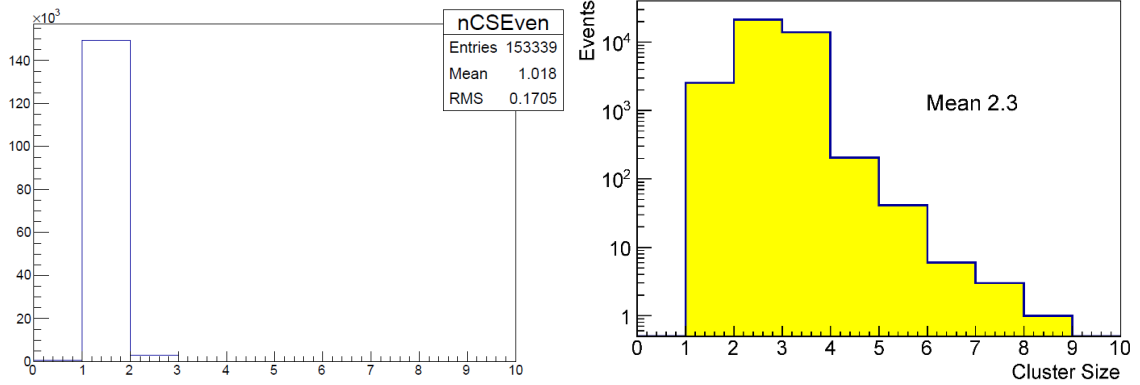


**Figure 5.19** Distributions of number of clusters (left) and the cluster size for one-cluster only events (right) at 6.5 kV.

### 5.3.3.3 Prompt charge signal

The 180 GeV/c muon signals from the glass RPC chamber are investigated directly without any amplification when detector is operated on the efficiency plateau. An example recorded signal on an oscilloscope with 50  $\Omega$  termination is shown in figure 5.20 when the chamber is operated at -6.6 kV. The signal seen on the oscilloscope is the prompt charge signal induced by moving electrons. The total amount of prompt charge for this particular event is measured to be 0.35 pC. Most of the events observed have signal amplitudes smaller than this one. The average prompt charge size is estimated to be at least a factor of two smaller than that from 2 mm gap RPCs used in the barrel of ATLAS spectrometer [157]. Signals from the 1 mm gap glass RPC have durations of less than 5 ns and the leading edges are expected to be smaller than 2 ns. This can also be observed from figure 5.20. It needs to be stress that when fast electronics with nanosecond level peaking time and

a comparable shaping time are used, thin gap RPCs with very short output pulses will possess a very low occupancy and will be very powerful to handle unexpectedly high trigger rates.

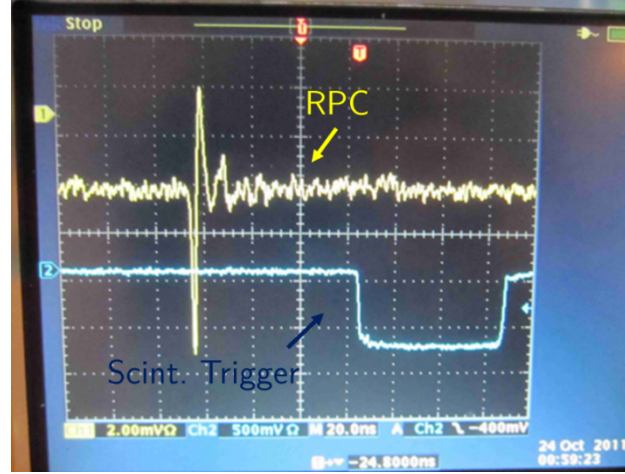


**Figure 5.20** Prompt charge signal from the 1.15 mm gap glass RPC signal operates at -6.6 kV

#### 5.3.3.4 Spatial resolution

The spatial resolution of the thin gap RPC is studied by comparing reconstructed hit positions in RPC ( $Y_{RPC}$ ) with those extrapolated from muon tracks reconstructed from sMDT ( $Y_{sMDT}$ ). The geometric relationship between the glass RPC and the sMDT chamber is shown in figure 5.21. For muon tracks reconstructed from the sMDT chamber, the slope parameter  $m$  and the intercept parameter  $b$  are given for the  $y$ - $z$  plane. The extrapolated positions at the glass RPC are plotted in figure 5.22. Regular low counting intervals appear about every 8 mm. A careful study shows that these are due to the lack of dedicated calibration of the sMDT chamber and tracks pass close to the wire or penetrate between tube walls are constructed with large uncertainty and low efficiency.

For detected muon events, typical charge-time structures on glass RPC strips are plotted in 3D histograms and results are shown in figure 5.23. For the event represented on the left side plot, the central strip with maximum induced charge has the minimum arrival time. The variation of

strip signal arrival time can be as much as 4 ns. This is believed to be due to the earlier threshold crossing for large signals. In some of the cases, as shown on the right side plot of figure 5.23, charges from two neighboring strips are quite comparable and the arrival time differences cannot be distinguished.

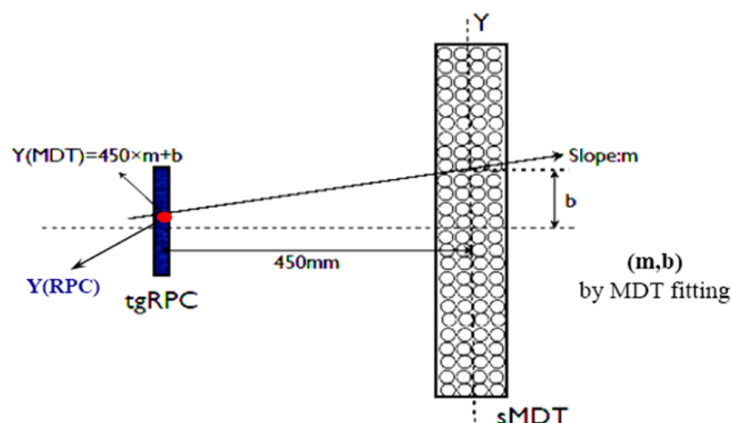


**Figure 5.21** Geometric relationship between the glass RPC and the sMDT chamber.

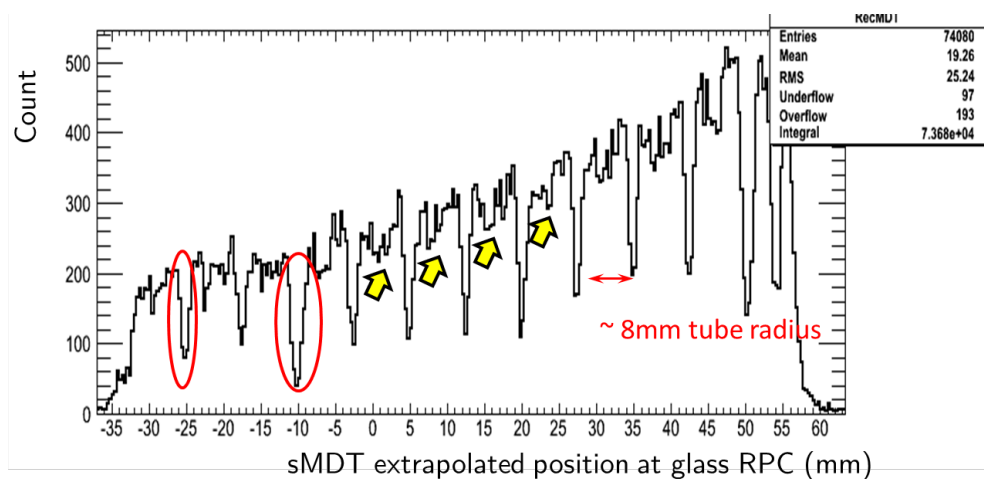


**Figure 5.22** Distribution of extrapolated muon hit positions at the glass RPC.

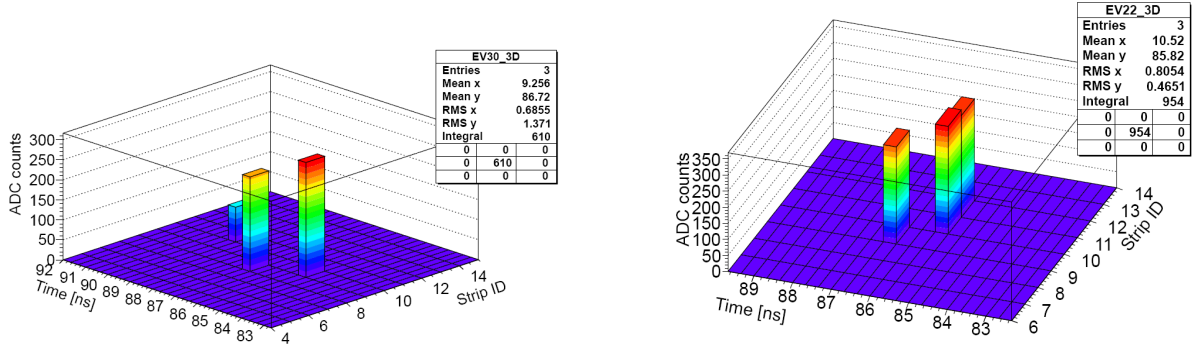


**Figure 5.23** Display of charge and signal arrival time on RPC strips for two muon events.

Given the charge and signal arrival time correlations from RPC readout strips, it is possible to reconstruct muon hit positions on RPC using a number of methods:

- **Single strip determination:** the muon hit position is considered to be the center of the strip with maximum charge or minimum signal arrival time.
- **Conventional charge centroid:** the muon hit position  $Y_{RPC}$  is calculated using

$$Y_{RPC} = \frac{\sum (72 - S_i) \cdot ADC_i \cdot 1.27}{\sum ADC_i} \quad (5.1)$$

where  $S_i$  and  $ADC_i$  are strip identification number and strip charge, respectively.

- **Reconstruction with only timing information:** the muon hit is determined to be

$$Y_{RPC} = \frac{\sum (72 - S_i) \cdot 1.27}{N_f} \quad (5.2)$$

where  $N_f$  is the number of fired strips.

The distribution of residuals between RPC reconstructed hit positions using single strips with maximum charges and the sMDT chamber predicted ones is shown in figure 5.24. The resolution including at least 100  $\mu\text{m}$  sMDT prediction uncertainty is found to be only 420  $\mu\text{m}$ . Even after

subtracting that prediction uncertainty, it is still worse than the expected single strip resolution of  $367 \mu\text{m}$  determined by  $1270 \mu\text{m} / \sqrt{12}$ . The reason has been found to be the variation of charge gain from different MDT readout channels. In some of the cases, hit positions are falsely assigned to neighboring strips. The residual distribution when hit positions in RPC are reconstructed using only strips with minimum signal arrival times is shown on the left hand side of figure 5.25. A single Gaussian fitting gives the overall resolution of  $374 \mu\text{m}$ . By subtracting the  $100 \mu\text{m}$  sMDT prediction uncertainty, RPC resolution is estimated to be  $360 \mu\text{m}$ , comparable with the expectation from single strip determination. Better resolution obtained using the later hit position determination method is due to the relatively small channel offset in time. It is also found that about 22% of the events have two strips with indistinguishable minimum arrival times. If one defines the hit position as the middle between two strips, as shown on the right hand side of figure 5.25, the resolution for those events with indistinguishable minimum signal arrival times from two strips are derived to be only  $290 \mu\text{m}$ . This improvement is due to the involvement of two strips in the determination of hit positions.

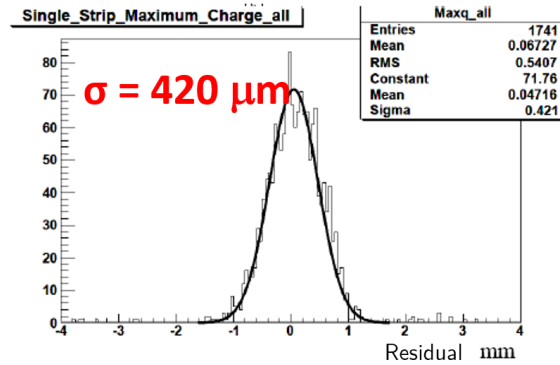


**Figure 5.24** Residuals between RPC reconstructed positons using maximum charge and sMDT predictions.

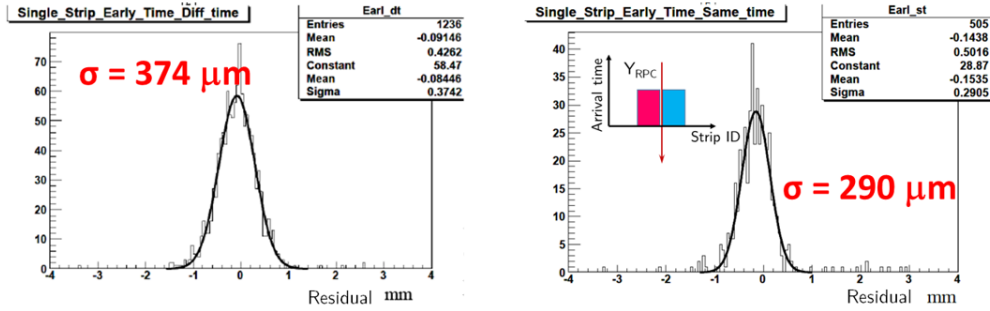


**Figure 5.25** Residuals between RPC reconstructed positons using minimum charge and sMDT predictions.

For the measurement of spatial resolution using charge centroid, those events with only one cluster, representing more than 95% of the total recorded events, are used. The general procedure is to find the strip with minimum arrival time and then open a 10 ns time window to find all validate hits of that cluster. The correlation between the reconstructed hit position in the glass RPC and those predicted by the sMDT reconstructed tracks is shown in figure 5.26. Good correlations are obtained expect small regions appearing every about 8 mm. The large dispersion of sMDT predicted positions in these regions are clearly visible. Unfortunately, we are unable to perform dedicated calibrations for the sMDT chamber and thus have to be selective for the regions to be used for position resolution study. Those regions with abnormally large deviations between the RPC reconstructed positions and sMDT predicted ones or with low statistics are abandoned. Measured RPC spatial resolutions across a 72-readout-strip region for two separate runs at the same running condition are shown in figure 5.27. Assumptions of  $100\ \mu\text{m}$  uncertainties from the sMDT predictions are made and believed to be conservative, as the RPC is quite far away and no correction or calibration has been performed for the sMDT chamber. On average, the spatial resolution obtained using charge centroid is around  $220\ \mu\text{m}$ . This result also includes the effect of any misalignment between the RPC and the sMDT chamber. Results for two runs are quite consistent with each other. The best single strip resolution, shown as an inset in figure 5.27, is found to be  $201 \pm$

$4\text{ }\mu\text{m}$  after subtracting the sMDT prediction uncertainty. However, it must be stressed that these results are greatly limited by the charge representation precision in MDT electronics, as they are primarily designed to record rough charge information for time-walk correction. Moreover, part of the large charge signals from the RPC saturates the electronics and causes the degradation of performance in position measurements.

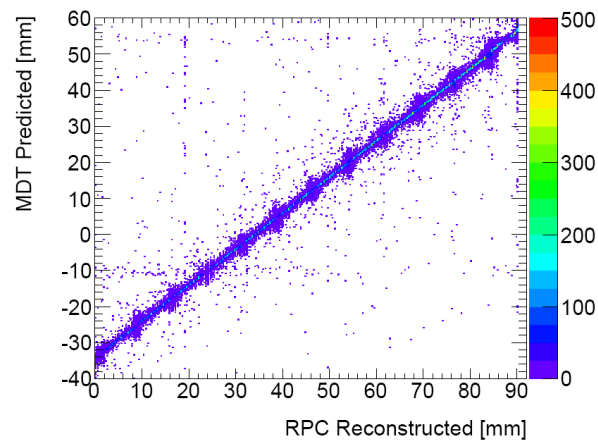


**Figure 5.26** Correlation between RPC reconstructed positions using charge centroid and sMDT track extrapolated positions.

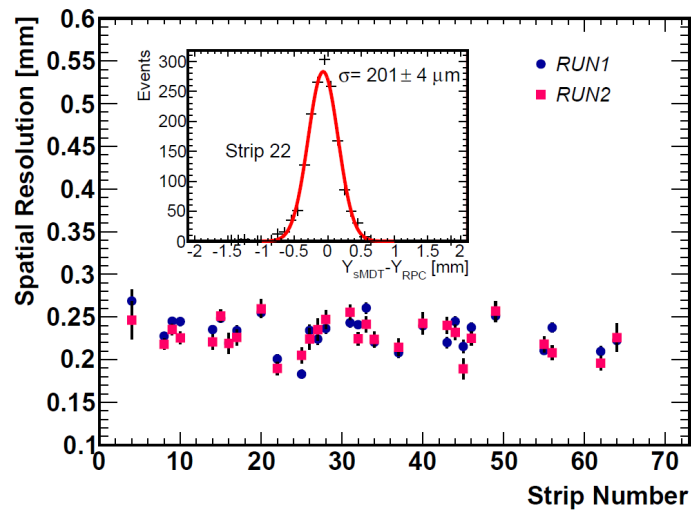


**Figure 5.27** Spatial resolution of the glass RPC using charge centroid method.

Time window (ns)	Cluster size	Spatial resolution (strip 57) ( $\mu\text{m}$ )
20	2.48	$215 \pm 7$
10	2.41	$215 \pm 7$
5	2.36	$236 \pm 8$
3	2.12	$290 \pm 9$
2	1.91	$315 \pm 10$
1	1.6	$467 \pm 13$

**Table 5.3** Impact of opened time window length on the cluster size and spatial resolution.

For a specific run, an analysis of the impact of the opened time window on the cluster size and spatial resolution is shown in table 5.3. A time window as short as 10 ns, started from the minimum signal arrival time of an event is more than enough to find all validate hits associated with a muon penetration of the detector. As the time window tightens to less than 5 ns, the cluster size reduces and the spatial resolution worsens rapidly due to the missing of information for centroid calculations. Compared with other gaseous detector with typically a few tens of nanoseconds or longer signal collection time, the small spread of signal arrival times will be very helpful to reduce the latency for triggering with high rate, provided that suitable fast electronics are equipped.

For the evaluation of thin gap RPC online precision trigger capability, spatial resolution study only using timing information is also performed. Fired strips are selected within a 20 ns time window from the earliest signal arrival time of an event. The hit positions are determined subsequently to be the average center of all fired strips. A typical distribution of the local residuals between RPC reconstructed positions using only timing information from fired strips and those sMDT predicted ones is shown in figure 5.28. The RPC spatial resolution in this case, after the assumed  $100 \mu\text{m}$  sMDT prediction uncertainty subtracted, is determined to be  $287 \pm 8 \mu\text{m}$ . The global residual

distribution from most of the readout strips with large statistics is shown in figure 5.29. Overall, spatial resolution using such “digital” readout without using charge information is found to be  $344\ \mu\text{m}$ , including contributions from misalignment and sMDT prediction uncertainty. It should be stress that this accuracy could be achieved at the on-line level with simple logics using only timing information from a few strips. It makes RPCs excellent precision detectors for muon triggering.

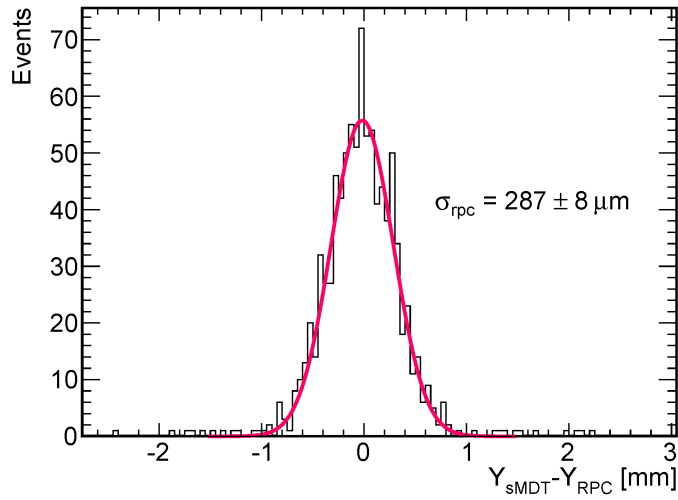


**Figure 5.28** Distribution of local residuals between sMDT predicted position and those reconstructed in RPC only using timing information of fired strips.

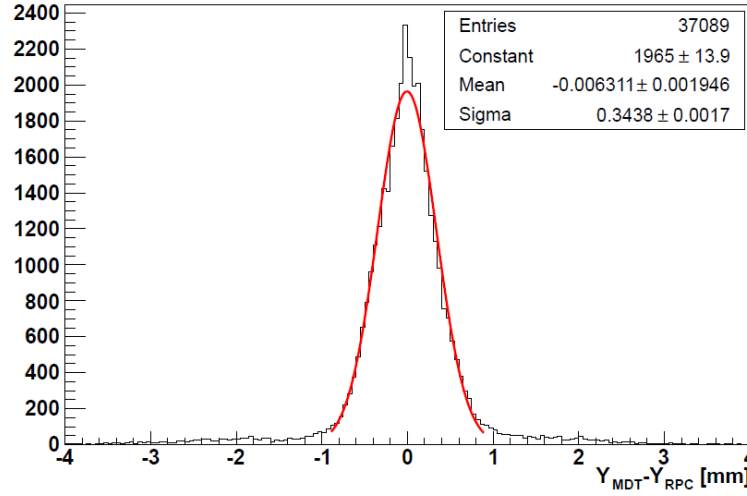


**Figure 5.29** Distribution of global residuals between sMDT predicted position and those reconstructed in RPC only using timing information of fired strips.

### 5.3.3.5 Time resolution

The time resolution of the glass RPC is also measured with the reference from the small scintillator. Typical distributions of strip signal arrival time, corrected by the small scintillator, are shown in figure 5.30 for two opposite ends of a strip. The measured time jitters on both ends are around 1.8 TDC counts, which are about 1.5 ns. As is common for all timing measurements with different signal amplitudes, the signal amplitudes and rise time have strong correlations. For a given threshold, smaller signals cross the threshold later than large amplitude signals with sharp front edges. A typical correlation between the corrected RPC time and the recorded charge is shown in figure 5.31. This information is used to correct the time jitter and the correction is usually called the slew correction.  $t_{corr}$ , the corrected time is given by

$$t_{corr} = t_{uncorr} - f_t(ADC) \quad (5.3)$$

Where  $t_{uncorr}$  and  $f_t(ADC)$  are the time before slew correction and the function describing the time and amplitude correlation. Distributions of slew corrected times are shown in figure 5.32. The

time jitters are found to be about 1.4 TDC counts, which are roughly 1.1 ns. These results include the jitter from reference scintillator, which is about 0.6 ns. The de-convoluted jitter from the glass RPC is less than 1 ns. However, it is mostly limited by the low TDC resolution of 0.78 ns.

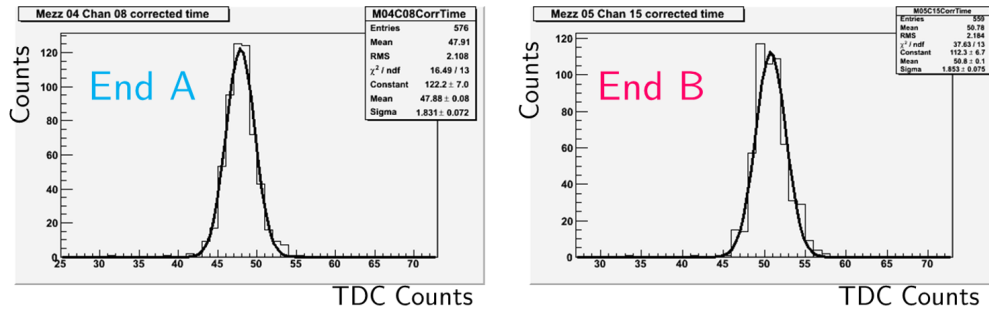


**Figure 5.30** Time distributions for two opposite ends of a RPC strip.

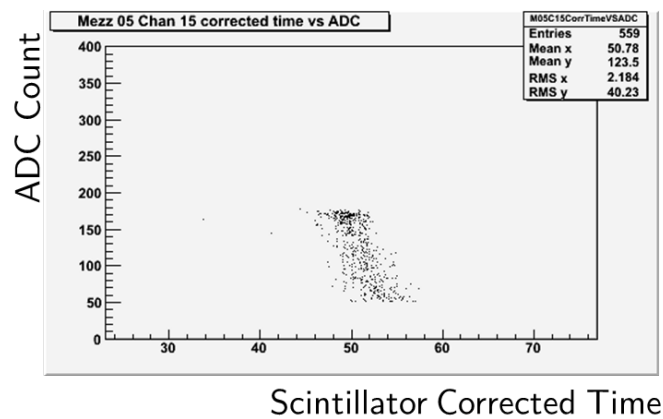


**Figure 5.31** Time-amplitude correlation of the recorded RPC signals.

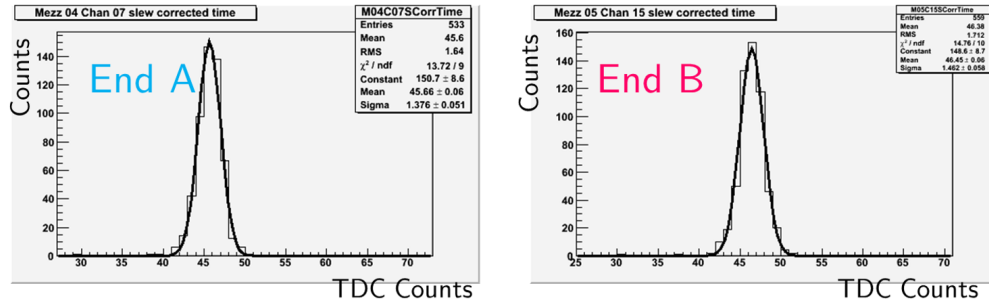


**Figure 5.32** Time distribution from both ends of a strip after slew correction.

## 5.4 Beam test using NINO based readout system

The beam test with MDT electronics shows that a good spatial resolution could be achieved with thin gap RPC for on-line tracking. However, the ultimate timing capability for the thin gap chamber design remain unexplored. We have therefore prepared three additional beam tests dedicated to thin gap RPC timing studies. The front-end readout electronics have been chosen to be the NINO electronics [158]. NINO is a fast front-end ASIC chip specifically designed for precision timing measurement of MRPCs used as time of flight detectors for ALICE experiment. Goals of these beam tests include:

- Measurement of RPC efficiency with NINO front-end electronics
- Measurement of time jitter from thin gap RPCs
- Verification of the idea of using RPC detectors as mean-timers
- Measurement of position resolutions using signal propagation time differences from two ends of a strip

With the help from two silicon detectors during the period of last beam test, spatial resolutions are also studied for RPCs with NINO readout.

### 5.4.1 Beam test setup

The side view of the first beam test is shown in figure 5.33. Basically, it is a combined test with Thin Gap Chambers (TGCs). Three RPC detectors are installed at the upstream. RPCs denoted as RPC1 and RPC2 are two 1.15 mm gas gap glass RPCs which are exactly the same design, shape and size as the one used for beam test with MDT electronics. The one denoted as RPC 3 is a 20 cm  $\times$  20 cm Bakelite RPC. It is made from standard 2 mm thick Bakelite used for RPCs at the barrel of the ATLAS detector. The gas gap is 1.0 mm. Two small scintillators, same as used in beam test with MDT readout system, are placed close to one of the glass RPC and used to check RPC local efficiencies. There are also two large scintillators along with several TGC doublets and quadruplets at the downstream of the beam line. For the arrangement of readout in these RPCs, signal pick-up boards with 1.27 mm strip pitches are still used at ground sides of RPCs when negative high voltages are applied on opposite sides. As illustrated in figure 5.33, strips for two glass RPCs are placed horizontally whereas strips are arranged along the vertical direction for the small Bakelite RPC. With such configuration, it is possible to use the Bakelite RPC as a reference for measurements of position resolution along the glass RPC strip length direction and vice versa. In occasional cases, two signal pick-up boards are coupled to both sides of the glass RPC (RPC1) at the downstream in order to compare the differential readout with the single side readout. The strips on two sides are roughly aligned so that two strips right facing each other at opposite sides could pick up signals of same absolute amplitudes and form a pair of differential signal. A photo of the entire beam line setup is shown in figure 5.34.

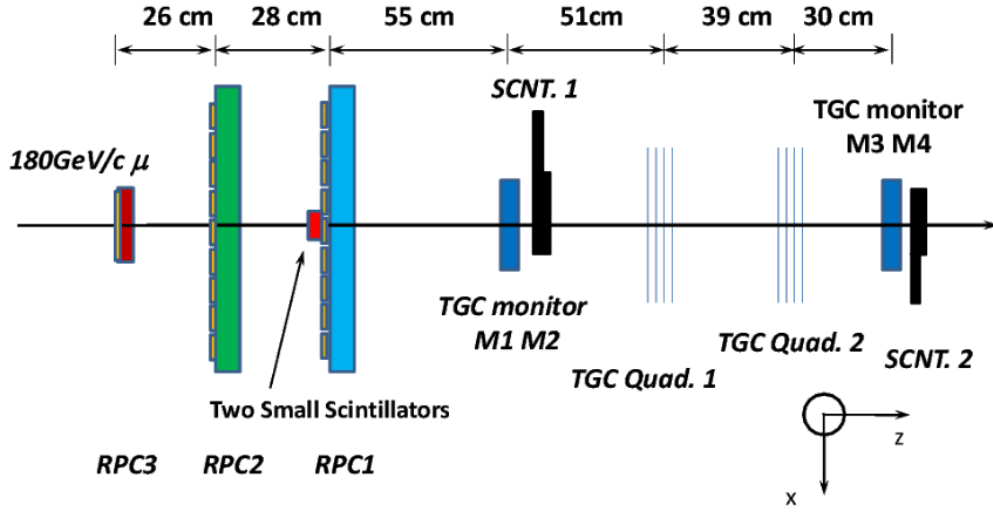


**Figure 5.33** Side view of the first beam test setup for RPCs with NINO front-end electronics.

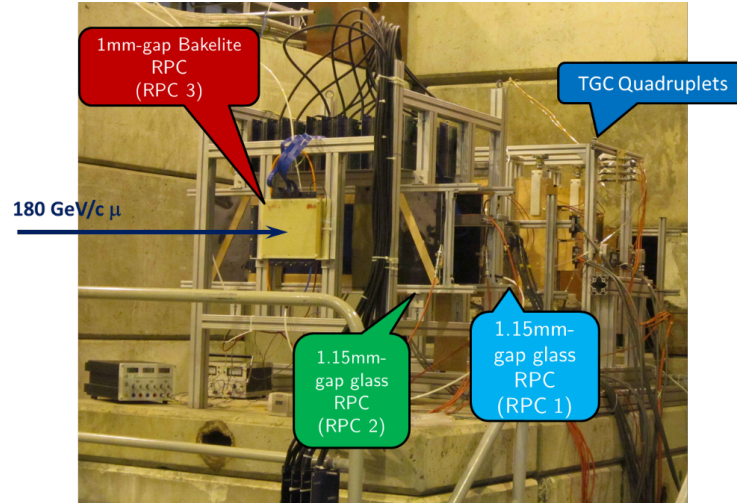


**Figure 5.34** A photo of the beam line setup for RPC tests with NINO ASIC.

Schematics of other two beam tests are shown in figure 5.35 and figure 5.36, respectively. In general the readout system is exactly the same as that in the first beam test. Setup is also similar except that a MRPC, with five 0.25 mm gaps and sized 87 cm × 52 cm, is installed during the

second beam test as a time reference for single gap RPCs and two silicon ladders are installed during the last beam test as references for precision position measurements.

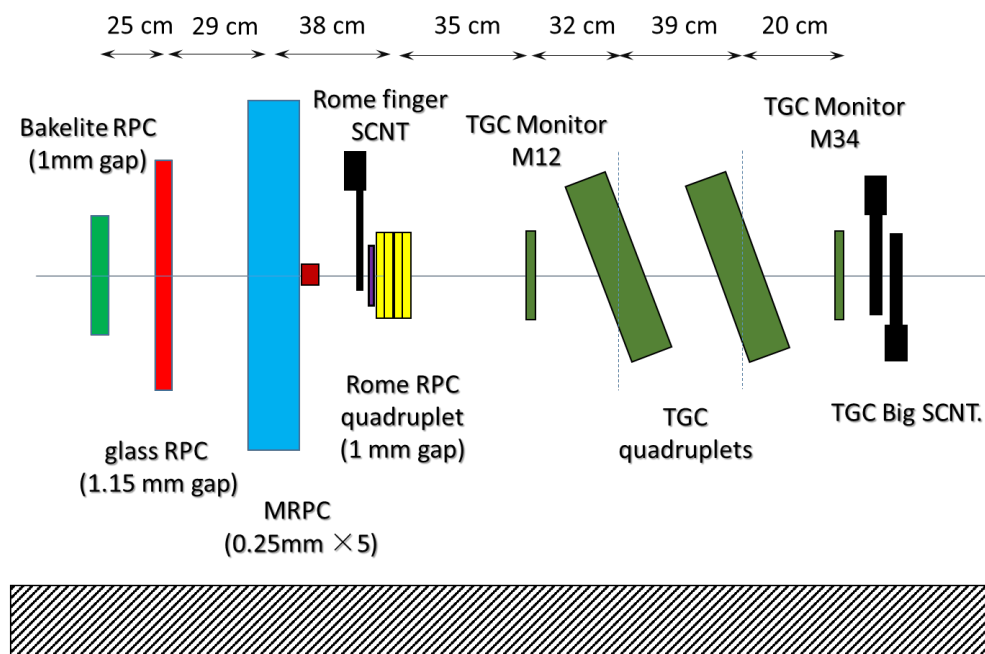


**Figure 5.35** Side view of RPC beam test with MRPC chamber installed in the beam line.

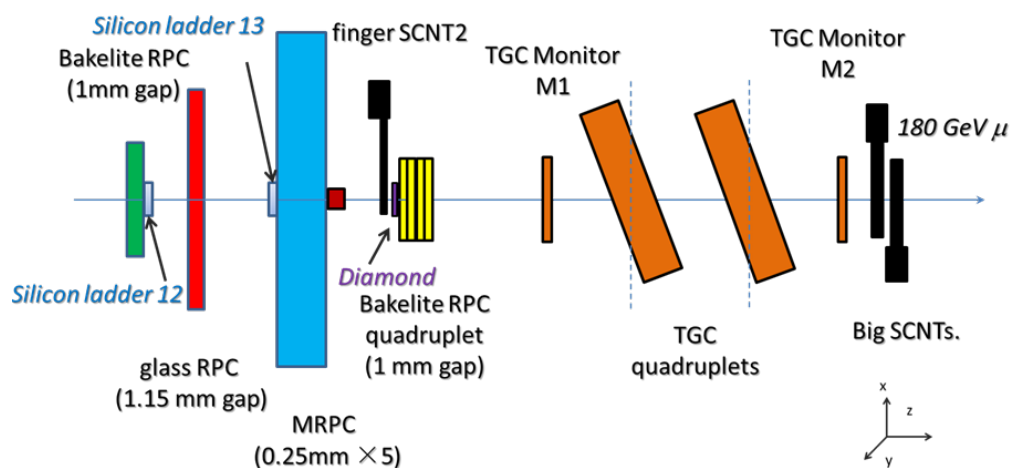


**Figure 5.36** Side view of RPC beam test with two silicon detectors for position resolution study.

## 5.4.2 NINO ASIC based readout system

### 5.4.2.1 Overview

The general scheme for the NINO based readout system is shown in figure 5.37. Signals either differential or single ended are brought to a NINO front-end card via a “strip adapter”. Each NINO card has three octal-channel NINO chips handling signals from 24 strips. Output signals from four NINO cards are transmitted to an interface board called “4to3 Adapter” board through specially shielded cables (VHDCI, Very High Density Cable Interconnect). Interface boards route input signals to three 32-channel connectors which could be linked with VME based TDC modules using twist-pair ribbon cables. Detailed connection to “4to3 adapter” is shown in figure 5.38. Digital signals sent to three TDC modules are digitized and then transmitted to DAQ machines via a VME bus controller. In order to synchronize the data from three TDCs modules, a clock replicator is designed to deliver 40 MHz system clocks simultaneously to three TDC modules. Common triggers are also given to three TDCs modules at the same time. A photo of the off-detector readout system fitted inside a crate is shown in figure 5.39.

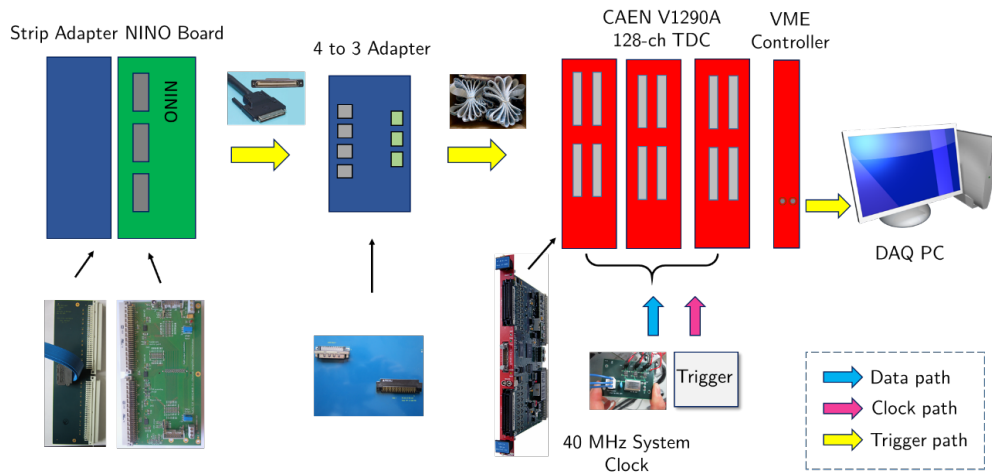


**Figure 5.37** General scheme of the NINO based readout system.

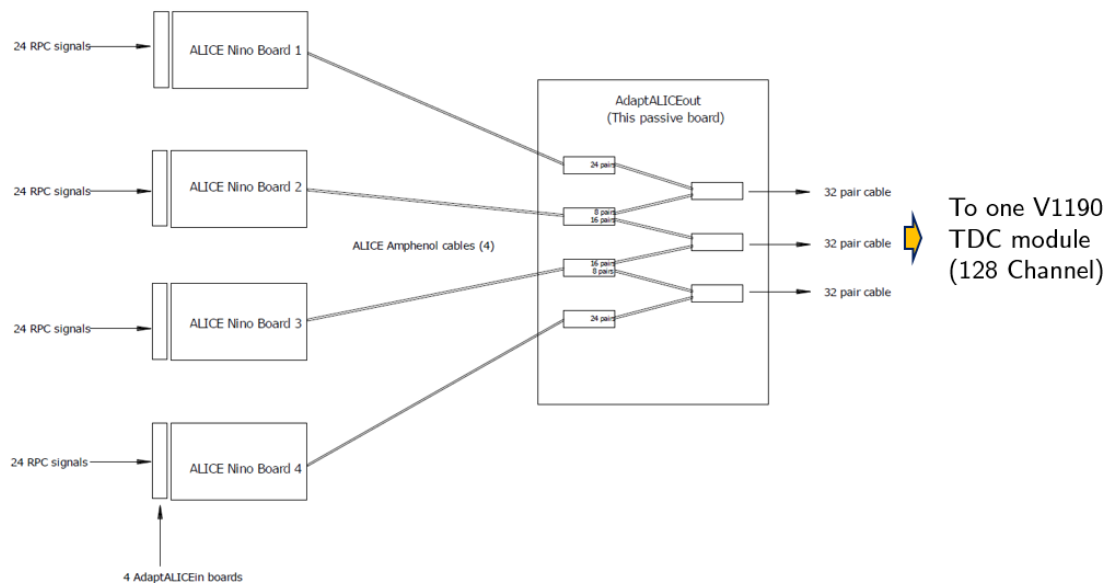


**Figure 5.38** Connections at 4to3 adapter board.

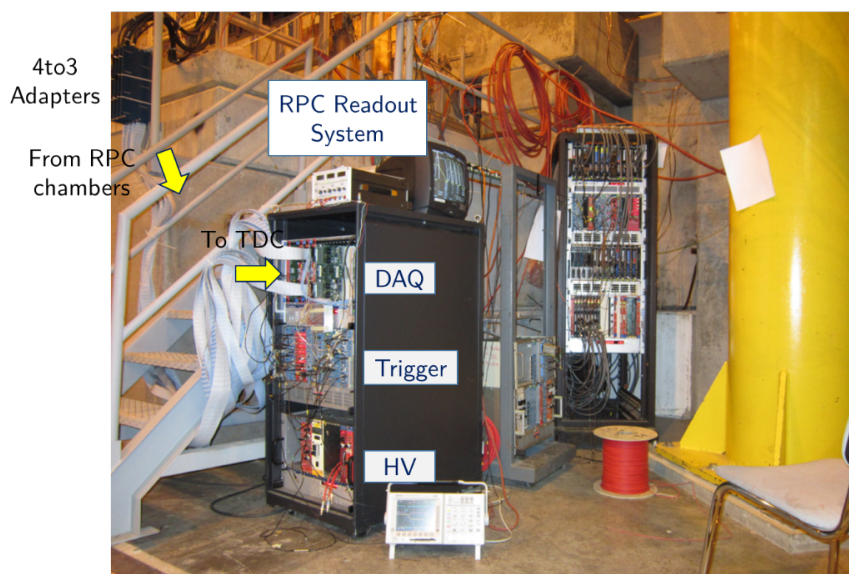


**Figure 5.39** A photo of the RPC readout system in the CERN SPS-H8 beam line.

The trigger logics are almost the same for three beam tests. The one for the first beam test are

shown in figure 5.40. Common triggers for RPC readout system as well as TGC and further added silicon detectors readout systems are all given by coincidences from large scintillators. However, special veto logics are implemented for the RPC readout system since the TDC reading actions will generate noises, also the TDC event buffer has a limited depth. The general logical flow is that after the initialization of the DAQ system, TDCs accept common triggers while they are counted down on a scalar. When the trigger counts reach a preset number, the counting scalar will send out a signal to block the common trigger and request the VME controller to execute read command so that data inside the TDC buffers will be read out. When the VME controller finished the reading action, signals are sent to three TDCs to clear their event buffers. In the meantime, signals are sent to scalar to reload the counting and enable the common trigger to TDCs. The various gate generators in the trigger logic system are used mainly for keeping the timing sequence of the trigger logic or converting high and low levels. The counting scalar is set to count down from 100 to 0 so that data from TDCs are read out every 100 events. This is to deal with data readout in burst environment, where a large number of hits come in a short time and TDC event buffers might be overflow before data are transmitted [159].

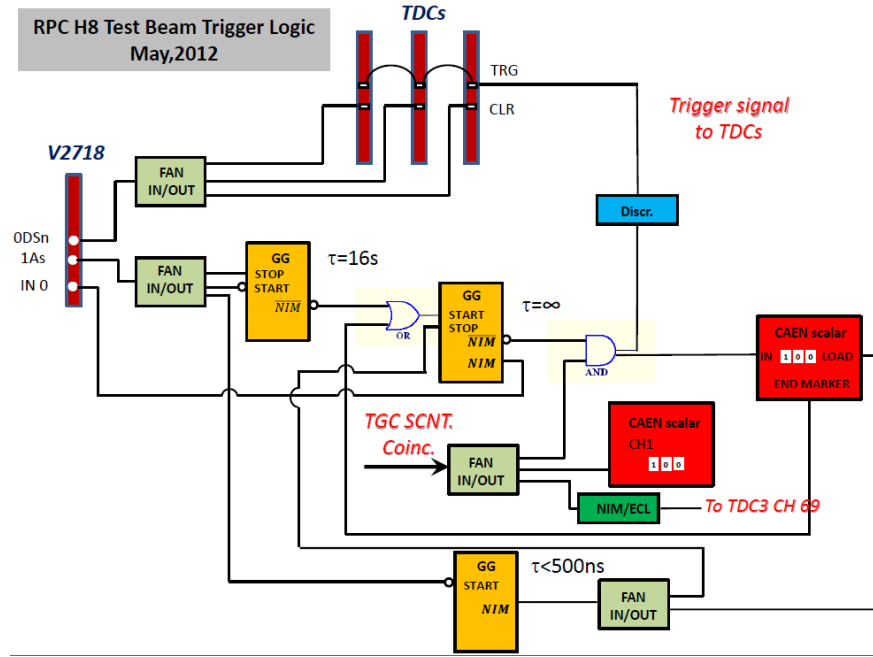


**Figure 5.40** Trigger logic for RPC beam test with NINO readout system.

#### 5.4.2.2 NINO ASIC

One of the core part of the readout system is the ultra-fast octal-channel NINO ASIC with pre-amplification and discrimination functions. The simplified block diagram of the chip is shown in figure 5.41. It utilizes differential signal processing throughout the entire chip to against the noise from the power supply and grounding. The input stage accepts differential signals from readout strips on two sides of a RPC chamber facing each other. Four stages of identical low gain, high bandwidth amplifiers in a cascade are followed. A pulse stretcher is implemented right before the LVDS output driver to stretch the pulse with a longer width. Since the output pulse width before stretcher stage is 2-7 ns, stretching is needed for use with some TDC chips, such as the HPTDC [160] chip in our beam test used TDC modules, in which only leading and trailing edges from pulses with widths greater than 6 ns can be registered. The final output stage of the NINO chip is an open-drain differential circuit which generates output signals with levels compatible to

LVDS standard.

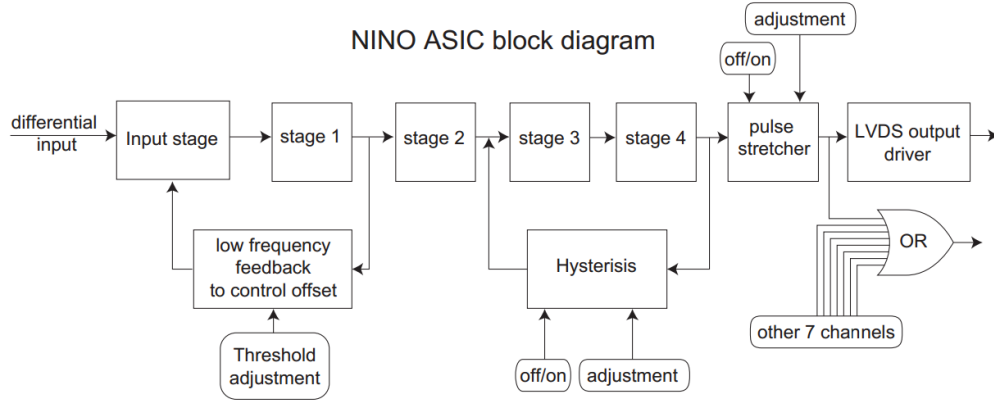


Fig. 3. Block diagram of the NINO ASIC.

**Figure 5.41** Block diagram of NINO ASIC chip [158].

A summary of the NINO ASIC specifications is shown in table 5.4. Input impedances of the chip can be adjusted between  $40\ \Omega$  and  $75\ \Omega$ . The peaking time is only around 1 ns and the front edge time jitter from the chip is less than 25 ps, giving a good performance for timing measurements. The threshold can be set from 10 fC to 100 fC and this best suits the relatively large signals from RPCs. The implementation of differential driving of output signals results in a good noise immunity. Output differential signals, with characteristic impedances of  $110\ \Omega$  are capable to be driven to a long distance before being digitized. In our application, output signals from NINO chips have been driven to more than 4 meters to the input of TDC modules.

A picture of the ALICE ToF NINO front-end board that has been used in our beam tests is shown in figure 5.42. There are three NINO chips per board accepting 24 channels of signals from the RPC strips. All signals from the RPC readout strips are AC coupled to the input of NINO chips through 1 nF capacitors. Meanwhile, strips are grounded through 1 M $\Omega$  resistors. For most of our applications, only negative signals from ground side strips are injected into the NINO chips. Positive input ports are capacitively coupled to the ground in this case.

Input/output type	differential
Input impedance	$40\ \Omega < Z_{in} < 75\ \Omega$
Noise level	ENC = 5000 e <sup>-</sup> rms
Peaking time	1 ns
Front-end time jitter	< 25 ns rms
Threshold	10-100 fC

**Table 5.4** Specifications for NINO ASIC.

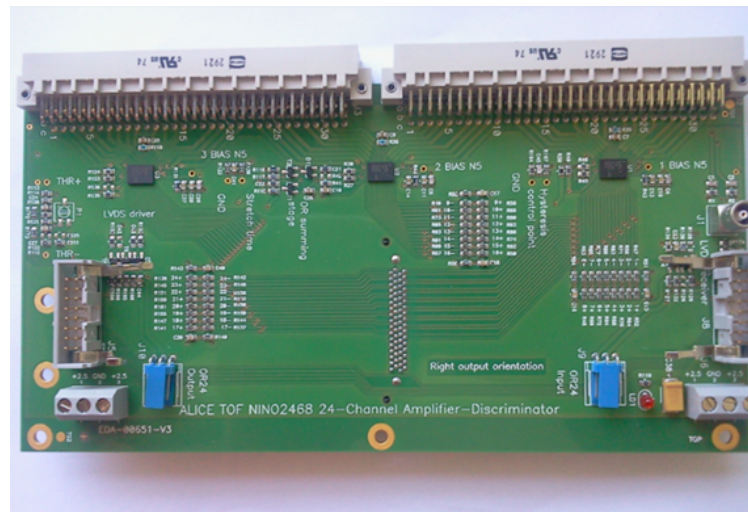


**Figure 5.42** A photo of an ALICE ToF NINO front-end board.

### 5.4.2.3 TDC and DAQ software

The 128-channel VME based TDC modules (CAEN v1190A) used for digitizing leading and trailing edges of discriminated signals from NINOs are implemented with four 32-channel HPTDC chips per module. The simplified block diagram of the HPTDC chip is shown in figure 5.43. In general the HPTDC has the same architecture as the AMT chip used in the MDT readout sys-

tem. The TDC chip can detect individual leading and trailing edges, therefore time-over-threshold (ToT) of NINO output signals could be measured to represent the charge from the readout strip. The HPTDC chip performs similar trigger matching functions as the AMT chip in order to find the correct hits associated with a trigger signal. However, HPTDCs in the v1190A module have higher digitization resolutions of 100 ps. This gives us the possibility to measure the sub-ns timing capability from thin-gap RPCs.

The data acquisition in the beam tests is performed using a LabVIEW based software, which is developed and adapted by Roman Zuyeuski from the DAQ software used for Extremely High Energy Event (EEE) project [161]. A snap shot of the DAQ software interface is shown in figure 5.44. Basically, it is composed of two sections: configuration and run control. The configuration section could set link parameters for the commutation among PC, VME controller and TDC modules. Trigger match parameters such as search window width, offset etc. could also be configured in this section. The second section simply sets all parameters related to running the system. All data are stored in binary formats for further analysis using ROOT software [162].

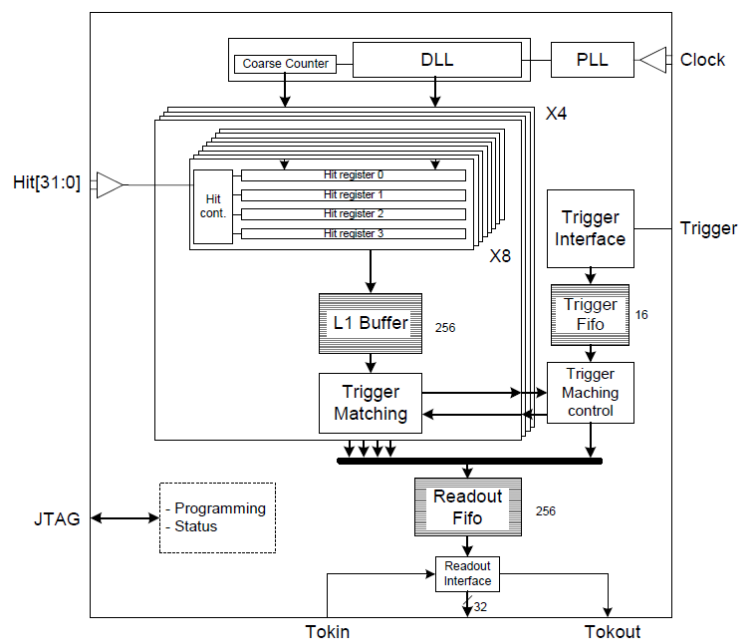


**Figure 5.43** Simplified Block Diagram of HPTDC chip.

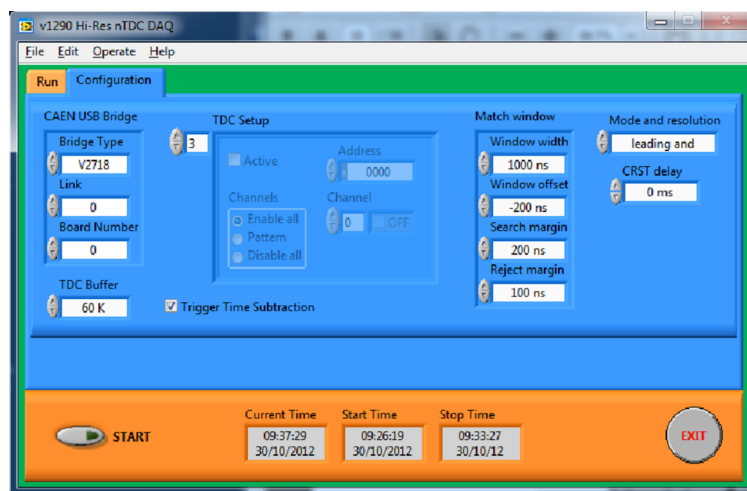


**Figure 5.44** A snapshot of the LabVIEW based data acquisition system interface.

### 5.4.3 Results

#### 5.4.3.1 Charge spectra, hit distributions and efficiencies

Typical charge spectra, represented by time-over-threshold, for two 1.15 mm gap glass RPCs and a 1 mm gap Bakelite RPC are shown in figure 5.45. Similar to the case when MDT electronics are used, deviations of charge spectra from Landau distribution is due to the non-linear representation of charge. Recalling that each TDC count refers to 0.1 ns, on average, discriminated signals from these thin-gap RPCs have a width of 120 ns at their nominal working condition. For some circumstance, when the voltage applied to the chamber is exceedingly high, a second peak or even multiple peaks could appear on the measured charge spectra. This is suspected to be the change of impedance when NINO is saturated by large signals [163]. However, a complete understanding is still missing. It is found that charge spectrum usually shows only one peak with the default NINO impedance setting, when detector is operated right at the knee of the efficiency plateau. Therefore, measurements of timing and spatial resolution are performed only in the condition that charge spectra are normal without multiple peaks.

Distributions of hits on both ends of strips when triggered by small scintillators and 12 cm × 12 cm sized large scintillators are shown in figure 5.46 and figure 5.47, respectively. Clean profiles of small round-shaped scintillator can be seen from both strip ends. Horizontal and vertical beam profiles are clearly revealed by two RPCs with orthogonal readout strips. The low counting region of a few mm shown in the middle of the plot on the right hand side of figure 5.47 is due to the inefficiency near the glass RPC spacer tube.

Local efficiencies measured in three types of RPCs as a function of high voltage in Freon:  $iC_4H_{10}:SF_6$  (94.7:5:0.3) mixture are shown in figure 5.48 for several NINO threshold settings. For 1.0 mm gap Bakelite RPC, lowering the threshold from 60 fC to 40 fC results in the knee of efficiency plateau moves 200 V to the lower end. Reducing the threshold from 40 fC to 30 fC does not alternate the efficiency curve. However, similar threshold change for 1.15 mm gap glass RPC

results in the shift of the plateau knee by 300 V. For the MRPC, it is applied with negative and positive high voltages of the same absolute potential on both sides of the chamber. Changes of efficiency curves with the threshold settings are substantial. The threshold change from 60 fC to 30 fC ends up with about 1 kV change of the plateau knee. In all cases, RPC chambers are able to be operated with efficiencies great than 97%.

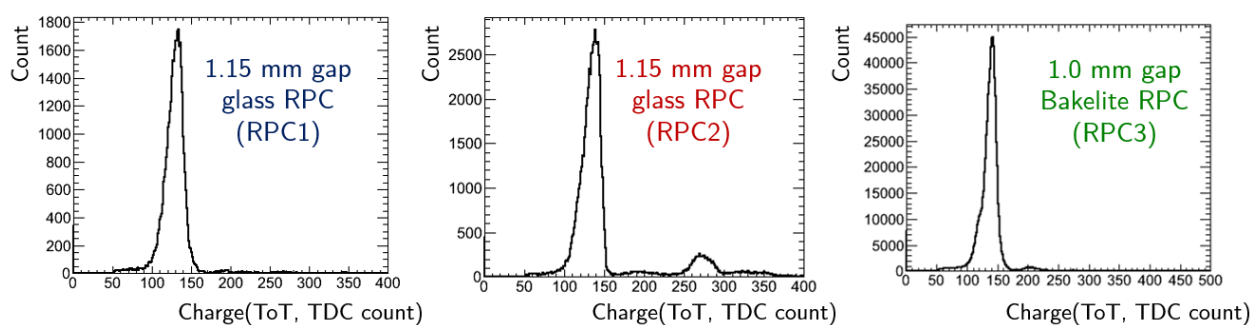


**Figure 5.45** Typical charge spectra recorded from 1.0 mm gap Bakelite RPC and 1.15 mm gap glass RPCs. Charge is represented by time-over-threshold (ToT).

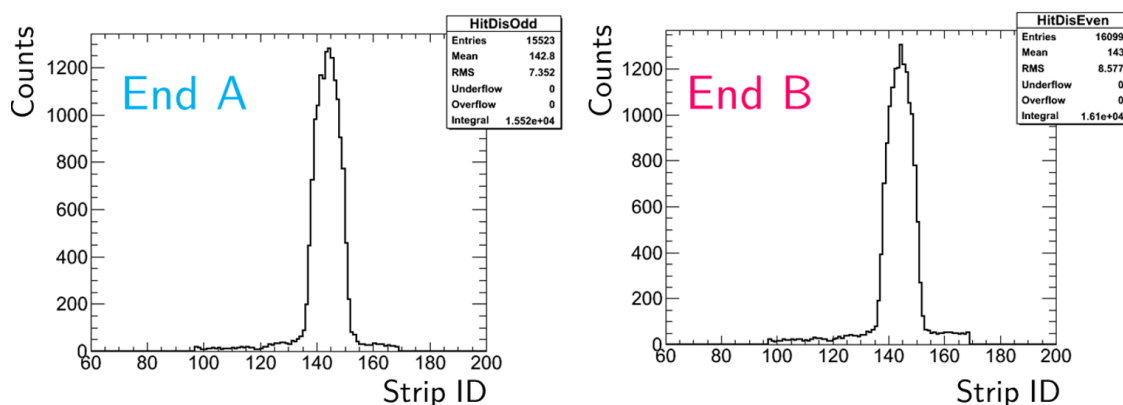


**Figure 5.46** Hit distributions on two opposite ends of strips triggered by small round-shaped scintillators.

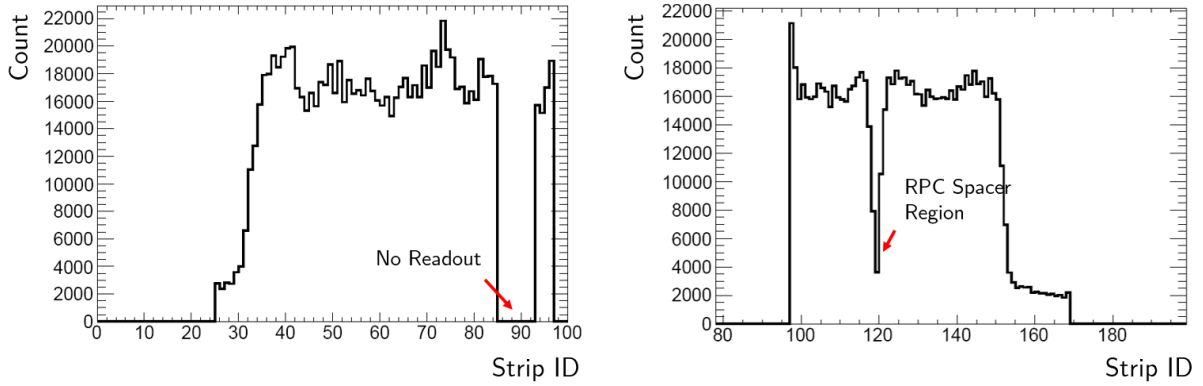


**Figure 5.47** Beam horizontal and vertical profiles recorded by 1.0 mm gap Bakelite RPC and 1.15 mm gap glass RPC, respectively.

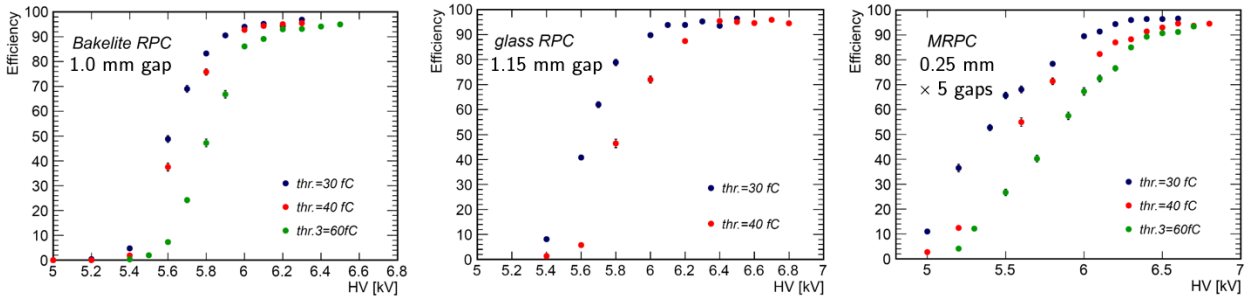


**Figure 5.48** Measured efficiencies for three different types of RPCs as a function of high voltage in Freon: $iC_4H_{10}$ : $SF_6$  (94.7:5:0.3) mixture. Actual voltage difference for MRPC is twice the number as shown in the plot.

#### 5.4.3.2 Time resolution

In order to measure time resolutions of these thin-gap RPCs, two types of detectors, small scintillators and a MRPC chamber, are used as references for timing measurement. The time jitter from two small scintillators (denoted as S1 and S2) is shown in figure 5.49. Neglecting the peak structure in the center of the timing distribution, a Gaussian fitting gives a time resolution of  $825 \pm 8$  ps. Assuming two scintillators have the same jitter, the time resolution for single scintillator is  $583 \pm 6$  ps. To further improve the accuracy of this timing “ruler”, the average time from two

scintillators is used. This results in a reference time uncertainty of  $413 \pm 4$  ps. Distributions of signal arrival time in 1.0 mm gap Bakelite RPC and 1.15 mm gap glass RPC, corrected by the average time from two scintillators, are shown on the left side plots of figure 5.50 and figure 5.51, respectively. The total jitter for 1.0 mm gap RPC is  $697 \pm 18$  ps. After subtracting 413 ps uncertainty from reference scintillators, the jitter is  $562 \pm 18$  ps. Similarly, the jitter for 1.15 mm gap glass RPC is derived to be  $574 \pm 15$  ps. After applying slew corrections, distributions of time jitter in two types of chambers are shown on the right hand side plots of figure 5.50 and figure 5.51. Time resolutions are determined to be  $453 \pm 15$  ps and  $510 \pm 13$  ps for 1.0 mm and 1.15 mm gap RPCs, respectively.

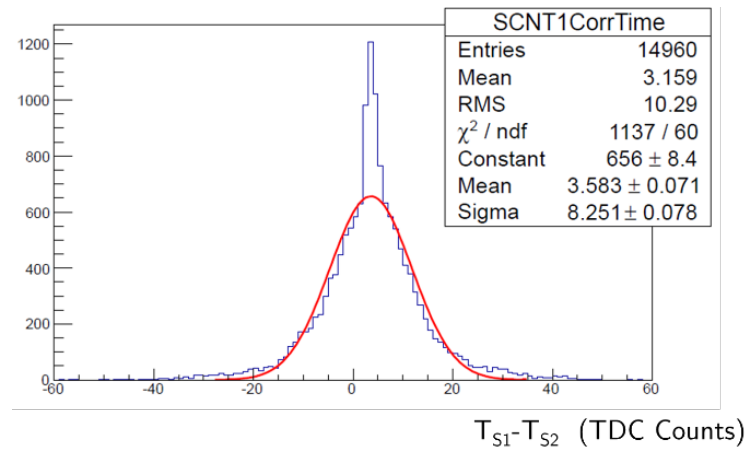


**Figure 5.49** Time jitter from two small scintillators.

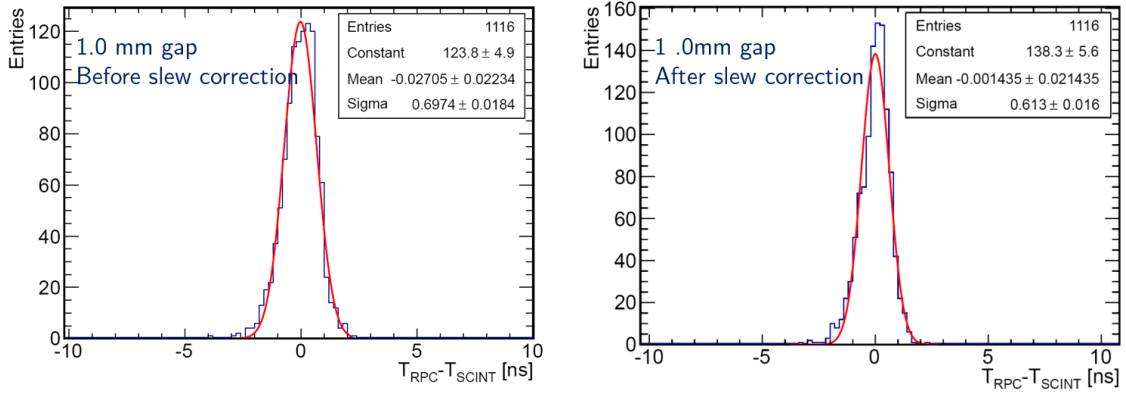


**Figure 5.50** Time jitters measured in 1.0 mm gap Bakelite RPC before (left) and after (right) slew correction. Results are convolved with 413 ps jitter from reference scintillators.

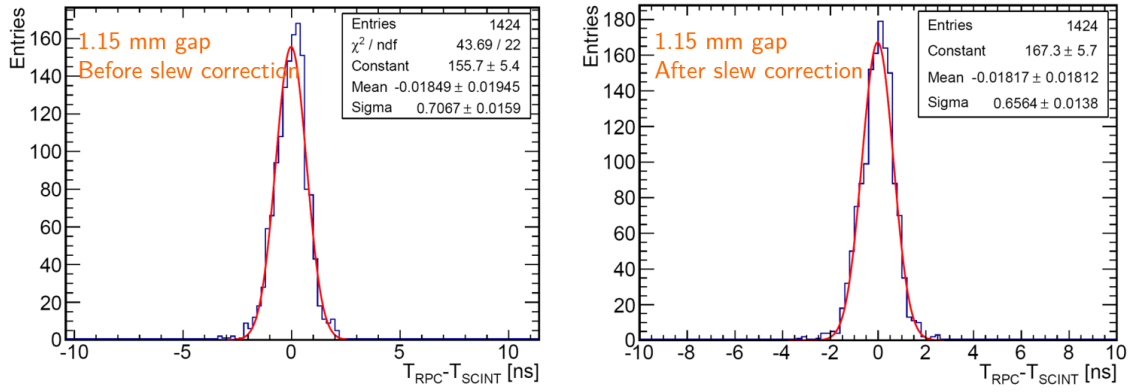


**Figure 5.51** Time jitters measured in 1.15 mm gap glass RPC before (left) and after (right) slew correction. Results are convolved with 413 ps jitter from reference scintillators.

Time resolutions from thin gap RPCs are also measured with the MRPC as a reference “ruler”. The obtained results without any slew correction are shown in figure 5.52. The time resolution for MRPC is not measured during the beam test and is conservatively assumed to be 100 ps, which is nominal performance before any correction applied. Subtracting this uncertainty from MRPC, time resolutions are about 521 ps and 529 ps for 1.0 mm gap Bakelite RPC and 1.15 mm gap glass RPC, respectively. Errors are not estimated because the uncertainty of the reference MRPC jitter

is actually unknown. This is roughly comparable with results obtained using small scintillators as references. The slight discrepancy measured with two references for 1.0 mm gap Bakelite RPC is likely due to the gap deformation. Nevertheless, the bottom line conclusion is that around 500 ps resolution can be achieved with RPCs of around 1 mm thick gaps. This performance is achieved without dedicated slew correction. It could be further improved at off-line after a number of corrections. For instance, by selecting minimum arrival times on certain strips thus eliminating fluctuations due to signal propagation to strips further from muon hit positions, the time jitter in a 1 mm gap RPC could be further reduced to less than 400 ps. An example timing distribution after such correction is shown in figure 5.53.

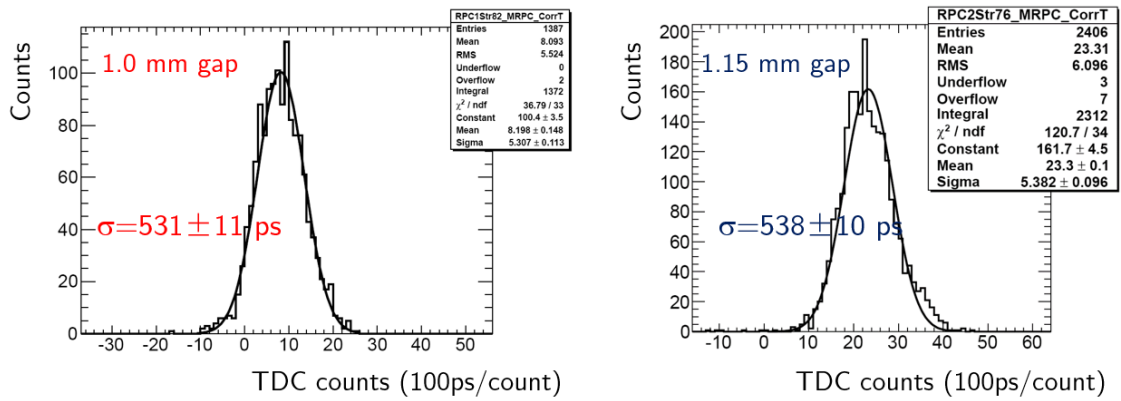


**Figure 5.52** Time jitters measured for 1.0 mm gap Bakelite RPC (left) and 1.15 mm gap glass RPC with the reference time from a MRPC.

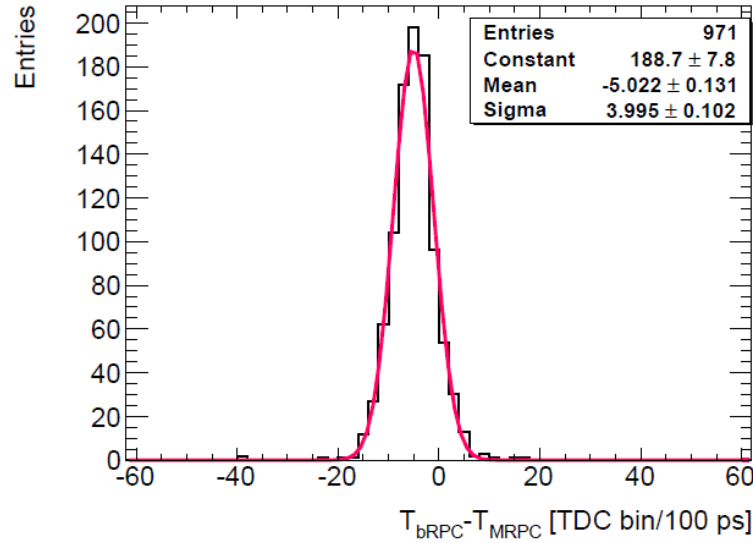


**Figure 5.53** Timing distribution of the 1.0 mm gap Bakelite RPC with only minimum signal arrival time of an event used for muon hit time determination.

#### 5.4.3.3 Mean-time measurements and spatial resolution along strips

Denoting signal arrival time at two ends of a strip as  $T_A$  and  $T_B$ , the mean-time which is the average signal arrival time from two ends is given by  $(T_A + T_B)/2$ . In principle this should be independent of muon hit positions since the total signal path is constant along the strip. The measured mean-time as a function of muon hit positions along a strip in the glass RPC is shown in figure 5.54. The predicted muon hit positions are obtained from the Bakelite RPC with orthogonal strips. It is found that there is no clear dependence of the mean-time with the hit position. Fluctuations of 14 ps are due to the TDC digitization accuracy. The mean-time from thin gap RPCs is expected to vary strip by strip and layer by layer, due to different strip and cable lengths, as well as circuit delays. However, these delays could be compensated by programmable delay circuits and after the compensation, the total time jitter of the system will dominantly be the intrinsic jitter of around 500 ps from the RPC. It is possible to do fast coincidences within 2-3 ns between RPC layers to reduce fake triggers from backgrounds in high level muon triggering.

The muon hit positions along a strip could be determined using the signal arrival time difference ( $\Delta t$ ) from two strip ends. Typical time difference as a function of muon hit position along the strip obtained in a 1.15 mm gap glass RPC is shown in figure 5.55. A linear function fitting indicates a signal propagation speed along the strip of 15 cm/ns, which is almost half of the speed of light in the vacuum. Signal propagation speeds are also measured for other readout strips and are found to be varying between 12 cm/ns to 16cm/ns.

Using the obtained signal propagation speed along horizontal readout strips of a glass RPC, residuals between muon hit positions determined by the Bakelite RPC with 1.27-mm-pitch vertical strips and those reconstructed using time differences are shown as the blue colored histogram in figure 5.56. A single Gaussian function fit gives a spatial resolution of 11 mm. Due to the use of fine pitch readout strips, there are usually 2-3 strips fired in a detected event. It is possible to reconstruct the hit position using

$$Y_{RPC} = \frac{1}{N} \sum_i^N \frac{T_{Ai} - T_{Bi}}{2} v_i \quad (5.4)$$

where  $N$  is cluster size of an event.  $T_{Ai}$ ,  $T_{Bi}$  and  $v_i$  are the signal arrival times at two ends of  $i^{th}$  strip and the signal propagation speed of  $i^{th}$  strip, respectively. The residual distribution using strip-averaging method is shown as the red colored histogram in figure 5.56. Resolution of 7.3 mm is obtained. Since reference positions given by 1.27-mm-pitch Bakelite RPC strips are less than 1 mm, these results reflect the localization capability along the strip using 100 ps resolution TDCs. Measurements are repeated for all three types of RPCs used in the beam tests. Results of the measured signal propagation speed as well as spatial resolutions obtained using single strip time differences are shown in figure 5.57. The results shown for the glass RPC is from another chamber different from the one shown in figure 5.56. It is found that around cm level spatial resolutions with 100 ps resolution TDCs are highly reproducible.

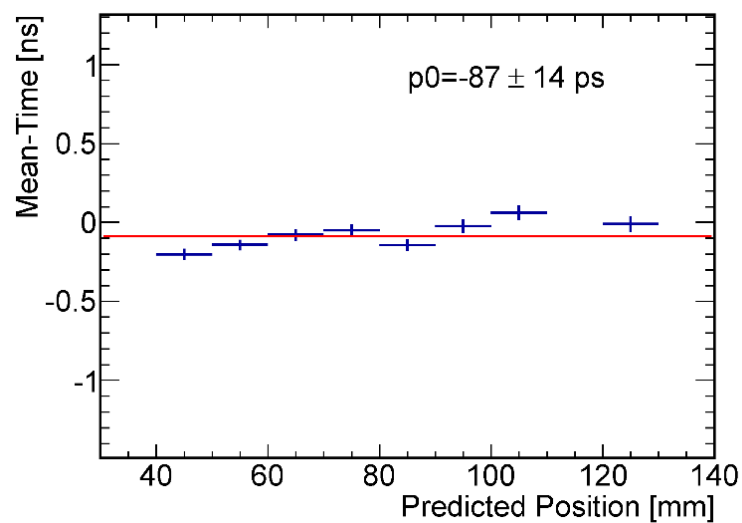


**Figure 5.54** Mean-time as a function of muon hit position along the strip. The mean-time has an arbitrary offset.

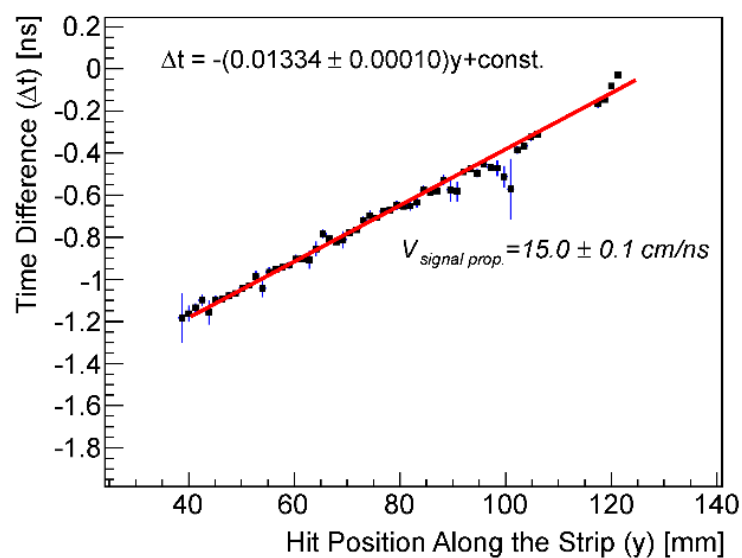


**Figure 5.55** Signal arrival time difference from two ends of a strip as a function of muon hit positions along the strip.

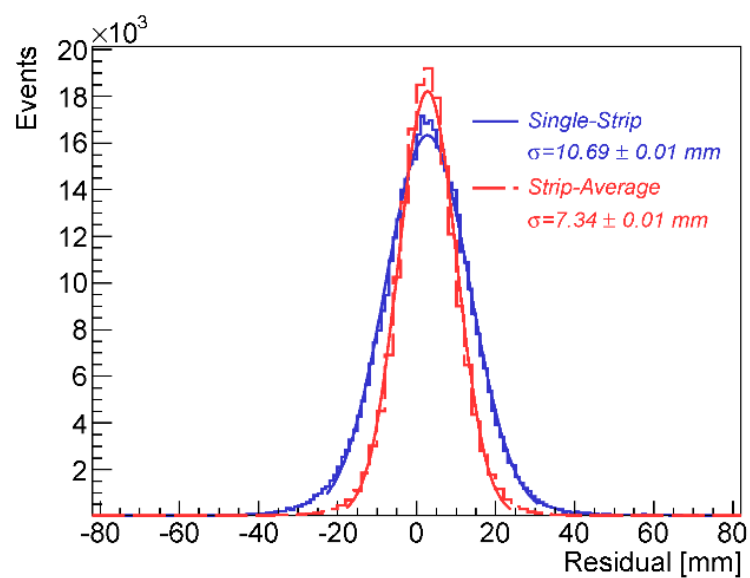


**Figure 5.56** Spatial resolution along the strip using signal arrival time information from two ends of a strip.

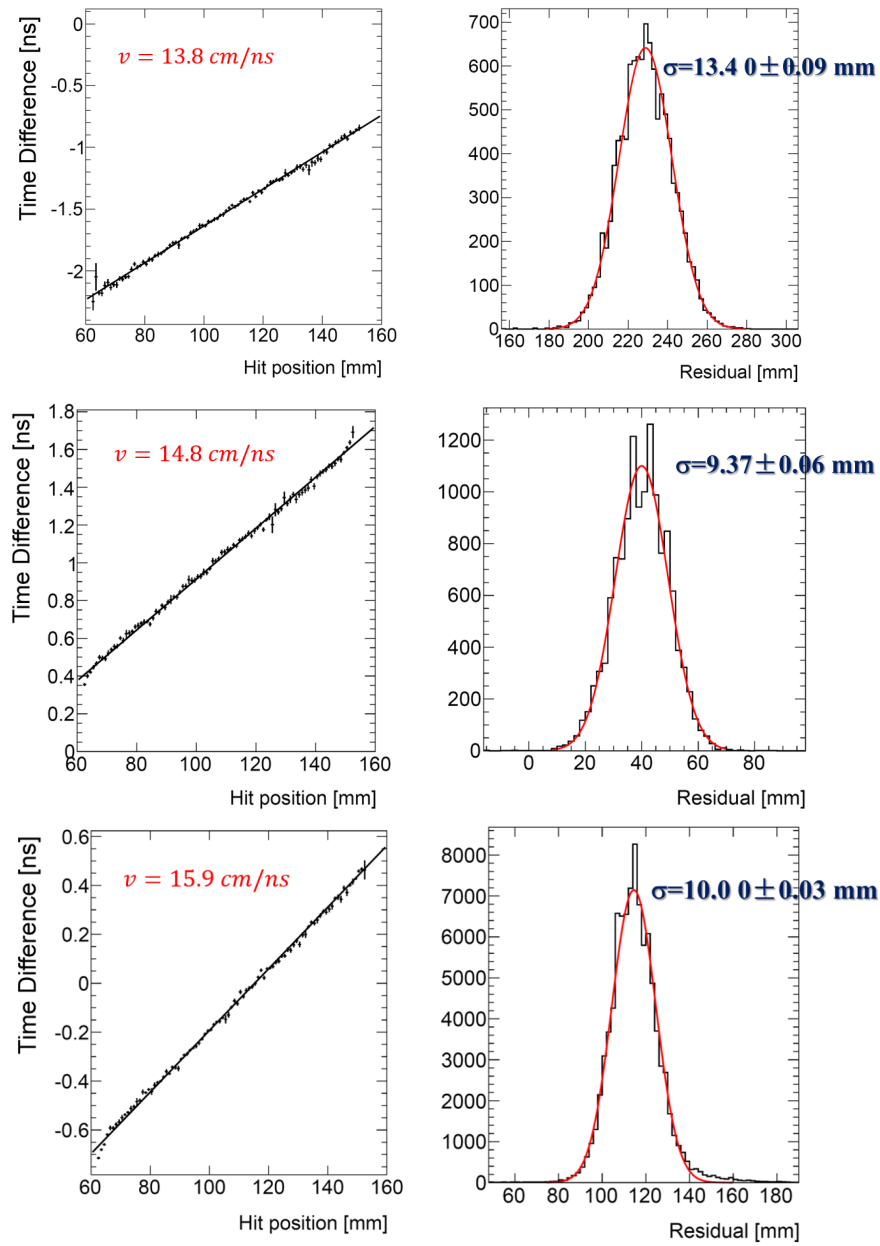


**Figure 5.57** Measured signal propagation speeds and spatial resolutions along strip directions in three types of RPCs. (From top to bottom: 1.0 mm gap Bakelite RPC, 1.15 mm gap glass RPC and  $0.25\text{mm} \times 5$  gaps MRPC)

#### 5.4.3.4 Precision coordinate spatial resolution

The precision coordinate spatial resolution of thin gap RPCs with NINO readout are measured with the reference from two silicon detectors. These silicon detectors are used for charged particle tracking and identification in AMS experiment [164]. Each silicon detector is called a ladder and has orthogonal readout strips on junction and ohmic sides with pitches of  $110\ \mu\text{m}$  and  $208\ \mu\text{m}$ , respectively. The spatial resolution for junction and ohmic sides are around  $10\ \mu\text{m}$  and  $30\ \mu\text{m}$ , respectively [165]. In order to check whether two silicon ladders are functioning normally, they are placed close to each other and residuals between two ladders for two orthogonal coordinates are measured. The results show that residuals have Gaussian sigma widths of less than  $70\ \mu\text{m}$ , mostly contributed by the beam divergence. Each silicon ladder is then placed close to one RPC to measure its spatial resolution. For the study of spatial resolution with NINO readout, RPCs are operated at the knee of their efficiency plateaus. On average, cluster size for the  $1.15\ \text{mm}$  glass RPC with  $1.27\text{-mm}$ -pitch strips is about 3 and is slightly larger for  $1.0\ \text{mm}$  gap Bakelite RPC due to a wider spread of charge in thicker electrodes. Muon hit positions are reconstructed using centroid with charge represented by ToT. Correlations of muon hit positions reconstructed in silicon ladders and Bakelite or glass RPCs are shown in figure 5.58. Periodic “fuzzy” structures every about  $1\ \text{mm}$  in the coordinate showing RPC constructed positions suggest substantially lower resolutions from these RPCs compared with the silicon detector. Residuals between muon hit positions reconstructed in silicon ladders and in the  $1.0\ \text{mm}$  gap Bakelite RPC or the  $1.15\ \text{mm}$  gap glass RPC are shown in figure 5.59. The obtained resolution for the Bakelite and glass RPCs are  $297\ \mu\text{m}$  and  $294\ \mu\text{m}$ , respectively. Since the contribution from the silicon detector is negligible, uncertainties are dominantly from RPCs. Besides beam divergence of around  $0.7\ \text{mrad}$  and misalignment due to only single points rather than precise tracks from one silicon ladder are used as references for each RPC, results are significantly worse than those obtained from RPC with MDT readout electronics. This is most likely due to the less ideal charge representation in NINO. As can be seen from

figure 5.60, ToTs which encode charges are in very similar amount for several readout strips in a cluster. Typically, ToTs from different strips fall within 1.5 ns. Considering that TDCs have resolutions of 100 ps, there are only 15 effective digits can be used for charge weighting. The inaccuracy in charge representation and the low charge digitization resolution are believed to be the reasons for worse resolution. It is concluded that in this particular case, electronics rather than the chamber are the limiting factors to reach higher localization precision.

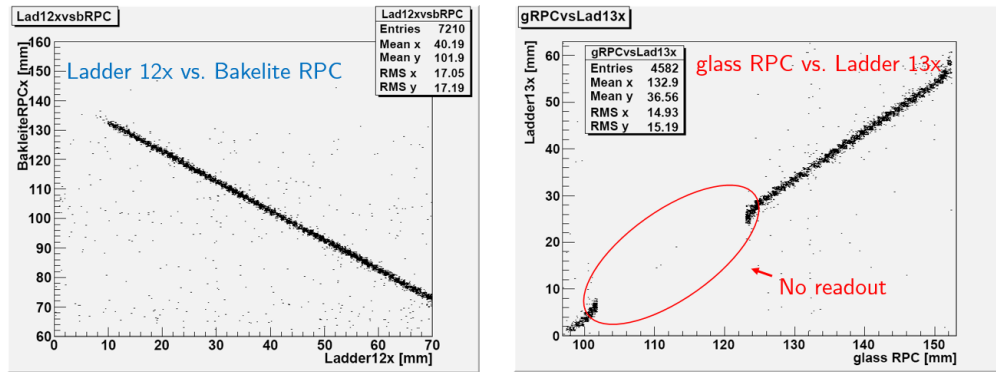


**Figure 5.58** Correlation between muon hit positions reconstructed in a silicon ladder and in a 1.0 mm gap Bakelite RPC (left) or a 1.15 mm gap glass RPC (right).

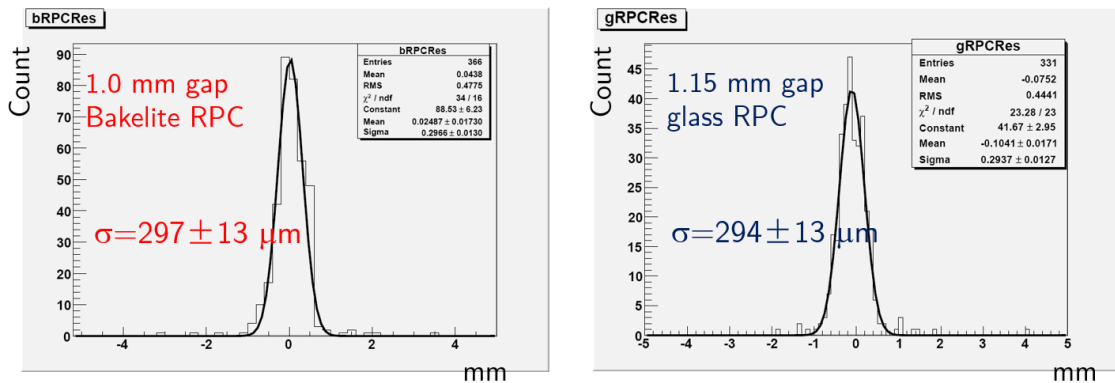


**Figure 5.59** Residuals between muon hit positions reconstructed in a silicon ladder and in a 1.0 mm gap Bakelite RPC (left) or a 1.15 mm gap glass RPC (right).

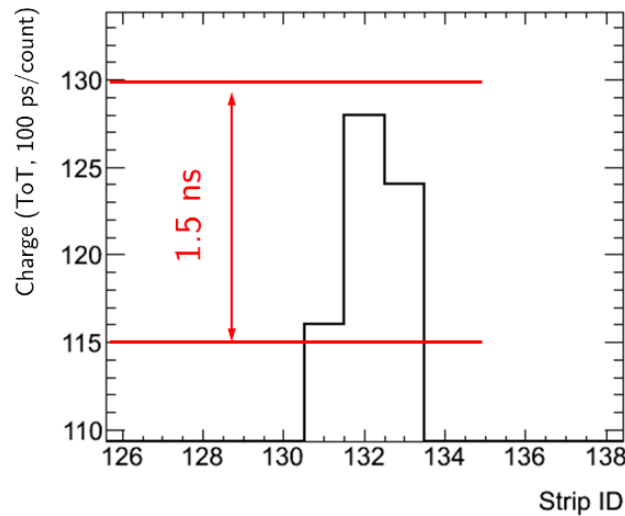


**Figure 5.60** Charge measured by NINO and encoded in TOT on three RPC readout strips for a typical muon detection event.

## 5.5 Rate capability measurements

### 5.5.1 Introduction

The present RPCs implemented in major collider experiments for muon triggering are designed with a rate capability of about  $1 \text{ kHz/cm}^2$  [166, 167] using  $10^{10}$ - $10^{11} \text{ } \Omega\cdot\text{cm}$  Bakelite plates. As present and future collider experiments are planned or will be designed to run at higher and higher luminosity, trigger detectors are required to operate at unprecedented high radiation backgrounds. For instance, trigger detectors at the innermost station of the ATLAS muon spectrometer forward direction need to work at a rate up to  $15 \text{ kHz/cm}^2$  after LHC upgrades its luminosity to  $7 \times 10^{34} \text{ cm}^{-2}\cdot\text{s}^{-1}$  in 2018.

The limiting factor for RPCs to operate at high rates is the high voltage drop across the gas gap due to current flow through high resistivity plates. The decrease of the effective electric field in the gas gap results in reduction of avalanche signal amplitudes and thus efficiency. Increasing the

high voltage is of no help because higher current will flow through the plates and the electric field remains low as long as the chamber is exposed to high rate environment.

In order to develop high rate RPCs, it is desirable to understand parameters that related to the voltage drop. The voltage drop across the gas gap  $\Delta V$  is determined by

$$\Delta V = RQ\rho h \quad (5.5)$$

where  $R$  is the detected particle rate in the RPC given in units of  $\text{Hz}/\text{cm}^2$ .  $\rho$  and  $h$  are the bulk resistivity and resistive plates total thickness given in units of  $\Omega\cdot\text{cm}$  and  $\text{cm}$ , respectively.  $Q$  is the total charge produced per detected particle. It should be noted that though the prompt charge can be quickly collected, ionic charges, slowing moving inside the gas gap, continue to induce charge current on the resistive plates and the induced currents need to flow through the resistive plates to the ground.

As can be seen from equation 5.5, methods to reduce the voltage drop include lowering resistive plate bulk resistivity or thickness and reducing the amount of charge delivered per particle detection. It is non-trivial to develop low bulk resistivity resistive plates. Resistivity stability and uniformity for plates with bulk resistivity slightly less than  $10^9 \Omega\cdot\text{cm}$  are extremely hard to maintain. Moreover, the spark protectiveness for RPCs with very low resistivity plates has not been proved. However, developing low resistivity plates with bulk resistivity around  $10^9 \Omega\cdot\text{cm}$  is still a possible way for improving the RPC rate capability as plates with similar resistivity have been used in the ALICE di-muon spectrometer [168]. The reduction of charge means limiting the avalanche development within the gas gap. It could be realized with small gas gap configuration. To maintain full efficiency for RPCs with smaller signals, on one hand, low-noise sensitive amplifiers need to be implemented. On the other hand, multiple-gap structures could be employed to add small signals from individual thin gas gaps. In order to explore the possibility to operate RPC at few  $\text{kHz}/\text{cm}^2$  or higher rate, a bi-gap RPC made from standard Bakelite plates used for ATLAS barrel RPCs is tested at CERN Gamma Irradiation Facility (GIF). Setup and brief results are reported.

### 5.5.2 Setup and results

The structure of the small bi-gap RPC tested is shown in figure 5.61. Three 2 mm thick Bakelite plates with bulk resistivity of around  $2 \times 10^{10} \Omega\cdot\text{cm}$  are separated by two 1 mm thick gas gaps. The chamber has a total active area of  $18 \text{ mm} \times 18 \text{ mm}$ . High voltage is applied at the outer surface of one Bakelite plate while the other side is grounded. Induced signals are readout by the signal pick-up board with a centimeter wide strips connected to sensitive low-noise front end amplifiers [169]. Amplified signals are further discriminated for counting.

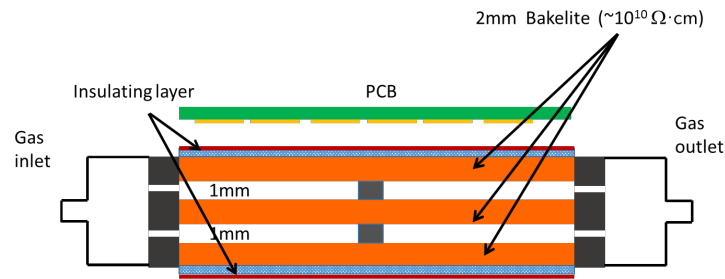


**Figure 5.61** Cross-sectional view of the bi-gap RPC.

The setup of the bi-gap RPC rate capability test in front of a  $^{137}\text{Cs}$  source with a radioactivity of about 740 GBq is shown in figure 5.62. The source mainly produces high flux 662 keV photons. However, low energy photons due to the Compton scattering are also present [170]. Three filtering lead plates of various thicknesses are installed in front of the source and they could be used to reduce the radiation rate. Photon rates could also be adjusted by placing the detector under test at different distances to the source. The bi-gap RPC is inclined to face the source opening. Four large scintillator paddles with two above the RPC (denoted as S1 and S2) and two below the chamber (denoted as S3 and S4) are shielded by lead blocks and placed vertically to trigger cosmic rays. A smaller scintillator (denoted as S5) with an area smaller than the bi-gap RPC active area is also employed and placed close the bi-gap RPC. Basic parameters of the RPC monitored during the tests are current inside the chamber, single count rate and the efficiency. The current inside the

chamber is monitored by the HV power supply module with current resolutions of around  $1 \mu\text{A}$ . The single counting rate is measured by counting total number of discriminated signals from the bi-gap RPC in a 10 ns time window. Since the noise rate of the chamber is on the order of few  $\text{Hz}/\text{cm}^2$  at nominal working point, the counting gives the number of detected photons in most cases. The logic for determining the bi-gap RPC efficiency is given by

$$\frac{(S1\&S2) \& S5 \& \text{RPC}_{\text{Bigap}}}{(S1\&S2) \& S5} \quad (5.6)$$

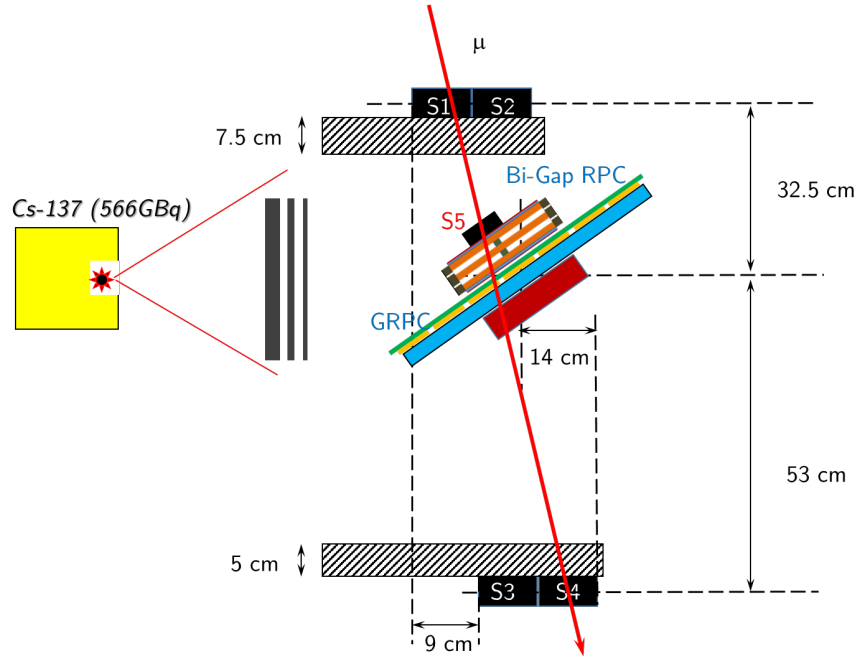


**Figure 5.62** Rate capability test setup in front of the intense  $^{137}\text{Cs}$  source at CERN GIF.

The measured efficiency and total counts as a function of applied voltage on the bi-gap RPC are shown in figure 5.63. Maximum efficiency of 95% is obtained when the chamber is not exposed to the source. 5% inefficiency is due to the spacers inside the chamber active area as well as geometric acceptance of the trigger setup. Compare with the measurement without source exposure, the bi-gap chamber reaches the same maximum efficiency when the radioactive source is fully opened at

a voltage of about 350 V higher. The total detected photon rate when the bi-gap RPC is operated at the knee of the efficiency plateau has exceeded  $18 \text{ kHz/cm}^2$ .

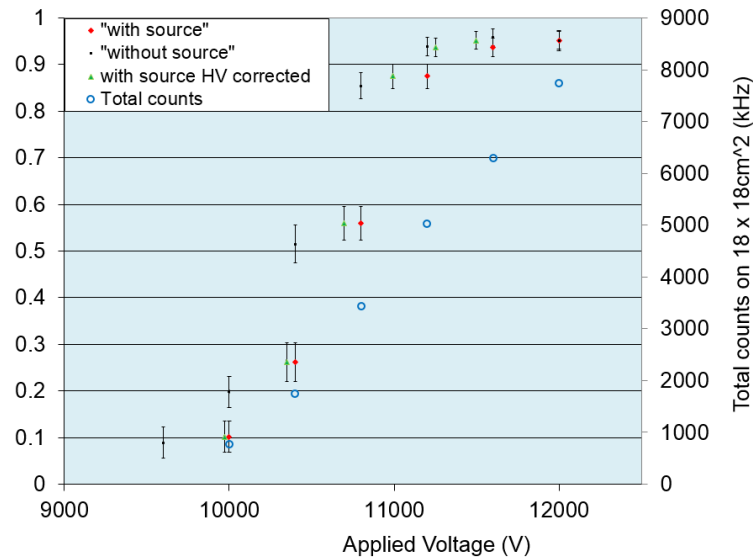


**Figure 5.63** Efficiency times acceptance and total counts as a function of applied voltage on the bi-gap RPC.

The current flowing through the chamber as a function of applied voltage is shown in figure 5.64. With the help of measured counting rates, the delivered charge per detected photon can be calculated using the current information. Calculated charge per count as a function of applied voltage is also shown in figure 5.64. The high charge per count at low applied voltage is due to the inefficiency from the RPC strip readout thus an underestimation of the photon counting rates. The measure results show that only 2 pC charge per count is delivered to the chamber at full efficiency. Considering that the charge per count for present ATLAS RPCs is about 30 pC, the rate capability compared with the present ATLAS RPC could be increased by a factor of 15 for the bi-gap chamber. This suggests that a rate capability of about  $15 \text{ kHz/cm}^2$  is achievable, which is consistent with our measurements shown in figure 5.64. It should also be stressed that reducing the charge production inside the chamber is also precious to the mitigation of chamber aging.

With all these measured results, we conclude that RPCs even with  $10^{10} \Omega \cdot \text{cm}$  Bakelite plates are capable to be operated with full efficiency at a detected photon rate of greater than  $10 \text{ kHz/cm}^2$ .

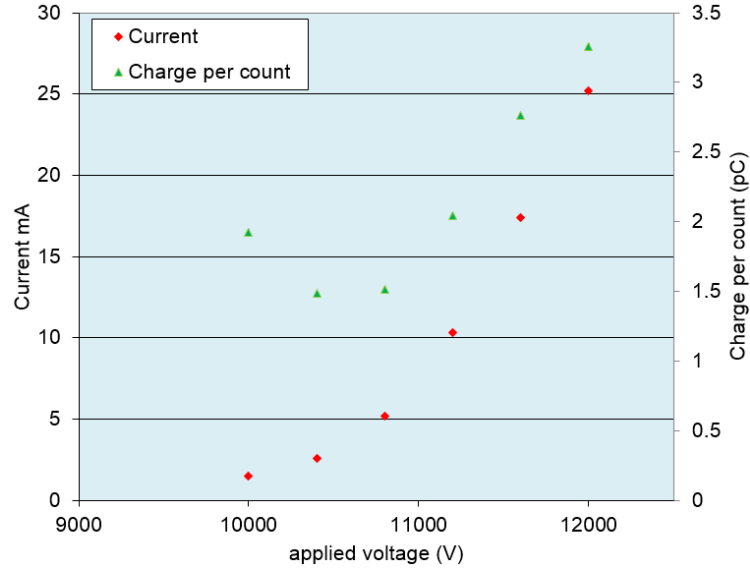


**Figure 5.64** Delivered charge per count, current as a function of applied voltage on the bi-gap RPC.

## 5.6 Summary

In this chapter, new studies on fast timing and high precision tracking based on RPCs are reported. Several beam tests as well as rate capability tests are carried out at CERN H8 muon beam line and Gamma Irradiation Facility in order to study the timing capability, spatial resolution and rate capabilities of thin gap RPCs constructed with around 1 mm gas gaps. Time resolutions from these RPCs are found to be about 500 ps. The spatial resolutions of less  $200 \mu\text{m}$  using charge centroid and less than  $300 \mu\text{m}$  only using on-line timing information are obtained from a meter long RPC with 1.27-mm-pitch strips read out by the ATLAS MDT readout electronics. It should be stressed that the offline spatial resolution using charge centroid in our beam test is limited by the non-linear representation of the charge by the MDT readout electronics and the ultimate spatial resolution

should be much better than that presented in this chapter. This could be verified from another RPC performance study performed by the ATLAS RPC community that spatial resolution of  $130\ \mu\text{m}$  is obtained with 8-mm-pitch strips [171].

A RPC readout scheme with readout from both strip ends is explored for fast triggering. The mean-time from two ends of a strip is verified to be independent of the hit position along the strip and the readout system jitter with such scheme is dominantly determined by the jitter from the chamber, which is only a few hundreds of picoseconds. This would allow one to do fast coincidence within a few nanoseconds between contiguous RPC layers to effectively reject uncorrelated backgrounds. The time difference from two ends of a strip could be used to determine the hit position along the strip. With 100 ps resolution TDCs, around 1 cm spatial resolutions along the strip length direction are obtained in a number of RPCs.

The rate capability of a bi-gap Bakelite RPC is measured with an intense  $^{137}\text{Cs}$  source. Results show that RPC made with  $10^{10}\ \Omega\cdot\text{cm}$  Bakelite plates is fully efficient at a detected photon rate of more than  $15\ \text{kHz}/\text{cm}^2$ . The reduction in gas gap compared with conventional RPC with 2 mm gas gaps results in a reduction of delivered charge per count by about 15 times at an operational condition with full efficiency. This is the key for operating RPCs at high rate environment.

With the thin ( $\sim 1\ \text{mm}$ ) gap design plus readout from both ends of fine pitched strips, it is possible to create ( $\text{sub-ns} \times \text{sub-mm} \times \text{cm}$ ) trigger logic cells using RPCs. The fine granularity in space, precision tracking capability at the on-line level, along with excellent timing capability can be very powerful to remove backgrounds as much and as soon as possible for high level muon triggering in a harsh and high rate environment, as well as improving high momentum muon selectivity.

# Chapter 6

## Small-strip Thin Gap Chamber

### 6.1 Introduction

The LHC will be upgraded in several phases with the goal of obtaining an instantaneous luminosity of  $5\text{--}7 \times 10^{34} \text{ cm}^{-2}\cdot\text{s}^{-1}$  at a center of mass energy of 14 TeV and integrated luminosity of 3000  $\text{fb}^{-1}$ . The ATLAS detector will also be upgraded in stages to cope with higher collision rates and radiation background. The ATLAS muon Small Wheel detectors cover the pseudo-rapidity range of  $1.3 < |\eta| < 2.7$  and provide forward muon precision tracking. Level-1 (L1) muon triggering is based on track segments in the TGC chambers of the Big Wheels detector. To reduce the problem with high muon trigger rates and degraded muon tracking at high luminosity, ATLAS plans to replace the present Small Wheel detectors with the New Small Wheels (NSW). The NSW will employ Micromegas detectors (MM) for precision tracking and small-strip, Thin Gap Multi-Wire Chambers (sTGC) for primary L1 triggering. The proposed NSW will be composed of two four-layer MM detector sandwiched between two four-layer sTGC quadruplets.

A schematic view of the sTGC structure is shown in figure 6.1. It is similar to the present TGC in ATLAS [172]. The distance between neighboring wires is 1.8 mm and the distance between the

wire and the cathode plane is 1.4 mm. There are a few changes compared with ATLAS TGCs:

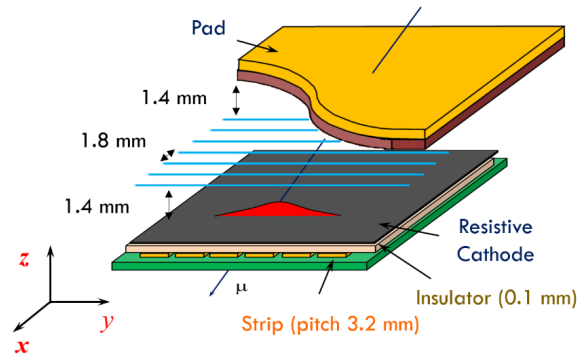


**Figure 6.1** The structure of the ATLAS NSW sTGC.

- **Lower cathode surface resistivity:** To reduce charge accumulations on the cathode when chamber operates at high rate, cathode surface resistivity is changed from  $M\Omega/\square$  to a few tens of  $k\Omega/\square$ .
- **Smaller cathode-readout plane distance:** The distance is reduced to 0.1 mm to increase the capacitive coupling between the cathode and readout plane.
- **Smaller strip pitch:** The pitch is reduced to 3.2 mm to improve the measurement of charge centroid position by charge interpolation.
- **Pad segmentation on one side of the cathodes:** Pads are used for fast pattern recognition of tracks to select strips for read out.

The sTGC detectors are required to identify each bunch crossing and to measure the muon trajectories with an angular resolution of less than 1 mrad for  $1.3 < |\eta| < 2.7$  at L1. The present TGC detector has wires along the  $\phi$  direction, the ATLAS NSW sTGC detector will have fine-pitch strips along the  $\phi$  direction and wires approximately aligned along the azimuthal direction, as illustrated in figure 6.2. An additional requirement is the ability to operate in a high neutron and

photon radiation environment with hit rates up to a few tens of  $\text{kHz}/\text{cm}^2$  in the innermost region of the NSW. The sTGCs will be operated at lower voltages than TGCs to minimize aging effects. Moreover, the chambers are exposed to stray magnetic fields from the nearby end-cap and barrel toroids and hence must tolerate modest magnetic fields without a loss in performance.

We have carried out various simulation studies of the characteristics and performance of the sTGC detector. This Chapter is organized as follows: Section 6.2 presents the simulation of the electric field inside the chamber that determines the electron drift behavior and the detector timing performance; Section 6.3 presents studies of the ionization from charged particles in the gas gap using the HEED program as well as results on electron transportation properties; Section 6.4 discusses avalanche and charge production processes simulated using the Garfield package together with the Magboltz program; Section 6.5 reports detailed studies on timing performance; Section 6.6 show the simulation of charge spread and modeling of sharing among readout strips.

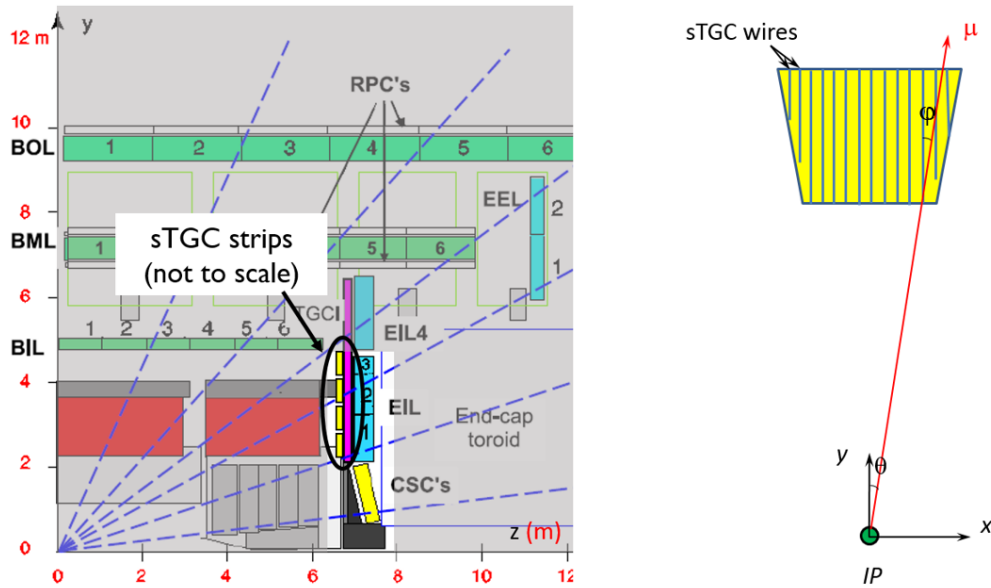


**Figure 6.2** The orientation of ATLAS NSW sTGC readout strips as viewed in the  $y$ - $z$  plane (left) and orientation of sTGC wires as viewed towards the  $z$  direction (right).

## 6.2 Electric field simulation

The simulation uses a coordinate system where  $x$  is along the strips,  $y$  is along the wires and  $z$  defines the chamber depth. The electric field inside the chamber is simulated using both the Ansoft Maxwell software based on a finite element method (FEM), and the neBEM package [173] using the nearly exact boundary element method. Both packages are able to perform three-dimensional simulation of electric field with arbitrary geometries. An example of the simulated normal component of the electric field in the  $y$ - $z$  plane with a high voltage of 3.0 kV is shown on the left hand side of figure 6.3. Results from two different methods are consistent and agree well with the two-dimensional analytical calculation in Garfield. The discontinuity of the simulated electric field near the wire surface using the FEM method is clearly visible. This is mainly due to the interpolation between element boundaries and the inadequate field approximation using low-order polynomials.

Normal components of the electric field in the  $y$ - $z$  plane, simulated by using the neBEM package with high voltages from 2.0 kV to 3.0 kV using a step size of 0.2 kV, are illustrated on the right hand side of figure 6.3. A field strength of a few kV/cm up to a few hundred kV/cm is seen for most regions. The electric field map in the  $y$ - $z$  plane for a typical operating high voltage of 2.85 kV is shown in figure 6.4 for half of the wire-to-wire region. The electric field is more than 1 kV/cm in 97% of the gas volume, with the weakest field only in a small region in the middle of the two neighboring wires.

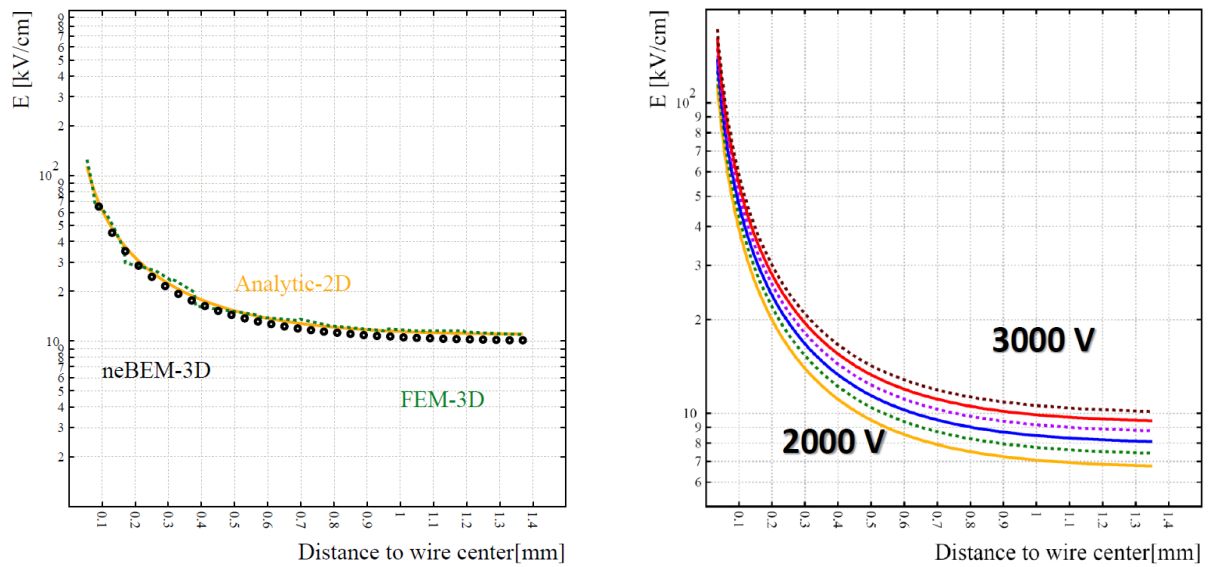


**Figure 6.3** Comparison of the sTGC electric field in the y-z plane simulated using different methods (left) and at different high voltages using the neBEM package (right).

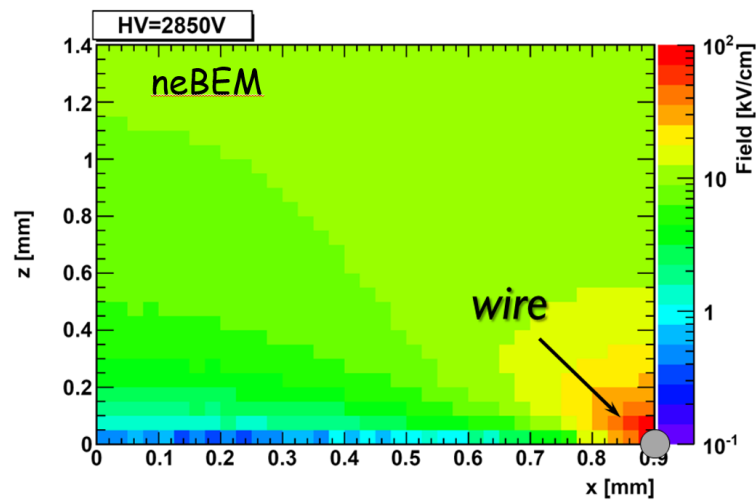


**Figure 6.4** A field map in the y-z plane for half wire pitch region at a applied voltage of 2.85 kV.

## 6.3 Ionization and electron transportation

### 6.3.1 Electron-gas molecular interaction and ionization

The operational gas for sTGC is a mixture of  $\text{CO}_2$  and n-pentane ( $\text{C}_5\text{H}_{12}$ ) with a ratio of 55:45 at atmospheric pressure. The electron energy distribution at different electric fields and electron interaction cross-sections in this gas mixture are shown in figure 6.5. With a typical field strength of a few kV/cm throughout most of the chamber volume, the average electron energy is less than 1 eV. The dominant process is elastic scattering and the contributions from the attachment process are negligible. The mean electron energy increases to several eV when the electron is within few tens of microns of wire surface where very high electric field is present. The attachment process occurring in that region will primarily affect the overall avalanche size rather than the timing performance of the detector, which is mainly determined by the uncertainty on the arrival time of the earliest arrival cluster.

Ionization statistics of MIPs in a sTGC chamber with 2.8 mm gas gap operated with  $\text{CO}_2$ :n-pentane (55:45) has been simulated with the HEED program. Distributions electron-ion pairs per cluster and total number of electrons produced in the gap by 180 GeV/c muons are shown in figure 6.6. On average, 22.8 clusters could be produced and each cluster has about 2 electron-ion pairs.

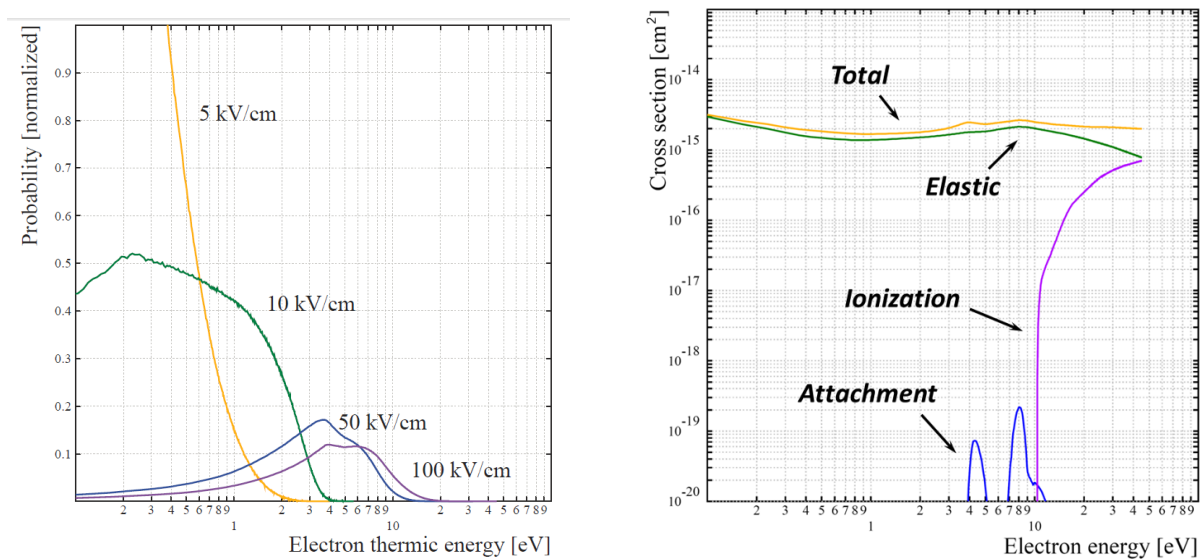


**Figure 6.5** Electron energy distributions (left) and various for electron-gas molecule interaction cross-sections (right) in a CO<sub>2</sub>:n-pentane (55:45) mixture.

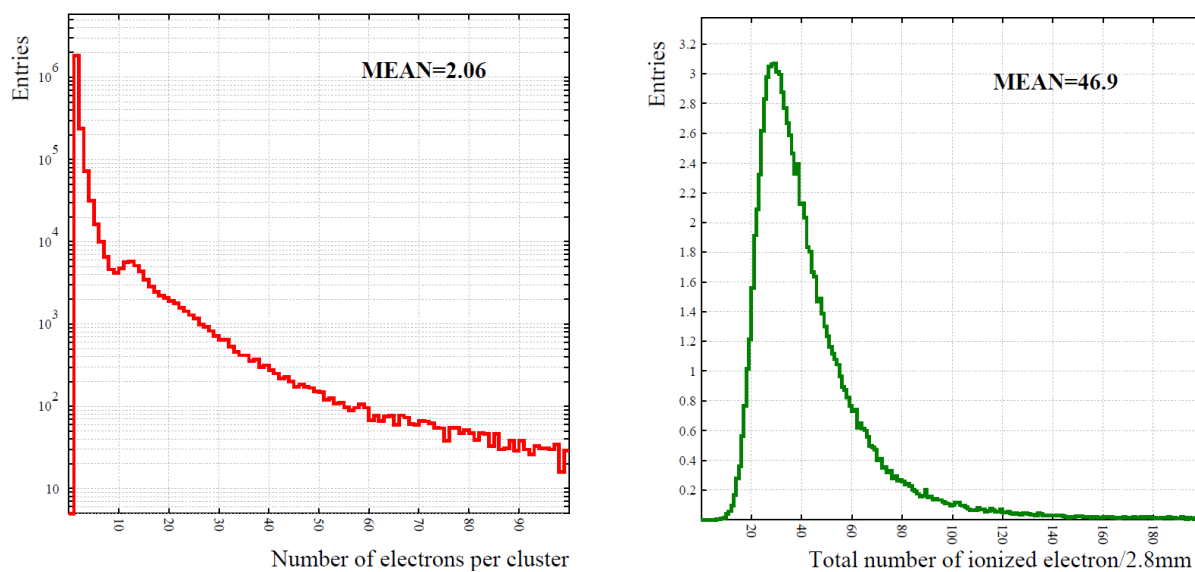


**Figure 6.6** Number of electron-ion pairs per ionization cluster (left) and total number of ionizations produced in a 2.8 mm gap (right) by 180 GeV/c muons. Simulation is performed for CO<sub>2</sub>: n-pentane (55:45) mixture.

### 6.3.2 Electron transportation

Ionized electrons drifting along the electric field towards the electrodes have frequent collisions with gas atoms and molecules and diffuse laterally and longitudinally with respect to the electric field direction. In addition, their motions will be affected by the external magnetic field. This is explicitly discussed in section 3.4.1. The simulated electron drift velocities in several CO<sub>2</sub> and n-pentane mixtures at atmospheric pressure are shown in figure 6.7. The n-pentane is liquid at room temperature and the gas blends are obtained by bubbling CO<sub>2</sub> through the liquid and mixing with saturated n-pentane vapor. The temperatures shown in the plot are what needed for obtaining various mixtures at atmospheric pressure. Additionally, the simulated drift velocity as a function of the electric field in a CO<sub>2</sub>:n-pentane (55:45) gas mixture is compared with the experimental data as reported in [174]. Good agreement is found up to 10 kV/cm.

In the presence of a magnetic field orthogonal to the electric field direction, the drift velocity is modified due to changes in mean collision time. Moreover, electron drift path, related to the Lorentz angle, could be elongated and the timing performance of the sTGC detector might be influenced. To understand the impact of magnetic field on the electron drift behavior, the electron drift velocity and the Lorentz angle in CO<sub>2</sub>:n-pentane (55:45) mixture with a magnetic field orthogonal to the electric field is simulated using Magboltz and results are shown in figure 6.8 (a) and figure 6.8 (b), respectively. The modification of the drift velocity with a magnetic field up to 1 T is found to be negligible. The Lorentz angles are relatively small and less than 7 ° for B-field less than 1 T. The predicted results are similar to those reported in [175–177], which show that gas mixtures with a significant amount of CO<sub>2</sub> generally have small Lorentz angles.

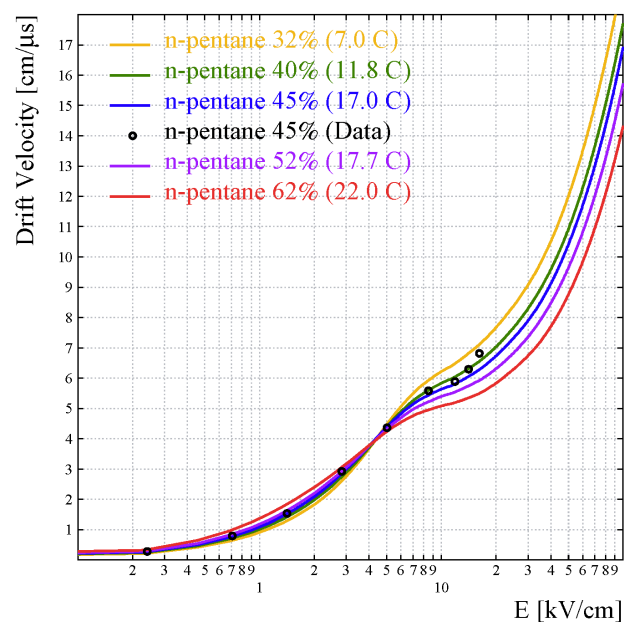
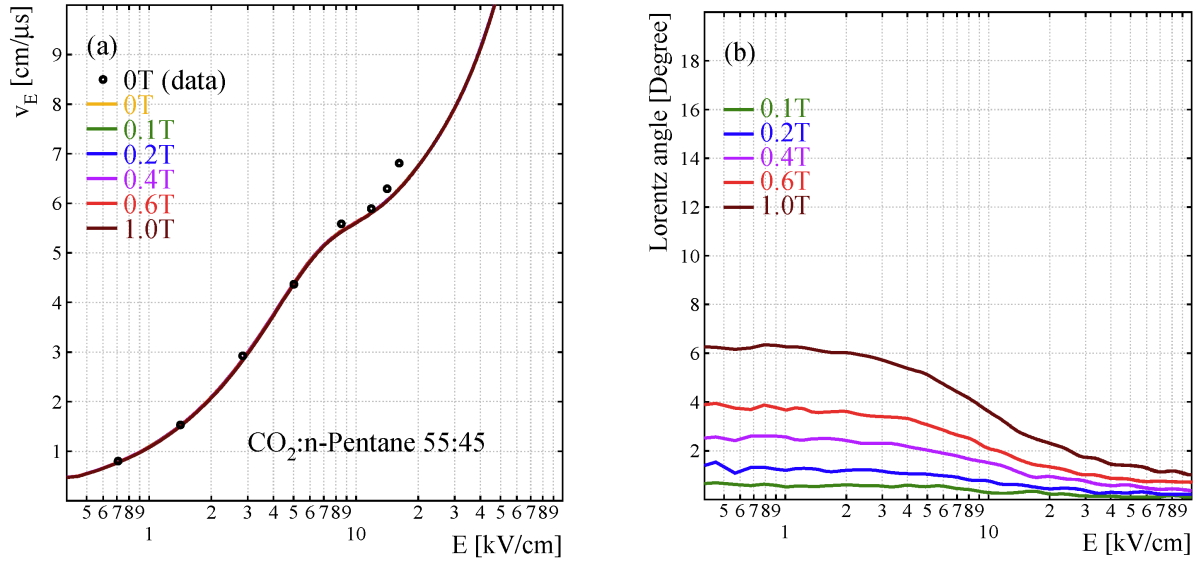


**Figure 6.7** Dependence of the electron drift velocity on the electric field in several CO<sub>2</sub> and n-pentane mixtures.



f

**Figure 6.8** Simulated electron drift velocity (a) and Lorentz angle (b) as a function of the electric field in  $\text{CO}_2$ :n-pentane (55:45) mixture with the presence of an orthogonal magnetic field.

The electron diffusion, the electron mean track deviation in any direction due to the scattering with gas molecules, over a distance  $S$  is given by:

$$\sigma_{L,T} = D_{L,T} \sqrt{S} \quad (6.1)$$

where  $D_L$  and  $D_T$  are longitudinal and transverse diffusion coefficients, respectively. Transverse diffusion of electrons in the plane orthogonal to the electric field vectors determines the lateral spread of the charge cloud and longitudinal diffusion of electrons along the electric field direction determines the fluctuation of electron arrival time on wires. Both coefficients as functions of the electric field and orthogonal magnetic field have been simulated and are shown in figure 6.9. The longitudinal and transverse diffusion of electrons over a drift length of 1.4 mm in sTGCs are expected to be less than  $40 \mu\text{m}$ .

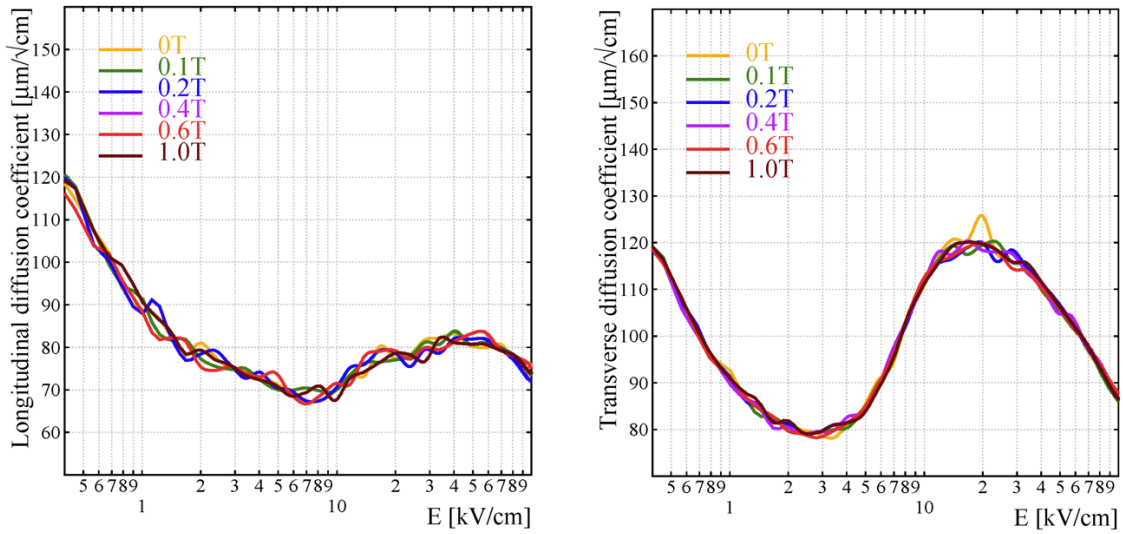


**Figure 6.9** Simulated dependence of transverse (a) and longitudinal (b) diffusion coefficients with electric field in  $\text{CO}_2$ :n-pentane (55:45).

## 6.4 Charge production

### 6.4.1 The electron avalanche and its fluctuation

The electron avalanche process in sTGCs is simulated using Garfield with a microscopic method, which traces electron interactions at the molecular level. An avalanche initiated by a single electron at 2.4 kV is illustrated in figure 6.10. Avalanches are usually developed within a few tens of microns of wire surface where strong electric field is present. The avalanche process is a stochastic process and fluctuations in the strong and non-uniform electric fields, as the case in sTGC, is discussed in section 3.5.2. In general, gas amplification fluctuations in sTGC could be described by the Polya distribution.

As mentioned at the beginning of this section, the microscopic method is used in Garfield and relies on both ionizing and non-ionizing inelastic collision cross-sections provided by Magboltz to

simulate the avalanche process. The simulated number of electrons produced by single electron avalanches at 2.5 kV and 2.7 kV in CO<sub>2</sub>:n-pentane (55:45) mixture are shown in figure 6.11. Fits of the simulated distributions with Polya functions result in relative width parameters ( $f$ ) of 0.71 and 0.59, respectively. It should be pointed out that CO<sub>2</sub>:n-pentane is a Penning mixture in which CO<sub>2</sub> molecules excited to certain levels could transfer energy to n-pentane molecules and give rise to ionization. The recuperation of part of the excitation energy leaves less room for fluctuations [178] and therefore reduces the relative width [179]. The simulation here thus gives upper limits of the gas gain fluctuations.

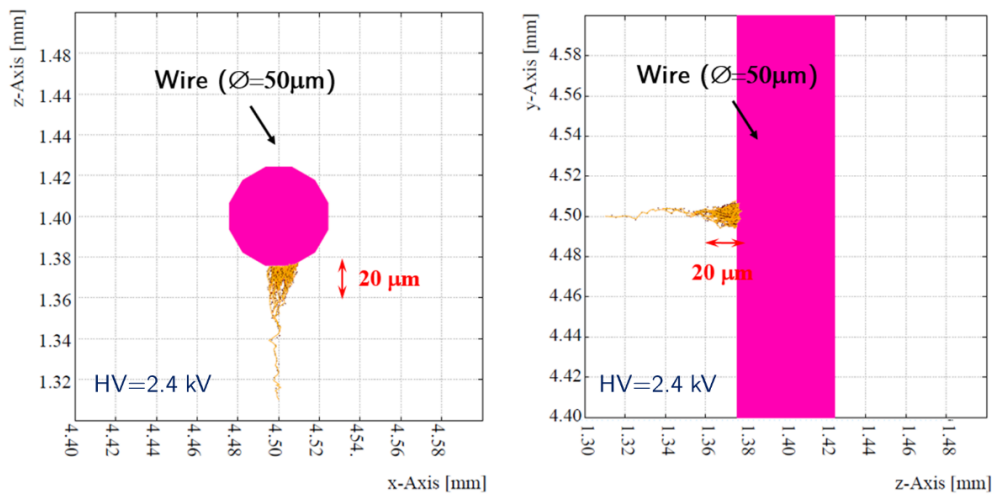


**Figure 6.10** Single electron avalanche profile viewed from the wire cross-section (left) and along the wire (right). Places where ionizations and excitations occur are marked with magenta and brown dots, respectively.

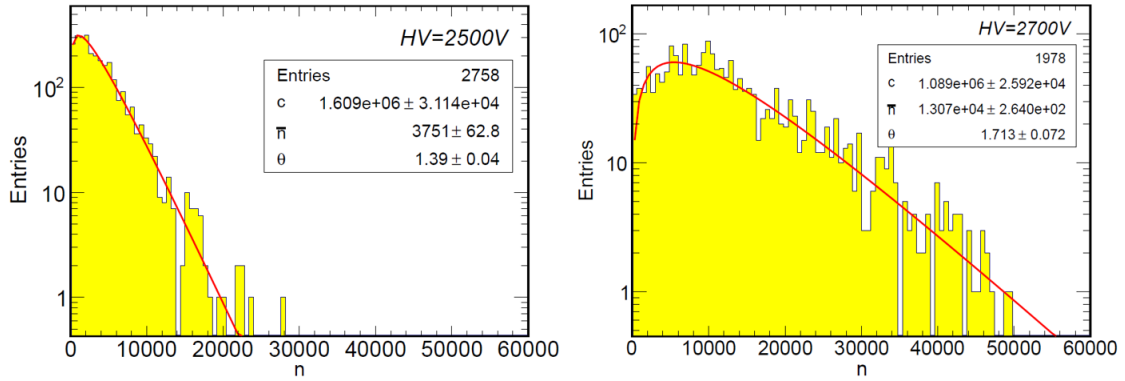


**Figure 6.11** Simulated fluctuations of single electron avalanches in sTGC with applied voltage of 2.5 kV (left) and 2.7 kV (right). Gas mixture used in the simulation is CO<sub>2</sub>:n-pentane (55:45).

### 6.4.2 Induced charge component and charge collection

By importing a three-dimensional electric field into Garfield, the induced current signals can be simulated. One typical example of the induced signals on a group of wires is shown in figure 6.12 for the first 30 ns after the passage of a muon. The spikes are electron induced currents from individual clusters and the long tails are due to ions. The integration of current over time gives the amount of charge collected.

According to Ramo's theorem, the induced current on electrodes is related to the electron and ion velocities. While the electron drift velocity is very well known from experiments, no knowledge on ion mobility in CO<sub>2</sub>:n-pentane (55:45) is available. Since only the mobility of the CO<sub>2</sub><sup>+</sup> ions in CO<sub>2</sub> gas was reported (close to  $1.1 \text{ cm}^2 \cdot \text{V}^{-1} \text{ s}^{-1}$ ) under an electric field of a few kV/cm [86] and the mobility is usually smaller in larger molecular-weight gases, the ion mobility in the simulation is varied from  $1.2 \text{ cm}^2 \cdot \text{V}^{-1} \text{ s}^{-1}$  to lower values. Due to the lack of an explicit model describing the dependence on the electric field, the ion mobility is assumed to be constant over the entire ion drift path in the simulation. The gas gain is fixed to  $10^5$  so that the total

number of electrons produced in the gas gap per event is the product of the fixed gain and the number of ionized electron, which can be retrieved from the Garfield terminal output. The Garfield program can automatically compute an avalanche profile based on the integral of the first Townsend coefficient over the electron drift path. Although this leads to an actual amplification slightly different to the specified one, rough correction of the gain is applied when calculating the total number of produced electrons.

The simulated fraction of integrated charge as a function of the integration gate width starting immediately after the muon incidence is shown in figure 6.13 for several assumed ion mobilities. The integrated charge is found to be proportional to the logarithm of the gate width. Results are also compared with measurements reported in [180] by normalizing the charge measured at a 100 ns gate width with the simulated charge collection ratio and scaling other measurements accordingly. Fairly good agreement is obtained with the assumption of an ion-mobility of  $0.4 \text{ cm cm}^2 \cdot \text{V}^{-1} \text{ s}^{-1}$ . This implies a very low  $\text{CO}_2^+$  mobility in the n-pentane gas if it is the main positive charge carrier.

In the simulation, it is also possible to look at the induced charges from electrons and ions separately. Results are shown in figure 6.14. After the passage of a muon, electron-induced signals can be collected within 25 ns while ion-induced signals arrive over a few tens of  $\mu\text{s}$ . About 60% of the charge collected in the first 25 ns is found to be induced by fast-moving electrons.

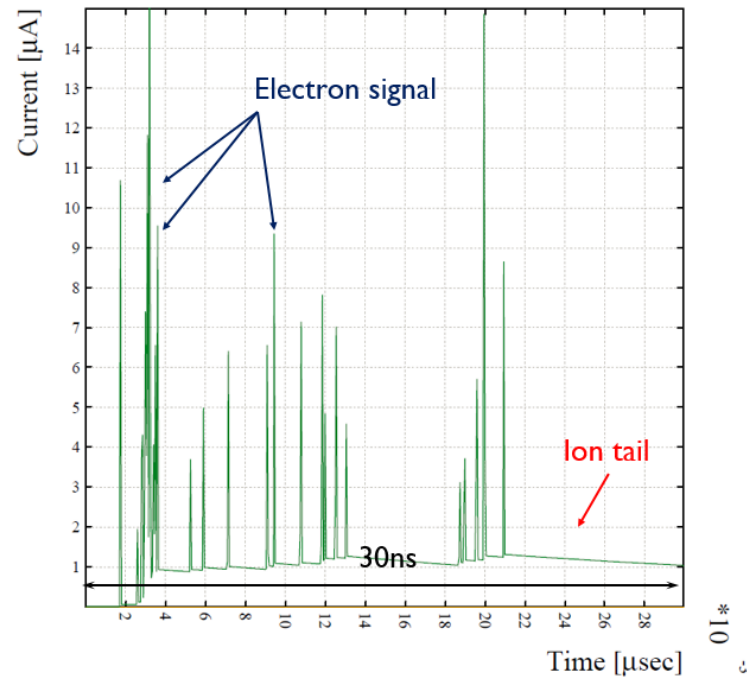


**Figure 6.12** Typical induced current signal on the wires.

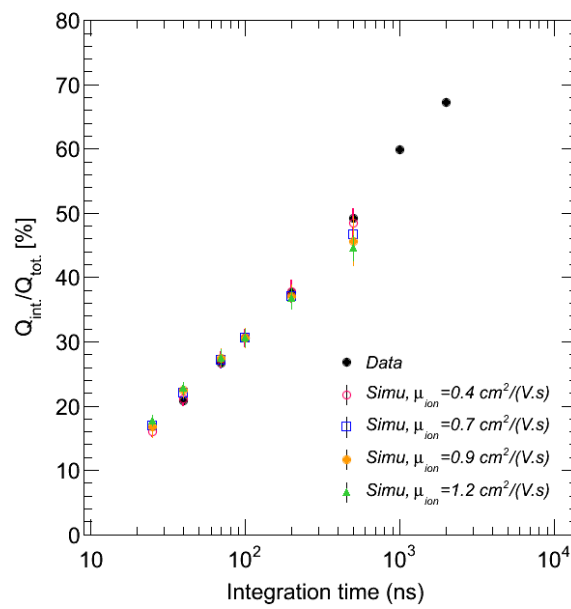


**Figure 6.13** Fraction of electron plus ion induced charge vs. integration time.

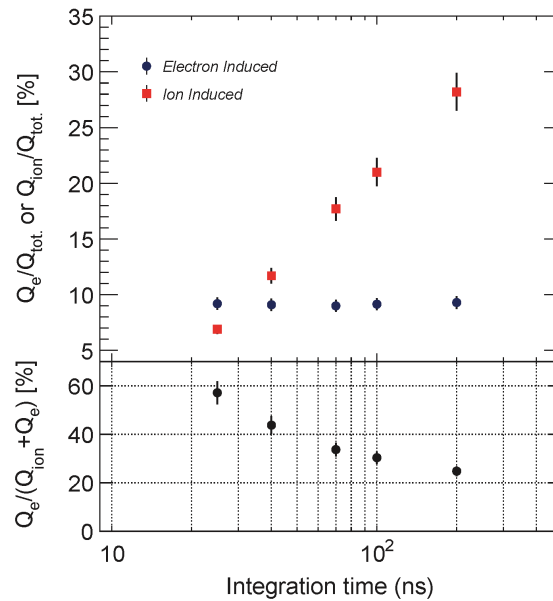


**Figure 6.14** Break-up fraction of electron and ion induced charge vs. time (upper); Electron induced charge component for the given time windows (lower).

### 6.4.3 Gas gain

Using the dependence of the charge collection on the integration gate width, the measured charge presented in [180], with the  $^{106}\text{Rh}$   $\beta$ -rays irradiation of a chamber with the same geometry as a sTGC, can be converted to obtain the gas gain. The ionization produced inside the chamber by  $^{106}\text{Rh}$   $\beta$ -rays with a maximum energy of 3.54 MeV is simulated in Garfield and the average number of electron-ion pairs created in a 2.8 mm gas gap is found to be 31. The usage of a gate width of 300 ns results in a collection of about 42% of the total charge created in the avalanche. The simulated gas gains can be extracted from Polya function fits of the single electron avalanche distributions. A comparison of simulated gains in  $\text{CO}_2$ :n-pentane (55:45) with two series of available experimental data with similar n-pentane concentrations (converted from the measured charge), is shown in figure 6.15. Though no measurement was performed with  $\text{CO}_2$ :n-pentane (55:45), the average gas gain is expected to be between the values measured in  $\text{CO}_2$ :n-pentane (60:40) and in

CO<sub>2</sub>:n-pentane (48:52) with the same operational voltage. The simulated gain curve has a similar slope to those from experimental data, but the absolute gain values are found to be only about one-quarter of the measured ones. Lower gas gain from the simulation is mainly due to that penning transfer rates are unknown and the transfer process is not implemented. It is foreseen that these discrepancies, combined with careful comparison of simulated avalanche fluctuations with experimental measurements, can be used to determine the Penning transfer rates in CO<sub>2</sub> and n-pentane mixtures in future studies.

With about 20% of the total avalanche charge collected in about 25 ns according to the results shown in figure 6.13 and about  $2 \times 10^5$  gas gain when running at 2.85 kV as shown in figure 6.15, the average charges collected by the electronics from the wires, pad, strips are expected to be about 0.3 pC, 0.15 pC, and 0.06 pC, respectively. Details of charge sharing among strips are in section 6.6. The sTGC detector in this condition will be operated in proportional mode instead of saturated avalanche mode.

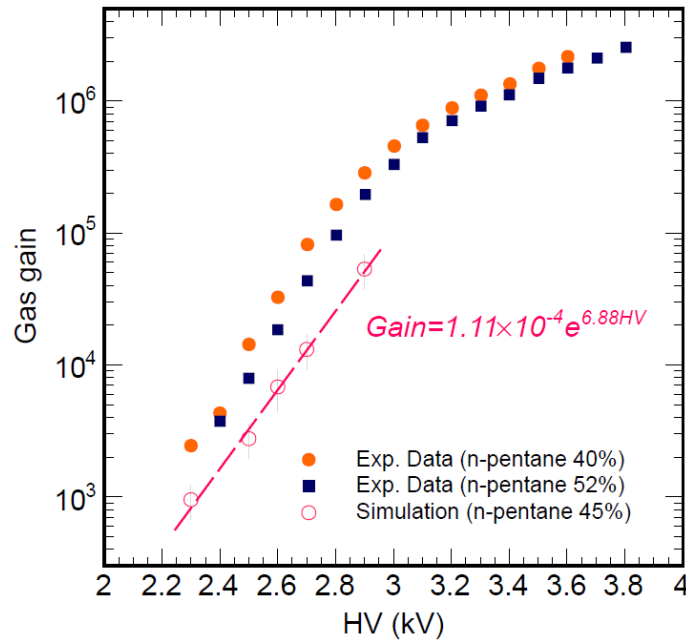


**Figure 6.15** Gas gain as a function of the high voltage.

## 6.5 Timing performance

The timing performance of sTGC is crucial for Level-1 triggering to enable the detector to identify single bunch crossings at a collision rate of 40 MHz. The jitter of the detector response time mainly arises from the variation of the drift time of electrons generated in different places along the charged particle track. The presence of complex magnetic fields in the NSW region as shown in figure 6.16 must also be accounted for (plots are generated using Persint [181]). Electron drift trajectories will change in the presence of magnetic fields.

The simulated maps of average electron drift time at different locations inside a sTGC unit cell are shown in figure 6.17 for a 1 T magnetic field orthogonal and parallel to wires, respectively. The magnetic fields are parallel to the detector cathode plane in both cases. Due to the small Lorentz angle of less than  $7^\circ$  up to 1 T and no electric field along the wire direction, a magnetic field that is perpendicular to wires will increase the electron drift length by less than  $10\ \mu\text{m}$ , and thus has negligible effect on the electron drift time. A magnetic field parallel to wires shrinks or elongates the electron drift lines depending on the electron position with respect to the wire location. This results in a “rotation” of the electron drift map around the wire by a small angle compared with the case without a magnetic field. For both cases, drift electrons from more than 80% of the gas volume could reach the wire within 25 ns. Exceptions only take place in the center of two wires or near the cathode plane due to relatively weak electric field. The detector response time, however, has more than 80% probability to fall within the 25 ns gate starting from the track enters the chamber. This is simply due to the fact that a few tens of clusters will be generated across the gas gap and the timing response is only determined by the earliest arrival time of a few clusters near the wire.

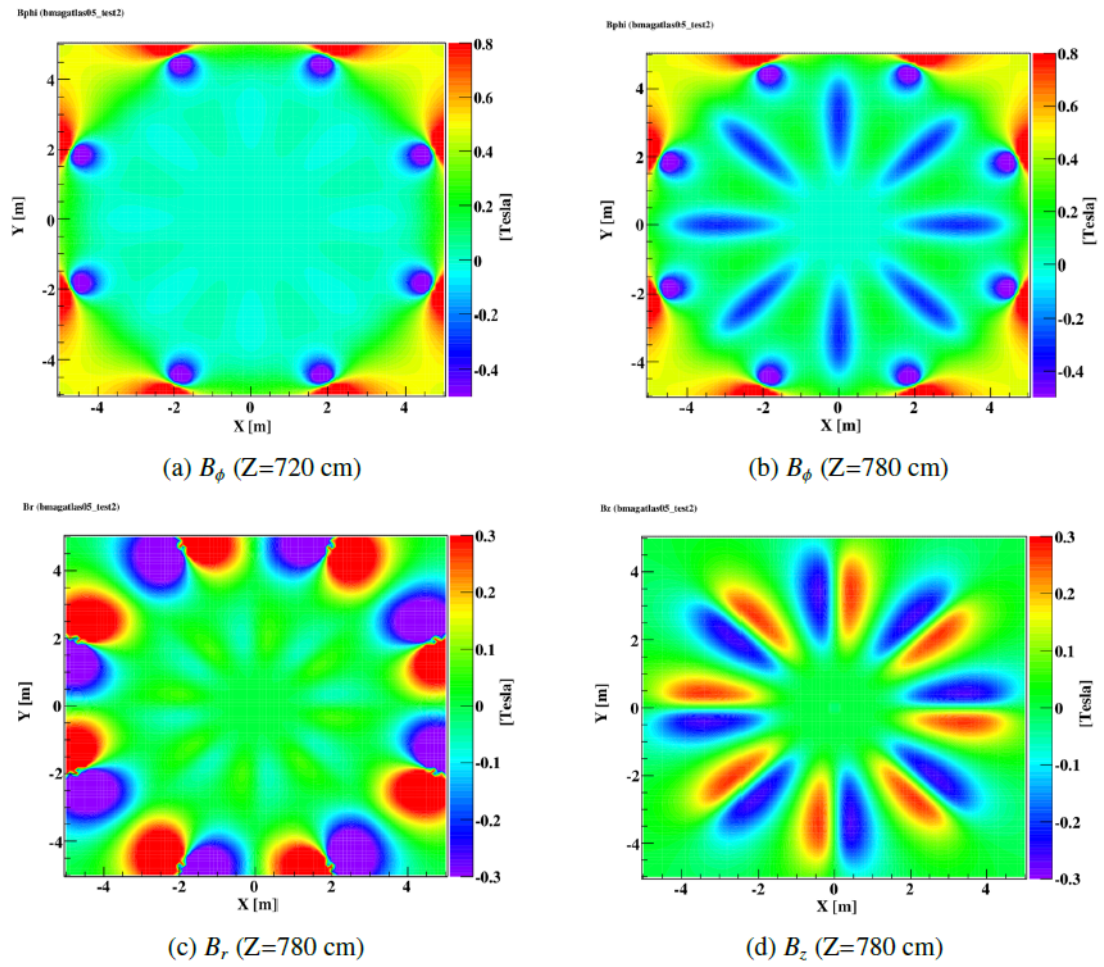


**Figure 6.16** Magnetic field around the ATLAS Muon Small Wheel.

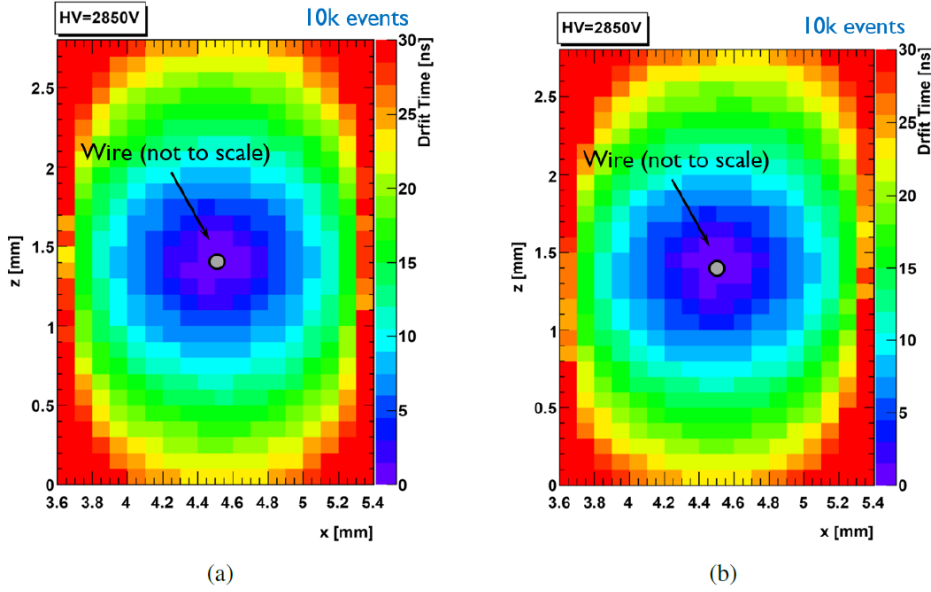


**Figure 6.17** Single electron drift time maps in a unit sTGC geometric cell with 1 T magnetic field parallel (a) and perpendicular (b) to the wires. Magnetic fields are parallel to the cathode plane in both cases.

### 6.5.1 Earliest cluster arrival time

Due to the strong electric field inside the small gas gap and relatively low electronics threshold (about a few fC) that can be used, amplifications of the first few clusters near the wire usually create a signal exceeding the discrimination threshold. Therefore the timing performance of the sTGC detector will be mainly determined by the earliest cluster arrival time. In other words, the fluctuations of the minimum drift time of clusters gives the physical limit of the detector time jitter.

The simulated earliest cluster arrival time distributions have been determined by tracing individual clusters and are shown on the left hand side of figure 6.18 for high voltages between 3.05 kV and 2.75 kV for perpendicular track incidence. The fraction of events with earliest cluster arrival time within the given time window as a function of the window width is shown on the right hand side of figure 6.18. Lowering the high voltage by 0.2 kV from the designed TGC operational

voltage of 3.0 kV, does not degrade the timing performance of the sTGC detector. More than 99% of the events have minimum cluster arrival time within the 25 ns time window.

The earliest cluster arrival time distributions for normal track incidence, with a 1 T magnetic field either parallel or orthogonal to the wire, are simulated and compared to the distribution without a magnet field in figure 6.19. The timing distributions with and without a magnetic field are found to be very close. A slightly smaller mean value of the distribution and hence a minor improvement of the timing performance is observed for a magnetic field that is parallel to the wire. This is mainly due to the effect illustrated in figure 6.20 where the presence of this magnetic field will deflect the tracks of drifting electrons and the path of the cluster near the wire thus could be shortened. Since the magnetic fields at the NSW are typically less than 0.5 T in any direction, the impact of the magnetic field on the sTGC timing performance is negligible.

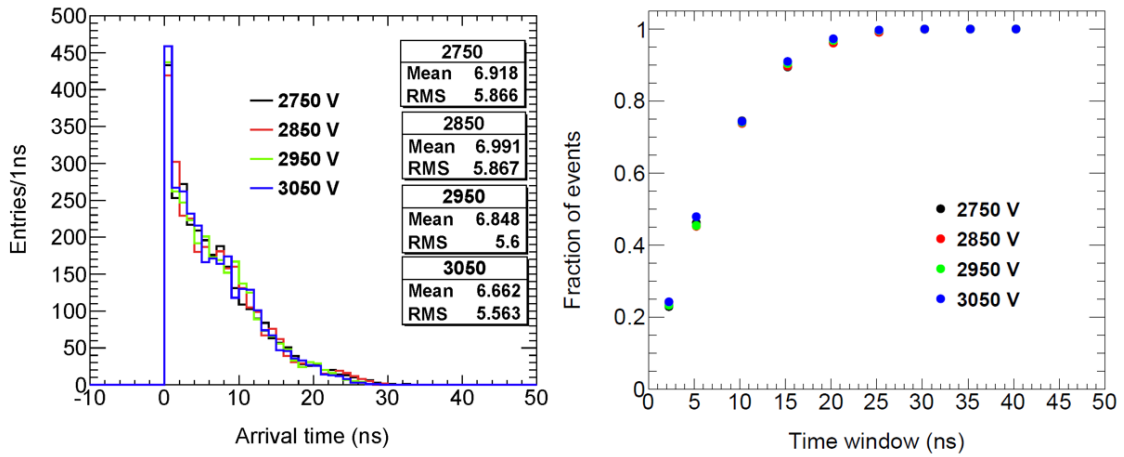


**Figure 6.18** Earliest cluster arrival time distributions for different high voltages (left) and the fraction of events with earliest cluster arrival time within the given time window (right).

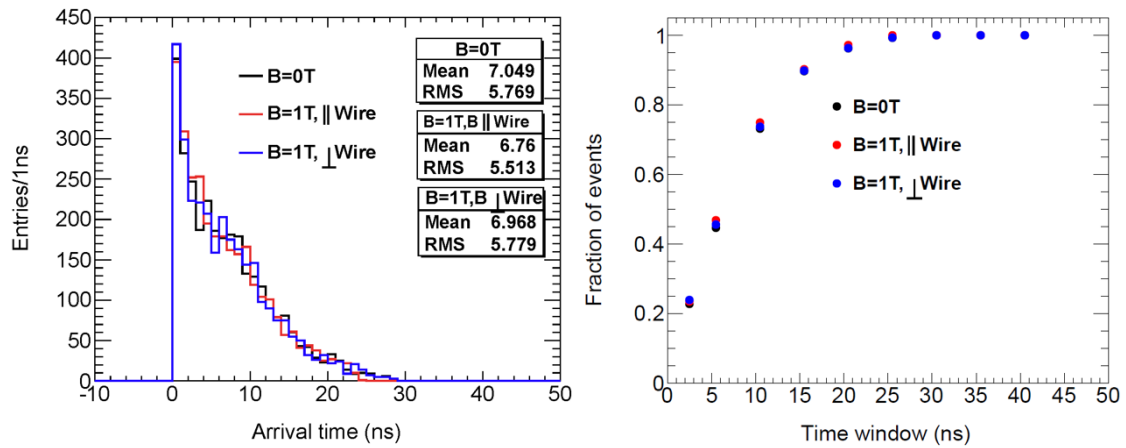


**Figure 6.19** Comparison of earliest cluster arrival time distributions with or without magnetic fields (left) and the fraction of events with earliest cluster arrival time within the given time window (right).

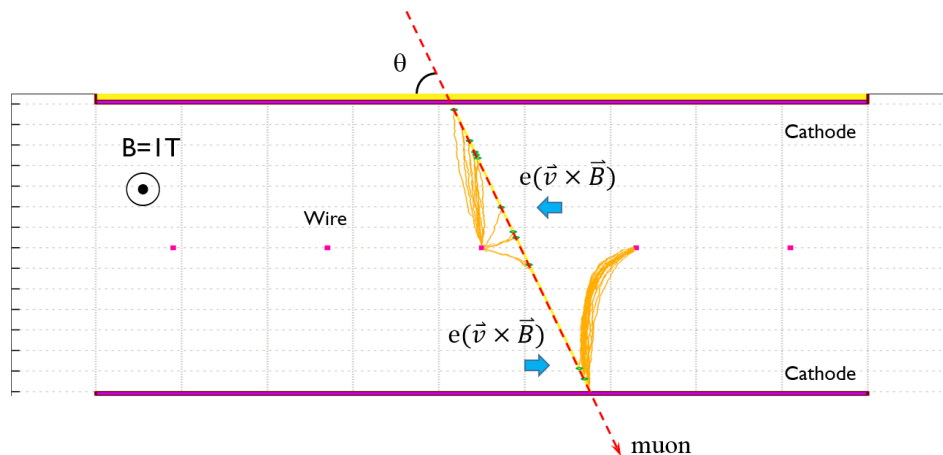


**Figure 6.20** An illustration of ionization clusters drifting towards the wire and the impact of magnetic field parallel to wires.

### 6.5.2 Single layer time spectrum

A complete simulation of the detector response time spectrum should take into account the gas gain fluctuations, electronics noise, electronics threshold as well as time jitter from external timing

references. We have performed a specific simulation of the sTGC detector, which is compared with experimental measurements taken with a 180 GeV muon beam, using the following steps. The electronics threshold is set to 10 fC ( $6.25 \times 10^4$  e-), which is about 8 times larger than the about 7500 equivalent noise charge for the front-end chip used in the beam test [182]. Electrons are traced using the microscopic method and drift times of individual ionization clusters are recorded. For each cluster an amplification factor is drawn from a Polya distribution with a mean of  $10^5$  and a  $\theta$  parameter of 1.4 based on the results of section 6.4.1. The resultant charge, calculated as the product of the number of electrons in the cluster and the sampled gas gain, is then summed when a cluster arrives on the wires. When the accumulated charge exceeds the threshold, the detector response time is assigned to be the arrival time of that cluster. For the last step, the detector response time is smeared with a Gaussian distribution that describes the timing uncertainties from external reference detectors and electronics.

The simulated time spectrum at 2.85 kV for perpendicular muon incidence is shown in figure 6.21. The result is compared with the time spectrum measured from a  $9 \text{ cm} \times 9 \text{ cm}$  size sTGC pad with 0.78 ns least count TDC modules in a muon beam test performed in 2012. The time jitter for the reference scintillator is less than 2 ns while the simulation is found to have better agreement with data if a 3 ns overall time uncertainty is assumed. More than 95% of the total events can be contained within a 25 ns time window. Thresholds of 20 fC and 40 fC were also tried and did not change the time spectrum.

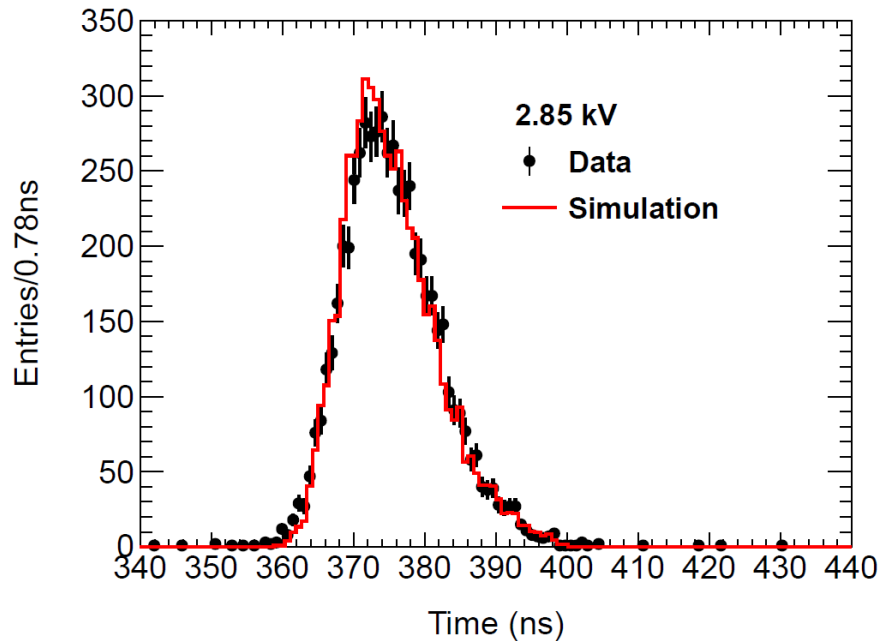


**Figure 6.21** Simulated time spectrum compared with one measured in the beam test with 180 GeV muons using 0.78 ns resolution TDCs. Muons tracks are perpendicular to the cathode plane and the horizontal axis has an arbitrary offset.

## 6.6 Strip charge sharing

Avalanches initiated by the ionized electrons and developed near wire surfaces will induce charges on the two symmetric cathode planes. The charges spread on the cathode plane, however, are constrained to be similar in size to the gas gap. Hence the charge sharing on 3.2 mm pitch readout strips underneath is insufficient to determine the charged particle hit position using a charge interpolation method. On the other hand, the localized charge on the cathode will diffuse through the resistive paint layer to the ground and image charges will be created on the readout strips, which are capacitively coupled to the resistive cathode. Therefore the resistive cathode not only provides the spark resistant functionality but also serves to disperse the charge over several readout strips to enhance tracking resolution. A simple model has been developed to describe the charge shar-

ing between sTGC strips. The model considers the spatial distribution and time development of raw induced charges on the cathode, and the propagation of induced signals through the resistive-capacitive network formed between the restive cathode and the readout plane.

Information about the raw induced charge on the cathode can be obtained from Garfield simulations without taking resistive layer into account. The charge dispersion phenomenon in resistive electrodes has been studied from streamer tubes in 1980's [183, 184] to micro-pattern gaseous detectors [185] recently. The method developed is also applicable for sTGC.

### 6.6.1 Raw charge spread on cathode

For multi-wire chambers, the induced charge density on a contiguous cathode plane due to a point charge deposited on the wire is described by the empirical function of Gatti *et al.* [186, 187]:

$$\Gamma(\lambda) = K_1 \frac{1 - \tanh^2 K_2 \lambda}{1 + K_3 \tanh^2 K_2 \lambda} \quad (6.2)$$

where  $\lambda (=x/h)$  is the distance normalized by the wire-cathode plane distance  $h$ , and  $K_1$  and  $K_2$  are related to  $K_3$  by:

$$K_1 = \frac{K_2 \sqrt{K_3}}{4 \tan^{-1} \sqrt{K_3}} \quad (6.3)$$

$$K_2 = \frac{\pi}{2} \left( 1 - \frac{\sqrt{K_3}}{2} \right) \quad (6.4)$$

where  $K_3$  is a parameter depending on the ratio between the wire-cathode plane distance ( $h$ ) and wire-wire separation ( $s$ ). Usually the FWHM of the cathode charge distribution is related to  $K_3$  and varies between  $1.3h$  to  $1.7h$ . In reality, the induced charge spread on the cathode can be slightly larger due to multiple avalanches from different ionization clusters as well as the diffusion of ionized electrons in the gas volume.

Practically, to evaluate the charge spread width on the detector cathode, the strip response function (SRF), which is the integration of cathode charge density over the strip width, can be conveniently obtained by measuring the signal amplitude of on the strip as a function of the distance

between incident track and strip center. The SRF for the determination of sTGC charge spread can also be obtained from the Garfield simulation. Estimations of the cathode charge distribution for inclined tracks and under magnetic fields in the simulation are also possible.

Simulation is performed by segmenting the whole sTGC cathode plane into fine pitch strips. The strip pitch is chosen to be 1.5 mm and is smaller than the expected charge spread width so that the accuracy will not be affected. The electric field together with the weighting field for each strip are generated using the finite element method to calculate the charge amplitudes. Muon tracks are uniformly generated across different strips. For each event, the charge on the strip is normalized by the total collected charge on the wire. The simulated ratio between the charge on the strip and the total charge on the wire as a function of distance between the muon hit position and the strip center for a perpendicular incident track is shown in figure 6.22. The distribution is well fitted by Gatti's function and can also be fitted approximately by a Gaussian function. The Gaussian fit of the SRF suggests that the raw induced charge spread on the cathode has a FWHM of 1.9 times the sTGC wire-cathode distance. This is wider than the distribution of the cathode charge induced by a single point charge deposited on the wire.

The SRFs are also simulated for different muon incident angles and results are shown in figure 6.23, where  $\lambda$  is the normalized distance between the hit position in the middle of the chamber and the strip center. The track incident angles indicated refer to the angles with respect to the normal of sTGC in the plane both orthogonal to the wire plane and strips. Fitting of the SRF with a Gaussian function shows that the width is slightly increased from  $1.9h$  to  $2h$  as the track angle increases from  $0^\circ$  to  $30^\circ$ . In addition, the SRF becomes asymmetric with inclined tracks. The asymmetry is believed to originate from different contributions to signals from the avalanches above and below the wire. For muons hit in the middle of the chamber equidistant to the left and right of a strip center, the avalanche centers above or below the wires in fact have different distances to the strip center hence induce different amounts of charges on that strip. Avalanches on

the side away from the strip are likely to be shielded by the wires and induce a smaller amount of charge on the strip.

The SRFs are also simulated with the presence of 1 T magnetic fields orthogonal to the wires, which potentially could modify the ionized electron drift path along the wire direction. The results are compared with those obtained without magnetic field in figure 6.24. As expected from the small Lorentz angle for sTGC operational gas, shapes of charge distributions and their widths remain unchanged.

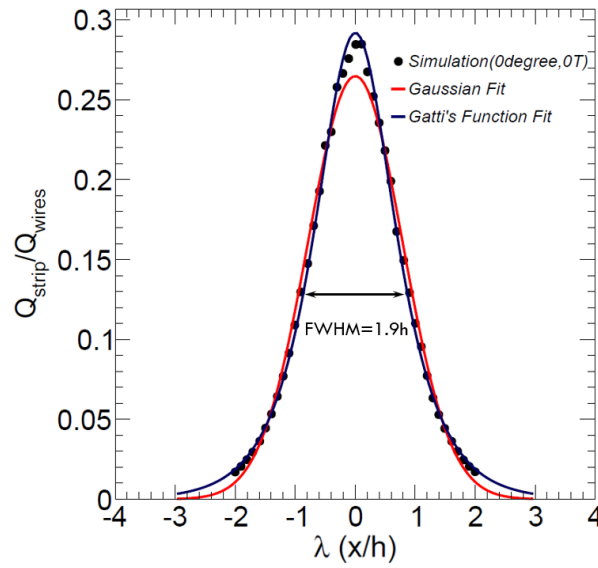


**Figure 6.22** Simulated strip response function-the fraction of charge collected by the strip as a function of muon hit position with respect to the strip center.

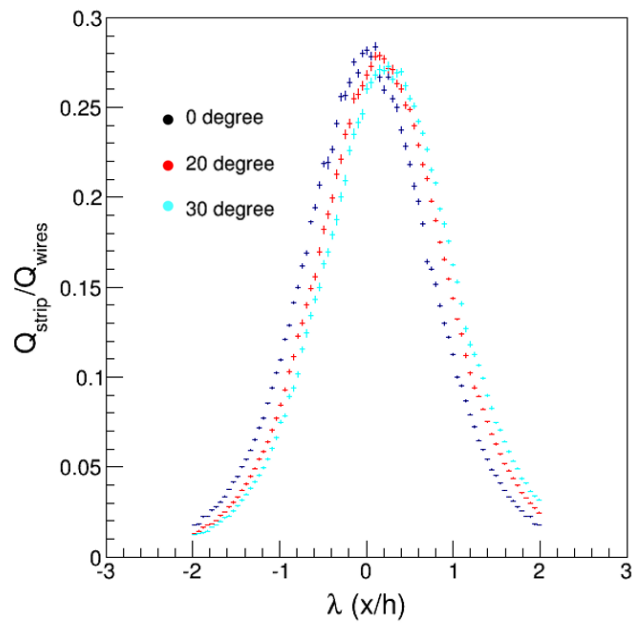


**Figure 6.23** The strip response function for different muon incident angles in the plane orthogonal to the wire plane.

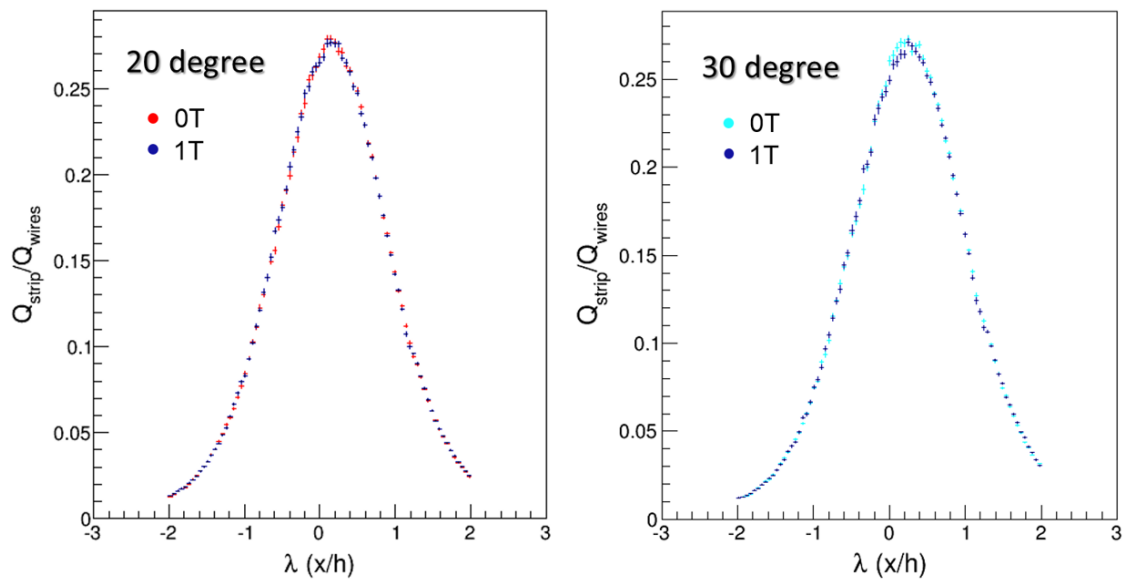


**Figure 6.24** Influence of magnetic field to raw induced charge spread on sTGC cathode plane.

### 6.6.2 Charge dispersion

Since sTGC strips only measure one coordinate of the muon tracks and because the resistive coating is supposed to have a uniform surface resistivity, the cathode and the readout strip plane can be treated as a one-dimensional  $R$ - $C$  network where  $R$  and  $C$  are resistive layer resistance and resistive layer-readout plane coupling capacitance per unit length, respectively. For sTGCs, the unit length resistance is around a few tens of  $k\Omega$  and the coupling capacitance can be a few tens to a few hundreds fF depending on the thickness of the cathode insulator and its dielectric constant.

The evolution of current or charge density on the cathode plane due to a point charge deposited at  $x = 0$ ,  $t = 0$  and diffusing through a 1D  $R$ - $C$  network is given by the solution of the diffusion equation:

$$\rho(x, t) = \sqrt{\frac{\tau}{4\pi t}} \cdot \exp\left(-\frac{\tau x^2}{4t}\right) \quad (6.5)$$

where  $\tau (=RC)$  is the characteristic time when the Gaussian distributed charge spread in space has a sigma of  $\sqrt{2}$  times the unit length. As shown in section 6.6.1, the spread of cathode charge induced by a charge  $Q$  on the wire can be approximated by a Gaussian distribution:

$$D(x) = \frac{Q}{\sqrt{2\pi}\sigma} \cdot \exp\left(-\frac{x^2}{2\sigma^2}\right) \quad (6.6)$$

where  $\sigma$  is about 1.2 mm. The charge density on the cathode is thereby given by the convolution of equation 6.5 and 6.6

$$\rho'(x, t) = Q \sqrt{\frac{\tau}{2\pi(2t + \sigma^2)}} \cdot \exp\left(-\frac{\tau x^2}{4t + 2\tau\sigma^2}\right) \quad (6.7)$$

A comparison of the diffusing charge densities for a point and a finite-size charge depositions are shown in figure 6.25. The dependence of the charge density as a function of time on certain readout strips can be derived from the integration of equation 6.7 between strip boundaries:

$$\rho'(t) = \int_{w_1}^{w_2} \rho'(x, t) dx = \frac{Q}{2} \left[ \text{Erf}\left(\frac{\sqrt{\tau}}{\sqrt{4t + 2\tau\sigma^2}} w_2\right) - \text{Erf}\left(\frac{\sqrt{\tau}}{\sqrt{4t + 2\tau\sigma^2}} w_1\right) \right] \quad (6.8)$$

where  $w_1$  and  $w_2$  are coordinates of two edge of a strip.

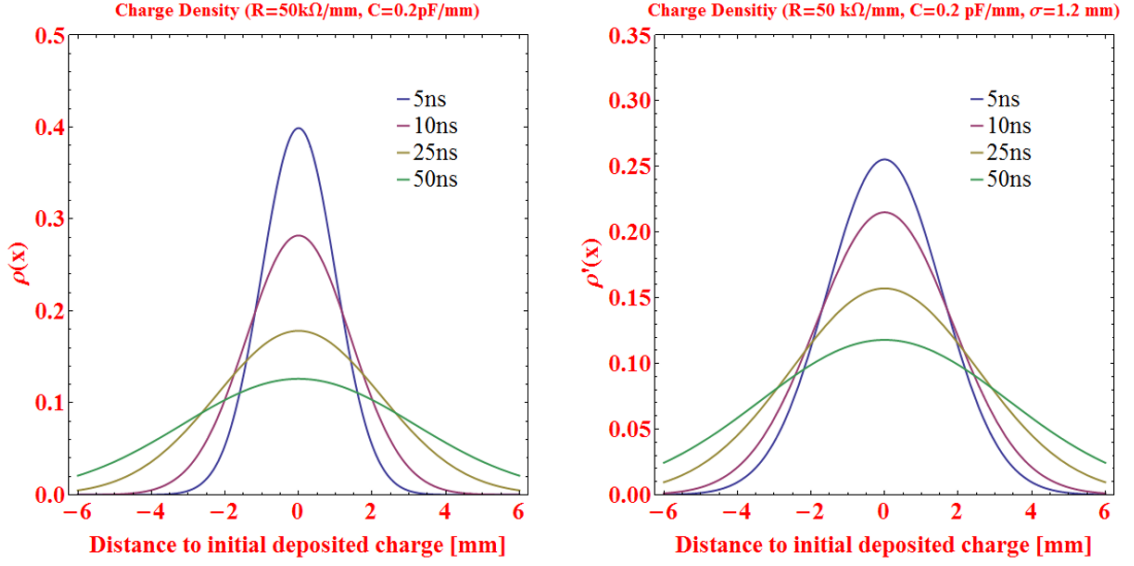


**Figure 6.25** The charge density distribution at different times for a point charge deposited at  $x=0$ ,  $t=0$  and diffusing through a 1- $D$  RC network (left) and for charge deposited at  $t=0$  with a finite spread in space (right).

As indicated in figure 6.13, induced charges on the cathode grow with the logarithm of time and the dependence can be described as

$$T(t) = \begin{cases} 0 & (0 < t < t_0) \\ C + s \cdot \ln(t + t_0) & (t \geq t_0) \end{cases} \quad (6.9)$$

where  $C$  and  $s$  are the intercept and the charge growth slope respectively.  $t_0$  could be considered to represent the average drift time of the first cluster which initiates the first set of avalanche on the wire. The final model for the charge density evolution on each strip is obtained by convolving  $\rho'(t)$  and  $T(t)$ . This is handled numerically.

Based on the above model, a Monte Carlo simulation has been performed to simulate the charge sharing among strips by comparing the charge on the neighboring strip with that on the central fired strip. The general procedures are as follows: At first, muon tracks with perpendicular incidence

are generated uniformly from the center of one strip to half the strip pitch. Therefore, it is possible to identify the strips with second, third or fourth largest charge by comparing their distances to the muon track. Then the integration time is chosen to be the typical value of 25 ns and the raw induced charge spread on the cathode is fixed at the number derived from the Garfield simulation for calculating total charge deposition on each strip. The charge dispersion time constant is left as a floating parameter. The charge density function on each strip is finally integrated with the given integration time with a specific dispersion time constant and the ratios of charges between each strip and the central strip are obtained. Since in reality there is an uncertainty in charge determination due to noise, the charge ratio is smeared with a few percent of a Gaussian distributed fluctuation.

To permit comparison with the experimental data from a muon beam test performed in 2012 (charges on strips are linearly represented by ADC counts), the dispersion time constant  $\tau$  is tuned so that the mean value of the simulated second-to-maximum charge ratio is the same as the measured one. A time constant of about 6.5 ns is suggested. Comparisons of the simulated and measured charge ratio distributions are shown in figure 6.26. The shape of the simulated second-to-maximum charge ratio distribution agrees well with the data. The distribution of the ratios for third, fourth and fifth maximum charges to maximum charge are found to be slightly smaller than the measured data. It is likely due to the unexpected larger spread of the raw induced charge as well as the inaccurate description of the charge profile using a Gaussian function. Both simulated and experimental data show that on average the second and third maximum charge strips can pick up charges equivalent to about 60% and 20% of the charge on the central strip with a pitch size of 3.2 mm.

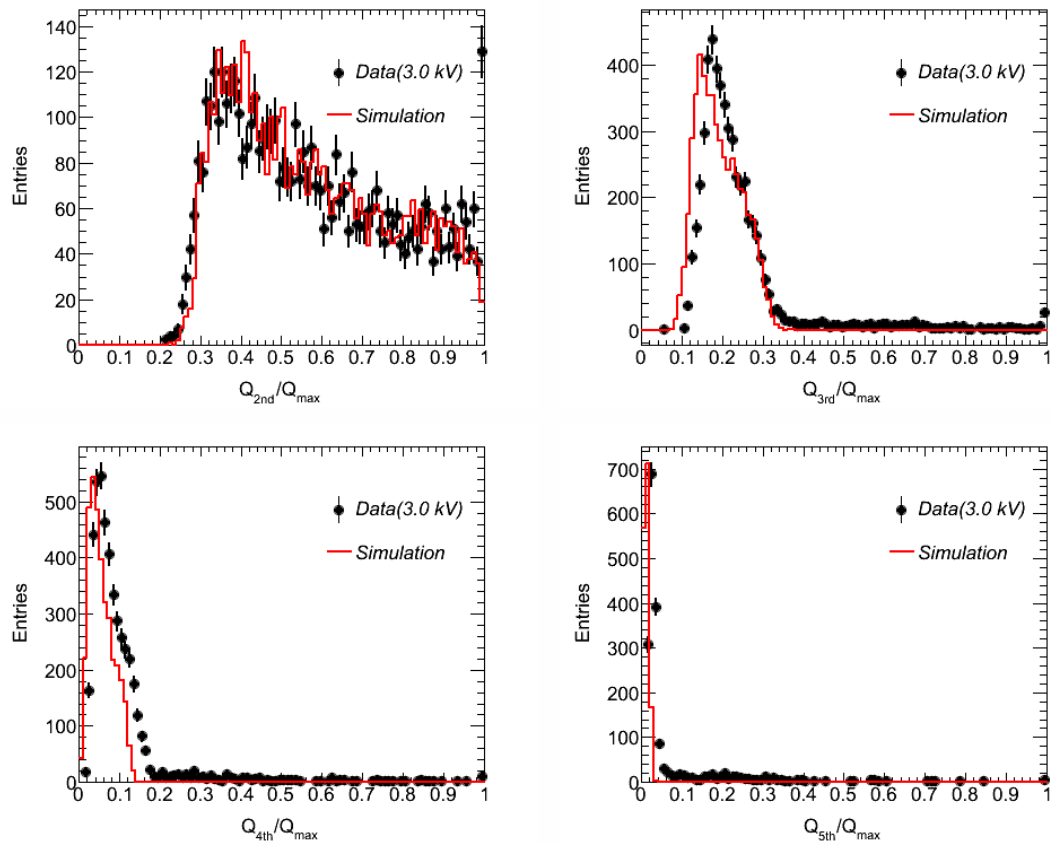


**Figure 6.26** Distributions of charge ratios between those induced on various strips and that on central strip, e.g.  $Q_{2nd}/Q_{max}$  is the ratio of second largest charge to largest. The experimental data is measured with ADCs. Simulated distributions are obtained with a raw charge spread of 2.8 mm (FWHM) and a RC time constant of 6.5 ns.

### 6.6.3 PSpice simulation

An approach to verify the developed analytical charge sharing model is to build the equivalent detector circuit model and simulating signal amplitude from different strips using PSpice [188]. The simulated sTGC current signals from Garfield can be used as inputs and the dispersed signal on the strips can be determined from their equivalent coupling capacitors. The schematics are illustrated in figure 6.27. Each resistor-capacitor cell represents certain length along the wire direction. The

Garfield generated signals used as PSpice program inputs are from segmented cathode strips so that the spatial extension of the raw induced charge is reproduced.

An example of simulated dispersing current signals from central and neighboring 3.2-mm-pitch strips are seen in figure 6.28 when muon incidence is in the middle of the central strip and a dispersion time constant is 10 ns. The integration of currents on these strips indicate that the amount of charge collected on the second maximum charge strip is about 32% of the charge on the central strip. For using the analytic model, the value is calculated to be about 30%, which reasonably agrees with the results obtained previously.

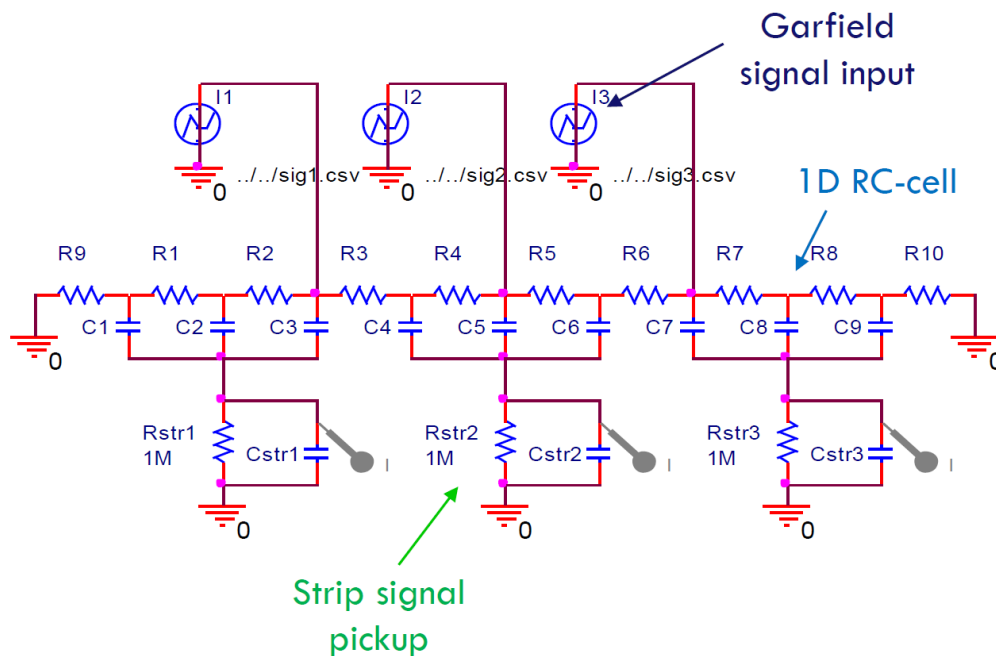


**Figure 6.27** 1-D resistive-capacitive network model built for the PSpice program.

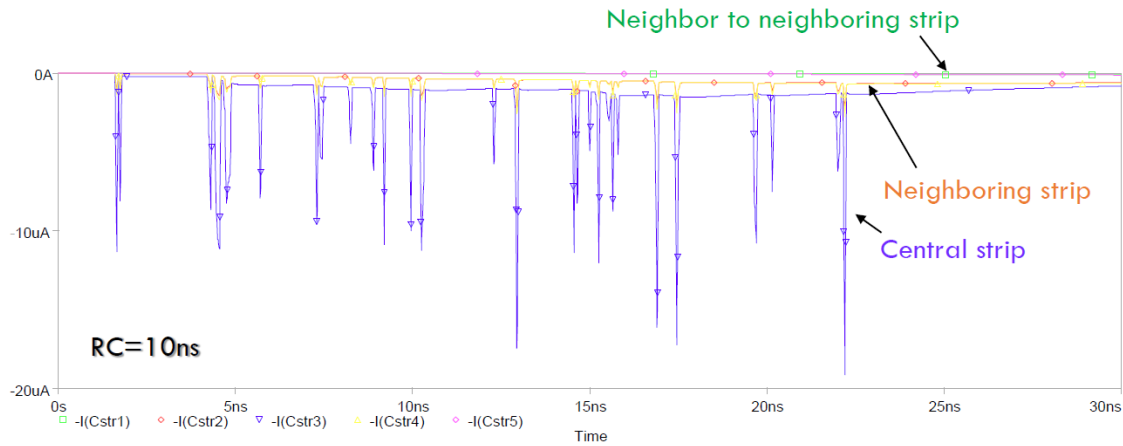


**Figure 6.28** The simulated signals picked up from 3.2-mm-pitch strips after charges were dispersed through the RC network. Signals are associated with a muon passing perpendicularly in the middle of the central strip.

## 6.7 Summary

Extensive simulations, including the electric field inside the chamber, electron transportation properties and charge production are performed in order to understand the operational principles of the sTGC detectors for the ATLAS NSW muon detector upgrade. Due to the strong electric field and small gas gap, most of the ionized electrons generated in the chamber will reach the wire within a few tens of nanoseconds. In addition, the amplification in the vicinity of the wire is sufficiently large so that the detector is sensitive to single clusters arriving at the wire. These features result in small time jitter together with fast collection of electron induced charges. Owing to the small Lorentz angle in the CO<sub>2</sub>:n-pentane (55:45) gas mixture, the timing performance of sTGC are not expected to be affected by the presence of the magnetic field in the NSW. The foreseen operation at lower high voltage of around 2.8 kV, compared with 3.0 kV for the TGCs currently used in ATLAS, does not degrade its timing capability. However, the gas gain is estimated to be reduced to about  $2 \times 10^5$  and thus the detector will be actually running in the proportional mode instead

of the saturated avalanche mode. Detailed simulation based on Garfield reproduce well a single layer sTGC detector time spectrum from a muon beam test. Results indicate that more than 95% of the total events can be identified within 25 ns in a single detector layer and thus fulfills the requirements for Level-1 triggering.

A simple analytical model has been developed to describe the charge sharing among sTGC strips. This includes the time structure of the charge development, raw induced charge spread on the cathode and its dispersion through the distributed resistive-capacitive network between the readout and cathode planes. Results show that with a few tens  $\text{k}\Omega/\square$  cathode resistivity and  $\sim 0.1$  mm cathode-readout plane separation, charges will be spread out on 3-4 strips with a pitch size of 3.2 mm. Depending on the real situation that whether a linear representation of charge such as flash ADC or logarithmic-like representation such as time-over-threshold (ToT) will be implemented in the front-end ASIC, the distance between the resistive cathode and the readout plane can be varied at a few hundreds of microns level to adjust the coupling capacitance hence the characteristic charge dispersion time. For instance, the use of ToT would prefer less dispersion of the charge so that the signals from central and neighboring strips can be distinguished.



# Chapter 7

## Summary and outlook

The muon tracking and triggering are confronted with big challenge after the upgrade of LHC to higher energy and luminosity or in future collider experiments. High rate capability, tracking precision and good timing performance from the gaseous muon tracking and trigger detectors are increasingly demanding at the same time. In the context of ATLAS muon upgrade program, extensive research and development on three types of advanced gaseous detectors are carried out. This dissertation presented our detailed studies of Micromegas, Resistive Plate Chamber (RPC) and Thin Gap Chamber (TGC) detectors with efforts to understand their characteristics and exploit them for muon tracking and triggering in the harsh high rate hadron collider environments.

The first part of the dissertation reports the development of a novel method to fabricate Micromegas detectors. This fabrication method is based on attaching a layer of woven wire micro-mesh on the anode printed circuit board to form one hundred microns thick avalanche gap using thermo-bond film spacers. Without employing dedicated photo-lithography processes, it allows convenient and economic construction of Micromegas or similar structures in most university or institutional labs with simple hot plates or hot press machines. Our test results of  $4\text{ cm} \times 4\text{ cm}$  thermo-bonded Micromegas prototypes show that gas gains up to  $2 \times 10^4$  and energy resolutions better than 14% (FWMH) for 5.9 keV X-rays could be achieved. The gain uniformity of about

20% around the mean is achieved and it should be sufficient for muon trigger and tracking applications. Our simulation as well as experiment on small prototypes suggest that the uniformity could be improved to within 10% using neon based mixtures as operational gases. The largest prototypes produced so far have areas of  $20\text{ cm} \times 20\text{ cm}$  with basic performance parameters comparable to those of bulk Micromegas. Further development towards larger areas, comparable to those used in COMPASS experiment, are still ongoing.

Thanks to the excellent bonding strength of thermo-bond film and the flexibility it offers, we have attempted to construct Micromegas with high resistivity anode and parallel ionization multiplier (PIM) structure with multiple micro-mesh layers and gaps. The former attempt explores a new approach to build spark-tolerant Micromegas. By attaching a thick layer of high resistivity material, with bulk resistivity of around  $10^{10}\text{ }\Omega\cdot\text{cm}$ , to the metallic anode, gas gains exceeding  $10^5$  have been obtained. Charges released in the discharges are limited to less than a few nC and discharge currents have durations less than a few hundred ns. Despite of occasional sparks due to large avalanches, prototype imperfection, all prototypes during the tests are found to be very robust when operated at a gas gain of a few tens of thousands. We believe it is an effective way to protect the front-end electronics and allow a high MIP detection efficiency in harsh hadron environment. The later attempt to improve the timing performance of micro-mesh parallel electrode structure detectors. We have designed a PIM structure with a drift gap of a few mm thick followed by a  $300\text{ }\mu\text{m}$  thick avalanche gap and one hundred microns thick induction gap. Our simulation and calculation show that a large fraction of prompt electron signal could be derived from the detector if electric fields in these gaps are properly configured so that amplifications mostly occur in the avalanche gap. This GEM-mode operation gives short electron induced pulses and an improved timing performance is expected compared with the Micromegas and the GEM detectors. We have constructed small prototypes which demonstrate that an effective gain of  $10^4$  could be achieved on the anode. It should be pointed out that compared with the GEM, only a single amplification stage

is required to achieve this gain. This PIM structure is potentially useful for MIPs tracking when good timing performance is also of concern.

The second part of the dissertation presents studies of precision tracking and fast triggering based on thin gap RPCs. RPCs with about 1 mm gas gaps are used and equipped with 1.27-mm-pitch readout strips. Strips are read out from both strip ends. Several beam tests are carried out at the CERN SPS-H8 muon beam line in order to study timing performances, spatial resolutions of these thin gap RPCs and assess viabilities of operating thin gap RPCs as mean-timers to do fast coincidences. Our test results show that about 500 ps time resolutions could be reached using around 1 mm gas gap RPCs. A spatial resolution of less than 200  $\mu\text{m}$  using charge centroid method are obtained. It should be stressed that the ultimate resolution should be much better than obtained due to the non-linear ADC-charge correlations from the used front-end electronics. A spatial resolution of less than 300  $\mu\text{m}$  is also obtained only using on-line timing information. The timing information from two ends of a strip could be used to give muon hit positions along the strip. With 100 ps TDCs, the position resolution of around 7 mm along the strip is achieved. Due to the independence of the average signal arrival time from two ends of a strip with muon hit positions, it is possible to build a trigger system with timing jitter only on the order of a few hundred picoseconds. Fast coincidences between multiple thin gap RPC layers within a few nanoseconds are allowed to reject fake hits. The constructed (sub-ns  $\times$  sub-mm  $\times$  cm) trigger cells using thin gap RPCs will be very powerful to remove backgrounds at first time and improve high momentum muon selectivity at high level triggering in high rate environments. Furthermore, we have conducted rate capability tests of Bakelite RPCs at CERN Gamma Irradiation Facility (GIF). Results show that even made with the standard 2 mm thick  $10^{10} \Omega\cdot\text{cm}$  Bakelite plates, the Bakelite RPC is fully efficient at a maximum detected photon rate of more than 15 kHz/cm<sup>2</sup>. It is found that one of the key approach to increase the RPC rate capability is to limit the avalanche development inside the gas gap and reduce the charge per detected count. It also worth pointing out that another study performed by

the ATLAS RPC community suggests the timing resolution of a thin gap RPC operated at few kHz/cm<sup>2</sup> is comparable with that sub-ns resolution obtained at very low rate. All these features make advanced RPCs are attractive to future muon triggering with very strict requirements.

The last part of the dissertation presents the simulation study of small-strip TGCs which have been selected as the primary trigger detectors for the ATLAS New Small Wheel (NSW). The ATLAS NSW sTGCs have cathode strips, pads as well as wire readout elements. Signals from four sTGC pad layers will be used to make coincidences and to form trigger towers. Only signals from strips underneath the candidate pad trigger towers will be read out and used to reconstruct muon hit positions at level-1. Our studies have particularly focused on the timing performance and the charge sharing among readout strips which will be useful to understand the determination of precision coordinates. Our simulation well reproduces the sTGC timing performance measured at the CERN SPS-H8 beam test with 180 GeV/c muons. Simulation results show that sTGC is capable of correctly identifying LHC bunch crossings happening every 25 ns. In addition, its timing performance is found to be unaffected by the magnetic field around the ATLAS muon Small Wheel, which has a strength up to 0.5 T. An analytical model is also developed to describe the charge dispersion in resistive cathode layers and charge sharing among sTGC readout strips. This model reasonably agrees with the strip charge distribution measured at the beam test. It will be very valuable to understand the impact of detector geometric parameters, such as strip pitch, graphite layer resistivity and graphite-strip plane distance, on the charge dispersion inside the chamber as well as the spatial resolution. Such model could also be used in the ATLAS main software framework-ATHENA for the digitization of sTGC strip responses. Further development of the model is still ongoing to include the electronics parameters such as pulse response function, shaping time etc. It is expected to be useful to better understand responses from gaseous detectors with resistive electrodes and optimize these detectors for better tracking accuracy.

# Bibliography

- [1] ATLAS collaboration, “Observation of a new particle in the search for the Standard Model Higgs boson with the ATLAS detector at the LHC,” *Physics Letters B* **716**, 1–29 (2012).
- [2] CMS collaboration, “Observation of a new boson at a mass of 125 GeV with the CMS experiment at the LHC,” *Physics Letters B* **716**, 30–61 (2012).
- [3] T. Kawamoto *et al.*, “New Small Wheel Technical Design Report,” CERN-LHCC-2013-006 (2013).
- [4] J. J. Thomson, “Cathode Rays,” *The Electrician* **39**, 104 (1897).
- [5] J. J. Thomson, “Cathode Rays,” *Philosophical Magazine* **44**, 293–316 (1897).
- [6] J. J. Thomson, “LVII. On the charge of electricity carried by the ions produced by Röntgen rays,” *The London, Edinburgh, and Dublin Philosophical Magazine and Journal of Science* **46**, 528–545 (1898).
- [7] J. J. Thomson, “LVIII. On the masses of the ions in gases at low pressures,” *The London, Edinburgh, and Dublin Philosophical Magazine and Journal of Science* **48**, 547–567 (1899).
- [8] V. F. Hess, “Über Beobachtungen der durchdringenden Strahlung bei sieben Freiballonfahrten,” *Z. Phys.* **48**, 1084–1091 (1912).

- 
- [9] T. Wulf, “On the radiation of high penetrating power that exists in the atmosphere,” *Z. Phys.* **1**, 152–157 (1909).
- [10] E. Rutherford, “An electrical method of counting the number of  $\alpha$ -Particles from Radioactive Substances,” *Proceedings of the Royal Society of London. Series A, Containing Papers of a Mathematical and Physical Character* **81**, 141–161 (1908).
- [11] J. S. Townsend, “XVII. The Conductivity produced in gases by the motion of negatively charged ions,” *The London, Edinburgh, and Dublin Philosophical Magazine and Journal of Science* **1**, 198–227 (1901).
- [12] J. S. Townsend, “LXVI. The conductivity produced in gases by the aid of ultra-violet light,” *The London, Edinburgh, and Dublin Philosophical Magazine and Journal of Science* **3**, 557–576 (1902).
- [13] E. Rutherford, “VIII. Uranium radiation and the electrical conduction produced by it,” *The London, Edinburgh, and Dublin Philosophical Magazine and Journal of Science* **47**, 109–163 (1899).
- [14] E. Rutherford, “XV. The magnetic and electric deviation of the easily absorbed rays from radium,” *The London, Edinburgh, and Dublin Philosophical Magazine and Journal of Science* **5**, 177–187 (1903).
- [15] H. Geiger and W. Müller, “Elektronenzählrohr zur messung schwächster aktivitäten,” *Naturwissenschaften* **16**, 617–618 (1928).
- [16] S. Korff, “How the Geiger Counter started to crackle: Electrical counting methods in early radioactivity research,” *Annalen der Physik* **525**, A88–A92 (2013).
- [17] H. Friedman, “Geiger counter tubes,” *Proceedings of the IRE* **37**, 791–808 (1949).

- [18] S. H. Liebson, “The Discharge Mechanism of Self-Quenching Geiger-Mueller Counters,” *Physical Review* **72**, 602–608 (1947).
- [19] L. G. Schulz, “A Direct Method of Determining Preferred Orientation of a Flat Reflection Sample Using a Geiger Counter X-Ray Spectrometer,” *Journal of Applied Physics* **20**, 1030–1033 (1949).
- [20] R. Giacconi, G. Herbert, R. P. Frank, and B. R. Bruno, “Evidence for X rays from sources outside the solar system,” *Physical Review Letters* **9**, 439–443 (1962).
- [21] J. Chadwick, “Possible existence of a neutron,” *Nature* **129**, 312 (1932).
- [22] J. Townsend, *The theory of ionization of gases by collision* (D. Van Nostrand Company, 1910).
- [23] J. W. Keuffel, “Paralle-Plate Counters,” *Review of Scientific Instruments* **20**, 202–208 (1949).
- [24] F. Bella and C. Franzinetti, “Spark counters,” *IL Nuovo Cimento* **10**, 1461–1479 (1953).
- [25] T. E. Cranshaw and J. F. D. Beer, “A triggered spark counter,” *IL Nuovo Cimento Series 10* **5**, 1107–1117 (1957).
- [26] S. Fukui and S. Miyamoto, “A new type of particle detector: the  $\ll$  discharge chamber  $\gg$ ,” *IL Nuovo Cimento Series 10* **11**, 113–115 (1959).
- [27] G. Danby *et al.*, “Observation of high-energy neutrino reactions and the existence of two kinds of neutrinos,” *Physical Review Letters* **9**, 36–44 (1962).
- [28] [http://www.bnl.gov/bnlweb/history/nobel/nobel\\_88.asp](http://www.bnl.gov/bnlweb/history/nobel/nobel_88.asp) .

- [29] A. N. May, “The mechanism of the geiger counter,” *Reports on Progress in Physics* **5**, 390 (1938).
- [30] R. Giles, “A proportional counter spectrometer for neutrons,” *Review of Scientific Instruments* **24**, 986–987 (1953).
- [31] G. Singh and N. K. Saha, “A new design of a multiple-wire spark counter and some studies with the single wire-plate spark counter,” *Nuclear Instruments and Methods* **13**, 321–329 (1961).
- [32] G. Charpak *et al.*, “The use of multiwire proportional counters to select and localize charged particles,” *Nuclear Instruments and Methods* **62**, 262–268 (1968).
- [33] D. R. Charpak, Georges and H. Steiner, “Some developments in the operation of multiwire proportional chambers,” *Nuclear Instruments and Methods* **80**, 13–34 (1970).
- [34] J. H. Walenta, Albert H. and B. Schörlein, “The multiwire drift chamber a new type of proportional wire chamber,” *Nuclear Instruments and Methods* **92**, 373–380 (1971).
- [35] T. Bressani *et al.*, “Track localization by means of a drift chamber,” (1969).
- [36] D. R. Nygren, “The time projection chamber: A new 4 pi detector for charged particles,” eConf 740805. **PEP-0144**, 58 (1976).
- [37] P. Nemethy *et al.*, “Gated time projection chamber,” *Nuclear Instruments and Methods in Physics Research* **212**, 273–280 (1983).
- [38] H. J. Hilke, “Time projection chambers,” *Reports on Progress in Physics* **73**, 116201 (2010).
- [39] H. Aihara *et al.*, “Spatial resolution of the PEP-4 time projection chamber,” *IEEE Transactions on Nuclear Science* **30**, 76–81 (1983).

- [40] C. Berger *et al.*, “Evidence for gluon bremsstrahlung in  $e^+ e^-$  annihilations at high energies,” *Physics Letters B* **86**, 418–425 (1979).
- [41] D. Heidorn, “Diplomarbeit,” DESY internal report PLUTO 84-02 (1984).
- [42] B. R. Stella and H.-J. Meyer, “ $Y$  (9.46 GeV) and the gluon discovery (a critical recollection of PLUTO results),” *The European Physical Journal H* **36**, 203–243 (2011).
- [43] G. Arnison *et al.*, “Experimental observation of isolated large transverse energy electrons with associated missing energy at  $s = 540$  GeV,” *Physics Letters B* **122**, 103–116 (1983).
- [44] M. Banner *et al.*, “Observation of single isolated electrons of high transverse momentum in events with missing transverse energy at the CERN pp collider,” *Physics Letters B* **122**, 476–485 (1983).
- [45] G. Arnison *et al.*, “Experimental observation of lepton pairs of invariant mass around 95 GeV/ $c^2$  at the CERN SPS collider,” *Physics Letters B* **126**, 398–410 (1983).
- [46] P. Bagnaia *et al.*, “Evidence for  $Z_0 \rightarrow e^+ e^-$  at the CERN pp collider,” *Physics Letters B* **129**, 130–140 (1983).
- [47] A. Astbury *et al.*, “A  $4\pi$  solid angle detector for the SPS used as a proton-antiproton collider at a centre of mass energy of 540 GeV,” No. CERN-SPSC-78-6. CM-P00043779 (1978).
- [48] <http://home.web.cern.ch/about/experiments/ua1> .
- [49] <http://cds.cern.ch/record/615824?ln=en> .
- [50] R. Santonico and R. Cardarelli, “Development of resistive plate counters,” *Nuclear Instruments and Methods in physics research* **187**, 377–380 (1981).

- [51] V. V. Parkhomchuck, Y. N. Pestov, and N. V. Petrovykh, "A spark counter with large area," *Nuclear Instruments and Methods* **93**, 269–270 (1971).
- [52] E. Cerron Zeballos *et al.*, "A new type of resistive plate chamber: the multigap RPC," *Nuclear Instruments and Methods in Physics Research Section A: Accelerators, Spectrometers, Detectors and Associated Equipment* **374**, 132–135 (1996).
- [53] A. Oed, "Position-sensitive detector with microstrip anode for electron multiplication with gases," *Nuclear Instruments and Methods in Physics Research Section A: Accelerators, Spectrometers, Detectors and Associated Equipment* **263**, 351–359 (1988).
- [54] Y. Giomataris *et al.*, "MICROMEGAS: a high-granularity position-sensitive gaseous detector for high particle-flux environments," *Nuclear Instruments and Methods in Physics Research Section A: Accelerators, Spectrometers, Detectors and Associated Equipment* **376**, 29–35 (1996).
- [55] F. Sauli, "GEM: A new concept for electron amplification in gas detectors," *Nuclear Instruments and Methods in Physics Research Section A: Accelerators, Spectrometers, Detectors and Associated Equipment* **386**, 531–534 (1997).
- [56] Y. Giomataris, "Development and prospects of the new gaseous detector "Micromegas"," *Nuclear Instruments and Methods in Physics Research Section A: Accelerators, Spectrometers, Detectors and Associated Equipment* **419**, 239–250 (1998).
- [57] A. Bressan *et al.*, "Beam tests of the gas electron multiplier," *Nuclear Instruments and Methods in Physics Research Section A: Accelerators, Spectrometers, Detectors and Associated Equipment* **425**, 262–276 (1999).

- [58] A. Balla *et al.*, “Construction and test of the cylindrical-GEM detectors for the KLOE-2 Inner Tracker,” Nuclear Instruments and Methods in Physics Research Section A: Accelerators, Spectrometers, Detectors and Associated Equipment **732**, 221–224 (2013).
- [59] A. Magnon *et al.*, “Tracking with  $40 \times 40 \text{ cm}^2$  MICROMEGAS detectors in the high energy, high luminosity COMPASS experiment,” Nuclear Instruments and Methods in Physics Research Section A: Accelerators, Spectrometers, Detectors and Associated Equipment **478**, 210–214 (2002).
- [60] J. Derre *et al.*, “Spatial resolution in Micromegas detectors,” Nuclear Instruments and Methods in Physics Research Section A: Accelerators, Spectrometers, Detectors and Associated Equipment **459**, 523–531 (2001).
- [61] H. A. Bethe, “Quantenmechanic der Ein- und Zwei-Elektronen Probleme,” Handbuch der Physik **24**, 273 (1933).
- [62] K. J. Lindhard, “Danske Videnskab,” Selskab, Mat.-Fys 28 (1954).
- [63] W. H. Barkas and M. J. Berger, “Tables of Energy Losses and Ranges of Heavy Charged Particles in Studies in Penetration of Charged Particles in Matter,” National Academy of Sciences-National Research Council **1133**, 103 (1964).
- [64] H. H. Andersen and J. F. Ziegler, “Hydrogen: Stopping Powers and Ranges in All Elements,” The Stopping and Ranges of Ions in Matter 3 (1977).
- [65] R. M. Sternheimer and R. F. Peierls, “General Expression for the Density Effect for the Ionization Loss of Charged Particles,” Physical Review B **3**, 3681–3692 (1971).
- [66] S. R. Kelner, R. P. Kokoulin, and A. A. Petrukhin, “Bremsstrahlung from muons scattered by atomic electrons,” Physics of Atomic Nuclei **60**, 576–583 (1997).

- [67] B. Rossi, *High Energy Particles* (Prentice-Hall, Inc., Englewood Cliffs, NJ, 1952).
- [68] J. Beringer *et al.*, “Review of particle physics,” *Physical Review D* **86** (2012).
- [69] C. Grupen and B. Shwartz, *Particle detectors*, 2nd ed. (Cambridge university press, 2008), Vol. 26, p. 6.
- [70] F. Sauli, “Principles of operation of multiwire proportional and drift chambers,” European Organization for Nuclear Research, Geneva (Switzerland) (1977).
- [71] L. Landau, “On the energy loss of fast electrons by ionization,” *J. Phys. ussr* **8**, 201 (1944).
- [72] H. Bichsel, “Straggling in thin silicon detectors,” *Reviews of Modern Physics* **60**, 663 (1988).
- [73] K. S. Kölbig and B. Schorr, “A program package for the Landau distribution,” *Computer physics communications* **31**, 97–111 (1984).
- [74] J. E. Moyal, “XXX. Theory of ionization fluctuations,” *Philosophical Magazine* **46**, 263–280 (1955).
- [75] <http://www.nist.gov/pml/data/xcom/> .
- [76] M. B. Chadwick *et al.*, “ENDF/B-VII. 1 nuclear data for science and technology: cross sections, covariances, fission product yields and decay data,” *Nuclear Data Sheets* **112**, 2887–2996 (2011).
- [77] F. M. Penning, “Über den Einfluß sehr geringer Beimischungen auf die Zündspannung der Edelgase,” *Zeitschrift für Physik* **46**, 335–348 (1928).
- [78] U. Fano, “Ionization yield of radiations. II. The fluctuations of the number of ions,” *Physical Review* **72**, 26 (1947).

- [79] E. P. De Lima *et al.*, “Fano factors of rare gases and their mixtures,” *Nuclear Instruments and Methods in Physics Research* **192**, 575–581 (1982).
- [80] I. K. Bronić *et al.*, “The Fano factor for electrons in gas mixtures,” *Nuclear Instruments and Methods in Physics Research Section B: Beam Interactions with Materials and Atoms* **71**, 366–370 (1992).
- [81] [http://www.kip.uni-heidelberg.de/~coulon/Lectures/Detectors/Free\\_PDFs/Lecture7.pdf](http://www.kip.uni-heidelberg.de/~coulon/Lectures/Detectors/Free_PDFs/Lecture7.pdf) .
- [82] G. Schultz, “Etude d’un detecteur de particules a très haute précision spatiale (chambre a drift),” *Analyse des phénomènes physiques liés au fonctionnement de ce détecteur*, CERN/EP pp. 76–19 (1976).
- [83] W. R. Blum, Walter and L. Rolandi, “Particle detection with drift chambers,” Springer (2008).
- [84] J. A. Hornbeck, “The drift velocities of molecular and atomic ions in helium, neon, and argon,” *Physical Review* **84**, 615 (1951).
- [85] R. N. Varney, “Drift velocities of ions in krypton and xenon,” *Physical Review* **88**, 362 (1952).
- [86] G. C. Schultz, G. and F. Sauli, “Mobilities of positive ions in some gas mixtures used in proportional and drift chambers,” *Revue de Physique Appliquée* **12**, 67–70 (1977).
- [87] A. Blanc, “Recherches sur les mobilités des ions dans les gaz,” *J. Phys. Theor. Appl* **7**, 825–839 (1908).
- [88] M. E. Rose and S. A. Korff, “An investigation of the properties of proportional counters. I,” *Physical Review* **59**, 850 (1941).

- [89] W. Diethorn, “A Methane Proportional Counter System for Natural Radiocarbon Measurements (Thesis),” No. NYO-6628. Carnegie Inst. of Tech., Pittsburgh (1956).
- [90] H. Schlumbohm, “Zur Statistik der Elektronenlawinen im ebenen Feld. III,” *Zeitschrift für Physik* **151**, 563–576 (1958).
- [91] W. Legler, “Die Statistik der Elektronenlawinen in elektronegativen Gasen, bei hohen Feldstärken und bei großer Gasverstärkung,” *Zeitschrift Naturforschung Teil A* **16**, 253 (1961).
- [92] W. Legler, “The influence of the relaxation of the electron energy distribution on the statistics of electron avalanches,” *British Journal of Applied Physics* **18**, 1275 (1967).
- [93] G. D. Alkhazov, “Statistics of electron avalanches and ultimate resolution of proportional counters,” *Nuclear Instruments and Methods* **89**, 155–165 (1970).
- [94] H. Schindler, “Microscopic Simulation of Particle Detectors,” Diss. CERN (2012).
- [95] E. H. Posch, C. and J. Oliver, “MDT-ASD, CMOS front-end for ATLAS MDT, ATLAS Muon Note,” ATL-MUON-2002-003, CERN (2001).
- [96] G. De Geronimo *et al.*, “VMM1-An ASIC for micropattern detectors,” Nuclear Science Symposium and Medical Imaging Conference (NSS/MIC), 2012 IEEE (2012).
- [97] S. Ramo, “Currents induced by electron motion,” *Proc. Ire* **27**, 584 (1939).
- [98] G. Barouch *et al.*, “Development of a fast gaseous detector: ‘Micromegas’,” *Nuclear Instruments and Methods in Physics Research Section A: Accelerators, Spectrometers, Detectors and Associated Equipment* **423**, 32–48 (1999).
- [99] E. Mazzucato, “The T2K Time Projection Chambers: first year of operation,” *Journal of Physics: Conference Series* **309**, 1–8 (2011).

- [100] D. Neyret *et al.*, “New pixelized Micromegas detector with low discharge rate for the COMPASS experiment,” *Journal of Instrumentation* **7**, C03006 (2012).
- [101] T. Alexopoulos *et al.*, “A spark-resistant bulk-micromegas chamber for high-rate applications,” *Nuclear Instruments and Methods in Physics Research Section A: Accelerators, Spectrometers, Detectors and Associated Equipment* **640**, 110–118 (2011).
- [102] J. P. Cussonneau *et al.*, “Test of the spatial resolution of MICROMEGAS detectors,” *Nuclear Instruments and Methods in Physics Research Section A: Accelerators, Spectrometers, Detectors and Associated Equipment* **419**, 452–459 (1998).
- [103] I. Giomataris *et al.*, “Micromegas in a bulk,” *Nuclear Instruments and Methods in Physics Research Section A: Accelerators, Spectrometers, Detectors and Associated Equipment* **560**, 405–408 (2006).
- [104] S. Andriamonje *et al.*, “Development and performance of Microbulk Micromegas detectors,” *Journal of Instrumentation* **5**, P02001 (2010).
- [105] [www.3m.com/](http://www.3m.com/) .
- [106] [www.transilwrap.com/](http://www.transilwrap.com/) .
- [107] Z. Zhang, “Study of a 20 cm  $\times$  20 cm sparking-resistant micromegas,” presented at the 4th China Micro Pattern Gaseous Detector Workshop (Weihai, China, July, 2014).
- [108] <http://ie.lbl.gov/toi/nuclide.asp?iZA=260055> .
- [109] [www.ortec-online.com/](http://www.ortec-online.com/) .
- [110] <http://www.nist.gov/pml/data/xraytrans/> .

- 
- [111] A. Bisi and L. Zappa, “Statistical spread in pulse size of the proportional counter spectrometer,” *IL Nuovo Cimento* **2**, 988–994 (1955).
- [112] H. S. Snyder, “Fluctuations for proportional counters,” *PHYSICAL REVIEW* **72** (1947).
- [113] S. Behrends and A. C. Melissinos, “Properties of argon-ethane/methane mixtures for use in proportional counters,” *Nuclear Instruments and Methods in Physics Research* **188**, 521–534 (1981).
- [114] A. Delbart, “Production and calibration of 9 m<sup>2</sup> of bulk-micromegas detectors for the read-out of the ND280/TPCs of the T2K experiment,” *Nuclear Instruments and Methods in Physics Research Section A: Accelerators, Spectrometers, Detectors and Associated Equipment* **623**, 105–107 (2010).
- [115] B. Surrow *et al.*, “Development of tracking detectors with industrially produced GEM foils,” *Nuclear Instruments and Methods in Physics Research Section A: Accelerators, Spectrometers, Detectors and Associated Equipment* **572**, 201–202 (2007).
- [116] M. Iodice, “Micromegas Chamber Components & Mechanical Requirements,” presented at the ATLAS muon new small wheel reviews meeting. Slides available at <https://indico.cern.ch/event/327869/> (CERN, July, 2014).
- [117] R. Veenhof, “GARFIELD, recent developments,” *Nuclear Instruments and Methods in Physics Research Section A: Accelerators, Spectrometers, Detectors and Associated Equipment* **419**, 726–730 (1998).
- [118] R. Veenhof, <http://garfield.web.cern.ch/garfield/>.
- [119] S. F. Biagi, “Monte Carlo simulation of electron drift and diffusion in counting gases under the influence of electric and magnetic fields,” *Nuclear Instruments and Methods in Physics*

- Research Section A: Accelerators, Spectrometers, Detectors and Associated Equipment **421**, 234–240 (1999).
- [120] S. Biagi, <http://consult.cern.ch/writeup/magboltz/> .
- [121] I. Smirnov, <http://heed.web.cern.ch/heed/> .
- [122] Ö. Şahin *et al.*, “Penning transfer in argon-based gas mixtures,” *Journal of Instrumentation* **5**, P05002 (2010).
- [123] Ansys Maxwell 3D, [Available at http://www.ansys.com/](http://www.ansys.com/) .
- [124] H. Raether, *Electron avalanches and breakdown in gases* (Butterworths, London, 1964), Vol. 26.
- [125] V. Peskov and P. Fonte, “Research on discharges in micropattern and small gap gaseous detectors,” arXiv preprint arXiv:0911.0463 (2009).
- [126] P. Breuil *et al.*, “Advances in the development of micropattern gaseous detectors with resistive electrodes,” *The European Physical Journal Plus* **128**, 1–16 (2013).
- [127] D. Thers *et al.*, “Micromegas as a large microstrip detector for the COMPASS experiment,” *Nuclear Instruments and Methods in Physics Research Section A: Accelerators, Spectrometers, Detectors and Associated Equipment* **469**, 133–146 (2001).
- [128] M. S. Dixit *et al.*, “Position sensing from charge dispersion in micro-pattern gas detectors with a resistive anode,” *Nuclear Instruments and Methods in Physics Research Section A: Accelerators, Spectrometers, Detectors and Associated Equipment* **518**, 721–727 (2004).
- [129] M. Dixit *et al.*, “Micromegas TPC studies at high magnetic fields using the charge dispersion signal,” *Nuclear Instruments and Methods in Physics Research Section A: Accelerators, Spectrometers, Detectors and Associated Equipment* **581**, 254–257 (2007).

- [130] J. Wotschack, “The development of large-area micromegas detectors for the ATLAS upgrade,” *Modern Physics Letters A* **28** (2013).
- [131] P. Fonte *et al.*, “A spark-protected high-rate detector,” *Nuclear Instruments and Methods in Physics Research Section A: Accelerators, Spectrometers, Detectors and Associated Equipment* **431**, 154–159 (1999).
- [132] J. J. Desautais, P. and V. Puill, “Performance of a new type of Micromegas detector with stainless steel woven wire mesh and resistive anode readout,” *Nuclear Science Symposium Conference Record, 2003 IEEE* **1** (2003).
- [133] Beijing glass research institute, <http://www.bgri.com> .
- [134] J. C. Dawson and C. J. Adkins, “Conduction mechanisms in carbon-loaded composites,” *Journal of Physics: Condensed Matter* **8**, 8321 (1996).
- [135] <http://www.westlakeplastics.com> .
- [136] D. Thers *et al.*, “Parallel ionization multiplier (PIM): a new concept of gaseous detector for radiation detection improvement,” *Nuclear Instruments and Methods in Physics Research Section A: Accelerators, Spectrometers, Detectors and Associated Equipment* **504**, 161–165 (2003).
- [137] J. Beucher *et al.*, “Parallel ionization multiplier: A gaseous detector dedicated to the tracking of minimum ionization particles,” *Nuclear Instruments and Methods in Physics Research Section A: Accelerators, Spectrometers, Detectors and Associated Equipment* **573**, 294–297 (2007).
- [138] J. Donnard *et al.*, “The micro-pattern gas detector PIM: A multi-modality solution for novel investigations in functional imaging,” *Nuclear Instruments and Methods in Physics Research*

- Section A: Accelerators, Spectrometers, Detectors and Associated Equipment **610**, 158–160 (2009).
- [139] A. N. Akindinov *et al.*, “Latest results on the performance of the multigap resistive plate chamber used for the ALICE TOF,” Nuclear Instruments and Methods in Physics Research Section A: Accelerators, Spectrometers, Detectors and Associated Equipment **533**, 74–78 (2004).
- [140] G. Aielli *et al.*, “Performance of a large-size RPC equipped with the final ATLAS front-end electronics at X5-GIF irradiation facility,” Nuclear Instruments and Methods in Physics Research Section A: Accelerators, Spectrometers, Detectors and Associated Equipment **456**, 77–81 (2000).
- [141] M. Abbrescia *et al.*, “Aging study for resistive plate chambers of the CMS muon trigger detector,” Nuclear Instruments and Methods in Physics Research Section A: Accelerators, Spectrometers, Detectors and Associated Equipment **515**, 342–347 (2003).
- [142] R. Arnaldi *et al.*, “Spatial resolution of RPC in streamer mode,” Nuclear Instruments and Methods in Physics Research Section A: Accelerators, Spectrometers, Detectors and Associated Equipment **490**, 51–57 (2002).
- [143] C. Carrillo, “The CMS RPC project, results from 2009 cosmic-ray data,” Nuclear Instruments and Methods in Physics Research Section A: Accelerators, Spectrometers, Detectors and Associated Equipment **661**, S19–S22 (2012).
- [144] S. Baranov *et al.*, “Estimation of radiation background, impact on detectors, activation and shielding optimization in ATLAS,” No. ATL-GEN-2005-001 (2005).
- [145] C. Young, “Timing of signal and background,” presented at the ATLAS muon upgrade regular review meeting. Slides available at: <https://indico.cern.ch/event/151136/> (CERN, 2011).

- [146] J. Chapman and J. Mann, “Digital mean timers for the straw tube tracking system at SDC,” Nuclear Science, IEEE Transactions **40**, 794–799 (1993).
- [147] J. Ye *et al.*, “Study on the position resolution of resistive plate chamber,” Nuclear Instruments and Methods in Physics Research Section A: Accelerators, Spectrometers, Detectors and Associated Equipment **591**, 411–416 (2008).
- [148] Q. Li *et al.*, “Study of spatial resolution properties of a glass RPC,” Nuclear Instruments and Methods in Physics Research Section A: Accelerators, Spectrometers, Detectors and Associated Equipment **663**, 22–25 (2012).
- [149] R. Cardarelli *et al.*, “Improving track resolution in the RPC chamber,” Nuclear Physics B-Proceedings Supplements **158**, 25–29 (2006).
- [150] G. Drake *et al.*, “A digital hadron calorimeter with resistive plate chambers for the linear collider,” International Journal of Modern Physics A **20**, 3830–3833 (2005).
- [151] J. Chapman *et al.*, “On-chamber readout system for the ATLAS MDT Muon Spectrometer,” Nuclear Science Symposium Conference Record, 2003 IEEE 1 (2003).
- [152] B. Bittner *et al.*, “Development of fast high-resolution muon drift-tube detectors for high counting rates,” Nuclear Instruments and Methods in Physics Research Section A: Accelerators, Spectrometers, Detectors and Associated Equipment **628**, 154–157 (2011).
- [153] E. H. Posch, Christoph and J. Oliver, “Mdt-asd, cmos front-end for atlas mdt,” (2007).
- [154] Y. Arai, “Development of front-end electronics and TDC LSI for the ATLAS MDT,” Nuclear Instruments and Methods in Physics Research Section A: Accelerators, Spectrometers, Detectors and Associated Equipment **453**, 365–371 (2000).
- [155] Y. Arai, “AMT-3 (ATLAS Muon TDC version 3) User’s Manual,” (2005).

- [156] P. Bagnaia *et al.*, “Charge-dependent corrections to the time response of ATLAS muon chambers,” Nuclear Instruments and Methods in Physics Research Section A: Accelerators, Spectrometers, Detectors and Associated Equipment **533**, 344–352 (2004).
- [157] A. Polini, “Design and performance of the detector control system of the ATLAS resistive-plate-chamber muon spectrometer,” Nuclear Instruments and Methods in Physics Research Section A: Accelerators, Spectrometers, Detectors and Associated Equipment **661**, S15–S18 (2012).
- [158] F. Anghinolfi *et al.*, “NINO: an ultra-fast and low-power front-end amplifier/discriminator ASIC designed for the multigap resistive plate chamber,” Nuclear Instruments and Methods in Physics Research Section A: Accelerators, Spectrometers, Detectors and Associated Equipment **533**, 183–187 (2004).
- [159] M.C.S. Williams, Private communication (2012).
- [160] M. Mota *et al.*, “A flexible multi-channel high-resolution time-to-digital converter ASIC,” Nuclear Science Symposium Conference Record, 2000 IEEE 2 (2000).
- [161] M. Abbrescia *et al.*, “The EEE Project: cosmic rays, multigap resistive plate chambers and high school students,” Journal of Instrumentation **7**, P11011 (2012).
- [162] <http://root.cern.ch/> .
- [163] K. Doroud *et al.*, “MRPC-PET: A new technique for high precision time and position measurements,” Nuclear Instruments and Methods in Physics Research Section A: Accelerators, Spectrometers, Detectors and Associated Equipment **660**, 73–76 (2011).
- [164] B. Alpat, “The alpha magnetic spectrometer (AMS) experiment on the international space station,” Nuclear Instruments and Methods in Physics Research Section A: Accelerators, Spectrometers, Detectors and Associated Equipment **461**, 272–274 (2001).

- [165] B. Alpat *et al.*, “The internal alignment and position resolution of the AMS-02 silicon tracker determined with cosmic-ray muons,” Nuclear Instruments and Methods in Physics Research Section A: Accelerators, Spectrometers, Detectors and Associated Equipment **613**, 207–217 (2010).
- [166] A. Di Ciaccio, “The ATLAS RPC trigger chamber system,” Nuclear Instruments and Methods in Physics Research Section A: Accelerators, Spectrometers, Detectors and Associated Equipment **572**, 48–49 (2007).
- [167] M. Abbrescia *et al.*, “Study of long-term performance of CMS RPC under irradiation at the CERN GIF,” Nuclear Instruments and Methods in Physics Research Section A: Accelerators, Spectrometers, Detectors and Associated Equipment **533**, 102–106 (2004).
- [168] R. Arnaldi *et al.*, “A low-resistivity RPC for the ALICE dimuon arm,” Nuclear Instruments and Methods in Physics Research Section A: Accelerators, Spectrometers, Detectors and Associated Equipment **451**, 462–473 (2000).
- [169] R. Cardarelli *et al.*, “High rate fast precision tracking trigger with RPCs,” plenary talk at RPC 2012 conference (Frascati, 2012).
- [170] S. Agosteo *et al.*, “A facility for the test of large-area muon chambers at high rates,” Nuclear Instruments and Methods in Physics Research Section A: Accelerators, Spectrometers, Detectors and Associated Equipment **452**, 94–104 (2000).
- [171] L. Paolozzi, “Performance of a new generation RPCs for particle physics at colliders of the next generation,” presented at the 13th Vienna Conference on Instrumentation (Vienna, 2013).

- [172] K. Nagai, “Thin gap chambers in ATLAS,” Nuclear Instruments and Methods in Physics Research Section A: Accelerators, Spectrometers, Detectors and Associated Equipment **384**, 219–221 (1996).
- [173] N. Majumdar and S. Mukhopadhyay, “Simulation of 3D electrostatic configuration in gaseous detectors,” Journal of Instrumentation **2**, P09006 (2007).
- [174] D. Lazic *et al.*, “Drift velocity in n-pentane mixtures and its influence on timing properties of thin gap chambers,” Nuclear Instruments and Methods in Physics Research Section A: Accelerators, Spectrometers, Detectors and Associated Equipment **410**, 159–165 (1998).
- [175] F. Hartjes *et al.*, “A drift chamber with variable drift velocity,” Nuclear Instruments and Methods in Physics Research Section A: Accelerators, Spectrometers, Detectors and Associated Equipment **256**, 55–64 (1987).
- [176] O. P. Kiselev, O. and A. Vorobyov, “Measurement of electron drift velocities and Lorentz angles in fast gas mixtures,” Nuclear Instruments and Methods in Physics Research Section A: Accelerators, Spectrometers, Detectors and Associated Equipment **367**, 306–310 (1995).
- [177] K. Hoshina *et al.*, “Lorentz angle measurement for CO<sub>2</sub>/isobutane gas mixtures,” Nuclear Instruments and Methods in Physics Research Section A: Accelerators, Spectrometers, Detectors and Associated Equipment **479**, 278–293 (2002).
- [178] R. Veenhof, Private communication (2013).
- [179] H. Schindler, S. F. Biagi, and R. Veenhof, “Calculation of gas gain fluctuations in uniform fields,” Nuclear Instruments and Methods in Physics Research Section A: Accelerators, Spectrometers, Detectors and Associated Equipment **624**, 78–84 (2010).

- [180] A. I. Mincer *et al.*, “Charge production in thin gap multi-wire chambers,” *Nuclear Instruments and Methods in Physics Research Section A: Accelerators, Spectrometers, Detectors and Associated Equipment* **439**, 147–157 (2000).
- [181] D. Pomarède and M. Virchaux, “The Persint visualization program for the ATLAS experiment,” *arXiv preprint cs/0305057* (2003).
- [182] O. Sasaki and M. Yoshida, “ASD IC for the thin gap chambers in the LHC ATLAS Experiment,” *IEEE Nuclear Science Symposium Conference Record* 1 (1998).
- [183] E. Gygi and F. Schneider, “Considerations about the charge collection on the Iarocci-tube,” No. CERN-EP-INT-83-06. CM-P00060301 (1983).
- [184] M. Ellilä, “Charge diffusion in the capacitive readout of resistive cathodes,” *Nuclear Instruments and Methods in Physics Research Section A: Accelerators, Spectrometers, Detectors and Associated Equipment* **277**, 507–512 (1989).
- [185] M. S. Dixit and A. Rankin, “Simulating the charge dispersion phenomena in Micro Pattern Gas Detectors with a resistive anode,” *Nuclear Instruments and Methods in Physics Research Section A: Accelerators, Spectrometers, Detectors and Associated Equipment* **566**, 281–285 (2006).
- [186] E. Gatti *et al.*, “Optimum geometry for strip cathodes or grids in MWPC for avalanche localization along the anode wires,” *Nuclear Instruments and Methods* **163**, 83–92 (1979).
- [187] E. Mathieson and J. S. Gordon, “Cathode charge distributions in multiwire chambers: II. Approximate and empirical formulae,” *Nuclear Instruments and Methods in Physics Research Section A: Accelerators, Spectrometers, Detectors and Associated Equipment* **227**, 277–282 (1984).

- 
- [188] Cadence PSpice, [http://www.cadence.com/products/orcad/pspice\\_simulation/pages/default.aspx](http://www.cadence.com/products/orcad/pspice_simulation/pages/default.aspx).



# Appendix A

## List of Publications

The following publications are based on works presented in this dissertation

### **Peer reviewed paper or public note**

- J. Chapman *et al.*, “Simulation Studies of Characteristics and Performances of small-strip, Thin Gap Chamber for the ATLAS New Small Wheel Upgrade”, ATL-MUON-PUB-2014-001 (2014).
- Y.H.Wei *et al.*, “Detection of Alpha Particles and Low Energy Gamma Rays by Thermo-Bonded Micromegas in Xenon Gas”, IEEE Transactions on Nuclear Science, 60.4 (2013): 3008-3013.
- G. Aielli *et al.*, “Studies on fast triggering and high precision tracking with Resistive Plate Chambers”, Nuclear Instruments and Methods in Physics Research Section A: Accelerators, Spectrometers, Detectors and Associated Equipment, 714 (2013): 115-120.
- L. Guan *et al.*, “Micromegas prototypes with thermo-bond film separators”, Chinese Physics C, 35.2 (2011): 163.

- J.J. Guo *et al.*, “Electron collection efficiency and gain of Micromegas”, Journal of University of Science and Technology of China, 6 (2010): 010.
- T. Alexopoulos *et al.*, “Development of large size Micromegas detector for the upgrade of the ATLAS Muon system”, Nuclear Instruments and Methods in Physics Research Section A: Accelerators, Spectrometers, Detectors and Associated Equipment, 617.1 (2010): 161-165.

### Conference proceedings

- R. Cardarelli *et al.*, "A high rate fast precision tracking trigger with RPCs." Proceedings of RPC 2012 conference.
- L. Guan *et al.*, "Micromegas and PIM-like with thermo-bond film frame and spacers." Nuclear Science Symposium Conference Record (NSS/MIC), 2010 IEEE.
- L. Guan *et al.*, "Micromegas with high resistivity anode." Nuclear Science Symposium Conference Record (NSS/MIC), 2010 IEEE.
- L. Guan *et al.*, "Simulation studies of Micromegas and parallel ionization multiplier with woven mesh." Nuclear Science Symposium Conference Record (NSS/MIC), 2010 IEEE.